Ken-ichi Tanaka

Dynamic Chemical Processes on Solid Surfaces

Chemical Reactions and Catalysis

Springer

Dynamic Chemical Processes on Solid Surfaces

Ken-ichi Tanaka

Dynamic Chemical Processes on Solid Surfaces

Chemical Reactions and Catalysis

Springer

Ken-ichi Tanaka
The University of Tokyo, Institute of Solid
State Physics
Kashiwa, Chiba
Japan

ISBN 978-981-10-2838-0 ISBN 978-981-10-2839-7 (eBook)
DOI 10.1007/978-981-10-2839-7

Library of Congress Control Number: 2016958979

Printed on acid-free paper

This Springer imprint is published by Springer Nature
The registered company is Springer Nature Singapore Pte Ltd.
The registered company address is: 152 Beach Road, #22-06/08 Gateway East, Singapore 189721, Singapore

Preface

The definition of materials is quite different in chemistry and physics. That is, a group of materials or compounds having novel functional or chemical properties are considered new materials in chemistry. From this point of view, the surface of a solid is quite interesting as a material, because chemical properties depend on the crystal planes; a different crystal plane has different chemical properties. For this reason, the property of solid materials known to us is that of their surface, and no one knows the real chemical property of the solid material itself.

If we consider a two-dimensional material such as graphene, graphite, and MoS_2, their surface is a one-dimensional edge. The different chemical property of a one-dimensional edge, the surface, is revealed by breaking it from that of the parent material. Graphite and MoS_2 are very stable materials chemically and thermally, but with their one-dimensional edge formed by breaking, the surface of two-dimensional materials provides active new materials. In fact, the edge of MoS_2 becomes an active catalyst as shown in this book.

If the surface formed by breaking provides a new chemical material, the reaction of surface atoms would provide additional new materials, although these could not be removed from the bulk. According to this idea, the numerous phenomena taking place on the surface are responsible for the new materials which can exist only in the two- or one-dimensional space. Some of these materials are passive, but some of them have unique reactivity in chemical reactions and catalysis, even though these materials can exist only on a specific surface. An additional important feature of the new materials is that the chemical reaction dynamics are restricted in two- or one-dimensional space as discussed in this book.

About 100 years ago, the first scientific page of catalysis in metals was opened. At that time, a metal surface was imagined to be an array of atoms like a chessboard. In the last 50 years, the remarkable development of vacuum technology and electronics has enabled us to detect feeble currents and to elucidate the inherent properties of the surface of solid materials. However, most work has focused on the crystal structure and the electronic structure of the surface in relation to those of solid materials, which are well rationalized by the band structure and the lattice energy calculations in relation to those of solid materials. However, it can be said

that little study has been done from a view point that the surface comprises new chemical materials, although metal clusters are recognized as new material.

This book throws some light on the surface as a realm of unexplored interesting materials existing on the solids. The following passage from Roald Hoffmann in *Solids and Surfaces—A Chemist's View of Bonding in Extended Structures* is relevant.

> A surface—be it of metal, an ionic or covalent solid, semiconductor—is a form of matter with its own chemistry. In its structure and reactivity, it will bear resemblance to other forms of matter: bulk, discrete molecules in the gas phase and various aggregated states in solution. And it will have differences. Just as it is important to find the similarities, it is also important to note the differences. The similarities connect the chemistry of surfaces to the rest of chemistry, but the differences make life interesting (and make surfaces economically useful).

The present book is composed of two parts: "Dynamic Chemical Processes on Metals" and "Dynamics of Chemical Reactions in Catalysis." Part I illustrates various unusual chemical processes on metal surfaces regulated by two-dimensional freedom, but the characteristic reactions of surface atoms are difficult to anticipate. When Cu(100) and Cu(110) surfaces are exposed to O_2 at room temperature, O_2 molecules dissociate into O(a) atoms on either a Cu(100) or Cu(110) surface. The O (a) atoms are stabilized by forming a minimum size of c(2 × 2) domains (made by several O atoms) on a Cu(100) surface, whereas O(a) atoms on a Cu(110) surface undergo reaction with surface Cu atoms and one-dimensional (–Cu–O–) strings are formed on a Cu(110) surface, referred to as "quasi-compounds" in this book.

To understand real catalysis, we must know the dynamic chemical processes on the surface. As discussed in Part II, it has been accepted that the kinetic equation of catalytic reaction depends on the rate determining the slow steps of the reaction, but the intrinsic activity of the surface as a catalyst depends on the steady concentration of active compounds formed on the surface.

The role of promoting materials is quite important in practical catalysis, but it remains an awkward common problem in catalysis. In Part II, Chap. 10, Sects. 10.4 and 10.5, the role of promoting materials in selective oxidation of CO in excess H_2 on metals is carefully discussed. It could be said that the cooperation of different functional materials over the same surface is a big advantage of heterogeneous catalysis. If efficient cooperation of two or more materials in a series of connected reactions could be designed, this would be the golden key to attaining a high-performance catalyst, as discussed in Sects. 10.4 and 10.5. In this sense, this book will be a good guide not only for the reader interested in the basic chemistry of solid surfaces but also for the reader anticipating the surface to be new materials and having an invaluable idea for designing high-performance catalysts.

Kashiwa, Japan Ken-ichi Tanaka
September 2016

Acknowledgements

Upon completing the writing this book, first of all I must express my grateful acknowledgment to Emeritus Prof. Kenzi Tamaru of The University of Tokyo, who first enlightened me in the interesting aspects of the dynamics of catalysis. I am indebted to Emeritus Prof. Yoshitada Murata of The University of Tokyo, who suggested that I bring the progress of surface sciences to catalysis. I also express my sincere thanks to Mr. Mitsushi Umino, President of Astec Co., for his long-time encouragement of my research work. The greatest appreciation is to my wife, Masako Tanaka, for her long-time support of my research life.

I deeply appreciate Prof. Flemming Besenbacher of the University of Aarhus for his fruitful discussions with me. His experiments using the STM convinced me of a new concept of low-dimensional quasi-compounds (one- or zero-dimensional compounds on a surface) in 1993. I also appreciate Prof. Ben E. Nieuwenhuys of the University of Leiden for his collaboration on a Pt–Rh(100) single crystal, which was the start of my series work on the Pt–Rh bimetals and Pt–Rh alloy catalyst and the idea of the formation of a "new two-dimensional Pt–Rh-ordered alloy" on the surface. I also want to express my sincere thanks to Prof. Hong He of the Research Center for Eco-Environmental Science, Chinese Academic of Sciences, and Prof. Zhao-Xiong Xie and Prof. Youzhu Yuan of Xiamen University for their collaboration and many fruitful discussions with me for my experimental work at the Saitama Institute of Technology.

For the experiments on which this book is based, I am indebted to my collaborators and the graduate students at the Research Institute for Catalysis, the Faculty of Engineering of Hokkaido University (1972–1984), the Institute for Solid State Physics of the University of Tokyo (1985–1998), and the Institute of Advanced Sciences of the Saitama Institute of Technology (1999–2003).

My deep appreciation goes to Mrs. Qingcai Feng of the Research Center for Eco-Environmental Sciences of the Chinese Academy of Sciences for her help in completing this book, and to Dr. Catherine Rice for her very careful and suitable improvement for my descriptions. I also thank Dr. Christopher Borroni-Bird for his help.

Finally, I wish to express my gratitude to the late Prof. George Blyholder and the late Prof. Samuel Siegel of the University of Arkansas in Fayetteville, Arkansas, USA, who had a great influence on me during my stay there as a postdoctoral researcher.

I also express my thanks to Dr. Shinichi Koizumi of Springer for his warm encouragement to publish this book.

September 2016 Ken-ichi Tanaka

Contents

Part I
Dynamic Chemical Processes on Metals

Chapter 1
Introduction

Abstract Various unique reactions and dynamic motions of atoms and molecules are known to occur on solid surfaces. In this chapter, the author throws light on these unusual new materials and their dynamic processes is on the surface. Removing unnecessary dynamic motion of adsorbed species on the surface is an important strategy to solve the reaction mechanisms and the roles of promoting materials in catalysis.

Keywords Intermediates · Dynamics · Pt–Rh alloy · Quasi-compounds · Adsorption · STM (scanning tunneling microscopy) · LEED (low-energy electron diffraction) · Activation of surface

Solid materials are necessarily surrounded by two-dimensional (2-D) materials formed by breaking as shown in Fig. 1.1a, and the property of surface is recognized as the property of solid materials. If we consider the two-dimensional materials such as graphite and MoS_2, the edge made by breaking, Fig. 1.1b, gives entirely different property from that of the materials. Similarly, one-dimensional molecule serves zero-dimensional radical or ion at the terminal end as shown in Fig. 1.1c. The array of atoms on the surface is well explained by the lattice energy calculations, and the electronic structure of the surface is also well described by the band structure at the surface, but it is quite difficult to assert the chemical properties of the surface. If the surface is considered as one-dimensionally lowered new materials, then the chemical reactions taking place on the surface are the dynamics of atoms and molecules restricted in one-dimensionally lowered space. As described in this book, the dynamics of atoms or molecules on the surface are quite different from our known reactions in 3-D space, because a surface process cannot be free from its mother material.

If we consider the lamellar compound MoS_2, the surface made by breaking (definition of the surface) is the edge of MoS_2, which is different from the two-dimensional basal plane of MoS_2 (Sulfur sheet); that is, one degree-of-freedom lowered materials are formed by breaking. If the atoms on the surface react with additional atoms or molecules, then additional new compounds are formed along

K. Tanaka, *Dynamic Chemical Processes on Solid Surfaces*,
DOI 10.1007/978-981-10-2839-7_1

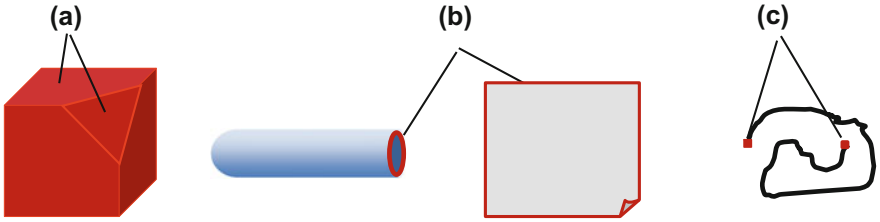

Fig. 1.1 One-dimensionally lowered new materials are formed by breaking: **a** Surface is two-dimensional materials formed by breaking three-dimensional solids. **b** Edge is one-dimensional materials made by breaking two-dimensional materials. **c** Zero-dimensional radial or ion is formed by breaking of long molecules

the edge. These newly formed compounds are evidently different from adsorbed atoms or molecules on the surface, because adsorbed molecules can be taken out from the surface, but these newly formed compounds on the surface cannot be taken out from the surface and can exist only on the mother material.

From this viewpoint, a STM experiment on a Ni(110) surface exposed to O_2 and H_2 reported by Besenbacher and his coworkers [1] in 1990 was a groundbreaking result, which proved definitively the difference of a reaction with surface atoms from the adsorption of atoms on the surface. With this experiment, we realized the formation of unknown compounds by the reaction of adsorbed O(a) and H(a) with surface Ni atoms. These compounds have their own stoichiometry and characteristic of low-dimensional molecule-like structure on specific metal surfaces, but their features are entirely different from those of our known molecules or compounds. These new materials are difficult to take out them from the surface; that is, these materials can exist only on the surface. Taking these facts into account, Tanaka [2] named these compounds "**pseudo-molecules**" or "**quasi-compounds**" as is explained in detail in Chap. 4 in **Part I**.

Formation of quasi-compounds is evidently different from the adsorption of atoms and/or molecules, which is clearly shown on the Cu(100) and Cu(110) surface exposed to O_2 as shown in Fig. 4.4 of **Part I**. That is, the adsorption of O(a) takes place on the Cu(100) surface, whereas the formation of the quasi-compound (–CuO–) proceeds on the Cu(110) surface. Furthermore, one can prepare additional quasi-compound (–CuO–) on a Ag(110) surface by using the reaction of (–AgO–) on Ag(110) with Cu atoms. Newly formed quasi-compound of (–CuO–) on the Ag (110) undergoes reversible reaction, $(Cu_2)_3 + O_2 \rightleftharpoons$ (–CuO–), which provides another quasi-compound $(Cu_2)_3$, on the Ag(110) surface. Furthermore, the reaction of Cu atoms with the quasi-compounds (–AgO–) and $Ag(CO_3)$ prepared on Ag (110) can control the selectivity by the electrostatic potential by using a Cu-coated STM W-tip, as shown in Figs. 5.1 and 5.2 in **Part I**.

From this point of view, the reaction of heteroatomic molecules such as CO, NO, and NH_3 with surface metal atoms formed is interesting because two or more quasi-compounds are simultaneously formed on the surface. The reaction of NO molecules on a Cu(110) surface is a prominent example. The adsorbed NO

molecules on the Cu(110) surface provide (–CuO–) strings and Cu_3N dots according to the equations of Eq. (1.1). If this surface is followed by exposing H_2 at room temperature, then (–CuO–) strings react with H_2, but Cu_3N dots cannot react with H_2. Accordingly, it is evident that the Cu(110) surface is inactive for the catalytic reduction of NO with H_2.

$$\begin{aligned}
&O_2 + Cu(110) \rightarrow p(2 \times 1)(-\mathbf{CuO}-)/Cu(110)\\
&N + Cu(110) \rightarrow p(2 \times 3) - \mathbf{Cu_3N}/Cu(110)\\
&NO + Cu(110) \rightarrow p(2 \times 3) - \mathbf{Cu_3N}/Cu(110) + p(2 \times 1)(-\mathbf{CuO}-)/Cu(110)\\
&NO + H_2 + Cu(110) \rightarrow p(2 \times 3) - \mathbf{Cu_3N}/Cu(110)
\end{aligned} \tag{1.1}$$

Taking these results into account, one can expect more interesting chemical processes on bimetal surfaces. In fact, a very striking phenomenon was observed not only on the Pt–Rh(100) alloy surface, but also on the Pt/Rh(100) or Rh/Pt(100) bimetal surfaces when these surfaces were exposed to O_2 or NO at 400 K. Pt(100) and Rh(100) are not active for the catalytic reduction of NO with H_2, and a Pt–Rh (100) alloy and the Rh/Pt(100) or Pt/Rh(100) bimetal surfaces are also not active for the catalytic reduction of NO with H_2. However, the alloy and bimetallic surfaces change to highly active catalysts at 400 K in O_2 or NO, and the catalytic reduction of NO with H_2 well proceeds at temperatures higher than 400 K. That is, a highly active surface is formed by a chemical reconstruction of the surfaces with O_2 or NO at 400 K. It was found that the active surface for the reaction of NO with H_2 is composed of an ordered array of Pt and Rh, which is an active surface responsible for highly active Pt–Rh three-way catalyst [3, 4], but the role of each Pt and Rh atom in the catalysis is still unclear.

To appreciate the present status of research on catalyst and catalysis, a brief history of catalysis and the development of surface science may be helpful. The fundamental concept of catalysis was established by kinetic studies on metals by Irving Langmuir (Nobel Prize 1932) [5], but the real role of the surface in catalysis was an enigma for a long time, because the surface itself has been an impenetrable black box, as was jokingly described, "the bulk was made by God but the surface was made by the Devil," by Wolfgang Pauli (Nobel Prize in 1945) in 1930. In fact, knowledge of the surface was speculative until its ordered structure was deduced by the tool of electron diffraction. Despite this, the potential of catalysis was highlighted in the early part of the twentieth century, which made remarkable development chemical industry by using the so-called heterogeneous catalysts. The hydrogenation of unsaturated hydrocarbons using a Ni catalyst by Paul Sabatier (Nobel Prize in 1912) and the synthesis of ammonia by the hydrogenation of N_2 using Fe and Os metals by Fritz Haber (Nobel Prize in 1918) are seminal works.

As is well known, a diffraction phenomenon suggesting the wave nature of electrons, predicted by De Broglie (Nobel Prize 1929), was accidentally found on a contaminated Ni surface by C.J. Davison (Nobel Prize 1937) and L.H. Germer, which was the most important groundbreaking events in removing the mysterious

veil of the surface. The study of solid surfaces was rapidly advanced after the Second World War (1945) by the low-energy electron diffraction (LEED) optics improved by L.H. Germer, who made a vital contribution to the development of surface studies. In 1964, he wrote in Physics Today: "*The most significant result that has been obtained up to this time from LEED studies is the observation of Reconstruction*" [6].

It is now not difficult to evaluate the shifting of atoms in the first several surface layers by intensity analysis of LEED patterns, but we are still surprised by various unexpected properties of the surface as materials in various chemical processes. Scanning tunneling microscopy (STM), invented by Binnig and Rohrer [7, 8] in **1983** (Nobel Prize in Physics, **1987**), caused a revolution in the study of conductive material surfaces, and it is now possible to directly touch the surface of various materials and detect the atoms and molecules adsorbed on a surface or the compounds formed by the reaction with surface atoms in atomic resolution. Adsorption of atoms, and molecules, and the formation of intermediates will create a local distortion of the surface atoms, but the dynamic changes of the local distortion with adsorption, reaction, and desorption are difficult to capture at the present time.

The dynamics of adsorbed atoms, molecules, and intermediate species on the surface are still a difficult subject, because it is essentially different from the dynamics of molecules in the gas phase or in the liquid phase. A good example is the simultaneous desorption of N_2 and NO from a Pd(110) surface at 490 K. When a Pd(110) surface with coadsorbed NO(a) and N(a) was heated in vacuum, NO and N_2 molecules are simultaneously desorbed at 490 K. Desorbed NO molecules take on a perpendicular distribution to the surface, but the simultaneously desorbed N_2 molecules exhibit two spatial distributions, one of which is normal to the surface, but the other takes ca. 38° off-normal from the perpendicular to the surface along the [001] direction as shown in Fig. 8.2 in **Part II**. However, the N_2 molecules formed by the catalytic reaction of NO with H_2 on Pd(110) surface showed a cos θ distribution. Catalysis is a series of connected chemical reactions over the surface, which is far more complex compared to those in the gas phase or in the liquid phase, and interesting dynamic processes taking place on the surfaces are discussed in detail in Chap. 8 of **Part II**.

It should be remembered that a freshly prepared surface is active for the adsorption and reaction of molecules, but it is not necessarily an active surface as a catalyst. Active functional surface or materials are formed during catalysis as schematically described in Fig. 1.2 [3], and each activation process will be discussed for practical catalytic reactions in **Part II**.

It should be pointed out that the real mechanism of catalysis cannot be clarified by the characterization of catalyst or by the first principle calculation by using statistic data attained by the characterization; that is, experimental evidence supporting the dynamics of a series-connected reaction is essential. We should be reminded that a catalytic reaction is accomplished by a series-connected chemical processes on the surface, but the contribution of some extra processes makes confuse the real mechanism of catalysis. One good example is the Horiuti–Polanyi mechanism, in which the two independent reactions cannot be distinguished by

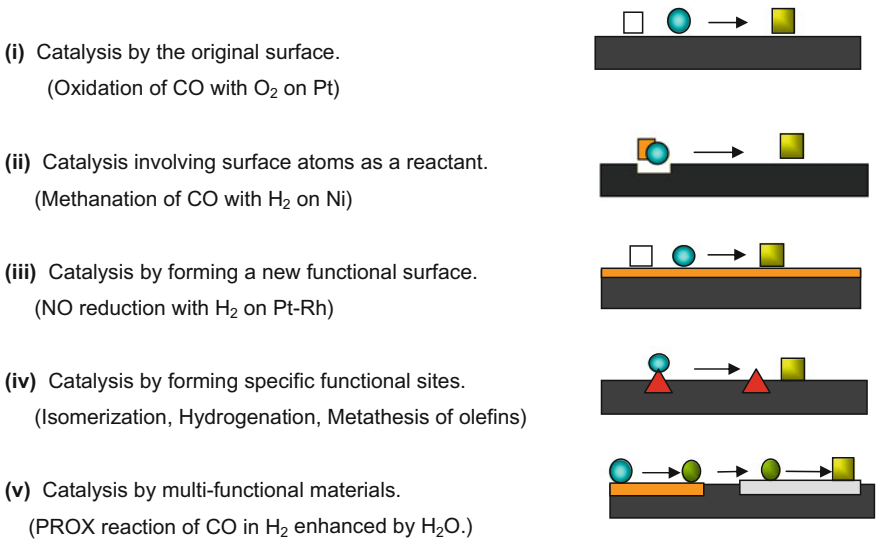

Fig. 1.2 Active catalyst is formed by various activation processes of the surface. Practical examples are shown in parentheses [3]

rapid surface scrambling of adsorbed hydrogen atoms. One strategy to clarify the real mechanism in catalysis is to remove unnecessary migration of intermediates during catalysis. Based on this idea, the isomerization and the hydrogenation of olefins were performed on MoS_2, where the reaction should take place on the sites existing in the one-degree lowered space of the edge of MoS_2. As a result, two alkyl intermediates, one of which is active for the isomerization and the other for the hydrogenation of olefins, are clearly distinguished on the MoS_2 catalyst [9, 10].

The importance of reaction dynamics in catalysis is discussed precisely in **Part II**. As the reaction rate depends on the rate-determining slow step, the importance of rapid processes in catalysis is very often ignored. In fact, if a rapid process is disturbed, the catalytic reaction stops, which is a paradox to consider in the reaction kinetics of catalysis. On the other hand, it should be remembered that the dynamic cooperation of two or more functional sites or materials on the surface is an advantageous function of heterogeneous catalysis. If a catalytic reaction accomplished by the cooperation of two different functional sites is considered, catalysis will be disturbed by stopping the transport of an intermediate between the two sites. However, it is difficult to confirm whether the activity is disturbed by stopping the transport of intermediates or the functional distortion of active sites. An illustrative example is the catalytic oxidation of CO with O_2 enhanced by H_2 (actually H_2O) on the Pt/CNT (carbon nanotubes) catalyst inferred from **Part II,** Sects. 10.4 and 10.5. In the case of Pt/CNT, the CNT have Ni–MgO at the terminal end. If the Ni–MgO is removed (CNT–p), the Pt/CNT–p has no catalytic activity for the oxidation of CO enhanced by H_2 at low temperature [11, 12]. In this case, Pt particles on the trunk of CNT are completely separated from the Ni–MgO localized at the terminal

end of the CNT, but these two are indispensable for the oxidation of CO enhanced by H_2 (actually H_2O). Taking these facts into account, a new concept is proposed for the selectivity, which depends on the dynamics. As it is precisely mentioned in Chap. 10, Sect. 10.4, the role of a H_2O molecule is expressed by the equation $CO + ½\ O_2 + n\ H_2O \rightarrow CO_2 + n\ H_2O$, where H_2O is a dynamic working molecular catalyst over the Pt/CNT catalyst [11–14].

In this case, it is evident that the role of Ni–MgO is neither the "activation of Pt metal" nor the "formation of an active form of Pt," but provides a new oxidation reaction of CO taking place by rapid transport of OH^- ion from Ni–MgO to the Pt particles as discussed in detail in Sect. 10.5 of **Part II**. The dynamic mechanism of the oxidation of CO enhanced by H_2 (H_2O) was clarified by in situ DRIFT spectroscopy, and a new concept for the selectivity was proposed, which is given by repeating dynamic contribution of one H_2O molecule. Another interesting phenomenon in catalysis is the selective catalysis regulated by the restricted dynamic motion of intermediates; that is, the selectivity is given by selective internal rotational motion of intermediates as shown in Fig. 10.5 in **Part II**. In this case, the internal rotation of a large group of the intermediate was prevented, so that the corresponding catalytic reaction was selectively restricted. Such an apparent paradox in catalysis can obscure the essential role catalysis. In fact, we can observe such a paradoxical phenomenon in the hydrogen exchange reaction between propene-$[^2H]_0$ and propene-$[^2H]_6$ on MoS_2 as shown in Fig. 10.6 in **Part II**.

Taking these results into account, a new concept of "dynamic working of H_2O molecule as a molecular catalyst" is proposed in Sects. 10.4 and 10.5 in this book. We can rationalize various unsolved phenomena in the highly selective preferential oxidation (PROX) reaction of CO in excess H_2 by this new concept. For example, a highly selective PROX reaction of CO was attained by Pt nanorods held inside SiO_2 nanotubes, while no such PROX reaction was catalyzed on Pt rods supported on the outer surface of SiO_2 nanotubes, as shown in Fig. 10.25 in **Part II.** More strange phenomena were observed in the PROX reaction of CO in H_2 on a Au/CeO_2 catalyst, on which selective oxidation of CO in H_2 had a remarked effect of the crystal shape of CeO_2 although the overall consumption of O_2 was not affected by the crystal shapes of CeO_2, as shown in Fig. 10.31. These phenomena are well rationalized by the concept of "dynamic working of H_2O molecule as a catalyst"; that is, the efficiency depends on the residence time of H_2O on the catalyst surface. In fact, the selectivity for the PROX reaction of CO in H_2 on the Au/CeO_2 catalyst depends on the ratio $(Au^+ + Au^{3+})/(Au^0 + Au^+ + Au^{3+})$, which has an influence on the residence time of H_2O. However, the sites responsible for the oxidation reaction of CO catalyzed by H_2O are still not clearly identified. The effect of alkali metal ions (Li^+, Na^+, and K^+) on the selective oxidation of CO in H_2 is also an interesting subject. Till now, the role of alkali metal ions has been explained by the formation of active sites, such as $PtO(OH)_x$ alkali metal ions and $Au–O(OH)_x$–(Na or K), but the oxidation reaction has been premised in almost all cases as the same reaction mechanism that has been confirmed to occur on the Pt surface. The oxidation reaction of formaldehyde ($HCHO + O_2 \rightarrow H_2O + CO_2$) on Pt/TiO_2 [15] and the water gas shift reaction ($CO + H_2O \rightarrow H_2 + CO_2$) on Au particles [16] are also

improved by alkali metals. Such a common effect of alkali metals has been miscast as a common effect caused by the formation of an active form of the metals, or a common synergistic effect on the metals. However, the real role of promoting materials is far more complex, as will be discussed in more detail in Sect. 10.5 of **Part II**.

The olefin metathesis reaction on the MoO_{3-x} catalyst, discussed in Sect. 10.3 of **Part II**, is a typical exchange reaction of alkylidene groups (=CHR) as described by $2\ R_1CH = CHR_2 \rightarrow R_1CH = CHR_1 + R_2CH = CHR_2$. In the metathesis reaction of propene, ethylene and but-2-ene are recognized as the products of a reaction given by $2\ CH_2 = CH–CH_3 \rightarrow CH_2 = CH_2 + CH_3–CH = CH–CH_3$. As described in detail in Sect. 10.3, where the reaction is promoted by the alternate reaction of propene with $Mo = CH_2$ and $Mo = CRCH_3$ sites, but the equal number of two sites does not mean equal contribution of the two sites in catalysis. That is, an undetectable hidden metathesis reaction, named as the degenerate metathesis reaction, is repeated on the same sites. If isotope-labeled molecules are used, one can determine the frequency of the hidden reaction of $(CH_2 = CH–CH_3 + {}^*CH_2 = {}^*CH–{}^*CH_3) \rightarrow ({}^*CH_2 = CH–CH_3 + CH_2 = {}^*CH–{}^*CH_3)$. Surprisingly, the turnover frequency of this hidden metathesis reaction of propene on the $Mo = CH–CH_3$ site is about 900 times faster than that on the $Mo = CH_2$ site on MoO_{3-x}, as shown in Sect. 10.3 [17]. As described in the outline of this book, an understanding of the real catalysis based on the dynamic processes taking place on the surface can be deduced only by well-planned experiments. In this respect, we should be deeply skeptical of experimentally unsupported dynamic mechanisms such as the one constructed to explain the catalytic oxidation of ethanol by $Mo_2(\eta–C_3H_5)_4$ supported on amorphous SiO_2, where the catalytic oxidation of ethanol was conjectured to involve dynamic conversion between $(O = Mo^{6+} = O)_2 \rightleftharpoons (O = Mo^{5+}–O–Mo^{5+} = O)$ without any experimental evidence supporting this dynamic process, only by an average Mo–Mo distance on a surface derived by using EXAFS [18, 19]. It will be clear that such a long-distance reversible conformational conversion linked with the frequency of reaction on the amorphous SiO_2 surface is implausible if you understand the real dynamics taking place on the surface, which is described in this book.

References

1. F. Jensen, F. Besenbacher, E. Laegsgaard, I. Stensgaard, Phys. Rev. B., 42 **(1990)** 9206.
2. K-I. Tanaka, Jpn. J. Appl. Phys., 32 **(1993)** 1389.
3. K-I. Tanaka and Hong He, Catal. Today, 201 **(2013)** 2.
4. K-I. Tanaka, ACS Symposium Series 656 Solid-Liquid Electrochemical Interfaces, Chapter 18 **(1997)** 245–273. Edt. By G. Jerkiewicz, M. P. Soliaga, K. Uosaki, and A. Wieckowski.
5. I. Langmuir, Trans. Faraday Soc.,17 **(1921)** 607.
6. L.H. Germer, Phys., Today,17, No. 7 **(1964)** 19.
7. G. Binnig, H. Rohrer, Ch. Gerber and E. Weibel, Phys. Rev. Lett., 50 **(1983)** 120.
8. G. Binnig and H. Rohrer, Surf. Sci., 126 **(1983)** 236.

9. K-I. Tanaka, Advances in Catalysis, Vol. 33, 99–158. Acad. Press **(1985).**
10. W. M. H. Sachtler, Faraday Discuss. Chem. Soc., 72 **(1981)** 7.
11. K-I. Tanaka, M. Shou, and Y.Yuan, J. Phys. Chem., C 114 **(2010)** 16917.
12. K-I. Tanaka, Hong He, and Y. Yuan, RSC, Advances, 5 **(2015)** 949.
13. K-T. Tanaka, Hong He, M. Shou, X. Shi, Catal. Today, 175 **(2011)** 467.
14. K-I. Tanaka, M. Shou, Hong He, and X. Shi, Catal. Letters, 110 **(2006)** 185.
15. C. Zhang, F. Liu, Y. Zhai, H. Ariga, N. Yi, Y. Liu, K. Asakura, M. Flytzani-Stephanopoulos and Hong He, Angew. Chem. Int., 31 **(2012)** 9628.
16. Y. Zhai, D. Pierre, R. Si, W. Deng, P. Ferrin, A.U Nilekar, G. Peng, J. A. Herron, D.C. Bell, H. Saltsburg, N. Mavrikakis and M.F. Stephanopoulos, Sci., 329 **(2010)** 1633.
17. K-I. Tanaka, Appl. Catalysis. A, General, 188 **(1999**) 37.
18. Y. Iwasawa, K. Asakura, H. Ishii, and H. Kuroda, Z. Phys. Chem., 144 **(1985)** 105.
19. Y. Iwasawa, Adv. in Catal. 35 **(1985)** 187.

Chapter 2
Surface Structures and the Crystal Habit of Growing Particles

Abstract A truncated single-crystal surface varies to a more stable two-dimensional array of atoms by raising the temperature. On the other hand, metal particles may grow via a two-dimensional precursor array of atoms. The (1 × 1) Au(111), Au(110), and Au(100) surfaces undergo reconstruction in electrolyte solutions at a certain negative electrode potential (vs. SCE). The icosahedral or decahedral Au particles are preferentially grown on an electrode held at the same negative electrode potential making reconstruction of Au crystal surfaces. The result suggests that metal particles may grow via precursor states of metal array which are similar to two-dimensional array of the reconstructed surfaces. Multi-twin Pt particles are also formed at highly negative electrode potential.

Keywords Reconstruction of metal surfaces · Pt(100) · Au(111) · Au(100) · Au (110) · Si(111) · Electrode potential · Multi-twin metal particles · Potential-induced surface reconstruction · Quasi-compounds · UPD (under-potential deposition) · Cu–Au alloy particles formed by UPD

A (1 × 1)-Pt(100) surface is stabilized by forming a hexagonal (5 × 20)-Pt(100) surface, and a (1 × 1)-Si(111) surface is reconstructed to a (7 × 7)-Si(111) surface. The reconstructed surface is directly observed by the scanning tunneling microscopy (STM) as shown in Fig. 2.1a and b [1]. In the case of a truncated (1 × 1)-Si (111) surface, every Si-atom has one unsaturated covalent bond called a "dangling bond," the surface is stabilized by lowering the number of Si atoms with a dangling bond in vacuum at ca. 1200 K, and a characteristic (7 × 7)-Si(111) surface is formed.

If atoms or molecules are adsorbed on a stabilized surface, the surface may undergo additional reconstruction, the so-called adsorption-induced reconstruction, whereby the total energy including the adsorption energy is lowered by the reconstruction. The reverse reconstruction from a stabilized (5 × 20)-Pt(100) clean surface to a metastable (1 × 1)-Pt(100) surface is attainable by using adsorption of CO and O_2 [1]. That is, the heat of adsorption of O_2 on the (1 × 1)-Pt(100) surface is higher than that on the hex-(5 × 20)-Pt(100) surface, which is the driving force

K. Tanaka, *Dynamic Chemical Processes on Solid Surfaces*,
DOI 10.1007/978-981-10-2839-7_2

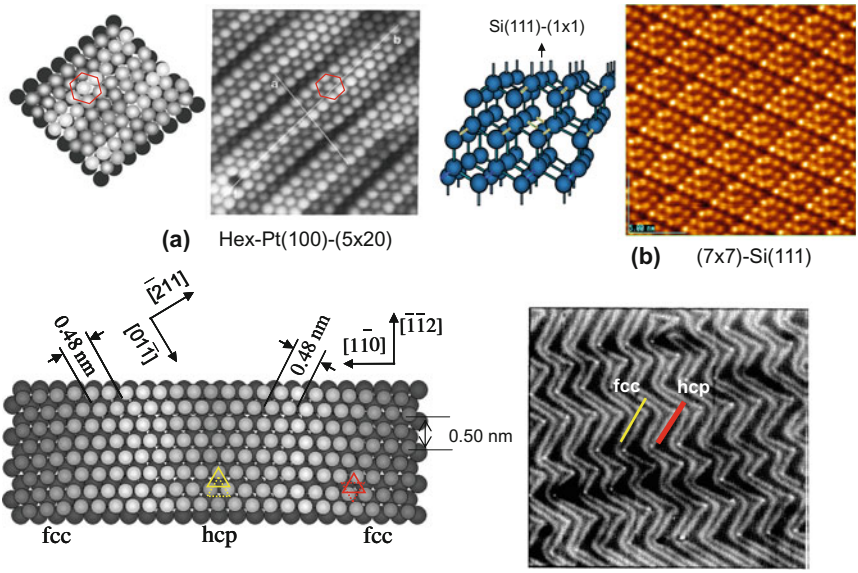

Fig. 2.1 Typical examples of the surface taking a 2-D stabilized conformation: **a** hex-(5 × 20)Pt (100) surface [1], **b** (7 × 7)-Si(111) surface, and **c** (22 × √3)-Au(111) surface, named herringbone structure, formed by alternated stacking of hcp and fcc regions, with bright ridge lines appearing between them, as shown by a model of (22 × √3)-Au(111) [3]

for the reverse reconstruction from (5 × 20)-Pt(100) to a metastable (1 × 1)-Pt (100) surface. By this process, a metastable (1 × 1)-Pt(100) surface is attainable by removing the adsorbed oxygen by reacting with H_2 at low temperature.

Reconstruction of the Au(111) surface is another interesting example, induced by anisotropic shortening of the lattice distance in the topmost layer. In this case, an anisotropic shortening of ~ 4.2% of the Au–Au lattice distance, from 0.50 to 0.48 nm, occurs in the topmost layer along the ⟨2 1 1⟩ direction on the (1 × 1)-Au (111) plane. As a result, the Au atoms in the topmost layer make an array of ABC/ABC (fcc structure) areas and AB/AB (hcp structure) stacking areas separated by ridges of atoms. Figure 2.1c shows an STM image of a reconstructed Au(111) surface, the so-called herringbone (22 × √3)-Au(111) surface, where the wider dark stripe corresponds to a fcc stacking area, the narrow dark stripe corresponds to a hcp stacking area, and the bright line between them is a ridge of Au atoms (the (1 × 1)-Au(111) surface has three equivalent axes) [3]. The Au–Au distance of the reconstructed (22 × √3)-Au(111) structure is reduced from the bulk distance of 0.50 to 0.48 nm along the ⟨1−1 0⟩ axis, which is a ca. 4.2% reduction in the Au–Au distance. As a result, a (22 × √3)-Au(111) surface with the slightly distorted chevron or "herringbone" pattern shown in Fig. 2.1c is formed. The (22 × √3)-Au (111) surface is energetically inhomogeneous due to lattice strain, which influences

the preferential growth of nanoparticles of Au [2], Co [3], Fe [4], Ni [5], and Ag [6] at the elbow sites on the (22 × √3)-Au(111) surface.

Another notable feature of the Au(111) surface is a reversible reconstruction in aqueous solution that can be induced by an electrochemical potential. The potential-induced reconstruction of the Au surface was first suggested by Hamelin [7] to explain the hysteresis of the electro-capacitance curve of an Au(111) surface, and the reconstruction was confirmed by Kolb et al. by using LEED [8]. A (1 × 1)-Au(111) surface changes to a (22 × √3) structure when it is biased at a certain negative electrochemical potential relative to the saturated calomel electrode (SCE) in an electrolyte solution, which is similar to the reconstruction taking place in vacuum on raising temperature. It is notable that Au(111), Au(100), and Au(110) surfaces all undergo reconstruction at an equally negative potential, but the electrochemical potential for the reverse reconstruction to the (1 × 1) surface depends on the crystal plane, Au(110) < Au(100) < Au(111), depending on the density of Au atoms, as shown in Fig. 2.2a [9, 10]. This result suggests that the array of the topmost Au atoms depends on the electrochemical potential in aqueous solution. If the structure of the two-dimensional array of Au atoms depends on the

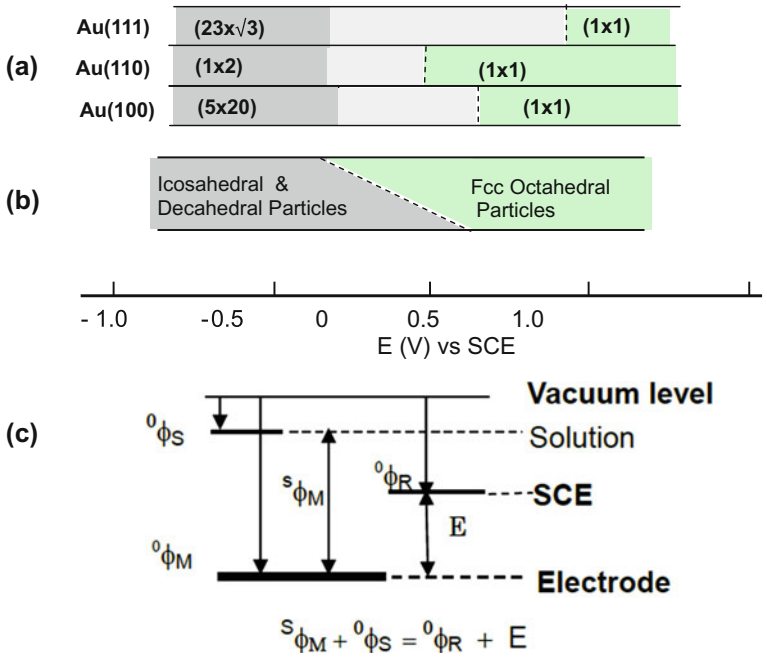

Fig. 2.2 **a** Stable surface structures of Au(111), Au(110), and Au(100) depending on the electrochemical potential (E) with respect to SCE in 0.1 M $HClO_4$ solution. **b** Au particles grown on a C-coated-Au-mesh electrode in 50 mM $HClO_4$ + 1 mM $HAuCl_4$ solution. Crystal habit of Au particles depends on the electrochemical potentials [11]. **c** Relative potential levels of an electrode ($^{0}\phi_M$) in an electrolyte solution with respect to the SCE and the Fermi level in the vacuum

electrochemical potential, the growth of Au particles from Au^{3+} ions on an electrode may be influenced by the electrode potential, which would be the array of Au atoms in a precursor state of the growth of a crystal. If this is the case, the electrode potential will give some effect on the growing form of crystals. As predicted, multi-twin Au particles grow on a carbon-coated Au gauze held at the electrochemical potential inducing the reconstruction of Au(111), Au(100), and Au(110) surfaces as shown in Fig. 2.2b [11, 12]. A more interesting fact is that a similar potential effect is observed not only on Au particles but also on most fcc metal particles, although potential-induced surface reconstructions have been reported only on Au surfaces.

If we consider the electrode potential ($^0\phi_M$) from the vacuum level, it is given by the equation: $^0\phi_M = {}^s\phi_M + {}^0\phi_s = {}^0\phi_R + E$ as illustrated in Fig. 2.2c, where the electrode potential E (V) is referred to SCE (the standard saturated calomel electrode). If the Fermi level of the electrolyte solution ($^0\phi_S$) can be presumed to be in the range of 0.1 ~ 0.2 V [13], one can estimate the electrode level ($^0\phi_M$) to the potential level of the SCE ($^0\phi_R$) from the vacuum. By the shift of the vibrational frequency of adsorbed CO on a Pt(111) electrode as a function of the electrostatic potential, one can evaluate the Fermi level of the metal in solution compared to that in vacuum. When the electrode potential is held at the zero-charge (E_{zc}) potential, the stretching vibrational frequency of adsorbed CO on the Pt electrode becomes equal to that of adsorbed CO on Pt(111) in vacuum [14]. Taking these results into account, the Fermi level of an electrode ($^0\phi_M$) from the vacuum level relative to SCE (E) is schematically shown in Fig. 2.2c. As shown in Fig. 2.2b, when an electrode is held at a negative potential with respect to SCE, the fractions of decahedral and icosahedral Au particles increase with decreasing (more negative) potential.

The left-hand-side TEM image shown in Fig. 2.3a shows an ordinary octahedral Au crystal particle formed at + 0.33 V and its electron diffraction pattern along the ⟨100⟩ direction, and the other two TEM images of Au crystal particles are formed at −0.30 and −0.55 V, respectively [11, 12]. The fractions of Au crystal particles formed on an Au-mesh electrode in a $HAuCl_4$ (1×10^{-3} M) + $HClO_4$ (0.5 M) solution at potentials ranging from 0.35 to −0.55 V (SCE) are shown in Fig. 2.3b. It is known that the shape of Au crystal particles is clearly affected by the electrochemical potential as shown by the TEM image, and the decahedral Au particles formed at −0.30 V and icosahedral Au particles at −0.55 V are shown in Fig. 2.3a. The ratio of multi-twin particles to the total particles per mm^2 (B/A) linearly increases with respect to the negative electrode potential as shown in Fig. 2.3b, and more than 60 % of Au particles were either icosahedral or decahedral, with the decahedral Au particles being preferred.

Potential-induced surface reconstruction of the Au(111) surface is caused by an anisotropic shortening of the Au–Au distance in 4–5 %, and radially shaped nanometer-sized Au particles resulted from the growth of multiply twinned particles [15]. Formation of multi-twin Au particles, as well as decahedral and icosahedral Au particles, was first observed by Ino and Ogawa [16] on a heated NaCl crystal plane in vacuum and also observed on a heated graphite surface by Wayman and

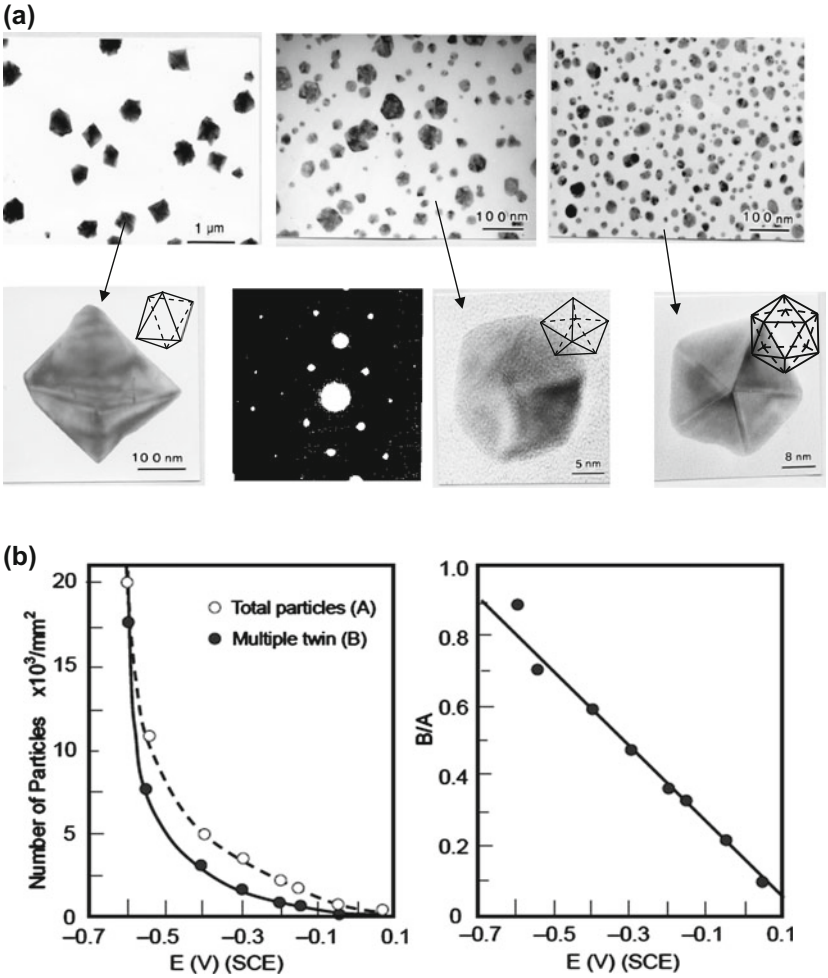

Fig. 2.3 **a** TEM images of octahedral Au particles grown at +0.33 V, and of decahedral and icosahedral Au particles attained at −0.30, and −0.55 V [11]. Electron diffraction pattern along the ⟨100⟩ direction of the fcc octahedral Au particles grown at 0.35 V. **b** Total number of Au particles (A) per mm^2 (○) formed in 60 s, and the number of decahedral and icosahedral multi-twin particles (B) (●) depending on the potential (E). The B/A ratio shows preferential growth of multi-twin particles (B) at negative electrochemical potentials [12]

Darby [17]. The decahedral and icosahedral Au particles were explained as resulting from the aggregation of five and twenty twin particles. Taking these results into account, the total surface energy of particles is lowered by forming twin boundaries, which is the driving force for the growth of icosahedral or decahedral multi-twin Au particles.

The reconstructed structure is released by keeping the Au surface at a positive potential (SCE) in solution, and the (1 × 1) surface is recovered. However, the icosahedral and decahedral Au particles cannot be changed to octahedral fcc particles by holding them at the corresponding positive potentials in solution. In other words, the two-dimensional array of Au atoms is reversible depending on the electrochemical potential, but once formed, bulk structure of Au particles cannot be reformed by the change in surface structure. It should be pointed out that potential-induced surface reconstruction has not been observed on other than Au surfaces, but the growth of decahedral and icosahedral particles was observed for Cu, Ni, Pd, and Ag particles at negative electrode potential (SCE) [18]. Pt is a highly stable metal giving no bulk phase reconstruction, but decahedral and/or icosahedral Pt particles were formed at −0.9 V (SCE) in a solution of 0.05 M $CsClO_4$ + 1 mM $PtCl_4$ at −0.5 V, where neither Cl^- nor ClO_4^- ions were adsorbed on the Pt surface [19]. These results might reflect the array of metal atoms in the precursor state of nano-sized metal particles growing in solution under the electrostatic field.

As is known, the electrochemical self-deposition of metal ions occurs at the Nernst equilibrium potential (E_r), but no electrochemical deposition proceeds at potentials more positive than the reversible Nernst equilibrium potential E_r. However, the deposition of foreign metal atoms occurs at potentials more positive than the Nernst self-deposition potential, which is known as the under-potential deposition (UPD) of foreign metal atoms. Figure 2.4 shows the under-potential deposition (UPD) of Cu^{2+} ions on a Au(111) surface in a H_2SO_4 solution given by Kolb et al. [20]. A ($\sqrt{3}$ x $\sqrt{3}$)R30 structure is adopted on the Au(111) surface with UPD-deposited Cu^+ ions, and it changes to a (1 × 1) structure on deposition of Cu^0 as illustrated in Fig. 2.4. In essence, UPD of Cu^{2+} ions creates a 2/3 monolayer of Cu^+ ions on the Au(111) surface, and one monolayer deposition of Cu^0 is formed at the lower electrode potential [21, 22]. Manne et al. [23] studied a stripped-down electrodeposited Cu layer on a Au(111) surface at an UPD potential in different electrolytes by atomic force microscopy (AFM), showed that the UPD monolayer formed different structures in different electrolytes, and showed that the deposited Cu atoms on Au(111) surface adopt a close-packed array with a spacing of 0.29 nm in a perchloric acid electrolyte solution, but take on a more open lattice spacing of 0.49 nm in a sulfate electrolyte.

When a carbon-coated Au-mesh electrode (C-coated Au) is held at the Nernst potential of Au^{3+} ion in a solution of (Au^{3+} + Cu^{2+}) ions, Au particles are formed, but no growth of individual Cu^0 particles occurs. However, the UPD of Cu^{2+} ions creates a Cu^+ or Cu^0 layer on the Au particles formed on the C-coated electrode; that is, Au^{3+} and Cu^{2+} ions are alternately deposited one after the other at the UPD potential of the Cu^{2+} ion. The composition of Cu/Au UPD particles formed on an Au-mesh electrode in a solution of 1 mM $HAuCl_4$ + 0.1 M $HClO_4$ + ξ M Cu $(ClO_4)_2$ (ξ = 0.10 M ∼ 0.001 M) varies depending on the concentration of Cu^{2+} ions and electrode potential as shown in Fig. 2.5b, and the Cu/Au ratio of alloy particles extrapolated to ($E - E_r \simeq 0$) in Fig. 2.5b suggests the formation of 50 % Cu and 50 % Au alloy particles [12, 24–27. The results are in good agreement with

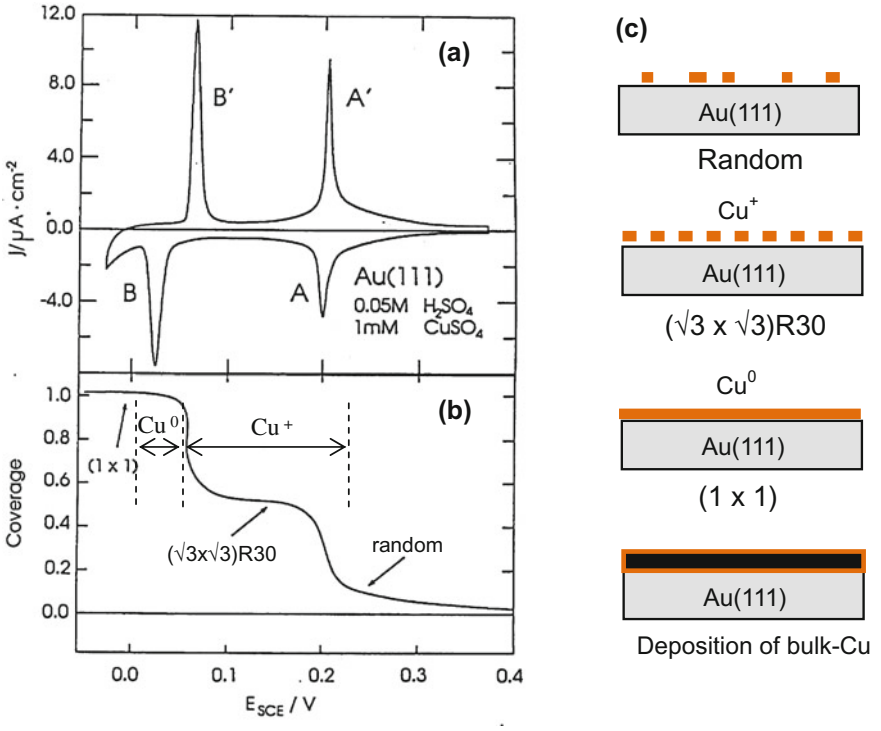

Fig. 2.4 Under-potential deposition (UPD) of Cu^{2+} ion on a Au(111) surface. **a** Cyclic current–potential curve (1 mV/sec) showing under-potential deposition (UPD) of Cu^{2+} ions on an Au(111) surface in 0.05 M H_2SO_4 + 1 mM $CuSO_4$. **b** The structure of Au(111) surface changed by the deposition of Cu^+ and Cu^0, where the coverage was derived from the charge of UPD Cu ions [20]. **c** Illustration of the deposited of Cu^+ and Cu^0 on the Au(111) surface

the UPD mechanism for the formation of Cu–Au alloy particles as one monolayer Cu^0 deposits on the Au(111) surface, as shown in Fig. 2.4.

When the electrode potential is held at higher than the UPD potential E_r ($E - E_r > 0$), the deposition rate of Au^{3+} ions to Au^0 is increased with increasing potential, whereas the UPD rate of Cu^{2+} ions may remain at a constant rate, so that the fraction of Au in the Cu–Au particles increases with electrode potential in a 1 mM Au^{3+} ion solution. It is a noteworthy result that the Cu/Au ratio maintains a constant value over a wide concentration range of Cu^{2+} ions (0.1–0.001 M) at potentials more positive than the Nernst potential of Au^{3+} ion ($E - E_r \simeq 0$). The layer-by-layer deposition of Au^{3+} and Cu^{2+} ions forming Cu–Au alloy was confirmed by the Debye–Scherrer rings as shown in Fig. 2.5a, where the lattice of the Cu–Au alloy (Cu 30 %) particles was shortened compared to that of Au. If the experiment is performed at lower than the Nernst equilibrium potential of Cu^{2+} ion ($E < E_r$), the deposition rate of Cu depends on the concentration of Cu^{2+} ion, so that

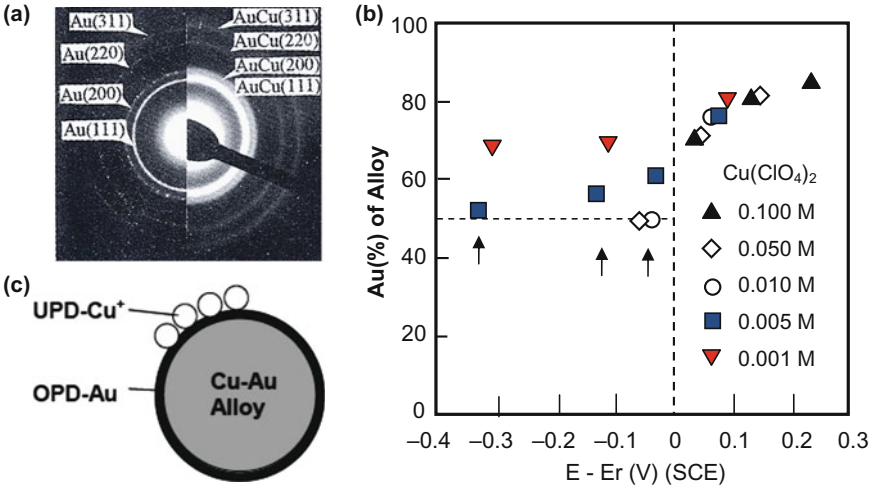

Fig. 2.5 Formation of Cu–Au alloy particles by simultaneous electrochemical deposition of Cu^{2+} and Au^{3+} ions in the UPD region of Cu^{2+} deposition on Au particles. **a** Debye–Scherrer ring of Au particles (*left*) prepared in 1 mM $HAuCl_4$ + 0.1 M $HClO_4$ at −0.5 V (SCE) and of Cu–Au alloy particles (Cu 30 %) formed in 1 mM $HAuCl_4$ + 0.1 M $HClO_4$ + 50 mM $Cu(ClO_4)_2$ at 0.1 V (SCE). **b** Au (%) in Cu–Au alloy particles depending on the electrode potential in a solution 1 mM $HAuCl_4$ + 0.1 M $HClO_4$ + ξ M $Cu(ClO_4)_2$, where the concentration of Cu^{2+} ion (ξ) was changed from 0.1 M to 0.001 M. E_r is the reversible Nernst potential of Cu^{2+} ion. Arrows indicate the potential for simultaneous formation of Cu_2O. **c** A model of UPD of Cu^+ on an OPD Au layer, which changes to a Cu–Au alloy particle [24]

the composition of the Cu–Au alloy particles depends on the concentration of Cu^{2+} ion in solution, as shown with the arrows in Fig. 2.5b. It is notable that Cu–Au alloy particles also form multi-twin particles, although the UPD of Cu^{2+} ion on Au particles occurs at a potential more positive than that required for the potential-induced reconstruction of Au surfaces, and also more positive than the formation potential of the decahedral and icosahedral multi-twin Au particles shown in Fig. 2.2a and b [18, 24, 28, 29]. This result may indicate that the shortening of the lattice distance by forming a Cu–Au surface alloy is responsible for the formation of multi-twin Cu–Au alloy particles.

References

1. A. Borg, A.-M. Hilmen, and E. Bergene, Surf. Sci., 306 **(1994)** 10.
2. C.A. Lang, M.M. Dovek, J. Nogami, and C.F. Quate, Surf. Sci., 224 **(1989)** L947.
3. B. Voigtländer, G. Meyer, and N.M. Amer, Phys. Rev. B 44 **(1991)** 10354.
4. B. Voigtländer, G. Meyer, and N.M. Amer, Surf. Sci. Lett. 255 **(1991)** L529.
5. D.D. Chambliss, R.J. Wilson, and S. Chang, Phys. Rev. Lett. 66 **(1991)** 1721.
6. D.D. Chambliss and R.J. Wilson, J. Vac. Sci. Technol. B 9 **(1991)** 928.

7. A. Hamelin, J. Electroanal. Chem., 142 **(1982)** 299.
8. M.D. Kolb, G. Lehmpfuhl, and M.S. Zei, J. Electroanal. Chem., 179 **(1984)** 289.
9. A. Hamelin, X. Gao, M.J. Weaver, J. Electroanal. Chem., 323 **(1992)** 361.
10. X. Gao and M.J. Weaver, Surf. Sci. 313 **(1994)** L 775.
11. D-L. Lu, Y. Okawa, K. Suzuki, and K-I. Tanaka, Surf. Sci., 325 **(1995)** L397.
12. D-L. Lu, Y. Okawa, M. Ichihara, A. Aramata, and K-I. Tanaka, J. Electroanal. Chem., 406 **(1996)** 101.
13. S. Trasatti, J. Electroanal. Chem. 150 **(1983)** 1.
14. S-C. Chang, X. Xiang, J.D. Roth, and M.J. Weaver, J. Phys. Chem, 95 **(1991)** 5378.
15. P-Y. Gao, W. Kunath, H. Gleiter, and K. Weiss, Z. Phys. D 12 **(1989)** 119.
16. S. Ino, J. Phys. Soc. Jpn, 21 **(1966)** 346; S. Ino and S. Ogawa, J. Phys. Soc. Jpn, 22 **(1967)** 1365.
17. C.M. Wayman and T.P. Darby, J. Cryst. Growth, 28 **(1975)** 55.
18. D-L. Lu and K-I. Tanaka, J. Phys. Chem. B 101 **(1997)** 4030.
19. D-L. Lu, K-I. Tanaka, Surf. Sci., 373 **(1997)** L339.
20. M.H. Holzle, U. Retter and D.M Kolb, J. Electroanal. Chem., 364 **(1994)** 286.
21. D.M. Kolb, Adv. Electrochem., 11 **(1978)** 125.
22. I.H. Omar, H.J. Pauling, K. Juttner, J. Electrochem. Soc., 140 **(1993)** 2187.
23. S. Manne, P.K. Hansma, J. Massie, V.B. Elings, A.A. Gewirth, Science, 251 **(1991)** 183.
24. D-L. Lu and K-I. Tanaka, J. Electroanal. Chem., 430 **(1997)** 69.
25. D-L. and K-I. Tanaka J. Solid Electrochem. 1 **(1997)** 187.
26. D-L. Lu and K-I. Tanaka, Surf. Sci.,,409 **(1998)** 283.
27. D-L. Lu and K-I. Tanaka, J. Electrochem. Soc., 143 **(1996)** 2105.
28. D-L. Lu and K-I. Tanaka, Langmuir, 18 **(2002)** 3226.
29. D-L. Lu and K-I. Tanaka, Phys. Rev. B 55 **(1997)** 13865.

Chapter 3
Self-Assembled Array of Atoms and Molecules on Metals

Abstract Molecules adsorbed on a metal surface are stabilized on the surface by adsorption or by reacting with surface atoms. By either adsorption or by reacting with surface atoms, they provide new chemical materials. A typical example is a two-dimensional crystal layer of n–$C_{17}H_{36}$ and n–$C_{36}H_{74}$ molecules formed on a $(22 \times \sqrt{3})$-Au(111) surface. They make a two-dimensional eutectic crystal layer on a $(22 \times \sqrt{3})$-Au(111) surface, which is an interesting two-dimensional new material. As discussed in Chap. 9, the phenomenon is similar to the formation of an ordered new alloy layer on a Pt–Rh(100) surface at 490 K in O_2, although Pt–Rh is a random mixing alloy. The reaction of adsorbed atom or molecule with surface atoms provides additional new two-dimensional materials named as "quasi-compound" in Chap. 4.

Keywords Surface reconstruction of Au(111) · Self-assembled array of alkane molecules · Two-dimensional crystal layer of n–$C_{25}H_{52}$ and n–$C_{28}H_{58}$ on $(22 \times \sqrt{3})$-Au(111) surfaces · Two-dimensional eutectic crystal layer · Structure of domain boundary · Ordering of alkane molecules with graphite surface

When a metal surface is exposed to simple molecules such as H_2, O_2, or N_2, adsorbed molecules react often with metal atoms on the surface to form new compounds. When heteroatomic molecules such as NO and CO are adsorbed on a metal surface, the reaction with metal atoms provides two different kinds of compounds on the surface. As the increase of compounds, they make characteristic two different arrays over the surface depending on the crystal plane, which is similar to the array of two sorts of molecules over the surface. When we consider the reaction of adsorption molecules with surface atoms, we have to consider again the features of surface defined in Fig. 1.1. Consider the coadsorption of two n-alkane molecules with one twice the length of the other on a $(22 \times \sqrt{3})$-Au(111) surface and on graphite. $(22 \times \sqrt{3})$-Au(111) is a reconstructed Au (111) crystal plane, but the basal

K. Tanaka, *Dynamic Chemical Processes on Solid Surfaces*,
DOI 10.1007/978-981-10-2839-7_3

plane of graphite is not the surface of graphite but the graphite itself, as shown in Fig. 1.1. If we compare the adsorption of the molecules on these two surfaces, one can realize the difference in adsorption of molecules between the $(22 \times \sqrt{3})$-Au (111) surface and the basal place of graphite.

When a clean Au(111) surface is heated in vacuum, the anisotropic shortening of the Au–Au length from 0.50 nm to 0.48 nm ($\sim$4.2 %) along the $\langle -2\ 1\ 1 \rangle$ direction takes place, which results in making a chevron structure, $(22 \times \sqrt{3})$-Au(111), as shown in Fig. 2.1c. When a $(22 \times \sqrt{3})$-Au(111) surface is dipped in a saturated solution of n–$C_{17}H_{36}$ with n–$C_{36}H_{74}$, alkane molecules are arrayed on the surface as shown in Fig. 3.1 as observed by Xie et al. [1], which is the formation of a two-dimensional eutectic crystalline layer of n–$C_{17}H_{36}$ and n–$C_{36}H_{74}$ at a ratio of 70:30, which is close to the composition of the saturated solution of the two alkanes. That is, a two-dimensional eutectic crystalline layer is formed on an anisotropic $(22 \times \sqrt{3})$-Au(111) surface. On the other hand, if graphite is dipped in a saturated solution of n–$C_{17}H_{36}$ with n–$C_{36}H_{74}$, a three-component phase of n–$C_{17}H_{36}$ and n–$C_{36}H_{74}$ with graphite is formed as observed in Fig. 3.1b. It was confirmed that the shorter n–$C_{17}H_{36}$ molecules move their location with time in the

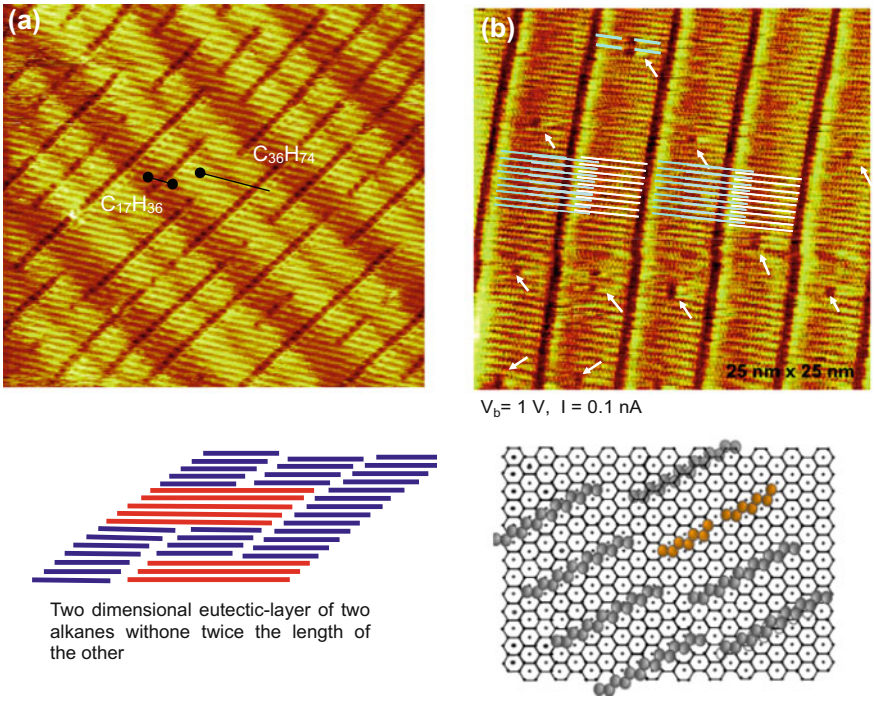

Fig. 3.1 **a** Two-dimensional eutectic nano-crystalline phase of n–$C_{17}H_{36}$ and n–$C_{36}H_{74}$ (70:30) formed on a $(22 \times \sqrt{3})$-Au(111) surface dipped in a saturated solution of n–$C_{36}H_{74}$ in n–$C_{17}H_{36}$ [1]. **b** Coadsorption of n–$C_{17}H_{36}$ and n–$C_{36}H_{74}$ on graphite. Short chains of n–$C_{17}H_{36}$ (*indicated with arrows*) move with time, suggesting equilibrium adsorption

STM image, that is, we can consider that the three components of equilibrium phase, n–$C_{17}H_{36}$, –$C_{36}H_{74}$ and graphite, are observed on the graphite. The phenomena observed on either the (22 × √3)-Au(111) or the graphite are the results attained by lowering the total free energy, but the physical meaning of the two phenomena are quite different. The eutectic crystalline layer of alkane molecules formed on the (22 × √3)-Au(111) surface is a new two-dimensional material which can exist only on the (22 × √3)-Au(111) surface by the optimization of mutual interaction of the alkane molecules.

On the other hand, graphite and graphene are two-dimensional large molecules, and the array of alkane molecules on graphite is recognized as a three-component system including graphite, so that the mutual interaction of alkane molecules and graphite depends on the chain length and graphite. If graphene or graphite is dipped in liquid alkanes, they make inhomogeneous three-component system made by two alkanes and graphite. Mutual interaction of the alkane molecules and graphite creates a three-component system with graphite. This phenomenon is essentially different from the new two-dimensional eutectic crystalline layer of alkane molecules stabilized on the (22 × √3)-Au(111) surface. We can more clearly realize the difference in the adsorption of alkane molecules on graphite and (22 × √3)-Au(111) surface as discussed below.

The two-dimensional eutectic layer of alkane molecules is provided merely on the (22 × √3)-Au(111) surface. That is, random liquid-phase alkane molecules are transferred to a two-dimensional eutectic layer on the (22 × √3)-Au(111) surface, where the Au–Au distance is shortened from 0.50 nm to 0.48 nm (about 4.2%) along the $\langle -2\ 1\ 1 \rangle$ direction. If it is explained by interaction energy, the two-dimensional anisotropic space with the 0.48 nm width along the $\langle -2\ 1\ 1 \rangle$ direction assists to the formation of a two-dimensional-ordered eutectic layer of alkane molecules by optimizing an attractive interaction between the alkane molecules in parallel to the $\langle 0\ 1\ -1 \rangle$ axis on the (22 × √3)-Au(111) surface. On the other hand, local free energy around the graphite is minimized by making two-dimensional-ordered array of long chain molecule with graphite, which is similar to the formation of an ordered structure of H_2O molecules on an electrode by electrostatic field. In this regard, the eutectic crystalline monolayer of n–$C_{17}H_{36}$ and n–$C_{36}H_{74}$ on the (22 × √3)-Au(111) surface is a new material existing only on a specific surface.

Zhang et al. [2] carefully studied the special orientation of terminal –CH_3 groups in the self-assembled alkane molecules on the (22 × √3)-Au(111) surface and deduced a repulsive interaction between the terminal –CH_3 groups that are facing each other across the two domains. Self-assembled adsorption of n-alkanes of C_nH_{2n+2} (n = 14–38) on the (22 × √3)-Au(111) surface is optimized by the attractive interaction of the alkane chains –$(CH_2)_n$– and the repulsive interaction of the two –CH_3 groups at the terminal ends of the chains. When the number of carbon atoms (n + 2) in CH_3–$(CH_2)_n$–CH_3 is even or the chain length is short, alkane molecules form an optimized array by sliding one –CH_2– length parallel to the molecular axis, by which the repulsive interaction of –CH_3 along the domain boundary may be lowered, as shown in Fig. 3.2b. In contrast, when the number of

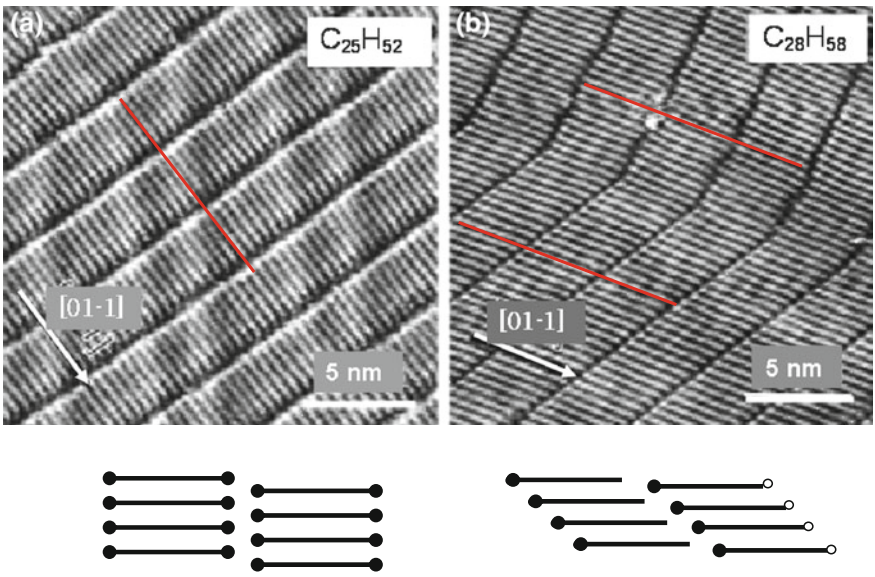

Fig. 3.2 Self-assembled arrays of n–$C_{25}H_{52}$ and n–$C_{28}H_{58}$ on $(22 \times \sqrt{3})$-Au(111) surfaces. **a** Domain boundary of alkane layers is perpendicular to the molecular axis in the adsorption of n–$C_{25}H_{52}$ (odd number of carbon atoms), in which the attractive interaction of –(CH_2)n– chains becomes maximized. **b** Sliding of array with the molecular axis at an angle to the domain boundary to lower the repulsive interaction by the terminal –CH_3 groups observed in the array of n–$C_{28}H_{58}$ (even number of carbon atoms) [2]

carbon atoms is odd, the two terminal –CH_3 groups of CH_3–$(CH_2)_n$–CH_3 take on the same special orientation to the molecular axis, so that the optimized array is made by maximizing the attractive interaction between alkane molecules, which results in a domain boundary perpendicular to the molecular axis. If alkane molecules become longer and longer, the terminal –CH_3 effect becomes lower and lower, and the total interaction energy given by the attractive interaction of –$(CH_2)_n$– is optimized by an array of the alkane molecules perpendicular to the domain boundary, as shown in Fig. 3.2a.

If adsorbed molecule reacts with surface atoms, an additional new compound is formed, as mentioned in Chap. 4. When the density of compound is increased, they make an ordered array on the surface. These compounds have own stoichiometry and two-dimensional specific conformation depending on the surface, which are like molecules although one cannot take them out from the surface. Therefore, these unusual materials were named "**quasi-compounds**" [3], and their details are described in Chap. 4.

References

1. Z.X. Xie,. X. Xu, B.W. Mao and K-I. Tanaka, Langmuir, 18 **(2002)** 3113.
2. H-M. Zhang, Z-X. Xie, B.W. Mao and X. Xu, Chem. Eur. J. 10 **(2004)** 1415.
3. K-I. Tanaka, Jpn. J. Appl. Phys., 32 **(1993)** 1389.

Chapter 4
Formation of Quasi-Compounds on Metals

Abstract When clean Ag(110), Cu(110), and Ni(110) surfaces are exposed to O_2, one can observe the growth of one-dimensional strings of (–AgO–) on Ag(110), (–CuO–) on Cu(110), and (–NiO–) on Ni(110) surface, which are evidently not the adsorption of O(a) on these surfaces, but the formation of new materials on these surfaces. The new materials are named "**quasi-compounds**," which take own stoichiometry and structure like that of a molecule or compounds. When a p(3 × 1) (–NiO–)/Ni(110) surface is exposed to H_2, H_2 molecules do not react with (–NiO–) strings, but a new quasi-compound of (–NiH–) strings is formed by the reaction of H(a) atoms with Ni atoms. In contrast, when a Cu(100) surface is exposed to O_2, O (a) atoms make minimum-size c(2 × 2)-O domains with adsorbed O(a) atoms instead of the formation of quasi-compound as observed on Cu(110) surface. If a quasi-compound reacts, an additional new quasi-compound is formed. A prominent example is the reaction of Cu atoms with (–AgO–) strings on the Ag(110) surface as will be mentioned in Chap. 5. The formation of (–CuO–).

Keywords Reaction of surface atoms with adsorbed molecules · Formation of quasi-compounds on metal surfaces · (–AgO–) on Ag(110) · (–CuO–) on Cu (110) · (–NiO–) on Ni(110) · (–NiH–) on Ni(110) · Adsorption of O(a) in nano–c (2 × 2)-O domains on Cu(100)

The heat of adsorption (E_{ad}) of molecules on metals bears an empirical linear relationship to the standard heat of formation of metal oxides (ΔH_o^o) per metal atom as shown in Fig. 4.1 [1]. However, the adsorption of molecules on metals is quite complex, and we can now distinguish the adsorption of molecules on metals from the formation of quasi-compounds by the reaction of adsorbed species with surface metal atoms.

One groundbreaking experiment was the adsorption of H_2 on a Ni(110) surface, which made clear the essential difference between the adsorption of H atoms and the reaction of H atoms with Ni atoms on the surface. When a Ni(110) surface is exposed to H_2 at temperatures below 220 K, the LEED pattern indicates a reversible change from the (1 × 1) LEED pattern to a (2 × 1) pattern at the hydrogen

K. Tanaka, *Dynamic Chemical Processes on Solid Surfaces*,
DOI 10.1007/978-981-10-2839-7_4

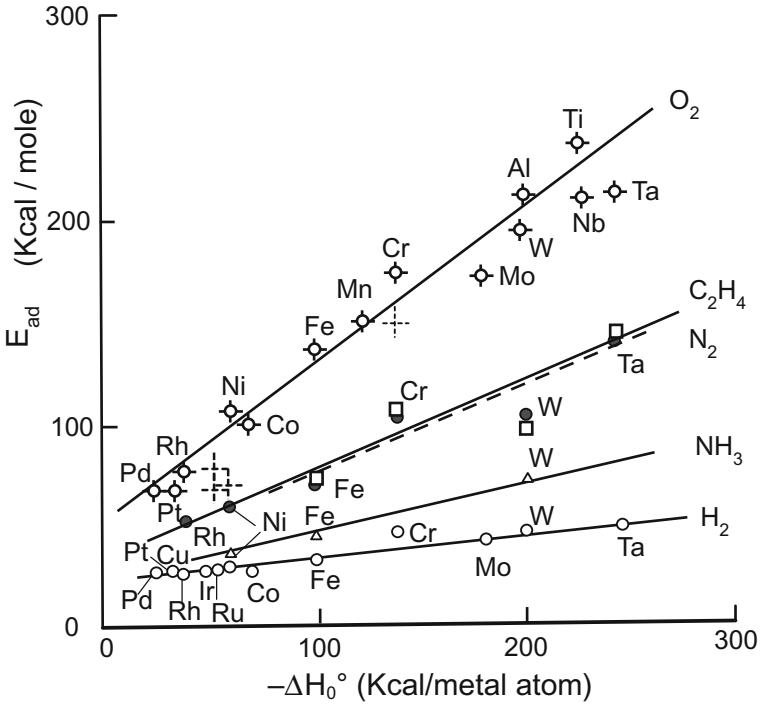

Fig. 4.1 Empirical linear relationship between the initial heat of adsorption of various molecules (E_{ad}) on metals and the standard heat of formation per metal atom for the highest oxidation state oxide ($-\Delta H_o°$) [1]

coverage of $\boldsymbol{\theta_H}$ = 1.0 ($\boldsymbol{\theta_H}$ = H/Ni) (spot at the open circle (1)), and the (2 × 1) surface is followed by a (1 × 2) pattern at $\boldsymbol{\theta_H}$ = 1.5 (spot at the open circle (2)) depending on the coverage of hydrogen, as shown in Fig. 4.2a. That is, when the coverage of H(a) is increased beyond $\boldsymbol{\theta_H}$ = 1.0, the (2 × 1) spots are weakened and new spots showing a (1 × 2) structure are established at a coverage of θ_H = 1.5 as reported by Ertl [2]. The intensity of the (2 × 1) and (1 × 2) spots is reversibly changed at 220 K depending on the coverage of H(a). This reversible change between the (1 × 2) structure at θ_H = 1.5 and the (2 × 1) structure at θ_H = 1.0 was explained by a model involving the local shifting of Ni atoms induced by adsorption of H(a), as shown in Fig. 4.2i.

In contrast to the reversible change of the Ni(110) surface by adsorption of H_2 at 220 K, an irreversible change of the (1 × 1)-Ni(110) surface to a (1 × 2)-Ni(110) surface in H_2 at room temperature was observed by in situ STM by Besenbacher and his coworkers [3]. That is, the irreversible ejection of Ni atoms and the subsequent growth of bright lines along the ⟨1–10⟩ direction are responsible for the irreversible change of the Ni(110) surface from the (1 × 1) to a (1 × 2) structure at room temperature, as shown in Fig. 4.2b. The bright lines are (–NiH–) strings stabilized on the Ni(110) surface by weak internal bonding of (–NiH–) along the

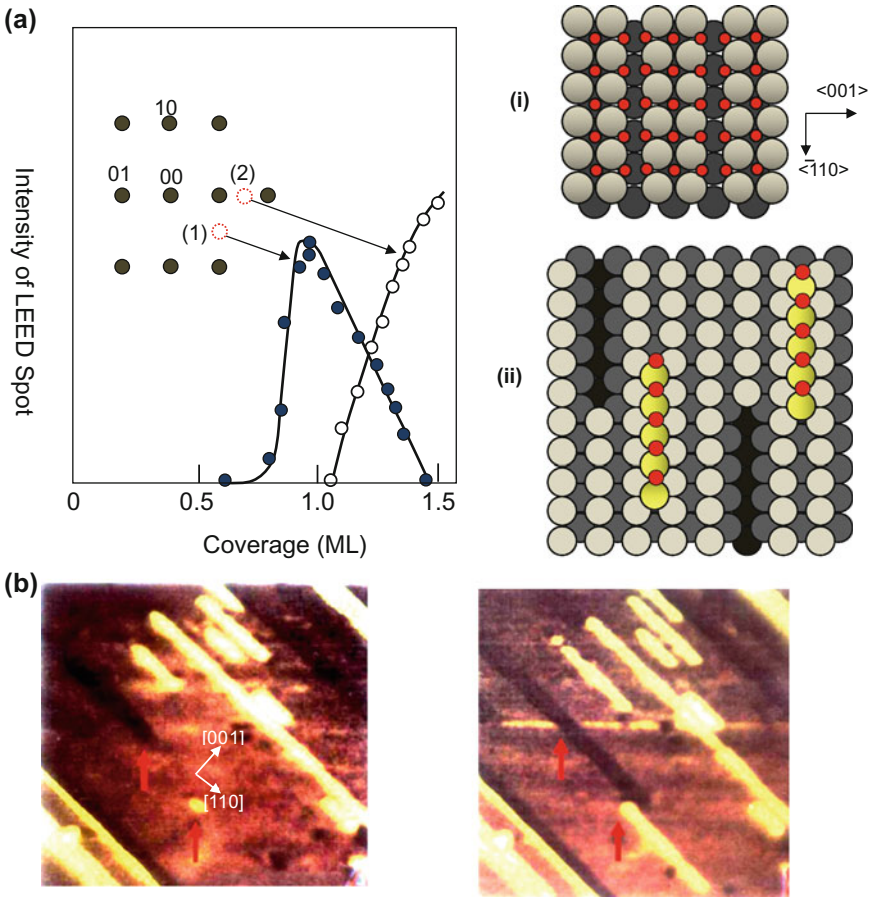

Fig. 4.2 **a** Changes in the LEED pattern of a Ni(110) surface with the adsorption of hydrogen at temperatures below 220 K. The LEED pattern changes from (1 × 1) ($\theta_H = 0$) to p(2 × 1) (a dot appears at *red open circle* (1)) with a maximum intensity at $\theta_H = 1.0$. When the adsorption of hydrogen exceeds $\theta_H = 1.0$, new spots (appearing at *red open circle* (2)) of a p(1 × 2) surface appear, and the intensity is maximized at $\theta_H = 1.5$ [2]. **b** The STM image shows irreversible change of a Ni(110) surface at room temperature by exposing to H_2. The bright lines show irreversible growth of (–NiH–) strings with dark troughs created by irreversible ejection of Ni atoms [3]. Model **i** and model **ii** show the reversible and irreversible changes of the Ni(110) surface, depending on the temperature

⟨1–10⟩ direction. With increasing density of (–NiH–) strings on the surface, the (–NiH–) strings form a (1 × 2) array on the Ni(110)–H surface at room temperature by a mutual weak interaction between (NiH) strings. The growth of (–NiH–) strings on the Ni(110) surface is undoubtedly different from the H atoms adsorbed on the Ni(110) at 220 K shown in Fig. 4.2a. Similarly, when a Ni(110) surface is exposed to O_2, (–NiO–) strings grow along the ⟨001⟩ direction. The growth of (–NiH–) and

(–NiO–) strings is clearly different from the adsorption of H(a) and O(a) atoms on the Ni(110) surface; that is, the H and the O atoms move together with Ni atoms over the surface to form (–NiH–) and (–NiO–) strings.

The important feature of these compounds is that they have own stoichiometry and the characteristic structure on the Ni(110) surface. Taking account of these characteristic phenomena on metals, Tanaka [4] proposed a new concept of "**quasi-compounds** (**pseudo-molecules**)" which are new materials existing only on a specific surface as specific materials. Most fcc metals form (–M–O–) strings along the ⟨001⟩ direction on the (110) surface on exposure to O_2, and they form a (n × 1) array with increasing density of (–M–O–) strings on the (110) surface, where the "n" is a characteristic value depending on the metal. This is similar to the self-assembly of alkane molecules along a suitable direction on the (22 × $\sqrt{3}$)-Au(111) surface, but the value of "n" changing with the coverage of (–M–O–) depends on metals. For example, (–CuO–) strings form a (2 × 1) array on the Cu(110) surface, but (–AgO–) strings form a (n × 1) array on the Ag(110) surface depending on the exposure to O_2, where the value of "n" changes n = 7–2 depending on the coverage of (–AgO–). In the case of the Ni(110) surface, the (–NiO–) strings form a (3 × 1) domain of (–NiO–) strings at low coverage and are compressed to a (2 × 1) array as increasing the (–NiO–) strings exposure to O_2.

For a long time, it was difficult to distinguish the adsorption of oxygen from the reaction of oxygen with surface metal atoms. We can now evidently distinguish these two processes; that is, metal atoms move with adsorbed species in the reaction, but metal atoms do not move together with adsorbed species in adsorption. In fact, when a metal surface is exposed to O_2, precursor state of O_2 molecule undergoes dissociation to O(a) or to follow the reaction with surface metal atoms on the surface depending on the temperature as well as on the crystal plane. A good example showing the essential difference between the adsorption and the reaction of oxygen atoms is observed on the Cu(100) surface and Cu(110) surface exposed to O_2 at room temperature. Adsorbed O(a) atoms migrate over the Cu(100) surface at room temperature, but no migration of Cu atoms occurs on this surface, and adsorbed O(a) atoms form small c(2 × 2) domains over the Cu(100) surface at low oxygen coverage. The O(a) atoms adsorbed on the Cu(100) surface are a little different from the O(a) atoms adsorbed on the other fcc metals. That is, the LEED pattern changes depending on the oxygen coverage, which gives "four-spot," c(2 × 2), and (2$\sqrt{2}$ × $\sqrt{2}$)R45 LEED patterns depending on the coverage of adsorbed O(a) atoms [5, 6]. The formation process of the (2$\sqrt{2}$ × $\sqrt{2}$)R45 Cu(100)–O surface was well studied by fine-structure LEED experiments [7–9]; that is, Cu atoms are ejected in rows parallel to the [010] direction by the strain induced by the adsorption of O(a). As mentioned below, the "four-spot" Cu(100)–O surface is given by minimum size of (2 × 2) domains of adsorbed O(a) atoms, which is in remarked contrast to the formation of the (2$\sqrt{2}$ × $\sqrt{2}$)R45 Cu(100)–O surface made by missing rows of Cu atoms.

The "four-split-spot LEED pattern" such as that shown in Fig. 4.3d was reported first by Lee and Farnsworth in 1965 [11], but the real surface structure responsible for the four-spot pattern was debated for a long time. To solve the structure of Cu(100)–O

surface giving the four-spot LEED pattern, many investigators applied newly developed cutting-edge tools such as HREELS (high-resolution electron energy loss spectroscopy) [8, 9], surface-extended X-ray absorption fine structure (SEXAFS) [12, 13], X-ray diffraction (XRD) [14], X-ray photoemission spectroscopy (XPS) [15], and scanning tunneling microscopy (STM) [16], but the surface structure giving the four-spot LEED pattern and its formation process was unsettled for nearly 30 years without yielding a conclusive answer(Fig. 4.3e).

The real structure of the Cu(100)–O surface giving four LEED spots was clarified by a time-resolved STM study by our group [17] in 1996. As shown in Fig. 4.3b, when the oxygen coverage is below 0.3, adsorbed O(a) atoms are dispersed by making nanometer-sized c(2 × 2)-O patches on the Cu(100)–O surface. When the oxygen coverage exceeds ca. 0.3, a large c(2 × 2)-O domain is formed by uniting several nano-sized c(2 × 2)-O patches, in which the local strain is increased by making large c(2 × 2)-O domains on the Cu(100)–O surface. The increased strain is removed by releasing Cu atoms from large c(2 × 2)-O domains,

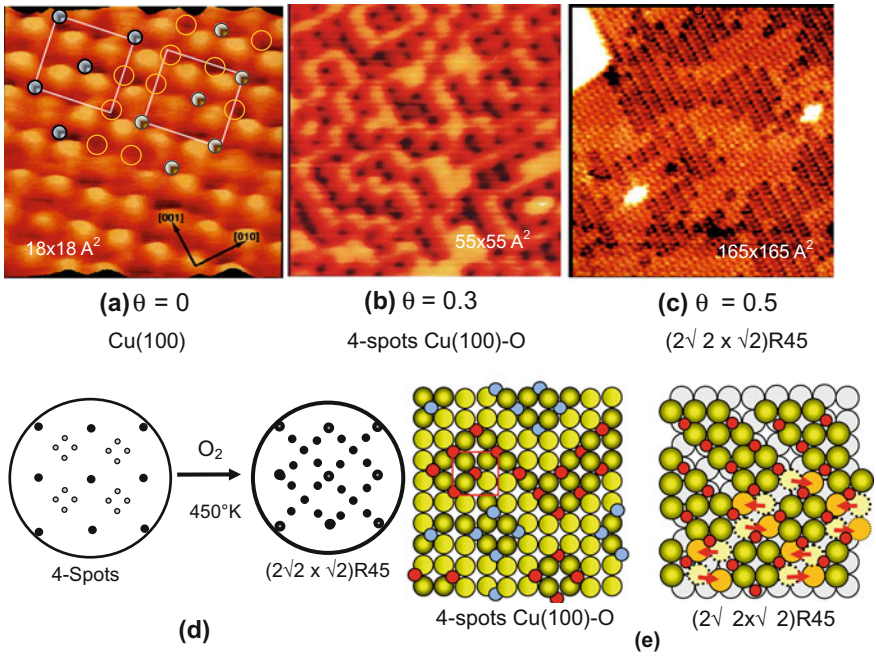

Fig. 4.3 STM images of a clean Cu(100) surface and the surface changed with oxygen coverage: **a** Clean Cu(100) surface (adsorption sites and adsorption unavailable sites); **b** nano-sized c(2 × 2)-O domains on Cu(100)–O with oxygen coverage of $\theta = 0.3$; **c** $(2\sqrt{2} \times \sqrt{2})$R45 Cu(100)–O surface at $\theta = 0.5$ formed by missing Cu atoms; **d** illustration of the four-spot LEED pattern of Cu(100)–O at $\theta = 0.3$ at room temperature, and the $(2\sqrt{2} \times \sqrt{2})$R45 pattern created by O_2 adsorption at 450 K; and **e** a model Cu(100)–O surface with nano-sized c(2 × 2)-O domains responsible for the four-spot LEED pattern and the $(2\sqrt{2} \times \sqrt{2})$R45–Cu(100)–O surface formed by missing Cu atoms [10]

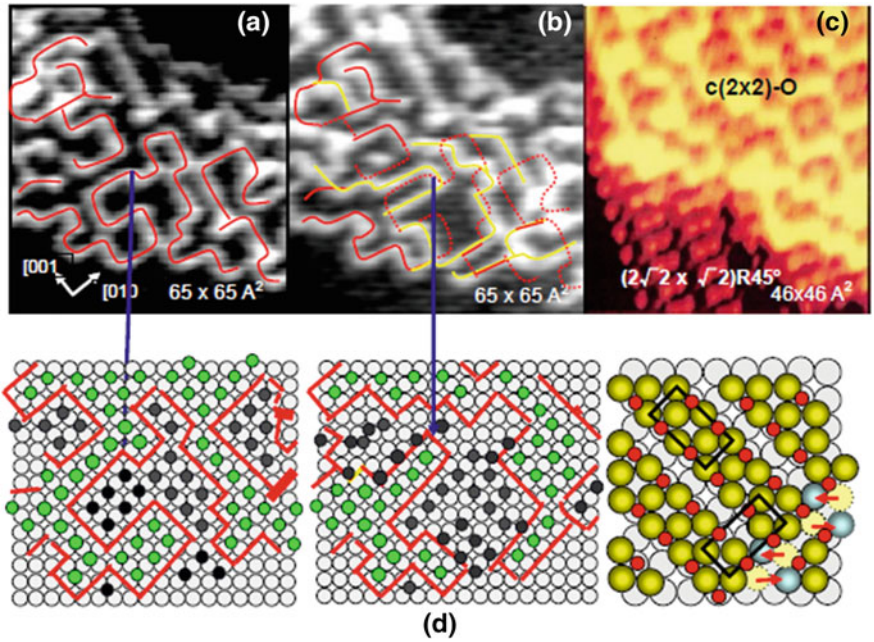

Fig. 4.4 STM image showing the move of adsorbed O(a) atoms at room temperature on a Cu (100)–O surface of 0.3 ML of oxygen coverage. The image was attained with an interval time of several minutes on the same area of a Cu(100)–O surface; **a** nano-sized c(2 × 2)-O domains moved to image **b** by maintaining at room temperature, where the domain size of c(2 × 2)-O does not increase. The boundary moved from the *red line* to the *yellow line* in a few minutes. **c** A large c (2 × 2)-O/Cu(100) domain was changed to the (2√2 × √2)R45° structure by ejection of Cu atoms to form the missing row structure [17]. **d** Illustration of how the domain boundaries of nano–c (2 × 2)-O domains (*red lines*) move with time, and a model for the reversible change of the (2√2 × √2)R45° domains by the movement of Cu atoms in the trenches

which is the reconstruction of the Cu(100)–O surface from the four-spot surface to the (2√2 × √2)R45 Cu(100)–O surface. Figure 4.3a–c shows the STM images of a clean (1 × 1)-Cu(100) surface, a four-spot Cu(100)–O surface ($\theta = 0.3$), and a (2√2 × √2)R45–Cu(100)–O surface ($\theta = 0.5$), and Fig. 4.3d shows a model for the missing row structure of the (2√2 × √2)R45–Cu(100)–O surface ($\theta = 0.5$) [17, 18].

Figure 4.4a, b shows a time-resolved STM image of the Cu(100)–O surface at $\theta \approx 0.3$ coverage, where nano-size c(2 × 2)-O patches undergo fluctuation over a time interval of several minutes. The zigzag lines in "**red**" in the STM image of (a) and (b) changed to "**yellow**" lines after a few minutes (b). The movement of the zigzag lines over time is caused by the movement of O(a) atoms from a c(2 × 2)-O domain to a neighboring c(2 × 2)-O domain at room temperature. This occurs to keep the domains at a small size. That is, if an O(a) is accepted in a domain, one of the other O(a) atoms needs to move from the c(2 × 2)-O domain to a neighboring c (2 × 2)-O domain. This is the driving force for the fluctuation of domain boundaries of c(2 × 2) domains and is also the driving force to disperse the adsorbed O(a)

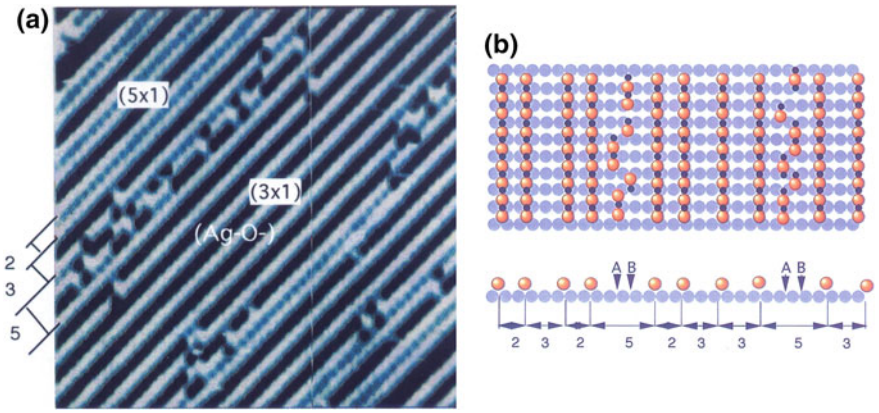

Fig. 4.5 **a** A quasi-compound of (–AgO–) strings in (n × 1) arrays on the Ag(110) surface along the [001] direction, and the phase boundaries of the (–AgO–) strings along (3 × 1) and (5 × 1) domains fluctuate. **b** Equivalent energy dual sites existing along the domain boundary are responsible for the fluctuation of (–AgO–) strings [20]

in small-sized c(2 × 2)-O domains with different phases [17, 18]. This dynamic stabilization of small-sized c(2 × 2)-O domains creates the surface responsible for the four-spot LEED pattern. In other words, the lattice strain is nonlinearly increased with the size of the c(2 × 2) domains, which prevents the growth of c(2 × 2)-O domains to a large size (Fig. 4.4e).

When the oxygen coverage is increased above 0.3, large c(2 × 2)-O domains with high lattice strain are formed. As a consequence, Cu atoms are released from the surface to lower the local lattice strain, which induces local reconstruction with a missing row structure of $(2\sqrt{2} \times \sqrt{2})$R45 as shown in Fig. 4.4c. Eventually, the whole surface is reconstructed to a $(2\sqrt{2} \times \sqrt{2})$R45 structure with missing rows when the oxygen coverage is reached to 0.5, as shown in Fig. 4.3c [17, 18]. From these results, we can confidently conclude that the four-spot Cu(100)–O surface in Fig. 4.3b is essentially different from a p(2 × 1) Cu(110)–O surface attained on a Cu(110) surface exposed to O_2, where (–CuO–) strings are formed. Figure 4.6a shows the growth of (–CuO–) strings along the ⟨001⟩ direction and their self-assembled (2 × 1) array even at very low coverage shown by Ertl [2]. It is evident that the formation of (–CuO–) strings on the Cu(110) surface is essentially different from the adsorption of O(a) atoms on the Cu(100) surface. These results may lead us to more careful study of the dynamics of the oxidation reaction of CO on Cu(100) and Cu(110) surfaces.

When a Ag(110) surface is exposed to O_2, we can recognize the growth of (–AgO–) strings in the ⟨001⟩ direction, which is similar to the growth of (–CuO–) strings on a Cu(110)–O surface. However, the (–AgO–) strings are dispersed in a (n × 1) array on the Ag(110) surface, and the "n" value changes to 6, 5, 4,…, 3, 2 with the increase in coverage. This phenomenon is similar to the dispersion of adsorbed O(a) on the Cu(100) surface by forming nano-size c(2 × 2)-O domains.

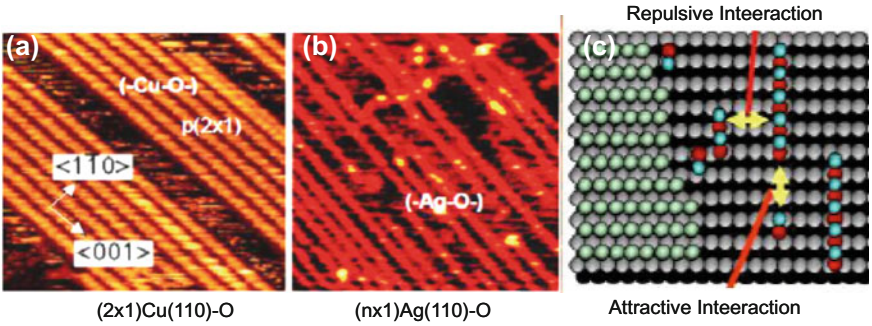

Fig. 4.6 **a** (–CuO–) strings self-assembled in a (2 × 1) array on Cu(110) surface [19]. **b** (–AgO–) strings dispersed in (n × 1) array on Ag(110) surface at a low coverage [20]. **c** Model of (–AgO–) strings growing along ⟨1–1 0⟩ direction on the Ag(110) surface and disperse in a (n × 1) array to lower the lattice strain induced by the array of (–AgO–) strings

The dispersion of (–AgO–) strings in (n × 1) arrays shown in Fig. 4.6b suggests a nonlinear increase in local lattice strain with the coverage of (–AgO–) strings on the Ag(110) surface [20], which is contrast to the growth of (2 × 1) domains of (–CuO–) strings in large on the Cu(110) surface.

Adsorption of O_2 on Ag catalysts has been studied by many investigators, because the Ag catalyst is a unique catalyst for the direct synthesis of ethylene oxide by the oxidation of ethylene with O_2. A pioneering work using a single-crystal Ag surface was carried out by Engelhardt and Menzel [21], who found a sequential change of the p(n × 1) LEED pattern, n = 7, 6,– – –, 3, 2, on a Ag(110) surface with the increase in adsorption coverage of O_2. At that time, there was no tool to confirm the real process taking place on the surface, so they explained the sequential change of the (n × 1) LEED pattern by the change of the array of adsorbed "**O(a) atoms**" on the Ag(110) surface. This was a curious explanation, because all the adsorbed O(a) atoms should be reshuffled when the "n" value is changed, but such a dynamic movement of all the adsorbed O(a) atoms over the surface is improbable. To make clear this interesting paradox, the actual dynamic process for the sequential change of the LEED pattern was clarified by a time-resolved STM study in 1992 [20].

As shown in Fig. 4.5a, time-resolved STM proved the change in the array of (–AgO–) strings and showed that the density of (–AgO–) strings arraying on the Ag (110) surface was not uniform. In addition, the fluctuation of a (–AgO–) string with time was observed along the phase boundaries of different (n × 1) domains. The STM image shown in Fig. 4.5a arises from an ordered array of (–AgO–) strings in a (3 × 1) and a (5 × 1) domain, where the (5 × 1) domain is made from a composite array of (–AgO–) strings in (2 × 1) + (3 × 1) arrays on the Ag(110) surface. From these results, the dispersion phenomenon of (–AgO–) strings in (n × 1) arrays on the Ag(110) surface is similar to the dispersion of adsorbed O(a) on the Cu(100) surface in nano-sized c(2 × 2) domains by the strain that increases nonlinearly with the size of c(2 × 2)-O domains. That is, the (–AgO–) strings are

dispersed in (n × 1) arrays on the Ag(110) surface, and the O(a) atoms are dispersed in small-sized c(2 × 2)-O(a) domains on the Cu(100) surface (Fig. 4.5b).

When a Ni(110) surface is exposed to O_2, (–NiO–) strings grow in the ⟨001⟩ direction. When the oxygen coverage is low, the (–NiO–) strings form (3 × 1) domains over the surface. When the coverage is increased, the (–NiO–) strings are compressed from a (3 × 1) array to a (2 × 1) array. From these results, it is deduced that the (3 × 1) (–NiO–) domain causes less strain on the Ni(110) surface compared to the (2 × 1) (–NiO–) domains. In the case of the Ag(110) surface, lattice strain may be increased as the "n" of (n × 1) (–AgO–) domains decreases. If the local strain of a Ni(110) surface exceeds a critical value, the surface undergoes reconstruction to lower the lattice strain. Taking these phenomena into account, we can anticipate the relaxation of local strain around the active sites by the coordination of intermediates during catalysis, which is so often observed as an induction time. The active site required for catalysis on MoS_2 is explicitly described as in Fig. 10.4 in **Part II**; an induction time observed in catalysis suggests the released of hindered rotation of intermediates by a change in the local conformation of sites, as shown in Fig. 10.6, but the release of lattice strain around the active sites during reaction is difficult to detect at the present time.

One clear piece of evidence showing the local compression of quasi-compounds was directly shown by Besenbacher and his coworkers [22]. As shown in Fig. 4.7, the (3 × 1) (–NiO–) array (a) on a Ni(110) surface is compressed into a (2 × 1) array (b) at room temperature by the adsorption of H_2, where the local strain of the Ni(110) surface should be changed with the growth of (–NiH–) strings perpendicular to the (–NiO–) strings. It should be reminded that the heat of adsorption of O_2 on Ni is much larger than that of H_2 as shown in Fig. 4.1, but the (–NiO–) strings are compressed from the (3 × 1) to the (2 × 1) structure by the growth of (–NiH–) strings along the ⟨1–10⟩ direction as shown in Fig. 4.7b. This phenomenon is difficult to explain by the competitive adsorption of H(a) and O(a) on a

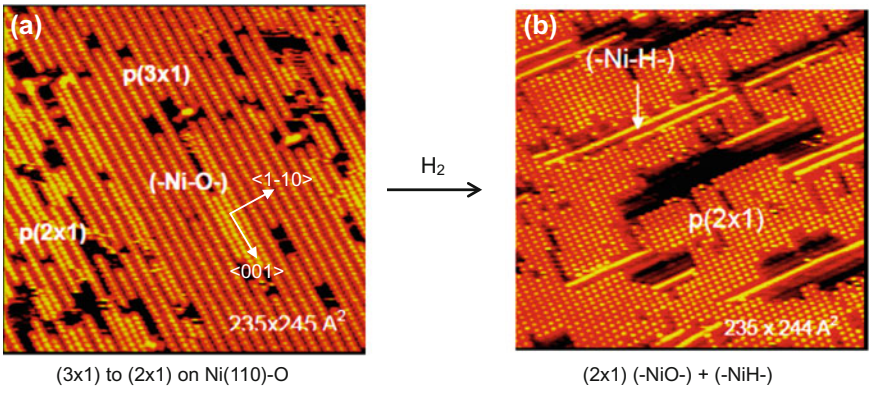

Fig. 4.7 (3 × 1) array of (–NiO–) strings formed on a Ni(110)–O surface, which is compressed to a (2 × 1) by exposure to H_2 at room temperature, where (–NiH–) strings grow in the ⟨1–10⟩ direction [22]

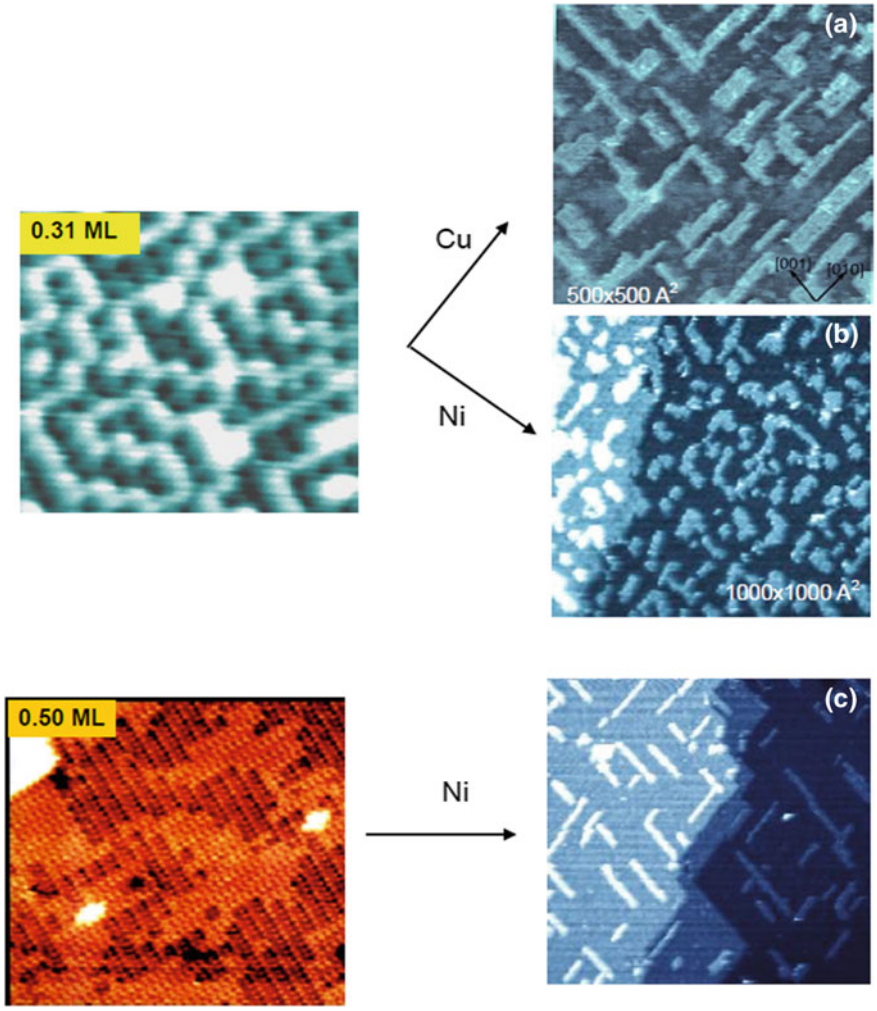

Fig. 4.8 Deposition of Cu and Ni atoms on a four-spot Cu(100)-O surface. Oxygen atoms on the Cu(100)-O work as a surfactant to foster the growth of one-atomic-height layers of Cu and Ni islands. **a** Growth of one-atomic-height Cu islands with the strain-released ($2\sqrt{2} \times \sqrt{2}$) R45–O structure. **b** Growth of Ni islands with no specific orientation on the c(2 × 2)Cu(100)–O surface. **c** Growth of nano-width Ni wires along the trough of missing Cu atoms on the ($2\sqrt{2} \times \sqrt{2}$)R45-O surface [23]

Ni(110) surface, but the growth of (–NiH–) strings can compress the (–NiO–) strings from the (3 × 1) to a (2 × 1) array on the Ni(110) surface, which is a case of competitive adsorption of quasi-compounds of (–NiH–) and (–NiO–).

This competitive growth of (–NiO–) and (–NiH–) strings strongly supports my idea of "***quasi-compounds***," which reflects the idea that "*the surface is a form of*

matter having its own chemistry." In other words, these materials formed on the surface are essentially different from our known ordinary compounds. If we consider the formation of quasi-compounds by adsorption of heteroatomic molecules such as CO, NO, and NH_3 on metals, two or more compounds are formed by reaction with surface metal atoms. These limited examples give a hint of the complexity of the surface during reaction, as discussed in the following chapter.

The most important fact is that the formation of quasi-compounds depends strongly on the crystal planes. As shown in Fig. 4.6a, a quasi-compound of (–CuO–) strings is formed on the Cu(110) surface on exposure to O_2, but no similar quasi-compound is formed on the Cu(100) surface. Adsorbed O(a) atoms form c(2 × 2)-O domains on the Cu(100) surface, but the growth of nano-size (2 × 2)-O domains into a large-size domain is inhibited by strain. However, if oxygen coverage exceeds a certain value ($\theta = 0.3$), a large c(2 × 2)-O domain is formed by unifying several nano-sized domains, and the local strain becomes high. When the size of a c(2 × 2)-O domain exceeds a critical value, ejection of Cu atoms occurs along the ⟨001⟩ or ⟨010⟩ directions to release the local strain from the c(2 × 2) Cu (100)–O surface, and a (2√2 × √2)R45 structure is established as shown in Fig. 4.3c and Fig. 4.4c [18].

If Cu or Ni atoms deposit on a Cu(100)–O surface covered with nano-sized c(2 × 2)-O domains, the deposited Cu or Ni atoms form one-atomic-height islands, as observed in Fig. 4.8a, b, where the O(a) atoms work as a surfactant to grow one-atomic-height Cu or Ni islands on the Cu(100) surface. It is worth noting that the deposited Cu atoms grow in strain-released one-atomic height Cu islands along the ⟨001⟩ and ⟨010⟩ direction with missing row structure, which forms an anisotropic (2√2 × √2)R45–Cu(100)–O-like structure. In contrast, the Ni atoms deposited on a nano-sized c(2 × 2)–O/Cu(100)–O surface form c(2 × 2)–Ni(100)–O islands among the nano-sized c(2 × 2)-O domains over the Cu(100) surface. On the other hand, if Ni atoms deposit on a reconstructed (2√2 × √2)R45–Cu(100)–O surface, the deposited Ni atoms grow in nano-width Ni lines along the trenches of missing Cu atoms, as shown in Fig. 4.8c [10, 18, 23].

References

1. K-I. Tanaka and K. Tamaru, J. Catal., 2 (**1963**) 366.
2. G. Ertl, Ber. Bunsenges. Phys. Chem., 90 **(1986)** 284.
3. F. Jensen, F Besenbacher, E.Laegsgaard, I.Stensgaard, Phys. Rev. B, 44 (**1991**) 13156.
4. K-I. Tanaka, Jpn. J. Appl. Phys., 32 (**1993**) 1389.
5. M. Sotto, Surf. Sci., *260* (**1992**) 235.
6. R. Mayer, C-S. Zhang, and K.G. Lynn, Phys. Rev. B, 33 (**1986**) 8899.
7. H.C. Zeng, R.A. McFarlane and K.A.R. Mitchell, Surf. Sci. 208 (**1989**) L7.
8. M. Wuttig, R. Franchy and H. Ibach, Surf. Sci., 224 (**1989**) L979.
9. M. Wuttig, R Franchy and H. Ibach, Surf. Sci., 213 (**1989**) 103.
10. K-I. Tanaka, Y. Matsumoto, T. Fujita, and Y. Okawa, Appl. Surf. Sci., 130/132 **(1998)** 475.

11. R.N. Lee and H.E. Farnsworth, Surf. Sci., 3 **(1965)** 461.
12. M.C. Asensio, M.J. Ashwin, A.L.D. Kilcoyne, D.P. Woodruff, A.W. Robinson, Th. Lindner, J.S. Somers, D.E. Ricken, and A.M. Bradshaw, Surf. Sci. 236 (**1990**) 1.
13. T. Lederer, D. Arvanitis, G. Comelli, L. Tröger and K. Baberschke, Phys. Rev. B, 48 (**1993**) 15390.
14. K. Robinson, E. Vlieg, and S. Ferrer, Phys. Rev. B, 42 (**1990**) 6954.
15. H. Tillborg, A. Nilsson, B. Hernnäs, and N. Mårtensson, Surf. Sci., 269/270 (**1992**) 300.
16. F.M. Leibsle, Surf. Sci., 337 (**1995**) 51.
17. T. Fujita, Y. Okawa, Y. Matsumoto and K-I. Tanaka, Phys. Rev., B, 54 **(1996)** 2167.
18. K-I. Tanaka, T. Fujita, and Y. Okawa, Surf. Sci.,401 **(1998)** L407.
19. G. Ertl, Ang. Chem. 102 (**1990**) 1258.
20. M. Taniguchi, K-I. Tanaka, T. Hashizume, and T. Sakurai, Chem. Phys. Lett. 192 **(1992)** 117.
21. H.A. Engelhardt and D. Menzel, Surf. Sci., 57 **(1976)** 591.
22. P.T. Sprunger, Y. Okawa, F. Besenbacher, I. Stensgaard, and K-I. Tanaka, Surf. Sci. 344 **(1995)** 98.
23. T. Fujita and K-I. Tanaka, Surf. Sci., 418 **(1998**) L 45.

Chapter 5
Reaction of Quasi-Compounds on Metal Surfaces

Abstract⟨−2 1 1⟩ When Cu atoms are vaporized on a (2 × 1)(–AgO–)/Ag(110) surface, the quasi-compound (–AgO–) strings react with Cu atoms and a new quasi-compound (–CuO–) string grows in the ⟨1–10⟩ direction on the Ag(110) surface; the (2 × 1)(–AgO–)/Ag(110) surface changes to (1 × 2)(Cu–O–)/Ag(110). This newly formed (–CuO–) string on the Ag(110) surface undergoes reversible reaction described by (–CuO–) string $\rightleftharpoons (Cu_2)_3 + O_2$ at moderate temperatures. When a (–AgO–)/Ag(110) surface is exposed to CO_2, a hybrid surface with (–AgO–) and Ag–CO_3 is formed. The Cu atoms vaporized on this hybrid [(–AgO–) + Ag–CO_3]/Ag(110) surface undergo selective reaction with the (–AgO–) strings. However, the reverse selective reaction of Cu atoms occurs by the sweep of the hybrid surface with a W-tip of STM contaminated with Cu atoms. That is, Cu atoms on a W-tip react selectively with $AgCO_3$ dots, and a [(–AgO–) + (–CuO–)] hybrid surface is formed by painting using a Cu/W-tip, which is named as "atom painting." The quasi-compound may be formed on the surface by reaction via a precursor state, although it is difficult to detect. The presence of precursor states is well proved by the dissociation of alcohol molecules on the 7 × 7-Si(111) surface, that is, the dissociation probability of alcohol molecule in a half unit cell depends on the local conformation of the sites, which strongly suggests the dissociation via a precursor state.

Keywords Reaction of Cu with quasi-compounds (–AgO–) · Passive Cu_3N on Cu (100) · Labile Ni_4C on Ni · Reversible change of (–CuO–) $\rightleftharpoons (Cu_2)_3 + O_2$ on Ag (110) · Reaction of quasi-compounds · Hybrid surface composed of different quasi-compounds · Layer-by-layer honeycomb stacking of Zn_3 on 7 × 7-Si(111) surface · Dissociates of C_2H_5OH via precursor state on 7 × 7-Si(111) surface · Atom number controlled growth of metal particles on a 7 × 7-Si(111)–C_2H_5OH · Layer-by-layer stacking of Ag nanoparticles and Zn nanoparticles

Formation of new materials named quasi-compounds is discussed in Chaps. 3–5. The structure and reactivity of quasi-compounds stabilized on the surface are quite different from these of our known ordinary compounds. In a catalytic reaction, all

K. Tanaka, *Dynamic Chemical Processes on Solid Surfaces*,
DOI 10.1007/978-981-10-2839-7_5

required chemical processes including rotation of intermediates and the effective diffusion of intermediates should proceed steadily on the surface. Such complex chemical processes are discussed in **Part II**.

The growth mode of ordinary materials on solid surfaces is quite different from the growth of quasi-compounds. The growth mode of ordinary materials on surface is explained by the three modes: (1) layer-by-layer growth on the surface (Frank-van der Merwe mechanism), (2) three-dimensional island growth (Volmer–Weber mechanism), and (3) layer growth followed by three-dimensional island growth (Stranski–Krastanov), and the growth mode of materials depends on the equation $\Delta\Gamma = (\Gamma_s - \Gamma_i) + \Gamma_f$, where Γ_s and Γ_f are the surface energies of the substrate and deposited layer, and Γ_i is the interfacial energy between them. If the interfacial energy (Γ_i) is high or the surface energy of the deposited layer (Γ_f) is low, that is, $\Delta\Gamma < 0$ ($\Gamma_s + \Gamma_f < \Gamma_i$,), we can expect Stranski–Krastanov type layer-by-layer growth. Conversely, when the interfacial energy is low or the surface energy of the deposited layer is high, that is, $\Gamma_s + \Gamma_f > \Gamma_i$ ($\Delta\Gamma > 0$), then three-dimensional self-growth of materials takes place on the surface.

Formation reaction of quasi-compound on the surface is quite different from these three modes of epitaxial growth. A prominent example was shown by Matsumoto et al. [1–3] by the reaction of Cu atoms with quasi-compound (–AgO–) strings on a p(2 × 1)(–AgO–)/Ag(110) surface. As shown in Fig. 5.1, the deposited Cu atoms react with the (–AgO–) strings according to a chemical reaction given by an equation of Cu + (–AgO–)/Ag(110) → Ag + (–CuO–)/Ag(110), where the (–CuO–) strings grow in the ⟨1–10⟩ direction perpendicular to the (–AgO–) strings, and the released Ag atoms create a new (110) terrace with one atomic height. This stoichiometric reaction provides a new composite Ag(110) surface, where the (–CuO–) strings are perpendicular to the (–AgO–) strings as shown in Fig. 5.1b. The released Ag atoms make a new terrace which is also covered with (–CuO–) strings shown as terrace **(iii)** in Fig. 5.1b. This result indicates that a perfect stoichiometric reaction takes place between the (–AgO–) strings and Cu atoms on the surface. The Ag(110) surface is eventually covered with a (1 × 2) array of (–CuO–) strings grown in the ⟨1–10⟩ direction, and the (1 × 2)(–CuO–)/Ag(110) is a newly formed quasi-compound on a Ag(110) surface. The (1 x 2) array of (–CuO–) strings on Ag(110) take an in-phase zigzag structure as shown in Fig. 5.1b-ii, which is expressed as (2 x 2)p2mg (–CuO–)/Ag(110) structure. This in-phase zigzag structure of the (–CuO–) strings cannot be recognized in the (1 x 3) array of (–CuO–) strings on Ag(110) as shown in Fig. 5.1 (c) [1, 4]. That is, this in-phase zigzag structure appears only on the (1 x 2) array of (–CuO–) strings on Ag(110) surface, but not on the (1 x 3) array of (–CuO–) on Ag(110), which suggests the existence of a short range dipole-dipole interaction between the (–Cu–O–) strings on the Ag(100) surface. These results suggest that the (–CuO–) strings on the Ag (110) surface are different from the (–CuO–) strings formed on the Cu(110) surface. In fact, the decomposition temperature is quite different between (1 x 3)(–CuO–)/Ag(110) and (2 x 1)(–CuO–)/Cu(110), that is, the (–CuO–) strings on Ag(110) surface decomposes readily at lower temperature than that on Cu(110) surface. As shown in Fig. 5.1c, the (1 × 3) (–CuO–)/Ag(110) surface readily decompose to

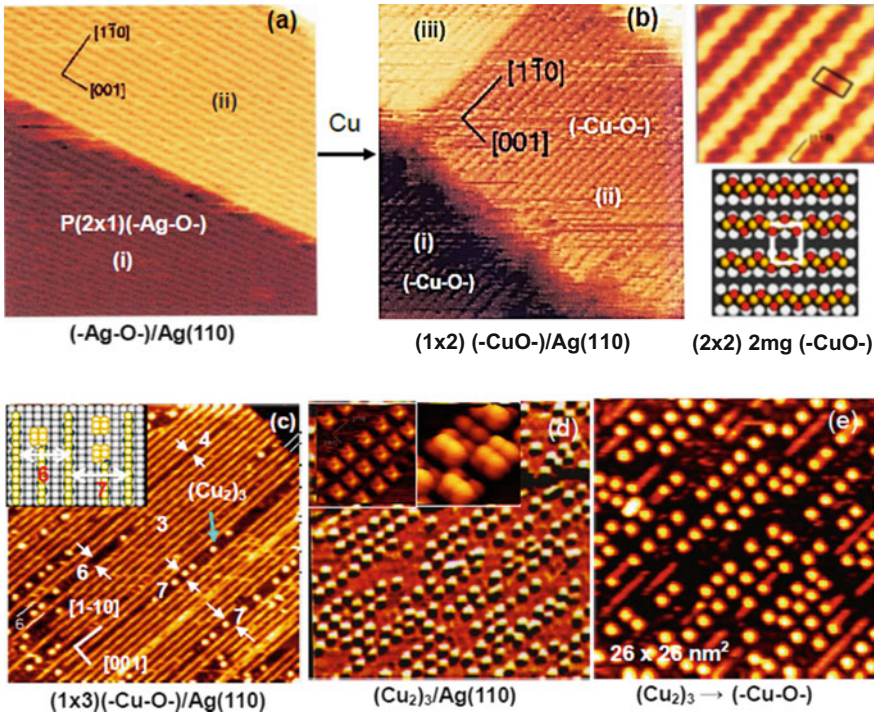

Fig. 5.1 **a** A Ag(110) surface covered with (–AgO–) strings in a (2 x 1) array. **b-i** A Ag(110) surface with the three terraces covered with (1 x 2) array of (–CuO–) strings formed by a stoichiometric reaction of (2 x 1) (–AgO–) + Cu → Ag + (1 x 2) (–Cu–O–) [2]. **b-ii** In-phase zigzag array of the (1 x 2) (–CuO–) strings in a (2 x 2) 2mg structure on the Ag(110) surface [1, 4]. **c** (–CuO–) strings on the (1 x 3)(–CuO–)/Ag(110) surface decompose to $(Cu_2)_3$ dots by raising temperature along the phase boundary with 7-lattice spacing. In-set image shows a model of $(Cu_2)_3$. **d** Completely decomposed (1 x 3)(–CuO–) strings to (Cu2)3 dots on Ag(110) surface at 570 K [1]. In-set image shows the raft structure of $(Cu_2)_3$ dots. **e** Regrowth of (–CuO–) strings by reacting $(Cu_2)_3$ dots with O_2 on the Ag(110) surface at room temperature

$(Cu_2)_3$ cluster dots at 550 K, which is a surprisingly low compared to the decomposition temperature of the (2 × 1) (–CuO–) strings on the Cu(110) surface.

Decomposition of (–CuO–) strings on the Ag(110) surface is quite unique. The decomposition proceeds preferentially along the phase boundary of the (1 × 3) (–CuO–) array, which is one lattice spacing wider than the spacing in the (1 × 3) (–CuO–) phase as illustrated by the model in Fig. 5.1c. The $(Cu_2)_3$ cluster exhibits a square shape, as the inset STM image shown in Fig. 5.1d. The phase boundary has 4-lattice spacing, so that the $(Cu_2)_3$ cluster formed along the phase boundary stays in the 7-lattice spacing (3 + 4 spaces), and the $(Cu_2)_3$ cluster takes an equal distance from either side of the (–CuO–) strings as shown in Fig. 5.1c. On the other hand, the $(Cu_2)_3$ dots formed by the decomposition of a (–CuO–) string in the (1 × 3) phase are in a 6-lattice spacing (3 + 3 spaces), so that the distance of a $(Cu_2)_3$ dot from one side (–CuO–) string is shorter than that from the other side. When $(Cu_2)_3$ dots on the

Ag(110) surface are exposed to O_2, regrowth of (–CuO–) strings occurs on the Ag (110) surface, where the regrowth of (–CuO–) strings takes place from the corner of square $(Cu_2)_3$ dots at room temperature as shown in Fig. 5.1e. These phenomena suggest that the (–CuO–) grown on Ag(110) are different from the (–CuO–) on Cu (110) surface. This is one feature of quasi-compounds which is essentially different from ordinary materials in three-dimensional space. A more interesting phenomenon is the regrowth of (–CuO–) strings by the reaction of $(Cu_2)_3$ dots with O_2, and the regrowth of (–CuO–) strings by the reaction of $(Cu_2)_3$ dots with O_2, where the regrowth of (–CuO–) proceeds at a fixed one corner of square $(Cu_2)_3$ dots.

When a (3 × 1)(–AgO–)/Ag(110) surface is exposed to CO_2 instead of Cu atoms, Ag–CO_3 dots are formed by the reaction of CO_2 with (–AgO–) strings, and the Ag(110) surface is covered with a composite quasi-compounds of [(–AgO–) + Ag–CO_3] as shown in Fig. 5.2a [4, 5]. The bulky Ag–CO_3 dots compress the (–AgO–) strings from a (3 × 1) array to a (2 × 1) array, which is a unique feature of quasi-compounds observed in the two-dimensional space of the surface. If Cu atoms are deposited on a hybrid [(2 × 1)(–AgO–) + Ag–CO_3 dots] surface, a new composite surface is formed by the selective reaction of Cu atoms; that is, the (1 × 2)(–CuO–) strings are formed by the reaction of the (–AgO–) strings with Cu grow in the ⟨1–10⟩ direction, and the Ag–CO_3 dots are redistributed among the(–CuO–) strings [5], that is, Ag–CO_3 dots are mobile on the Ag (110) surface as shown in Fig. 5.2b.

It is evident that the deposited Cu atoms react selectively with (–AgO–) strings on the [(–AgO–) + (Ag–CO_3)-dots]/Ag(110) surface. However, if the same [(–AgO–) + (Ag–CO_3)-dots]/Ag(110) surface is scanned with a W-tip coated with Cu, the Cu atom on the W-tip selectively reacts with Ag–CO_3 dots, as shown in Fig. 5.2c, d [6]. That is, "**the reaction of quasi-compounds can be controlled by local electrostatic potential!**". This result suggests a possibility of atom scale patterning on the surface by suitable chemical reactions controlled by electrostatic field, so that it is named as "**atom painting**" [6]. Figure 5.2e shows a real-time selective reaction of a composite surface of [(–AgO–) + (–CuO–)] on a Ag(110) surface with CO at room temperature for 20 min, where the (–AgO–) strings preferentially react with CO to form Ag(CO_3) dots.

We know now the reaction of quasi-compounds is controlled by the local potential gradient, although these are not reactions in catalysis, we could anticipate the complexity of the reaction in catalysis. In fact, the local electrostatic gradient established in the presence of H_2O between two materials with different proton activity has a marked effect on the activity and selectivity of catalytic reactions, as discussed in Sect. 10.4 of **Part II** (Scheme 5.1).

$$\begin{aligned}&[\underline{(-\mathbf{AgO}-)} + (\mathrm{Ag} - \mathrm{CO_3})] + \mathbf{Cu} \rightarrow [\underline{(-\mathbf{CuO}-)} + (\mathrm{AgCO_3})] + \mathrm{Ag}\\ &[(-\mathrm{AgO}-) + \underline{(\mathbf{Ag} - \mathbf{CO_3})}] + \mathbf{Cu} \,/\, \text{W-tip} \rightarrow [(-\mathrm{AgO}-) + \underline{(-\mathbf{CuO}-)}] + \mathrm{Ag} \;+ \mathrm{CO_2}\end{aligned} \tag{5.1}$$

As shown in Fig. 4.7b, the array of (–NiO–) strings on a Ni(110) surface is compressed from the (3 × 1) to a (2 × 1) array upon exposure to H_2, with the

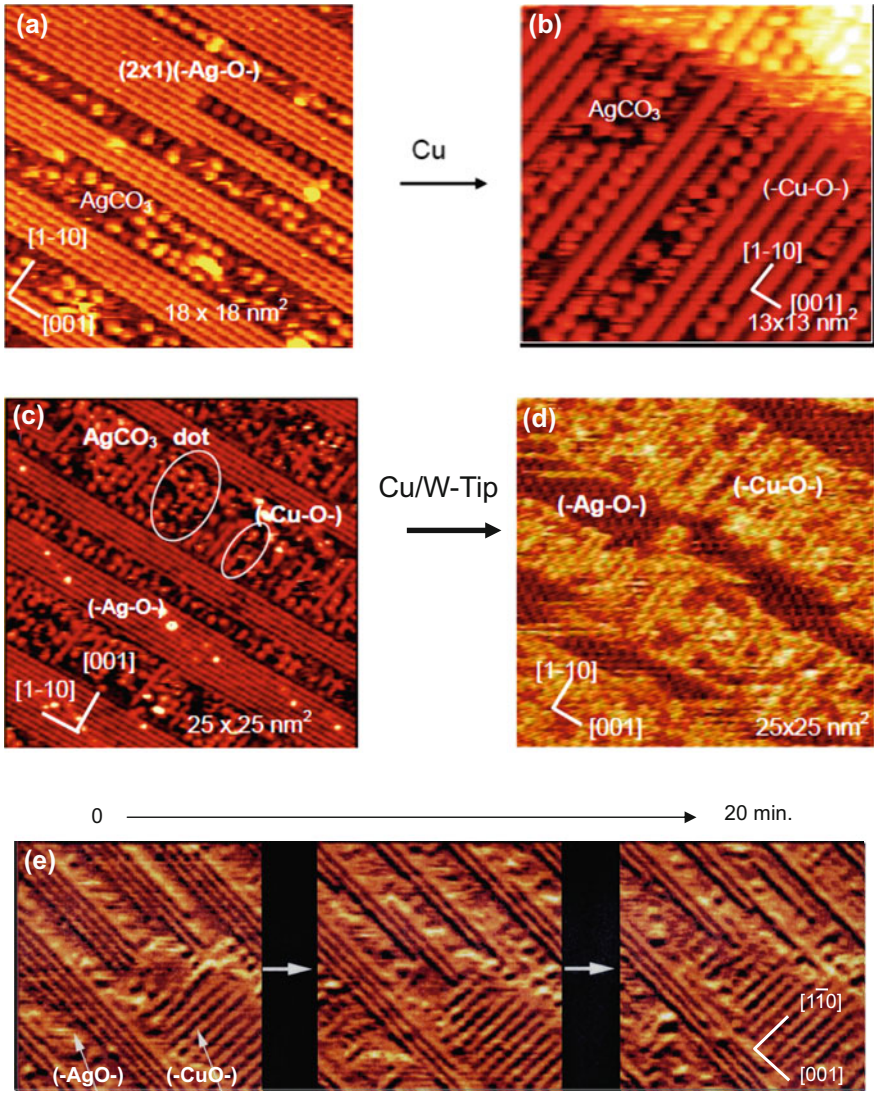
(a)
(2x1)(-Ag-O-)
AgCO3
[1-10]
[001]
18 x 18 nm2
Cu
(b)
AgCO3
(-Cu-O-)
[1-10]
[001]
13x13 nm2
(c)
AgCO3 dot
(-Cu-O-)
(-Ag-O-)
[001]
[1-10]
25 x 25 nm2
Cu/W-Tip
(d)
(-Ag-O-)
(-Cu-O-)
[1-10]
[001]
25x25 nm2
0
20 min.
(e)
(-AgO-)
(-CuO-)
[1$\bar{1}$0]
[001]

◂**Fig. 5.2** **a** Reaction of (3 x 1)(–AgO–)/Ag(110) surface with CO_2 provides a hybrid [(2 x 1)(–AgO–) + Ag–CO_3–dots], where the (3 x 1) (–AgO–) strings are compressed to a (2 x 1) array by forming Ag–CO_3 dots. **b** Cu atoms sublimated on the [(2 x 1)(–AgO–) + Ag–CO_3–dots] surface undergo selective reaction with the (–AgO–) strings, and a new hybrid surface of [(1 x 2)(–CuO–) + Ag–CO_3–dots] is formed [5]. **c** When a [(2 x 1)(–AgO–) + Ag–CO_3–dots]/Ag(110) surface is scanned with a W-tip coated with Cu atoms (Cu/W-tip), Cu reacts selectively with Ag–CO_3–dots, and a new hybrid surface of [(2 x 1)(–AgO–) + (–CuO–)]/Ag(110) is formed [6]. **e** Selective reaction of (–AgO–) with CO on a [(–AgO–) + (–CuO–)] /Ag(110) surface at room temperature for a 20 min. $P_{CO} = 1.0 \times 10^{-8}$ Torr

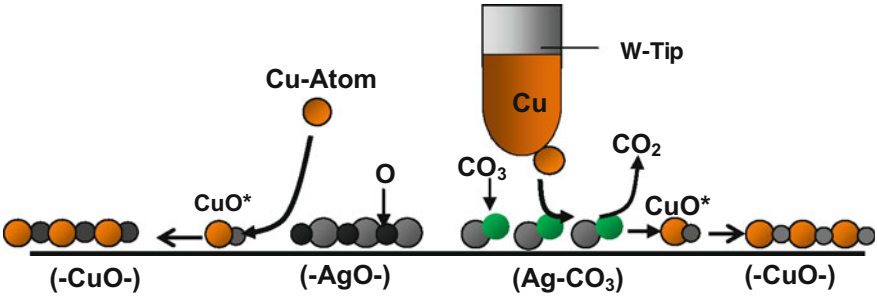

Scheme 5.1 Atom painting with Cu-coated W-tip: Sublimated Cu atoms on a hybrid [(–AgO–) strings + Ag–CO_3] Ag(110) surface react selectively with (–AgO–) strings to form a hybrid [(–CuO–) strings + Ag–CO_3] Ag(110) surface. In contrast, scanning with a W-tip with Cu atoms, a [(–AgO–) strings +(–CuO–)] Ag(110) surface is formed by the opposite selective reaction of the Cu atoms with Ag–CO_3 dots under a bias potential [6]

growth of (–NiH–) strings [7]. If heteroatomic molecules such as CO, NO, and NH_3 are adsorbed and react with surface metal atoms, the surface is covered with different kinds of quasi-compounds. If two or more quasi-compounds are formed on a surface, they may induce complex local lattice distortion over the surface, which will have complex influences on the mobility, stability, and reactivity of quasi-compounds. Such complex local distortion may occur on metal catalysts during reaction.

It is well known that the Cu surface is inactive toward the dissociation of N_2 molecules, but if Cu(100), Cu(110), and Cu(111) surfaces are exposed to N^+/N_2^+ ions made by discharge, N atoms react with Cu atoms at room temperature, and characteristic ordered structure depending on the crystal planes by raising the temperature above 500 K. The N atoms deposited on a Cu(111) surface form a c(2 × 2)-Cu(111)–N structure, which is not the adsorption of N atoms but the growth of a Cu_3N(100)-like plane on the Cu(111) surface [8, 16]. Interestingly, a Cu_3N(100)-like plane grows not only on the Cu(111) surface but also on Cu(110) and Cu(100) surfaces. The formation of a common layer on different crystal planes is similar to the formation of molecule like Ni_4C on the Ni(111), Ni(100), and Ni(110) surfaces as shown in Fig. 6.2, and Ni_4C is a key intermediate on

any Ni catalyst for the formation of CH_4 by hydrogenation of CO with H_2. Therefore, the catalytic activity of Ni catalyst is structure independent as shown in Fig. 6.1. However, Cu_3N is stable and inactive with respect to H_2 on any Cu surface, so that no formation of NH_3 occurs at ordinary reaction temperatures. In contrast, Fe_xN formed on the Fe surface is a key intermediate for the ammonia synthesis reaction, as shown in Fig. 6.4 in Chap. 6.

When a Cu(110) surface is exposed to NO molecules, the molecules dissociate and react with Cu atoms at room temperature, and the surface is covered with the two different quasi-compounds, (–CuO–) and (Cu_3N), as shown in Fig. 5.3a. As mentioned above, the (–CuO–) strings are ordered in a (2 × 1) array on the Cu(110) surface, whereas the Cu_3N dots are randomly situated over the Cu(110) surface at room temperature because Cu_3N dots cannot move on the surface. The reaction of N atoms with Cu atoms is an exothermic reaction, but the exothermic heat is

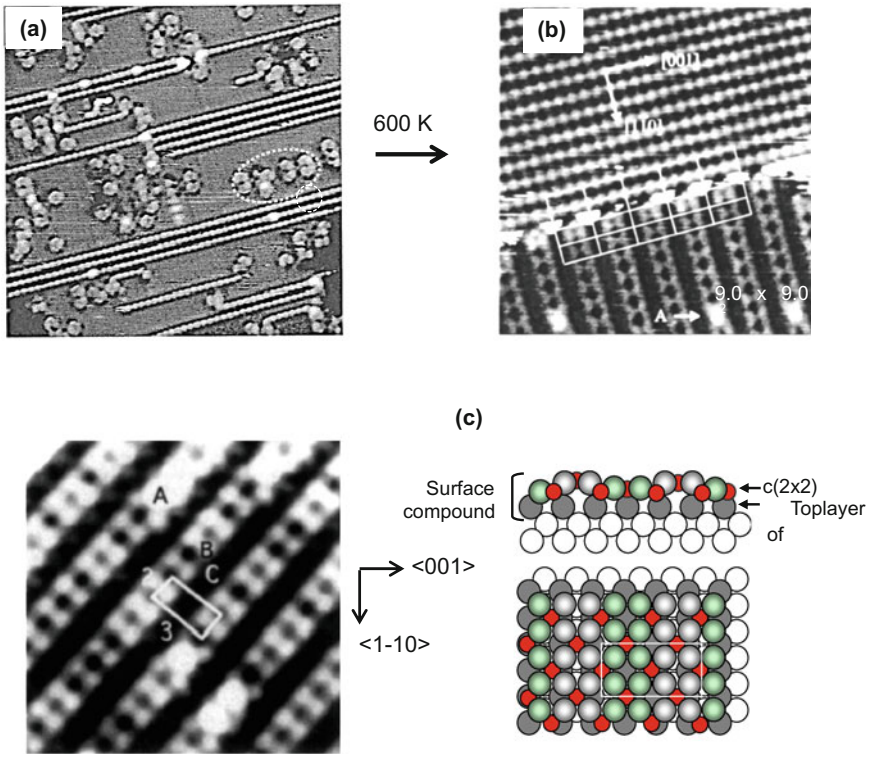

Fig. 5.3 **a** A (2 × 1) array of (–CuO–) strings and randomly dispersed Cu_3N dots are formed on a Cu(110) surface by adsorption of NO at room temperature. **b** Formation of a hybrid layer composed of an ordered (2 × 1) (–CuO–) domain and p(2 × 3)Cu_3N clusters (*rectangular* mesh) on the Cu(110) surface by raising temperature to 600 K [10]. The *bright dots* "A," shown with an arrow, are the 2nd layer. **c** STM image of an area of the (2 × 3)–Cu(110)–N domain, and the *top view* and *side view* model of (2 × 3)-Cu(110)–N [11]

quenched rapidly on the Cu(110) surface so that the Cu_3N dots are randomly distributed on the surface at room temperature [10]. When this surface is heated in UHV at 600 K, the Cu_3N dots are ordered in a (2 × 3) array on the Cu(110) surface, so that the Cu(110) surface is covered with the two domains of (2 × 1) (–CuO–) and p(2 × 3) Cu_3N, as shown in Fig. 5.3b.

The direct decomposition of NO according to an equation of 2 NO → N_2 + O_2 is thermodynamically favorable, but it is not feasible. As shown in the Cu(110) surface, the formation of stable compounds like Cu_3N prevents the catalytic decomposition of NO, because the Cu_3N formed on Cu(110) is not only stable on the Cu(110) surface but also inactive toward reaction with H_2. Accordingly, Cu (110) does not act as a catalyst for the direct decomposition of NO to N_2 nor the reduction of NO with H_2. These results suggest an important prerequisite for the catalytic reduction of NO, NO + H_2 → 1/2 N_2 + H_2O, is the formation of reactive N(a) or a reactive nitride. As will be discussed in Chap. 9 of **Part II,** a Pt–Rh alloy and/or Pt/Rh bimetal surface fulfills this prerequisite for the catalytic reaction of NO + H_2 → 1/2 N_2 + H_2O, because the N(a) does not form a stable compound on Pt and/or Rh, and O atoms form reactive (–Rh–O–) strings on the surface.

As mentioned above, if a Cu(100) surface bombarded with N ions is annealed at 500 K, a grid-like surface is formed by paving the Cu(100) surface with square Cu_3N(100) patches. The lines remained between the square patches are composed of inlay-like clean Cu lines. The grid-like lines and their intersections, which are clean Cu(100) surface, work as a "**mold**" for the growth of metal particles on this surface [13, 14]. A Cu(110) surface bombarded with N ions forms a (2 × 3)-Cu (110)–N surface upon annealing at 650 K [8]. Bradshaw and his coworkers [15] suggested the growth of a pseudo-c(2 × 2)-Cu(100)–N layer on Cu(110) surface by using fully dynamic LEED, which is similar to the epitaxial growth of Cu_3N(100) patches. A Cu(111) surface bombarded with N ions at 300 K is covered with a random array of Cu_3N(100) patches, which are ordered into three Cu_3N(100) domains on the Cu(111) surface at 500 K [8, 16].

Figure 5.4a, b shows the Cu_3N(100) patches (5.2 ± 0.4 nm^2) formed on a Cu (100) surface by annealing at 600 K observed by Leibsle et al. [17]. The Cu–Cu distance in the Cu_3N(100) patch is approximately 5% longer than that on the Cu (100) surface, but the LEED pattern revealed lattice mismatch between the Cu_3N (100) and Cu(100) surfaces is very small, under 0.05%. Therefore, they speculated that the lattice strain around the square edge of the Cu_3N(100) patch was released by the ejection of 56 Cu atoms (4 × 14) from the Cu(100) surface. Taking their result into account, Komori and his coworkers [18, 19] studied the fine structure of the Cu(100)–N surface by using high-resolution STM and concluded that the lattice distortion localized in the vicinity of the square patches is responsible for the formation of uniform-sized square Cu_3N(100) patches. It is noteworthy that the array of square Cu_3N(100) patches on the Cu(100) surface is similar to the Ni_4C carbide inlaid on the Ni(100), Ni(110), and Ni(111) surfaces. The local strain induced on the Ni(100) surface by inlaid Ni_4C is released without the release of Ni atoms but by rotating Ni_4C patches, as discussed in Fig. 6.2 in Chap. 6. The size of

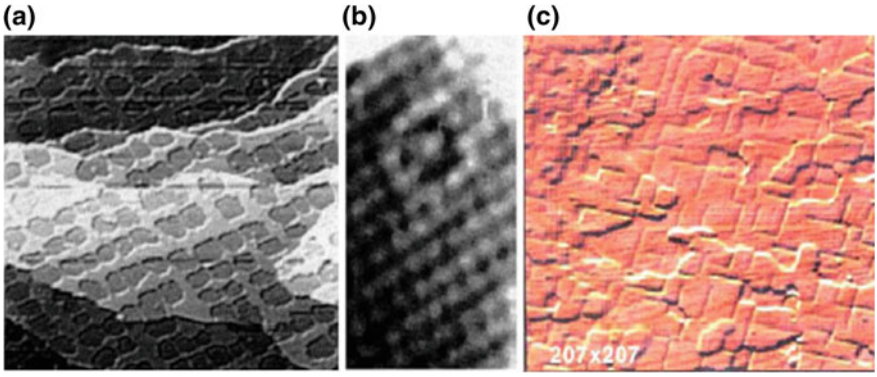

Fig. 5.4 **a** Cu(100) surface covered with square c(2 × 2)-N patches. **b** A high-resolution image of a c(2 × 2)-N patch (ca. 5 × 5 nm^2) [17]. **c** A Cu(100) surface fully covered with c(2 × 2)-N layer [20])

the 5 × 5 nm^2 square $Cu_3N(100)$ patches is decided by lattice distortion in the vicinity of $Cu_3N(100)$. The width of clean grid-like Cu(100) lines (bright lines) becomes narrower and narrower as increasing the number of 5 × 5 nm^2 patches on the Cu(100) surface [19], and the whole Cu(100) surface is eventually covered with a $Cu_3N(100)$ plane, as shown in Fig. 5.4c [20].

When Ni atoms are deposited on a clean Cu(100) surface, they undergo epitaxial growth on the surface even though the lattice constant of Ni is 2.5% shorter than that of Cu [21–23]. If Ni atoms deposit on a Cu(100) surface covered with square $Cu_3N(100)$ patches, epitaxial growth of a one-atom-thick Ni layer prevails on the less distorted crossing of the clean Cu(100) lines, as shown in Fig. 5.5a, and the Ni particles grow according to the Stranski–Krastanov mode [20]. That is, the growth of Ni particles is regulated by the interfacial energy (Γ_i), and the particle size is decided by the "**molding effect**" of square $Cu_3N(100)$ patches surrounding Ni particles.

This phenomenon indicates that the deposited Ni atoms undergo rapid diffusion along the narrow lines of Cu(100) and are stabilized by forming Ni dots at the less distorted cross-lines. Co and Fe atoms grow also in rather uniform-sized Co [14, 19] and Fe [19, 24] particles at the crosses of clean narrow Cu(100) lines made by 5 × 5 nm^2 square $Cu_3N(100)$ patches. The growth mode of Fe particles is similar to that of Ni particles, that is, one-atomic-height Fe particles grow at the intersection of clean Cu(100) lines. With the deposition of more Fe atoms, the clean Cu(100) lines are paved with a one-atomic-height Fe layer, and Fe particles grow as two-atomic-height particles as schematically described in Fig. 5.6. In the deposition of Co atoms, however, the grid-like clean Cu(100) lines are covered first with one-atomic-height Co layer, which means the interfacial energy of a Co layer on the Cu(100) surface is larger than that of a Ni layer or Fe layer. Further deposition of

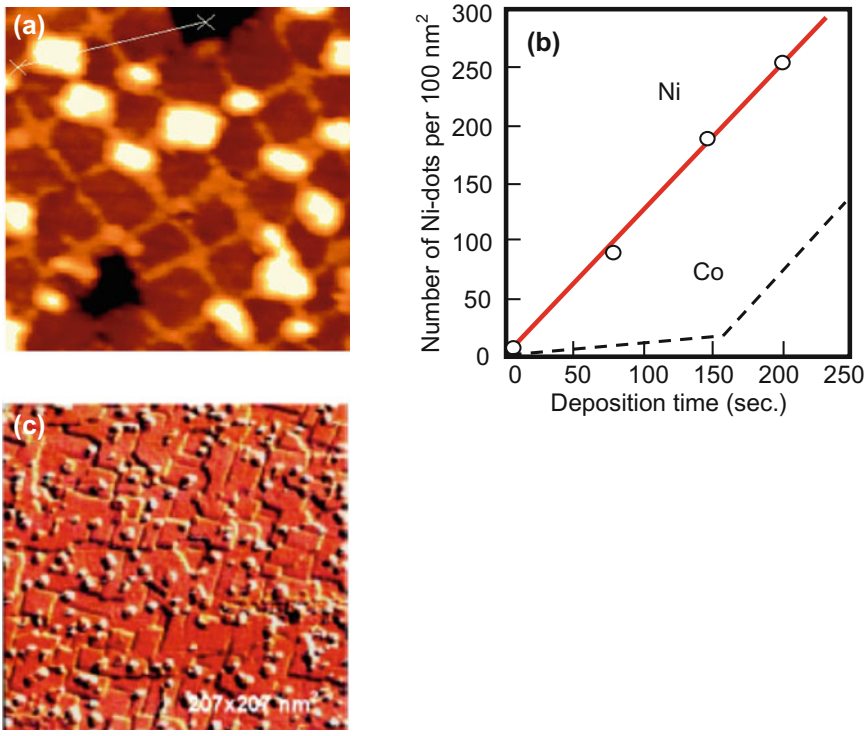

Fig. 5.5 **a** Deposited Ni atoms on a Cu(100)–N surface grow in particles at the crosses of the clean Cu(100) *lines* between 5 × 5 nm^2 square Cu_3N(100) patches formed by annealing at 650 K. **b** Increase in number of Ni particles with deposition time, and the expected growth pattern of Co particles at the *crosses* after the completion of a Co layer on the *lines*. **c** Growth of large Ni particles with two or three atomic layers on a Cu(100) surface fully covered with Cu_3N(100) layer [20]

Co atoms creates two-layer Co particles at the intersections, as described by the model in Fig. 5.6 [13].

Atoms stopping for a time on a surface can be detected by STM, but the atoms rapidly moving on surface are difficult to detect by STM. As shown in Fig. 7.1, Sn atom rapidly moving in a half unit cell on the (7 × 7)-Si(111) surface would be a good model to imagine a precursor state in adsorption. Similarly, adsorption of molecule proceeds via a precursor state on the surface, but the precursor state is difficult to detect by STM. We can presume precursor state molecule in the dissociation of molecule forming covalent bond with adsorption sites from their adsorption kinetics. The adsorption of CH_3OH, C_2H_5OH, and $(CH_3)_2CHOH$ on the (7 × 7)-Si(111) surface is a good example. A truncated (1 × 1)-Si(111) surface is stabilized by forming a reconstructed (7 × 7)-Si(111) surface, which is composed of two half unit cells with different local density of state as shown by Hammers et al. [25]. One has a stacking fault (F-half), while the other has no stacking fault (U-half), which are

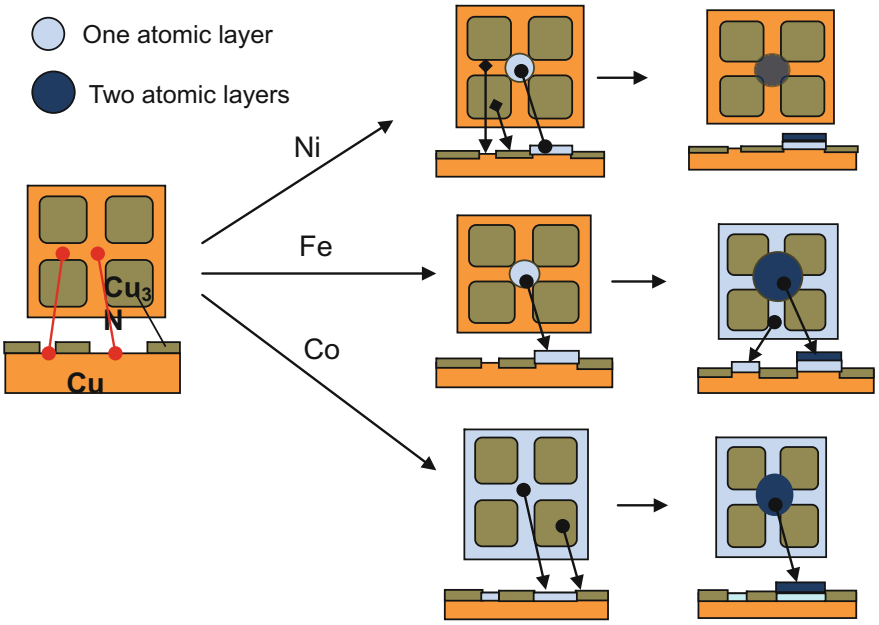

Fig. 5.6 Growth mode of metal particles depends on their interfacial energy on a Cu(100) surface covered with square planar $Cu_3N(100)$ patches. Growth of particles at the intersection is regulated by the molding effect of the array of square $Cu_3N(100)$ patches [13]

distinguishable by a filled-state STM image attained at negative bias potential, as shown in Fig. 5.7a [24–27]. Photoemission and inverse photoemission spectroscopy suggest that the dangling bond on the rest Si atom is almost filled with a pair of electrons, while that of the Si adatom is nearly empty as schematically shown with a model in Fig. 5.7 [24].

If a clean (7 × 7)-Si(111) surface is exposed to CH_3OH or C_2H_5OH (R–OH), the molecules dissociate into Si–OR and Si–H on a pair of (Si adatom/Si rest atom) as described schematically in Fig. 5.7b [9, 28]. As describe below, the alcohol molecule (ROH) does not directly dissociate by collision at a pair of Si adatom/Si rest atom, but undergoes dissociation via a precursor state on either a center-Si-adatom or on a corner-Si-adatom site. As shown in Fig. 5.8c, the dissociation probability of a precursor state molecule is four times larger on the **center** Si adatom compared to that on the **corner** Si adatom in either the F-half or U-half unit cells on the (7 × 7)-Si(111) surface. This fact suggests that the dissociation probability of a precursor state alcohol molecule depends on the number of Si rest atoms to the Si adatoms, which is one to a corner Si adatom but two to a center Si adatom.

As shown in Fig. 5.7 with a model, a corner Si adatom has one adjacent Si rest atom, whereas a center Si adatom has two adjacent Si rest atoms. The dissociation probability of a precursor state ROH molecule depends on the number of Si rest

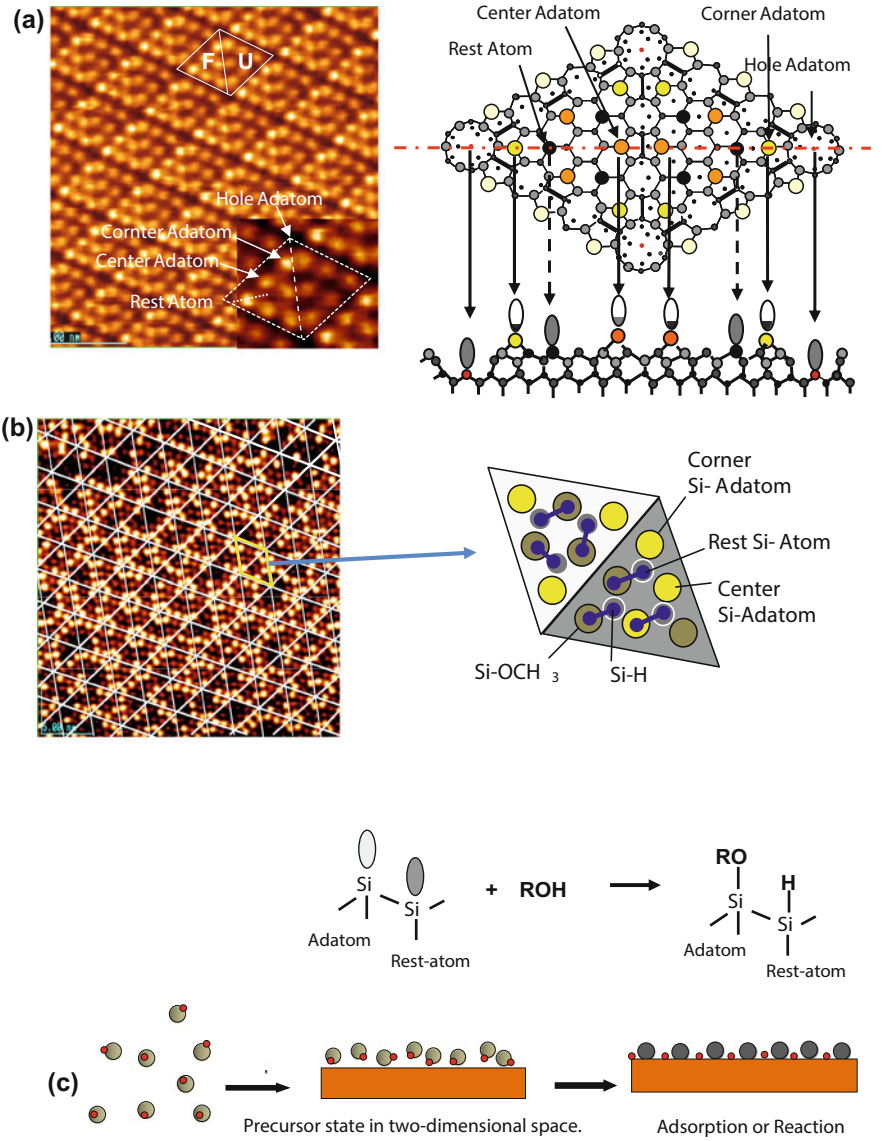

Fig. 5.7 **a** STM image of faulted (F) and unfaulted (U) half unit cells obtained at 2.0 V, DAS model of (7 × 7)-Si(111) surface, and *inset* image obtained at −1.5 V with 0.2 nA. **b** STM image of a (7 × 7)-Si(111) surface saturated with the adsorption of CH_3OH attained at a bias potential of 2.0 V with a tunneling current of 0.2 nA. Three intact Si adatoms (*bright spots*) remain in each half unit cell at saturation [28]. **c** Transport of molecules from the 3-D gas phase to the 2-D space of the surface via precursor state

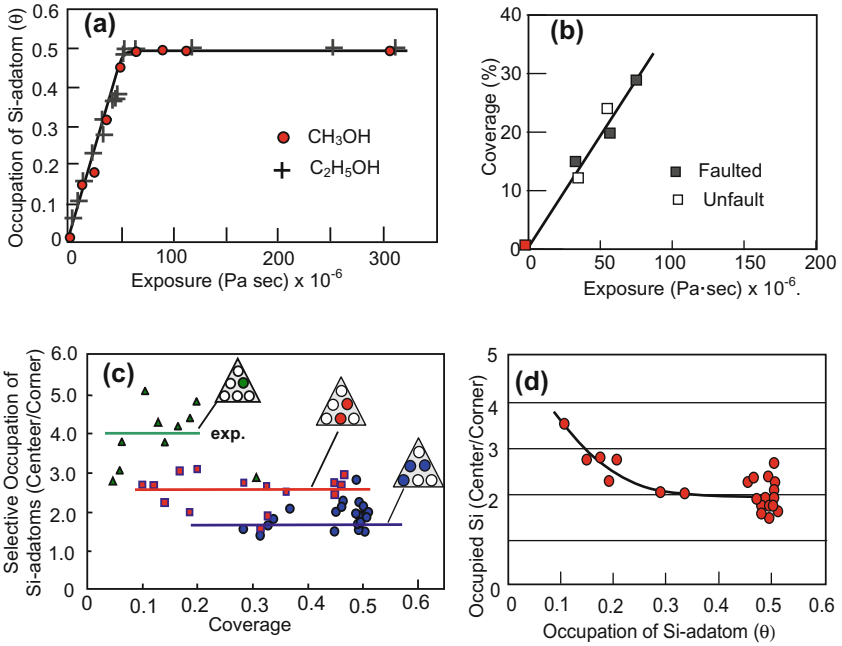

Fig. 5.8 Dissociation of CH_3OH via precursor state on the (7 × 7)-Si(111) surface at room temperature. **a** Constant sticking probability of CH_3OH and C_2H_5OH on the (7 × 7)-Si(111) surface. **b** Equal sticking probability of CH_3OH on faulted half and unfaulted half unit cells. **c** Dissociation probability of ROH on the center Si adatoms is fourfold greater than that on the corner Si adatoms. **d** The ratio of occupied center Si adatoms to corner Si adatoms decreases from 4 to 2 with increasing coverage [9, 28, 29, 34]

atom(s) adjacent to Si adatom, which is one on the corner Si adatom but two on the center Si adatom. The dissociation probability of precursor state alcohol molecule is four times larger on the center Si adatom with two Si rest atoms compared to that on the corner Si-adatom with one Si rest atom, respectively [9, 29]. As a result, the ratio of unoccupied center Si adatoms to unoccupied corner Si adatoms becomes finally 0.5 at the saturated adsorption of alcohol. That is, corner Si adatoms remain twice as many on the (7 × 7)-Si(111) saturated with adsorption of alcohol. It is worth noting that the adsorption (dissociation) probability of methanol (CH_3OH) is exactly equal to that of ethanol (C_2H_5OH) and their adsorption probability has a constant value up to the saturation, as shown in Fig. 5.8a. These results strongly suggest that dissociation of alcohol molecules occurs via a precursor state, and Fig. 5.7c shows a model for the dissociation process via a precursor state, where a precursor state alcohol molecule in a half unit cell undergoes dissociation far more rapidly than its desorption, and the dissociation probability depends on the number of adjacent Si rest atoms, either one or two Si adatom. The dissociation of iso-propanol $(CH_3)_2CHOH$ also occurs via a precursor state on the (7 × 7)-Si(111)

surface, but the dissociation probability becomes low when the coverage exceeds 0.4. This might be due to the restricted mobility of the precursor state iso-propanol in a half unit cell due to preceding adsorbed $(CH_3)_2CHO$-Si adatom. It is worthy of note that the results suggest the possibility for the formation of a chiral Si(111) surface by the adsorption of chiral alcohol.

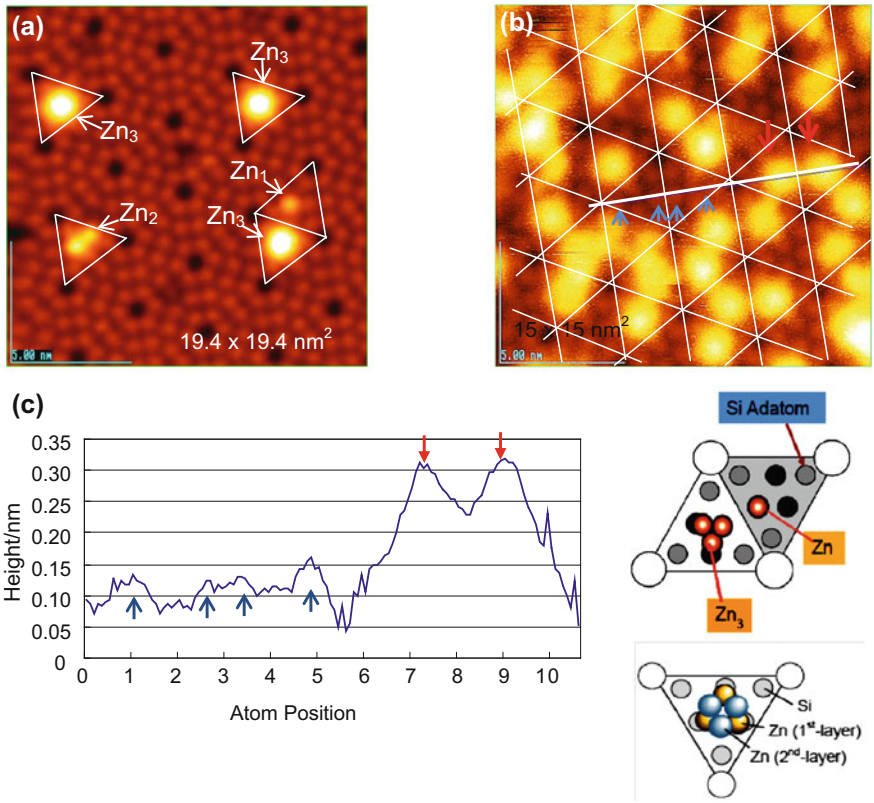

Fig. 5.9 Zn atoms stabilized on a clean (7 × 7)-Si(111) surface [32]. **a** Zn atoms are stabilized on the center Si adatoms in the form of Zn, Zn_2, and Zn_3. **b** *Bright dot* is a Zn_3 cluster stabilized in a half unit, and the Zn_3-dots form a honeycomb array on the (7 × 7)-Si(111) surface. Corrugation peaks along the *broken line* occur at the corner Si adatoms, center Si adatoms, and Zn3 cluster on the three center Si adatoms. **c** A corrugation *curve* along the *broken line*. The peaks appeared at the corner Si adatoms, center Si adatoms, and Zn_3 cluster on the three center Si adatoms. Formation models of Zn, Zn_3, and the 2nd layer of Zn_3 cluster. **d** STM image of multiply stacked honeycomb layers of Zn_3 clusters, and a model for the one and two stacking layers of Zn_3 clusters. **e** The STS curves obtained for a multiple honeycomb array of Zn_3 clusters on a (7 × 7)-Si(111) surface, where the band gap is observed in the 1st to 3rd layers but disappeared in the 4th layer

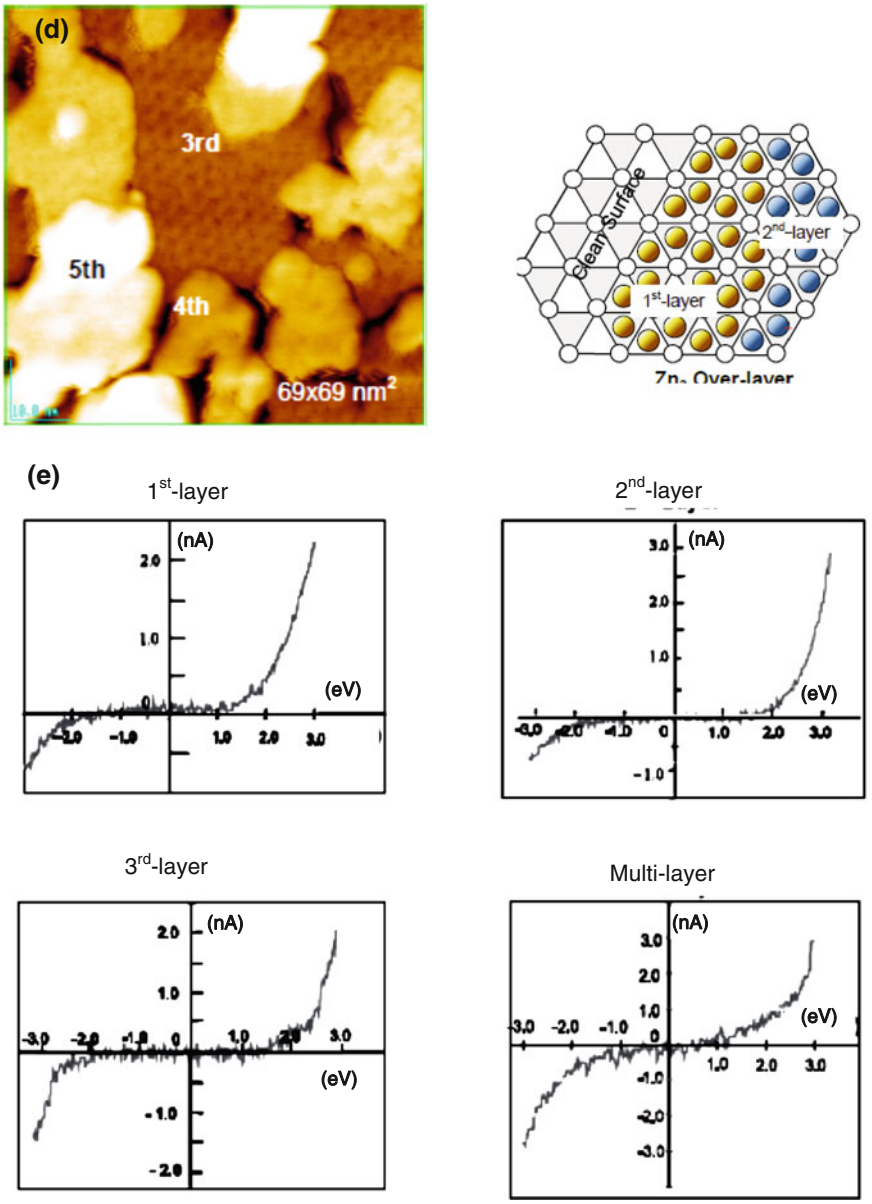

Fig. 5.9 (continued)

It is known that some metals deposited on a (7 × 7)-Si(111) surface react to form silicides. However, if a deposited metal atom does not react with Si adatoms, we can expect two different selectivity in adsorption on a clean (7 × 7)-Si(111)

surface: One is the selectivity for either U-half or F-half unit cells, and the other is for either center Si adatom or corner Si adatom. Most metals (Tl, Li, K, Na, Pb, Y, Cu, Ag, and Au) prefer to adsorb on the F-half unit cell of the (7 × 7)-Si(111) surface, whereas Sn [30, 31, 38, 39], Zn [32], and In [30] adsorb equally on the F-half and U-half. Zn atom is adsorbed selectively on the center Si adatoms, that is, no adsorption occurs on the corner Si adatoms. Zn, Zn_2, and Zn_3 are formed on the three center Si adatoms on a clean (7 × 7)-Si(111) surface, but no adsorption of Zn atoms occurs on the corner Si adatoms, as shown in Fig. 5.9a [32].

Finally, a half unit cell is filled by a Zn_3 cluster on the (7 × 7)-Si(111) surface, and the (7 × 7)-Si(111) surface is covered with Zn_3 clusters in a honeycomb-like structure around the corner holes on the (7 × 7)-Si(111) surface as shown in Fig. 5.9b [32]. When the 1st honeycomb layer of Zn_3 clusters is completed, the 2nd and the 3rd honeycomb layers follow. A notable feature is the stacking structure of the 2nd layer, which is a commensurate stacking of the Zn_3 cluster with 60° rotation to the 1st layer to form the 2nd layer, and subsequent stacking forms the 3rd layer as described in Fig. 5.9c. The honeycomb structure is held in place by commensurate stacking of Zn_3 clusters in the 3rd layer, but no more commensurate stacking of Zn_3 clusters continues for the 4th layer as shown in Fig. 5.9d. It is known that the electronic structure is changed from the semiconducting 1st to 3rd honeycomb layers to the metallic 4th layer as shown in Fig. 5.9e, where the band gap of the honeycomb layers disappears in the 4th layer [32].

It should be remembered that a honeycomb structure is formed by stacking of Zn_3 clusters with weak attractive interaction of Zn_3 clusters on the (7 × 7)-Si(111) surface. This is analogous to the two-dimensional self-assembly of alkane molecules by forming a two-dimensional eutectic nano-crystalline phase on the reconstructed (22 × $\sqrt{3}$)–Au(111) surface as shown in Fig. 3.1a. The adsorption probability of C_2H_5OH on a (7 × 7)-Si(111) surface shows a fourfold difference between the center Si adatoms and corner Si adatoms as shown in Fig. 5.8c, so that twice as many unoccupied Si adatoms remain on corner Si adatoms as on center Si adatoms on the (7 × 7)-Si(111)–C_2H_5OH surface as shown in (d) (the ratio of occupied Si adatoms).

If a Zn atom is deposited on this (7 × 7)-Si(111)–C_2H_5OH surface, nonselective adsorption of the Zn atom occurs on the three unoccupied Si adatoms, so that the number of Zn atoms adsorbed on corner Si adatoms is twice that on the center Si adatoms on the (7 × 7)-Si(111)–C_2H_5OH surface. As a result, deposited Zn atoms are stabilized more around the corner holes as observed in Fig. 5.10a, and more Zn particles grow around corner holes with the deposition of Zn as observed in Fig. 5.10b [33, 35].

Rapidly migration of Ag-atom over the Si-adatoms on a clean (7 x 7)-Si(111) surface at room temperature was explained by hopping of Ag atom via Si-rest atoms [37]. In fact, the Ag atom deposited on the (7 × 7)-Si(111)–C_2H_5OH surface (Si rest atoms are changed to Si–H) cannot migrate as shown in Fig. 5.10c, that is, the Si rest atoms are occupied with H atoms on the (7 × 7)-Si(111)–C_2H_5OH surface,

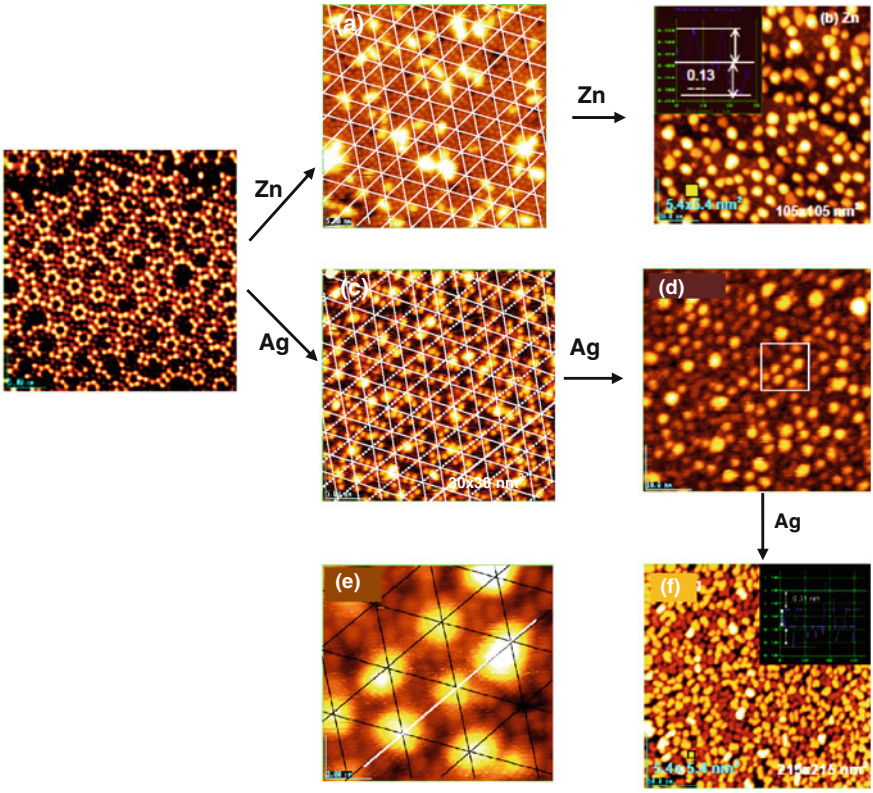

Fig. 5.10 Zn and Ag atoms deposited on a Si(111)–7 × 7–C_2H_5OH surface. **a** STM image of Zn atoms deposited on a (7 × 7)-Si(111)–C_2H_5OH surface, and **b** the growth of nano-size Zn particles [33, 35]. **c** STM image of a single Ag atom deposited on intact Si adatoms on a (7 × 7)-Si(111)–C_2H_5OH surface attained at V = 2.2 V and I = 0.2 nA. 30 × 30 nm^2. **d** Growth of nano-crystalline Ag dots around the corner holes makes a line. The image was attained at V = −2.3 V, I = 0.2 nA, 50 × 50 nm^2. **e** Expanded STM image of the *square area* in (**d**), indicating preferential growth of Ag dots around the corner holes. **f** Uniform height of Ag dots suggests a layer-by-layer growth of nano-crystalline Ag dots on (7 × 7)-Si(111)–C_2H_5OH [35, 36]

so that the Si–H rest atoms prevent the motion of Ag atoms on the (7 × 7)-Si(111)–C_2H_5OH surface as shown in Fig. 5.10c, d. As a result, the growth of Ag particles is regulated in a uniform size of ca. 5 nm and a uniform height on the Si adatoms remaining surrounding a corner hole, as shown in Fig. 5.10e, f. The difference in height between dark and medium bright dots is by ca. 0.25 nm (one atomic layer) and that between the medium bright to brightest dots is also ca. 0.25 nm. The vertical growth of 5 nm size Ag dots continues for more than 10 layers. This result suggests that a kinetically controlled layer-by-layer growth takes place for the nano-size Ag dots over the (7 × 7)-Si(111)–C_2H_5OH surface. As a result, the nucleation and subsequent growth of Ag particles lead to the growth of rather

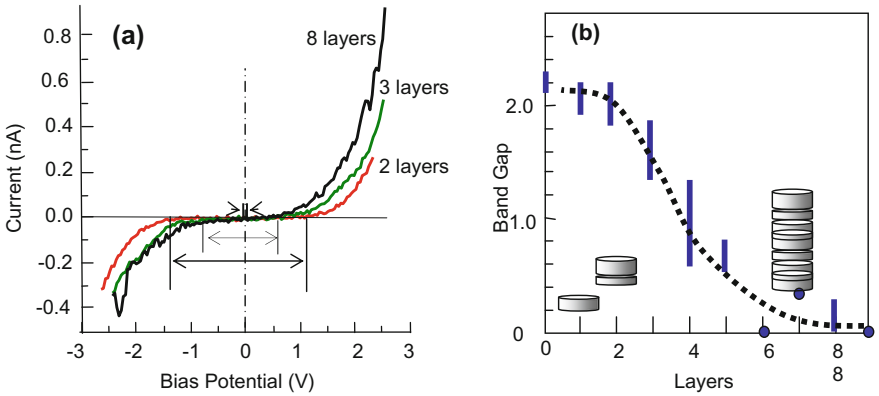

Fig. 5.11 I–V profiles of Ag dots on a (7 × 7)-Si(111)–C_2H_5OH surface. **a** The I–V profile dependence on the number of layers. **b** Conversion of Ag dots from a semiconducting to metallic state, based on the number of layers [36]

uniform size (ca. 5 nm) Ag dots in a hexagonal mesh (5.4 nm) made of six half unit cells surrounding a hole.

The growth of Zn particles on the (7 × 7)-Si(111)–C_2H_5OH surface shown in Fig. 5.10a is entirely different from the Zn_3 clusters formed on a clean (7 × 7)-Si (111) surface as shown in Fig. 5.9b. The growth of Zn clusters (particles) is regulated on the (7 × 7)-Si(111)–C_2H_5OH surface by the "**mold effect**" of C_2H_5O-Si groups [33, 35]. The growth of Ga and Ag particles is also regulated by the mold effect of C_2H_5O-Si groups on the (7 × 7)-Si(111)–C_2H_5OH surface [23, 35].

It is known that clean (7 × 7)-Si(111) surface is known to be metallic [25], but nano-size Co, In, Ag, and Sn particles formed on a clean (7 × 7)-Si(111) surface are nonmetallic [30, 32–34, 36], that is, formation of a band structure depends on the number of stacked layers as shown in Fig. 5.11. The (7 × 7)-Si(111)–C_2H_5OH surface has a band gap of 2.2 V [32], while Ag particles of ca. 5 nm size with 1–2 layers on the (7 × 7)-Si(111)–C_2H_5OH surface have a clear band gap of ca. 2.0 V. However, this band gap becomes narrower as layers increase from 3 to 5, and Ag particles with more than 5 layers are metallic, as shown in Fig. 5.11b [23]. The chemical properties of Ag particles depending on the size are an interesting subject.

References

1. Y. Matsumoto and K-I. Tanaka, Surf. Sci., 350 **(1996)** L 227.
2. Y. Matsumoto, Y. Okawa, and K-I. Tanaka, Surf. Sic. 325 **(1995)** L435.
3. Y. Matsumoto, Y. Okawa, and K-I. Tanaka, Surf. Sic. 336 **(1995)** L762.
4. Y. Matsumoto, K. Sakamoto, Y. Okawa, S. Suto,and K-I. Tanaka, J. Chem. Phys., 107 **(1997)**1.
5. Y. Okawa and K-I. Tanaka, Surf. Sci., 344 **(1995)** 1207.
6. Y. Okawa and K-I. Tanaka, Appl. Phys. Lett., 70 **(1997)** 3371.

7. P.T. Sprunger, Y. Okawa, F. Besenbacher, I. Stensgaard, and K-I. Tanaka, Surf. Sci. 344 **(1995)** 98.
8. J.F. Skelly, T. Bertrams, A.W. Munz, M.J. Murphy, and A. Hodgson, Surf. Sci.,415 **(1998)** 48.
9. K-I. Tanaka and Z-X. Xie, J. Chem. Phys., 122 **(2005)** 054706.
10. N. Takehiro, F. Besenbacher, F. Laegsgaard, K-I. Tanaka, and I Stensgaard, Surf. Sci. 397 **(1998)** 145.
11. F.M. Leibsle, R. Davis, and A.W. Robinson, Phys. Rev., B 49 **(1994)** 8290.
12. F.M. Leibsle, C.F.J. Flipse, and A.W. Robinson, Phys. Rev. B, *47* (**1993**) 15865.
13. K-I. Tanaka, Materials, 3 **(2010)** 4518.
14. S.K. Mukai, Y. Matsumoto, K-I. Tanaka, and F. Komori, Surf. Sci., 450 **(2000)** 44.
15. S. Moré, W. Berndt, S. Stampfl, A.M. Bradshaw, Surf. Sci., 381 **(1997)** L589.
16. H.C. Zeng, R.N.S. Sodhi, and K.A.R. Mitchell, Surf. Sci.,188 **(1987)** 599.
17. F.M. Leibsle, C.F.J. Flips, and A.W. Robinson, Phys. Rev. B (47 **(1993)**15865.
18. S. Ohno, K. Yagyuu, K. Nakatsuji, and F. Komori, Surf. Sci. 547 **(2003)** L 871.
19. F. Komori, S. Ohno, K. Nakatsuji, J. Appl. Phys., J. Phys. Cond. Matter, 14 **(2002)** 8177.
20. Y. Matsumoto and K-I. Tanaka, Jpn. J. Appl. Phys., 37 **(1998)** L 154.
21. Shen and J. Kirschner, Phys. Rev. B.52 (1995) 8454.
22. M.A. Abu-Joudeh, B.M. Davies, and P.A. Montano, Surf. Sci.,171 **(1986)** 331.
23. J.W. Evance and M.C.Bartelt, Langmuir, 12 **(1996)** 217.
24. F.J. Himpsel, Surf. Sci. Report, 12 **(1990)** 1.
25. R.J. Hamers, R.M. Tromp, and J.E. Demuth, Phys. Rev. Lett., 56 **(1986)** 1972.
26. T.M. Parker, L.K. Wilson, N.G. Condon, F.M. Liebsle, Phys. Rev. B, 56 **(1997)** 6458.
27. Ph. Avouris and R. Wolkow, Phys. Rev. B 39 **(1989)** 5091.
28. Z-X. Xie, Y. Uematsu, X. Lu, and K-I. Tanaka, Phys. Rev., B 66 **(2002)** 125306.
29. K-I. Tanaka, Y. Nomoto, and Z-X. Xie, J. Chem. Phys., 120 **(2004)** 4486.
30. M. Yoon, X.F. Lin, I. Chizhov, H. Mai, and R.F. Willis, Phys. Rev. B 64 **(2001)** 085321.
31. Z-X. Xie and K-I. Tanaka, Surf. Sci. 479 **(2001)** 26.
32. Z-X. Xie, K. Iwase, T. Egawa, K-I. Tanaka, Phys. Rev. B 66 **(2002)** 121304.
33. X. Jiang, Z-X. Xie, M. Shimojo, and K-I. Tanaka, J. Chem. Phys. 127 **(2007)** 144705.
34. H-J. Liu, Z-X. Xie, H. Watanabe, J. Qu, and K-I. Tanaka, Phys. Rev. B 73 **(2006)** 165421.
35. K-I. Tanaka, X. Jiang, and M. Shimojo, Surf. Sci. 601 **(2007)** 5093.
36. X. Jiang, Z-X. Xie, M. Shimojo, and K-I. Tanaka, Appl. Phys. A, 97 **(2009)** 567.
37. M.S. Ho, C.C. Su and T.T. Tsong, J. Appl. Phys., 45 **(2006)** 2382.
38. Z-X. Xie and K-I. Tanaka, Surf. Sci. 479 (2001) 26.
39. K-I. Tanaka, Z-X. Xie, T. Egawa, and M. Aramata, J. Mol. Catal. A: Chemicals 199 (20039 19.

Chapter 6
Formation of Labile Surface Compounds and Catalysis

Abstract As mentioned in Chap. 5, various unusual compounds are formed by the reaction of adsorbed atoms and molecules with metal atoms, but these compounds are not necessarily active as catalyst. In the methanation of CO with H_2, $CO + 3H_2 \rightarrow CH_4 + H_2O$, on the Ni catalyst, a steady amount of active Ni_4C and Ni–CH_2 are detectable on the Ni catalyst during steady reaction. The surface of Fe catalyst in ammonia synthesis reaction is similar. The dissociation of N_2 is the rate-determining step in the ammonia synthesis reaction. That is, the reaction rate is controlled by dissociation rate of N_2, but the activity depends on a steady amount of labile Fe_xN on the Fe catalysts. Therefore, the role of promoting materials is to increase the density of labile Fe_xN on the surface. A steady amount of Fe_xN, NH, and NH_2 observed in the ammonia decomposition reaction and in ammonia synthesis reaction suggests a significant potential barrier between NH(a) and NH_2(a) on Fe catalyst and also on other metals.

Keywords Methanation reaction · Ammonia synthesis reaction · Intermediates · Catalytic activity and the rate-determining step · Decomposition of NI_4C intermediate · Catalytic activity of Fe(111), Fe(110), and Fe(100) surfaces on ammonia synthesis reaction · The role of Al_2O_3 · Hydrogen isotope effect in ammonia synthesis · Kinetics of NH_3 decomposition reaction on various metals

Catalysis is so often caused by the active key compounds formed on the surface during reaction. A prominent example is the methanation reaction of CO with H_2, $CO + 3H_2 \rightarrow CH_4 + H_2O$, on Ni catalysts. The activity for the formation of CH_4 exhibits an almost equal turnover frequency (molecule/Ni·site sec) on various forms of Ni catalysts, that is, the activity takes no influence of the particle size, support materials, and crystal planes as shown in Fig. 6.1a [1]. It was also shown that a steady amount of carbon atoms on the Ni (measured by Auger spectroscopy) is maintained by a dynamic balance between the deposition of carbon atoms on Ni from CO and its hydrogenation to CH_4 by H_2 as shown in Fig. 6.1b. As it is mentioned below, the reactive intermediate is not C atom but Ni_4C formed on the surface as described by Eq. (6.1).

K. Tanaka, *Dynamic Chemical Processes on Solid Surfaces*,
DOI 10.1007/978-981-10-2839-7_6

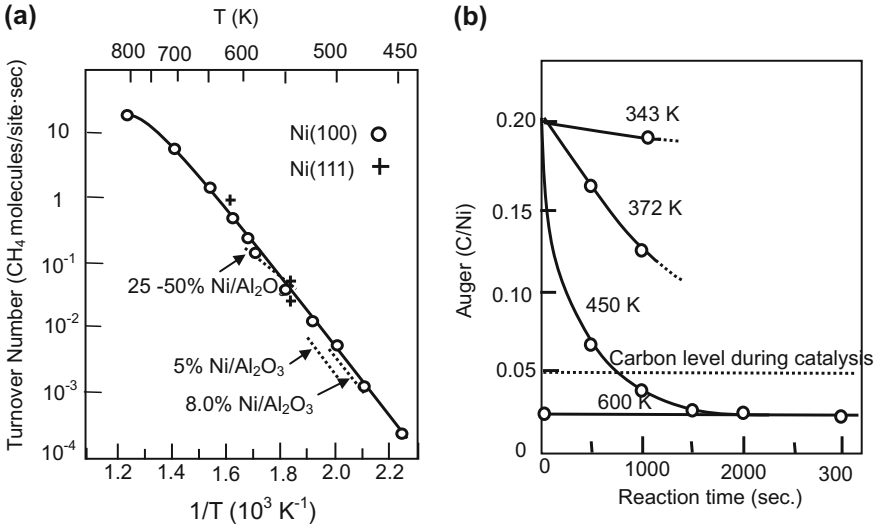

Fig. 6.1 **a** Surface structure-independent turnover number of methanation reaction, 3 H_2 + CO → CH_4 + H_2O, on Ni catalysts. **b** Decrease in C atoms on Ni with reaction time by hydrogenation at various temperatures. The *broken line* shows a steady carbon-level observed in a steady methanation reaction [1]

$$\mathrm{CO} \rightarrow \left\{ \mathbf{Ni_4C} \rightleftharpoons \mathrm{Ni_xCH} \rightleftharpoons \mathbf{Ni_x}\mathrm{CH_2} \rightarrow \mathbf{Ni}\text{-}\mathrm{CH_3} \right\} \rightarrow \mathrm{CH_4} + \mathrm{Ni} \qquad \textbf{Eq. (6.1)}$$

It is evident that the methanation reaction is not the hydrogenation of adsorbed CO on Ni, but the hydrogenation of nickel carbide formed on Ni surface [2]. Model reaction proving this mechanism was carried out on single-crystal Ni surfaces.

If a single crystal of Ni was heated in vacuum, impurity carbon was segregated at 550–600 K, and the characteristic LEED patterns p4 g(2 × 2)Ni(100)–C, p(4 × 5) Ni(110)–C, and (39 × 39)Ni(111)–C as shown in Fig. 6.2a were attained. The LEED pattern indicates the different array of Ni_4C on the different crystal planes, but the three different p4 g(2 × 2)Ni(100)–C, p(4 × 5)Ni(110)–C, and (39 × 39)Ni(111)–C surfaces change to the (1 × 1) clean surfaces by raising temperature at ca. 680–690 K in vacuum as shown in Fig. 6.2b. The same decomposition temperature suggests the existence of the same compound on the three crystal surface, and the C atoms formed by the decomposition are dissolved into Ni crystals instead of desorption. The LEED pattern (iii) in Fig. 6.2a is composed of the three patterns for the three domains of the (39 × 39)Ni(111)–C surface. The LEED pattern (ii) was attained at a single domain part on the (39 × 39)Ni(111)–C surface. It should be mentioned that no CH_4 formation takes place by the hydrogenation of these surfaces, because these Ni surfaces are inactive for the dissociation of H_2. However, the coverage of C (actually Ni_4C) becomes low, the surface becomes active for the dissociation of H_2, and the hydrogenation of Ni_4C proceeds via CH_2

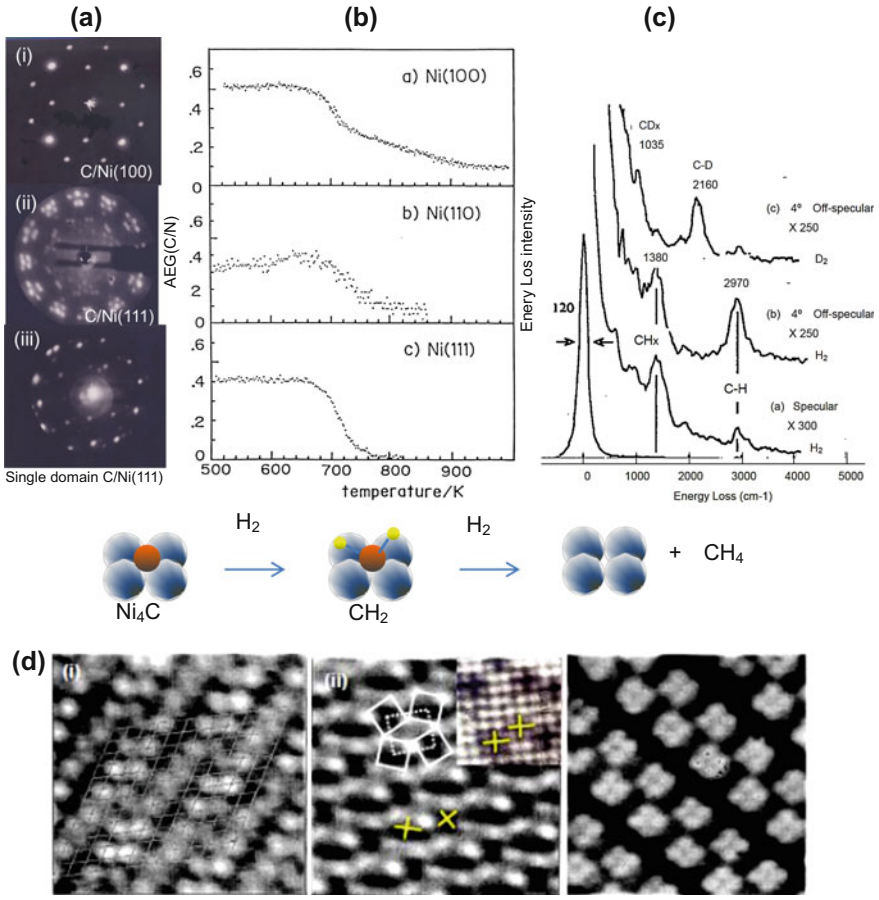

Fig. 6.2 **a** LEED patterns (i) Ni(100)–C, (ii) Ni(111)–C full domain, (iii) Ni(111)–C Single domain, which is similar to (i). **b** Decrease in C atom AES peaks due to the decomposition of Ni_4C at 680–690 K [2]. **c** High-resolution electron energy loss spectrum (HREELS) showing the formation of CH_2 on the Ni carbide/Ni(100) surface by on exposure to H_2 (1×10^{-7} Torr) [5, 6]. **d** The STM images of Ni_4C formed by annealing at 550 K on Ni(111), Ni(100), and Ni(110) surfaces. (i) ($\sqrt{3}$9x $\sqrt{3}$9) Ni(111)–C, (ii) (2 × 2)p4 gNi(100)–C, and (iii) c(4 × 5) Ni(110)–C. Inset image in (ii) shows random segregation of Ni_4C in an initial atage. [3, 4]

intermediates as descried schematically in Fig. 6.2. That is, methanation reaction of CO, $CO + 3\ H_2 \rightarrow CH_4 + H_2O$, is attained as observed in Fig. 6.1b. This is the mechanism of structure-independent methanation reaction of CO on Ni catalyst. The array of Ni_4C on single-crystal Ni surfaces was precisely studied by Besenbacher

and his coworkers [3, 4]. As shown in Fig. 6.2d-ii, dark crosses are randomly appeared on the Ni(100) surface by heating in vacuum. Local lattice distortion induced by forming Ni_4C on the surface makes disperse the dark crosses in random on the Ni(100) surface. Therefore, the Ni(100) surface with Ni_4C lower than 0.2 monolayers gives a (1 × 1) LEED pattern.

However, when the coverage exceeds 0.2 MLs, the cross-shaped Ni_4C molecules undergo rotation alternately on the surface to reduce local lattice strain as indicated with the red crosses, and finally, a p4 g(2 × 2) Ni(100)–C structure shown in Fig. 6.2d-i is established. Similarly, the Ni(110) and Ni(111) surface fully covered with the Ni_4C species give the characteristic LEED patterns as shown in Fig. 6.2d-ii, iii, and the STM images of these surfaces are shown in Fig. 6.2d.

If single-crystal Ni surface covered with Ni_4C is heated in vacuum, clean Ni surface is recovered at ca. 680–690 K on the three crystal surfaces as shown in Fig. 6.2b [2]. This fact indicates the formation of same compound on the three different Ni crystal surfaces. This is the essential reason why any crystal planes and any supported Ni catalyst give equal catalytic activity for the methanation reaction of CO. As mentioned below, the rate-determining slow step of $CH_2(a) + H(a) \rightarrow CH_3(a)$ is responsible for the equal turnover frequency per Ni atom on any Ni planes.

It should be reminded that the dissociation of H_2 is a necessary process for the hydrogenation of Ni_4C with H_2. Therefore, the Ni surface should keep a moderately covered with Ni_4C during catalysis; that is, some bare Ni surface area is required for the dissociation of H_2. When a p4 g(2 × 2)Ni(100)–C surface was exposed to 1×10^{-7} Torr of H_2 (D_2) at room temperature, the rapid formation of CH_2 (or CD_2) species was detected by the growth of the stretching vibration peaks of C–H at 2970 cm^{-1} and C–D at 2160 cm^{-1} and from the scissors mode peaks of CH_2 at 1380 cm^{-1} and CD_2 at 1035 cm^{-1} in EELS spectra, as shown in Fig. 6.2c. However, the formation rate of CH_4 was very slow at 313 K. Notably, the peaks at 2970 and 1380 cm^{-1} of the CH_2 species rapidly disappear with evacuation of H_2. If D_2 is replaced with H_2, the C–D peak at 2160 cm^{-1} diminishes with the growth of the C–H peak at 2970 cm^{-1}. The results indicate that rapid reversible hydrogen exchange reaction, $Ni_4C + 2\,H(a) \rightleftharpoons Ni_xCH_2$, takes place on the Ni surface at 313 K, but the subsequent hydrogenation of $CH_2(a)$ to CH_4 via $CH_3(a)$ is rather slow on the p4 g (2 × 2) Ni(100)–C surface at 313 K [5, 6]. When a p4 g(2 × 2)Ni(100)–C is exposed to 10 Torr H_2 at 450 K, the surface changes to (2 × 2)Ni(100)–C and subsequently to (1 × 1)Ni(100)–C at a coverage of $\theta \approx 0.2$, which is almost equivalent to a steady coverage of C (actually Ni_4C) on Ni catalysts in the catalytic reaction CO + H_2 (10 Torr) [1]. Taking these results into account, we can conclude that the hydrogenation reaction of $CH_2(a) + H(a) \rightarrow CH_3(a)$ is the rate-determining slow step in the methanation reaction of CO with H_2 on the Ni catalyst ($\theta_c \approx 0.2$), as described by Eq. (6.1).

It may be appropriate to consider the ammonia synthesis reaction related to the methanation reaction, because the mechanism of catalysis is very similar to the hydrogenation of Ni_4C with H_2 on Ni. The hydrogenation of N_2 is one of the most important discoveries in catalysis, and this historic reaction is now receiving renewed interest as a reaction for hydrogen storage in the emerging hydrogen energy society. It is substantiated that this reaction is favorable at lower temperatures by the thermodynamics, so that the development of a low-temperature active catalyst is expected. Based on a huge number of experiments, it has been accepted that the dissociation of the N_2 molecule is the rate-determining slow step for the catalytic synthesis of NH_3. As we have no fundamental idea to improve this step, improvement of catalysts has been done by empirical manner. However, it should be reminded that activity of the surface working as catalyst depends on the density of active materials or active sites on the surface.

As has been discussed in Chap. 5, the formation of specific compounds on metal surfaces is evidently different from the adsorption of atoms or molecules on metals. However, if the dissociation of N_2 is the rate-determining slow step of ammonia synthesis reaction, it is still unsettled whether adsorbed N(a) atoms are hydrogenated to NH on metals or the formation of labile metal nitrides is responsible for the ammonia synthesis reaction. As discussed below, I could say that the formation of labile metal nitrides is essential of the catalytic activity of metals for ammonia synthesis reaction, that is, to increase the active materials. It is known that Fe is a moderate metal for the ammonia synthesis reaction. As discussed below, the formation of active Fe_xN by the reaction of adsorbed N(a) with surface Fe atoms may be responsible for the catalytic activity of Fe surface, which is similar to the formation of Ni_4C during the methanation reaction of CO on Ni catalysts. Formation of Fe_xN during catalytic decomposition of NH_3 on a Fe surface is known; the Fe_xN undergoes decomposition on the Fe surface by heating; and N_2 is formed. If the ammonia synthesis reaction and ammonia decomposition reaction is a reversible reaction on the Fe catalyst, it is described by Eq. (6.2).

$$N_2 \rightleftharpoons N + Fe \rightleftharpoons \mathbf{Fe_xN} \rightleftharpoons FeNH \rightleftharpoons FeNH_2 \rightleftharpoons NH_3 + Fe \tag{6.2}$$

If we consider Ni surface, N_2 molecules cannot dissociate on a clean Ni surface, so that Ni is inactive for the ammonia synthesis reaction. However, the decomposition of NH_3 takes place on the Ni surface. Roman and Riwan [7] achieved the formation of a p(2 × 3)Ni(110)–N surface by bombarding a Ni(110) surface with the N^+ and/or N_2^+ ion, and the N atom coverage was estimated at about a half monolayer. Kuwahara et al. [8] surmised the adsorption of N atoms on long bridge sites based on HREELS measurements. As it is mentioned below, p(2 × 3)Ni(110)–N surface is not the Ni(110) surface with absorbed N atoms, but with nickel nitride such as Ni_3N formed by the reaction of N atoms with Ni atoms on Ni(110) surface. It should be pointed out that the p(2 × 3)Ni(110)–N surface is inactive toward the reaction with H_2, which is similar to the Cu_3N on Cu(110) being inactive toward the

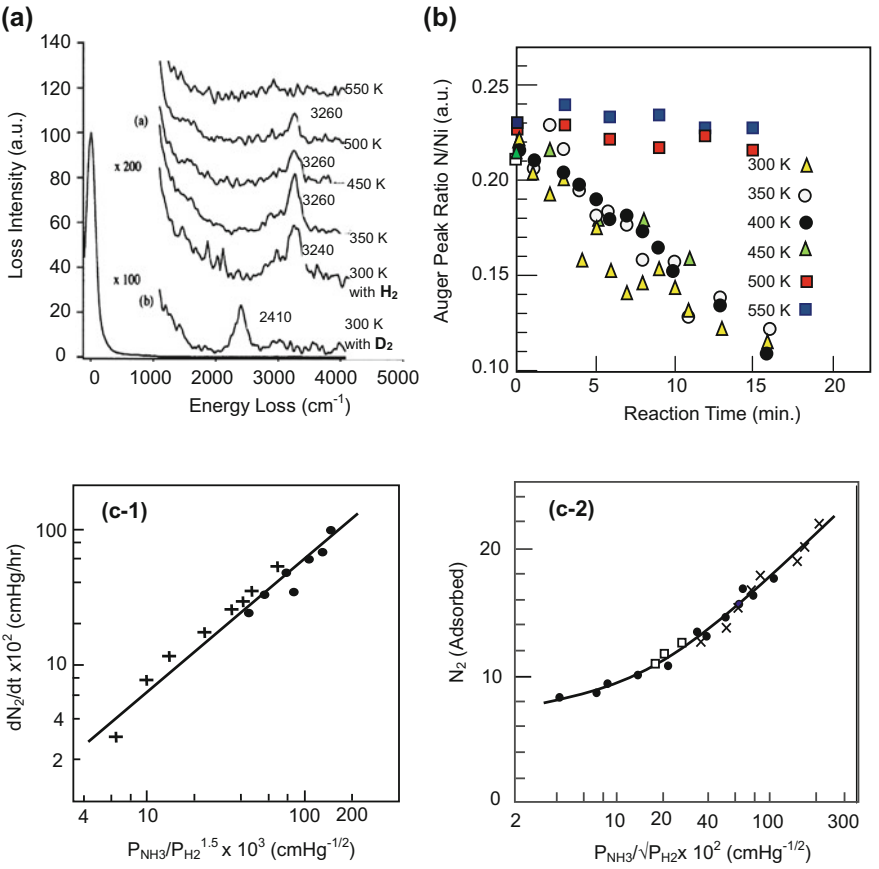

Fig. 6.3 **a** HREEL spectra showing formation of NH(a) on a p(2 × 3)Ni(110)–N surface by exposing to H atoms below 550 K. **b** Temperature-independent decrease in N atoms on the p(2 × 3)Ni(110)–N surface by reaction with H atoms in H_2 (2.0×10^{-6} Torr) at the temperature below 450 K, but no decrease in N atoms occurs at temperatures above 500 K [10]. **c-1** Decomposition rate of ammonia depends on $P_{NH3}/\sqrt{P}_{H2}{}^{1.5}$ on Ni powder catalyst at 573 K. **c-2** Total amount of N (N and NH_x) on the Ni powder catalyst during the decomposition of NH_3 at 573 K correlates with $P_{NH3}/\sqrt{P}_{H2}$, which suggests that most of the adsorption during the decomposition of ammonia would be due to NH_2 [11]

reaction with H_2 as shown in Fig. 5.3. Takehiro et al. [9, 10] found quite important phenomenon on a p(2 × 3)Ni(110)–N surface (Auger ratio of N/Ni = 0.25). They performed the chemical reaction NO + H_2 → N(a) + H_2O at 650 K in a highly H_2-rich environment (NO/H_2 = 1/150). If the p(2 × 3)Ni(110)–N surface was exposed to H atoms made by thermal dissociation of H_2 (2.0×10^{-6} Torr) on a hot W filament, formation of N–H was observed on the p(2 × 3)Ni(110)–N surface at 300 K by a HREELS (high-resolution electron energy loss spectroscopy) at about 3240 and 3260 cm^{-1} in the temperature range of 300–500 K as shown in Fig. 6.3a,

and the amount of N on the p(2 × 3)Ni(110)–N was decreased by exposing to H atoms with the formation of NH_3 [10]. However, the decreasing rate of N atoms from the p(2 × 3)Ni(110)–N surface by reacting with H atoms was temperature independent in a range of 300–450 K as shown in Fig. 6.3b. If the temperature was raised above ca. 500 K, neither the loss of N atoms nor the formation of NH(a) was observed, as shown in Fig. 6.3a, b, and temperature-programmed desorption of a p(2 × 3)Ni(110)–N surface gave a N_2 peak of the desorption at 830 K [10].

As mentioned above, Ni(110) surface is inactive for the dissociation of N_2, but the formation of NH_2(a) was reported on the Ni(110) surface by the decomposition of NH_3 and the two energy loss peaks assignable to NH_2(a) appeared at 1520 and 3240 cm^{-1} with an intensity ratio of about 3 : 1 [23–25]. However, no scissors' peak showing the formation of NH_2 at 1520 cm^{-1} was observed on a p(2 × 3) Ni(110)–N surface by exposing to H atoms as shown in Fig. 6.3a [10]. How can we rationalize these two phenomena observed on the Ni(110) and p(2 × 3)Ni(110)–N surface?

When a p(2 × 3)Ni(110)–N was exposed to a constant flux of H atoms, the amount of N atoms (Auger intensity) is decreased with a constant rate by forming NH_3 as shown in Fig. 6.3b; that is, the temperature-independent zero-order decrease in N atom took place in the range of 300–500 K. It is noteworthy that no NH_2 peaks were observed during hydrogenation of the p(2 × 3)Ni(110)–N surface with H atoms, even though the concentration of N atoms on the surface was decreased by forming NH_3. This result clearly indicates that the hydrogenation rate of NH_2(a) to NH_3 is faster than hydrogenation of N(a) to NH(a), so that a steady concentration of NH_2(a) becomes very low during hydrogenation. If the dissociation of N_2 on a metal is slow process with very high potential barrier (actually no dissociation of N_2 occurs in this experiment), the surface is inactive for the ammonia synthesis reaction although the decomposition of NH_3 takes place. Detectable amount of NH_2(a) on Ni(110) surface is observed by the decomposition of NH_3, but no detectable amount of NH_2(a) is observed by hydrogenation of p(2 × 3)Ni(110)–N surface with H atoms. The two phenomena suggest the existence of rather high potential barrier between the NH(a) and the NH_2(a), NH(a) + H(a) $\rightleftharpoons$ NH_2(a), on Ni(110) surface. A more unexpected phenomenon is the reaction of N atoms with H-atoms at temperatures above ~500 K, that is, the reaction of N atoms with H-atoms on a p(2 × 3) Ni(110)–N surface discontinously stops. This is an interesting example establishing high-temperature stability of the surface not by forming a passive p(2 × 3)Ni(110)–N surface at ~500 K, but the p(2 × 3)Ni(110)–N surface is held by rapid dynamic process of the decomposition of NH(a) to N(a) which exceeds the hydrogenation of NH(a) to NH_2(a) and NH_3 on the surface. That is, the NH(a) on the p(2 × 3)Ni(110)–N surface becomes unstable at temperatures higher than ca. 500 K, and the rate of decomposition of NH(a) to N(a) becomes more rapid than its hydrogenation to NH_2 at ~500 K. As a result, the p(2 × 3)Ni(110)–N surface becomes apparently passive for the reaction with H atoms, and p(2 × 3)Ni(110)–N is stable up to ~830 K. These dynamic phenomena are described by the following equations.

(i) p(2x3) Ni(110)-N + H_2 ⟶ NH(a)/Ni (No hydrogenation with H_2).

(ii) p(2x3) Ni(110)-N + H-atom ⟶ NH/Ni (Slow) ⟶ NH_2/Ni (300~500 K).

Very rapid

NH_2/Ni + H(a) ⟶ NH_3 (300~450 K); probably reaction with adsorbed H(a).

(iii) $NH(a)/Ni \rightarrow p(2 \times 3)Ni(110) - N + 1/2H_2$; Rapid decomposition of NH > 500 K

$p\,(2 \times 3)\ Ni\,(110) - N \rightarrow N_2 + Ni\,(110)$; decomposition of Ni_3N at 830 K.

In early experiments by Tamaru et al. [11], the amounts of adsorbed N(a) and H(a) atoms were measured on the Ni powder catalyst by volumetric material balance of the reactant gases during the decomposition of NH_3 at 573 K (a little higher than critical temperature of 500 K) and found that the amount of N (N and NH_x) on the Ni powder changed according to $P_{NH3}/P_H^{1/2}$ as shown in Fig. 6.3c-2, which suggested predominant adsorption of NH_2(a) on the Ni catalyst by the decomposition of NH_3. This result is in reasonable agreement with the formation of NH_2(a) by the adsorption of NH_3 on the Ni(110) surface, but it is in marked contrast to the main species of NH(a) in the hydrogenation of N(a) with H atoms. Conversely, the decomposition rate of NH_3 (dP_{N2}/dt) on the Ni powder catalyst depends on $kP_{NH3}/P_H^{1.5}$ as shown in Fig. 6.3c-1, which suggests the rate-determining slow desorption of N_2 by N(a) ⟶ 1/2 N_2 [11]. As mentioned previously, the p(2 × 3)Ni(110)–N surface is inactive toward hydrogenation of N(a) with H_2, because the surface has no ability to dissociate H_2 molecules. It is similar to the (39 × 39)Ni(111)–C surface being inactive for the hydrogenation because of no ability for the dissociation of H_2. However, NH(a) is formed on the p(2 × 3)Ni(110)–N surface on exposure to H atoms in the temperature range of 300–500 K as shown in Fig. 6.3a. It should be pointed out that energy loss peaks suggesting NH_2(a) were not observed, although the amount of N atoms on the p(2 × 3)Ni(110)–N surface was decreased by forming NH_3. The results suggest the existence of a potential barrier between NH(a) and NH_2(a), but the barrier from NH_2(a) to NH_3 is low, so that NH_2(a) becomes the predominant species formed in the decomposition of NH_3, whereas NH(a) is the predominant species in the hydrogenation reaction of N(a) with H(a). It should be noted that the decomposition rate of NH(a) to N(a) on the Ni(110) surface becomes faster than the hydrogenation of NH(a) to NH_2(a) on the p(2 × 3)Ni(110)–N surface when the temperature exceeds ca. 500 K, so that the p(2 × 3)Ni(110)–N surface becomes in passive to H atoms in the temperature range of ca. 500–830 K as shown in Fig. 6.3b. This intriguing dynamic stabilization of the p(2 × 3)Ni(110)–N surface in the presence of H atoms up to ca. 830 K may provide a novel concept to protect a wall from the attack of high-temperature gas; that is, the wall is protected by a dynamic process of more rapid decomposition than the subsequent reaction of specific surface compounds. This might be interesting when we design such a wall for a nuclear-fusion reactor to protect them from high-temperature H, D, and T atoms.

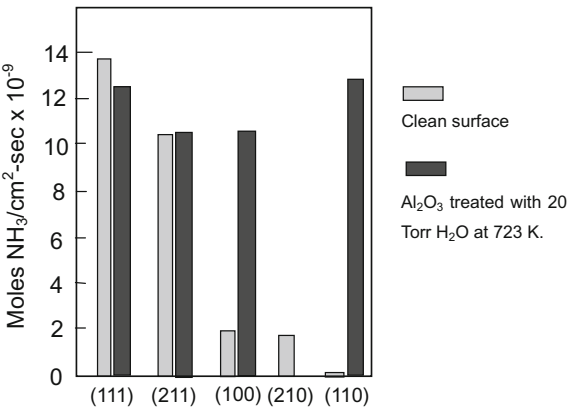

Fig. 6.4 Catalytic activity of Fe surface for ammonia synthesis reaction depends markedly on the crystal plane. All crystal planes take as active as that of the Fe(111) plane after depositing 2 ML of Al_2O_3 followed treating in H_2O vapor at 728 K [12, 13]

Based on the results on Ni catalysts, we consider again the practical ammonia synthesis reaction on the Fe catalyst. In 1980, Somorjai and his coworkers [12–16] carried out a series of pioneering high-pressure experiments on single-crystal Fe surfaces. They observed highly structure-dependent catalytic activity of the single-crystal Fe surfaces in the ammonia synthesis reaction, and the relative activity was given by the ratio of Fe(111): Fe(100): Fe(110) = 415: 25: 1. The Fe(111) plane was the most active for the ammonia synthesis reaction and the Fe (211) plane was also active, but the Fe(110) plane was almost inactive for the same ammonia synthesis reaction, and the Fe(210) and Fe(100) look to indicate planes were several ten of times more active than the inactive Fe(110) plane. These results look to indicate that ammonia synthesis on the Fe catalyst is extremely sensitive to the surface structure. An even more noteworthy result was the promoting effect of Al_2O_3 on the Fe crystals. That is, highly structure-dependent catalytic activity of the Fe crystal planes changed to structure-independent active surface on deposition of 2 ML Al_2O_3 on the Fe crystal planes followed by the treatment with H_2O vapor at 723 K. That is, all crystal planes of Fe take on almost equal catalytic activity, which is almost equal to the most active Fe(111) plane as shown in Fig. 6.4. From these results, Somorjai considered that the formation of a specific conformation of the Fe atoms is responsible for the catalytic activity. Based on this idea, the role of Al_2O_3 might be to provide such Fe atoms with a specific conformation, and presumed a peculiar site named as the C_7 site involving seven Fe atoms in the topmost 3 layers. This curious paradox that the structure-independent activity observed on the Fe crystal surfaces covered with Al_2O_3 was explained by the Fe sites with a specific structure, such as named the C_7 site.

We should remember that the reaction rate and kinetics are controlled by the rate-determining slow step in a series of connected chemical reactions, but the activity depends on the number of active materials contributed to the catalysis. Based on this fundamental idea of catalysis, a more likely mechanism is the formation of labile Fe_xN by the reaction of adsorbed N(a) with surface Fe atoms. If this is the case, steady activity depends on a steady amount of Fe_xN on the surface.

Accordingly, an optimized density of the reactive Fe_xN is responsible for the structure-independent catalytic activity of the Al_2O_3/Fe crystal surfaces.

When we remember the adsorption of O_2 on Cu(100) and Cu(110) surfaces, adsorbed O(a) atoms form small-sized c(2 × 2) domains on the Cu(100) surface, whereas O(a) atoms adsorbed on Cu(110) undergo reaction with surface Cu atoms to form (–CuO–) strings. Catalytic reaction proceed by either O(a) or (–Cu–O–), the role of surface in catalysis should be quite different. If the reaction of adsorbed N(a) with surface Fe atoms forming active Fe–nitride (Fe_xN) depends on the crystal plane, catalytic activity depends on the crystal planes, but the promoting materials (Al_2O_3) may maximize the density of reactive Fe_xN on the surface. The structure-dependent activity of the Fe single crystals and the structure-independent activity of the Fe single crystals covered with Al_2O_3 are well rationalized by the population of reactive Fe_xN on the surface, just like the structure-insensitive activity of Ni catalysts for the methanation reaction.

It should be remembered that Pt and other precious metals are active for the decomposition of NH_3, but these metals are inactive for the ammonia synthesis reaction. N(a) atoms can adsorb on these metals, but no nitrides are formed on the precious metals. If this idea is appropriate, the key process for the ammonia synthesis reaction is the formation of reactive metal nitrides by reaction with N atoms.

Catalytic ammonia synthesis is a reversible chemical reaction expressed by the equation $N_2 + 3H_2 \rightleftharpoons 2\ NH_3$. The decomposition of NH_3 is well rationalized by the rate-determining desorption of N_2 on various metals, not only on the active metals for the ammonia synthesis reaction, but also on the metals inactive for the ammonia synthesis reaction.

If the key step in the ammonia synthesis reaction is the dissociation of N_2 with subsequent formation of Fe_xN, a steady concentration of Fe_xN on the surface is given by a dynamic balance of the formation of Fe_xN and its hydrogenation to NH_3 according to the following Eq. (6.3):

$$[\mathrm{Fe}] + \mathrm{N_2} \xrightarrow{\text{(i)}} \mathbf{Fe_xN} + \mathrm{H_2} \xrightarrow{\text{(ii)}} \mathrm{NH_x} \xrightarrow{\text{(iii)}} \mathrm{NH_3} + [\mathrm{Fe}] \tag{6.3}$$

If the formation of Fe_xN, step (i), is slow, and the subsequent steps of $Fe_xN \rightarrow NH \rightarrow NH_2 \rightarrow NH_3$ in Eq. (6.3) are rather rapid, a steady concentration of Fe_xN and NH_x during catalysis depends on their relative reaction rates. If the formation of Fe_xN by the reaction of adsorbed N_2 with Fe atoms is the rate-determining slow step, the reaction rate is described by the adsorption rate of N_2 as $P_{N2}(1 - \theta_{NHx})^2$, where $(1 - \theta_{NHx})$ is the Fe surface unoccupied with NH_x (including Fe_xN). Ozaki, Taylor, and Boudart [17] studied the ammonia synthesis reaction by using H_2 and D_2, $N_2 + 3\ D_2 \rightarrow 2ND_3$ (r_D) and $N_2 + 3\ H_2 \rightarrow 2NH_3$ (r_H), on a doubly promoted K_2O/Al_2O_3/Fe catalyst at temperatures of 213–302 °C, and they observed an unusually large inverse hydrogen isotope effect of $r_D/r_H = 2–3$ (it is the over-all reaction rate instead of the rate constant explained by the zero point energy of activated complex). This large inverse isotope effect was well explained by the rate-determining dissociation (adsorption) of N_2 expressed by $P_{N2}(1 - \theta_{NHx})^2$,

where the reaction is suppressed by NH_x species adsorbed on the catalyst. The inverse isotope effect suggested that the coverage θ_{NHx} on the Fe surface is much higher for $NH_x(a)$ than $ND_x(a)$ (x = 1 or 2), $\theta_{NHx} > \theta_{NDx}$, so that the rate-determining dissociation rate of N_2 has an inverse hydrogen isotope effect ($r_D/r_H > 1$). The calculation suggested suppression of the adsorption rate of N_2 by predominant adsorption of ND(a) and NH(a); that is, $(1 - \theta_{ND})^2$ and $(1 - \theta_{ND})^2$ are responsible for the isotope effect of $r_D/r_H = 2–3$. The predominant adsorption of NH (a) on the doubly promoted K_2O/Al_2O_3/Fe catalyst is in good agreement with the spectroscopic observation of NH(a) instead of $NH_2(a)$ on various metals in the hydrogenation of N(a) on the Ni(110) surface, that is, rather high potential barrier between NH(a) + H(a) $\rightleftharpoons$ $NH_2(a)$. Taking these results into account, we can deduce significant potential barrier between NH(a) and $NH_2(a)$ on various metals, whereas the potential barrier should be low in the hydrogenation of $NH_2(a)$ to NH_3. Accordingly, $NH_2(a)$ is detectable on various metals in the decomposition of NH_3, whereas the predominant species existing on metals is NH(a) instead of $NH_2(a)$ during the ammonia synthesis reaction. This is very similar on Pd(100), Rh(100), Pt(111), and Pt–Rh(100) surfaces; the hydrogenation of N(a) on these metals produces NH(a) as shown by HREELS, but no detectable amount of $NH_2(a)$ is observed, because $NH_2(a)$ formed by the hydrogenation of NH(a) is quickly removed from the surface by forming NH_3.

As was mentioned previously, it is difficult to accumulate N atoms on the Pt surface by the chemical reaction NO + H_2 $\rightarrow$ N(a) + H_2O, but Amorelli et al. [18] did succeed in accumulating N(a) atoms on a Pt(111) surface by oxidation of NH_3 with adsorbed O(a). Mudiyanselage et al. [19, 20] carefully reacted NH_3 with O_2 on the Pt(111) surface at 85 K, and a p(2 × 2)Pt(111)–N surface was attained by annealing at 400 K. It should be noted that the N atoms adsorbed on Pt(100), Pt(111), Pt(110), Pd(100), and Rh(100) surfaces do not form metal nitrides by reacting with surface metal atoms. Therefore, the desorption of N_2 at 453 K on the Pt(111) surface is not the decomposition temperature of a surface nitride, but it may reflect the surface migration temperature of N atoms to form N_2 on the Pt(111) surface. If a p(2 × 2)Pt(111)–N surface is exposed to H_2, NH(a) is formed [19], but the reaction of adsorbed N(a) with H(a) is essentially different from the hydrogenation of metal nitrides such as Fe_xN, Cu_3N, and Ni_3N. Similarly, when the surfaces of (2 × 2)Pd(100)–N, c(2 × 2)Rh(100)–N, and c(2 × 2)Pt–Rh(100)–N are exposed to 10^{-7} Torr of a 1 : 1 mixture of H_2 + D_2, energy loss peaks assignable to N–H and N–D appear at 3240 and 2420 cm^{-1} at 400 K, lower than the migration temperature of N(a) to N_2, as shown in Fig. 6.5a [21, 22]. The intensity of the energy loss peak of N–H on Rh(100)–N varies according to $P_H^{1/2}$ of hydrogen pressure as shown in Fig. 6.5b, which indicates that the pressure-dependent surface equilibration expressed by N(a) + 1/2 H_2 $\rightleftharpoons$ NH(a) is established on the surface. This means that the subsequent hydrogenation of NH(a) to $NH_2(a)$ is not as rapid, but $NH_2(a)$ to NH_3 is quick, which is described as (i) N(a) $\rightarrow$ NH(a) $\rightleftharpoons$ $NH_2(a)$ and $NH_2(a)$ $\rightleftharpoons$ NH_3. As mentioned above, step (ii) is slow, but steps (i) and (iii) are rapid on most metals, so that the population of $NH_2(a)$ is lower than the detectable level in the hydrogenation of N(a) on most metals. That is, NH(a) is detectable, but $NH_2(a)$ is

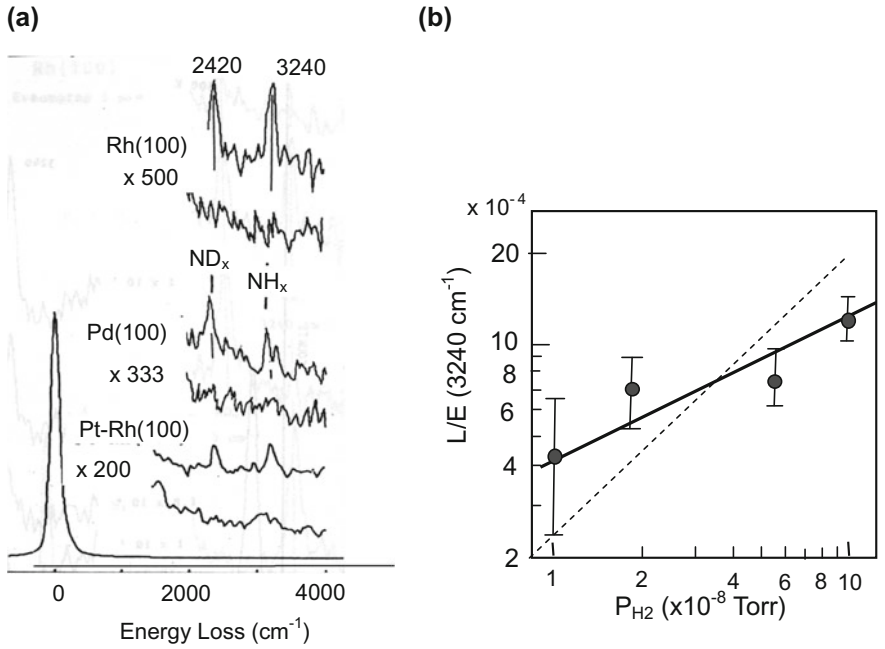

Fig. 6.5 **a** In situ HREEL spectrum showing the formation of N–H and N–D by exposing c(2 × 2)Rh(100)–N, Pd(100) and Pt–Rh(100) surfaces to a 1 : 1 mixture of (H_2 + D_2) (10^{-7} Torr) at 400 K. **b** Intensity of electron energy loss peaks as a function of H_2 pressure on Rh(100)–N surface; $P_H^{0.5}$ (*solid line*) and $P_H^{1.0}$ (*broken line*). [22, 23]

lower than the detectable level in the hydrogenation of N(a) on precious metals as shown in Fig. 6.5a.

The features of adsorbed NH_x(a) observed in the decomposition of NH_3 and in the hydrogenation of N(a) on metals are well explained by the slow step of the hydrogenation of NH(a) to NH_2(a), and vice versa for the reverse processes. Taking these results into account, the rate of ammonia decomposition and the reverse ammonia synthesis reaction is described by Eq. (6.4), where the desorption of N_2 (r) in the decomposition of NH_3 is expressed by the fugacity of adsorbed N(a) at decomposition equilibrium as described below.

Hydrogenation of NH(a) to NH_2(a) is much slower than that of NH_2(a) to NH_3 on most metals, but the dissociation of N_2 forming a labile metal nitrides strictly depends on the type of metal. The latter property, that is, the formation of a labile metal nitride, may be responsible for the activity of a catalyst for the ammonia synthesis reaction. Accordingly, one can detect adsorbed NH(a) on various metals in the hydrogenation of N atoms, but NH_2(a) is lower than the detectable level in the hydrogenation of N(a) on most metals as shown on Pd, Rh, and Pt–Rh [21, 22],

and Ni [10]. However, NH_2(a) becomes predominant in the adsorption of NH_3 on most metals [23–25], which is well explained by the kinetic barrier between NH_2(a) and NH(a) on most metals.

Taking these results into account, the ammonia synthesis reaction on metals depends on the rate-determining dissociation of N_2, $N_2 \rightarrow 2$ N(a), with subsequent formation of labile metal nitrides, N(a) + (x Fe) $\rightarrow$ Fe_xN, and the following step of the formation of NH(a) is rapid, but its hydrogenation to NH_2(a) has a certain barrier, which are described by Eq. (6.4). According to this mechanism, the rate of decomposition of NH_3 is given in any case by the desorption rate of N_2(r) as described below, where P_N* is the fugacity of adsorbed N(a) at the decomposition equilibrium [11].

$$NH_3 \rightleftharpoons \left(\mathbf{NH_2} \leftrightarrows \mathbf{NH} \rightleftharpoons \mathbf{N(a)} \right) \rightarrow N_2 + 3\,H_2 \qquad \textbf{Eq. (6.4)}$$

$$\begin{aligned} K &= P_H{}^3 P_N / P_{NH3}{}^2 \\ \alpha P_N{}^* (1-\theta_N)^2 &= \theta_N{}^2; \quad \alpha P_N{}^* = \theta_N{}^2 / (1-\theta_N)^2 \approx \theta_N{}^{2/\delta} \\ \theta_N &\approx (\alpha P_N{}^*)^{\delta/2} \\ P_N{}^* &= K P_{NH3}{}^2 / P_H{}^3 \\ r &= \kappa (\theta_N)^2 = \kappa (\alpha P_N{}^*)^{\delta} \\ &= \kappa (\alpha K P_{NH3}{}^2 / P_H{}^3)^{\delta} = k P_{NH3}{}^3 / P_H{}^y \\ 0 &\le \delta \le 1.0 \end{aligned} \qquad (6.5)$$

where P_H, P_N, and P_{NH3} are the pressure of H_2, N_2, and NH_3, and P_N* is the fugacity of N(a) at coverage θ_N. The "α" is an equilibrium constant for the dissociative adsorption of N_2 on metals, and K is the equilibrium constant of 2 $NH_3 \rightleftharpoons$ N_2 + 3 H_2. The "δ" is an approximation parameter that varies between $0 \le \delta \le 1.0$ depending on the adsorption strength of N(a) on metals (δ = 1 for weak adsorption and δ = 0 for strong adsorption). According to this equation, the desorption rate (r) of N_2 is given by Eq. (6.5) at coverage θ_N, which corresponds to the experimental equation $r = kP_{NH3}{}^x/P_H{}^y$.

In the experimental rate equation $r = kP_{NH3}{}^x/P_H{}^y$, the "x" varies over a large range of values depending on the metal, but the ratio of y/x exhibits a rather constant value slightly larger than 1.5 as shown in Fig. 6.6a [11]. The $(-\Delta H_0^\circ)$ is a parameter related to the heat of adsorption of various gases on metals shown in Fig. 4.1. If this general rule established on metals is applicable to the adsorption of N(a) provided on metals by the decomposition of NH_3, log α (α: equilibrium constant of the adsorption of N(a)) is related to the parameter $(-\Delta H_0^\circ)$. In fact, the parameter "δ" obtained from the experiments varies from ca. 1 to 0 according to the parameter $(-\Delta H_0^\circ)$ of metals, as shown in Fig. 6.6b.

Adsorption of heteroatom molecules such as NO and CO and their reaction with surface metal atoms is more complex than the adsorption and reaction of homo-atomic molecules. For example, the adsorption of NO on Cu(110) surface

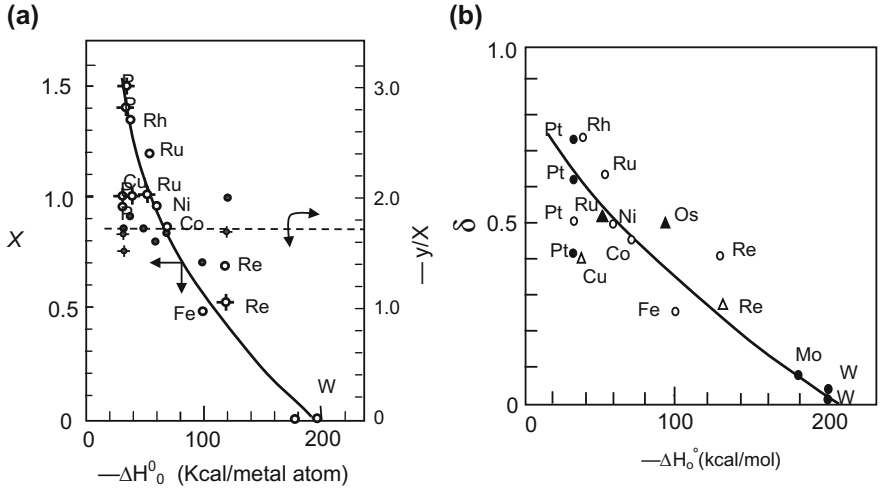

Fig. 6.6 **a** (x) and (−x/y) values of the rate equation of $r = kP_{NH3}{}^{x}P_{H}{}^{y}$ in the decomposition of NH_3 on various metals, which varies in relation to an empirical parameter for the adsorption strength ($-\Delta H_0^o$) shown in Fig. 4.1 [11]. **b** **δ** value in Eq. (6.5) varies from 1 to 0 depending on a parameter ($-\Delta H_0^o$) related to the adsorption strength

provides two different quasi-compounds: One is one-dimensional (–Cu–O–) strings and the other is Cu_3N, as shown in Fig. 5.3. They make different domains over the surface, and their chemical properties are quite different as mentioned in Chap. 4. The most important function of the surface in catalysis is to recycle a series connected reactions including the formation of active sites or active compounds. I could say this is the origin of the complexity of catalysis as discussed in **Part II**. The dissociation of heteroatom molecules on alloy and bimetal surfaces is more complex. A typical example is the adsorption of NO and catalytic reduction of NO with H_2 on Pd(100), Rh(100), Pt/Rh(100), Rh/Pt(100), and Pt–Rh(100) alloy surfaces, which are quite interesting as will be discussed in Chap. 9 in **Part II**.

References

1. D.W. Goodman, R.D. Kelley, T.E. Madey, and J.T. Yates, Jr. J. Catal., *63* (**1980**) 226.
2. H. Hirano and K-I. Tanaka, J. Catal.,*133 (***1992**) 461.
3. C. Klink, L. Olesen, F. Besenbacher, I. Stensgaard, E. Laegsgaard, and N.D. Lang Phys. Rev. Lett., 71 (**1993**) 4350.
4. C. Klink, I. Stensgaard, F. Besenbacher, and E. Laegsgaard, Surf. Sci. 342 (**1995**) 250.
5. Hong He, J. Nakamura, and K-I. Tanaka, Catal. Lett., 16 (**1992**) 407.
6. H. He, Y. Okawa, and K-I. Tanaka, Surf. Sci., 376 (**1997**) 310.
7. E. Roman and R. Riwan, Surf. Sci., 118 (**1982**) 682.
8. Y. Kuwahara, M. Fujisima, M. Onchi, and M. Nishijima, Surf. Sci., 207 (**1988**) 17.
9. N. Takehiro, Y. Matsumoto, Y. Okawa, and K-I. Tanaka, Phys. Rev. B,53 (**1996**) 4094.

10. N. Takehiro, K. Mukai, and K-I. Tanaka, J. Chem. Phys. 103 **(1995)** 1650.
11. K. Tamaru, K-I. Tanaka, S. Fukasaku, and S. Ishida, Trans. Farad. Soc.,61 **(1965)** 765.
12. D.R. Strongin, J. Carrazza, S.R. Bare, and G.A. Somorjai, J. Catal., 103 **(1987)** 213.
13. D.R. Strongin, S.R. Bare, and G.A. Somorjai, J. Catal., 103 **(1987)** 289.
14. D.R. Strongin and G.A. Somorjai, Catal. Letters 1 **(1988)** 61.
15. S.M. Davis, F. Zaera, B.E. Gordon, and G. A. Somorjai, J. Catal.,92 **(1985)** 240.
16. N.D. Spencer, C. Schoonmaker, and G.A. Somorjai, J. Catal., 74 **(1982)** 129.
17. A. Ozaki and H.S. Taylor and M. Boudart, Proc. Roy. Soc., A258 **(1960)** 47.
18. T.S. Amorelli, A.F. Carley, M.K. Rajumon, M.W. Roberts, and P.B. Wells, Surf. Sci. 315 **(1994)** L990.
19. E. Herceg, J. Jones, K. Mudiyanselage, and M. Trenary, Surf. Sc. 600 **(2006)** 4563.
20. K. Mudiyanselage, M. Trenary, and R.J. Mayer, J. Chem. Phys. 111 **(2007)** 7127.
21. T. Yamada and K-I. Tanaka, J. Am. Chem. Soc., 113 **(1991)** 1173.
22. T. Yamada and K-I. Tanaka, J. Am. Chem. Soc., 111 **(1989)** 6880.
23. M. Huttinger and J. Kupper, Surf. Sci.130 **(1983)** L277.
24. C. Klauber, M.D. Avery, and T. Yates, Jr. Surf. Sci.154 **(1985)**139.
25. I.C. Bassinnana, K. Wagemann, J. Kuppers and G. Ertl, Surf. Sci.175 **(1986)**22.

Part II
Dynamics of Chemical Reactions in Catalysis

Chapter 7
Overview of Catalysis

Abstract To understand the catalytic reaction, the dynamic chemical processes on the surface should be elucidated. Typical examples are the isomerization and hydrogenation of olefins, mentioned in Sects. 10.1 and 10.2, and the role of promoting materials in the oxidation of CO in H_2 mentioned in Sect. 10.4. Detection of non-mobile atoms or molecules on the surface is not very difficult, but it is very hard to detect moving species over the surface. When a molecule transfers from the gas phase to the surface or vice versa, the molecule should change its degrees of freedom via a precursor state. A good example suggesting a precursor state in adsorption is observed in the adsorption of an alcohol (ROH) molecule on the 7×7-Si(111) surface. Dissociation of ROH depends on the dissociation probability of precursor state ROH depending on the local confirmation of the sites. It is also difficult to detect the precursor state in desorption of molecule. From this view point, an interesting phenomenon is a simultaneous desorption of N_2 and NO from the Pd(110) surface at ca. 490–495 K. The most remarkable result is that N_2 takes a very steep off-normal of spatial distribution along the $\langle 001 \rangle$ axis, as discussed in Chap. 8.

Keywords Sn atoms moving on 7×7-Si(111) · Adsorption of alcohol molecules on 7×7-Si(111) · Rapid migration of precursor species · Precursor state of molecules in adsorption and desorption · Dissociation of alcohol molecule via a precursor state on 7×7-Si(111) · Intermediates of isomerization and hydrogenation of olefins · Langmuir–Hinshelwood Mechanism · Promoting materials in catalysis

The conversion of alcohol (C_2H_5OH) to different molecules using heated clay was already known in the eighteenth century, and the word "catalysis" was coined by J. Jakob Berzelius for this interesting function of solid materials. The theoretical definition of "catalysis" based on the thermodynamics of chemical reactions was given by Wilhelm Ostwald (Nobel Prize in 1909) at the end of the nineteenth century, which inspired us to produce desired chemicals by using catalysts, and a variety of chemical industries were developed in the twentieth century by using

K. Tanaka, *Dynamic Chemical Processes on Solid Surfaces*,
DOI 10.1007/978-981-10-2839-7_7

catalysts. In the late part of the twentieth century, people realized the importance of protecting the environment from industrial pollution and the exhaust gas of automobiles, and to save natural resources, and the topic of catalysis has been awakened again as the key to solving these difficult problems.

As described in **Part I**, it is not so difficult to detect atoms and/or molecules located on the surface at atomic scale, but improved catalysts are still prepared by empirical methods, as described in **Part II**. If we could observe the dynamic chemical processes taking place on the surface more directly, we could understand the real process in catalysis. As it was mentioned in **Part I**, the atoms or molecules adsorbed on the surface are evidently distinguished from the specific compound named as a "quasi-compound" formed on the surface by the reaction with surface atoms. The growth of (–Ag–O–) on Ag(110) in O_2 and the growth of (–Ni–H–) on Ni(110) in H_2 are typical examples, but their formation process is difficult to follow at the present time.

If adsorbed species or quasi-compounds stay in a limited space, however, we can follow their dynamic motion on the surface. Figure 7.1 shows the Sn atoms moving in a limited space on the 7 × 7-Si(111) surface; that is, a single Sn atom moving over the three Si adatoms in a half unit cell gives fuzzy noise in the STM image of a half unit cell on a Si(111)-7 × 7 surface at room temperature [1]. If an additional Sn atom comes into the half unit cell, the Sn atoms stop on a Si adatom in the half unit cell; that is, the mutual interaction stops the hopping motion of the atoms. These phenomena reveal the importance of short-range weak forces in the dynamic motion of adsorbed species, which is suggestive of the dynamic motion of molecules on active sites in catalysis. In addition, the hopping motion of Sn atoms within a limited space gives us an image of the precursor state of molecules in adsorption.

Before we consider the "Dynamics of Chemical Processes in Catalysis," we should consider the adsorption and desorption processes of molecules. Adsorption and desorption processes of molecules are as not simple as the model described by a potential energy curve in Fig. 7.2. The adsorption rate of molecules is usually described by the sticking probability (adsorption/collision) in relation to the

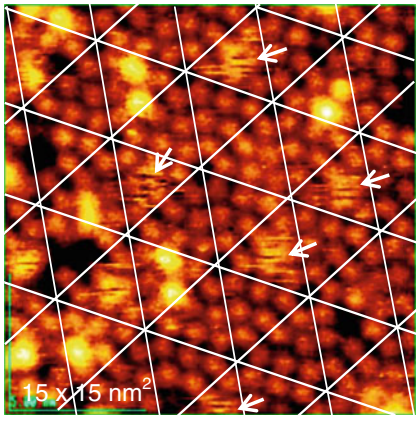

Fig. 7.1 *Arrow* indicates single Sn atom migrating within a half unit cell on the Si(111)-7 × 7 surface, V_b = –2.0 V, I_t = 0.20 nA. Single Sn atom is hopping on intact Si adatoms in a half unit cell, but additional Si adatom is adsorbed in the half unit cell and Sn atoms stop the migration by forming bright two spots [1]

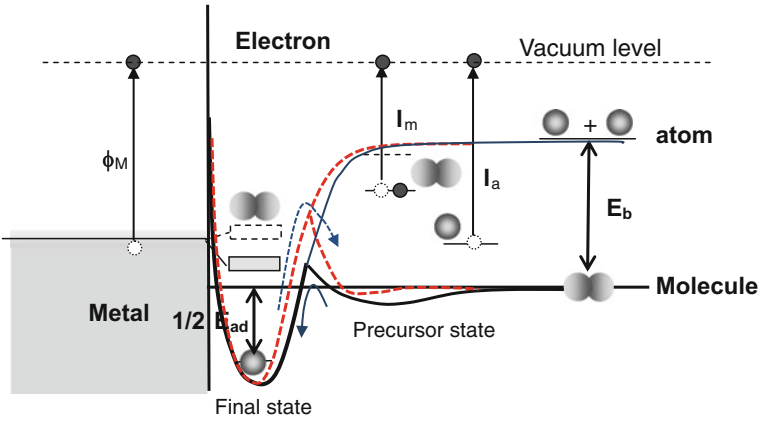

Fig. 7.2 Schematic description of the adsorption and desorption process via a precursor state, where *broken the line* shows the desorption potential. E_b is the bonding energy of a molecule, and 1/2 E_{ad} is the adsorption energy. Desorption process is more complex than the process of adsorption because the migration and/or surface reaction are incorporated. Ionization energy of the metal (ϕ_M), molecule (I_m), and atom (I_a) from the vacuum level

coverage. If the adsorption occurs via a precursor state, the adsorption is not simple as can be described by a potential energy curve perpendicular to the surface. The desorption process is more complex, because two-dimensional anisotropic processes including some reactions should take place before the desorption. If we consider the formation of N_2 by the catalytic reaction of NO with H_2, we can realize the difference between the catalytic reaction and the desorption of N_2 by the recombination of N(a) or the formation of N_2 via surface reaction. The difference between a surface reaction and a catalytic reaction on the surface is an essential problem to consider.

The alcohol molecule (ROH) does not dissociate on a 7 × 7-Si(111) surface by direct collision with a pair site of Si adatom/Si-rest atom, but dissociates via a precursor state into Si–OR and Si–H. The precursor state molecule may be moving in a half unit cell like a hopping Sn atom in a half unit cell shown in Fig. 7.1. The life of the precursor state alcohol molecules in a half unit cell is enough for dissociation to occur on a Si-adatom/Si-rest-atom pair site, so that the adsorption of alcohol proceeds with a constant sticking probability until saturation, as shown in Fig. 5.8a. The ROH dissociated into RO–Si and H–Si does not migrate on the surface, so that the dissociation probability of a precursor state ROH changing with local conformation is evaluated on the center-Si-adatom/Si-rest-atom and corner-Si-adatom/Si-adatom sites. As discussed in Fig. 5.7b in Chap. 5, the dissociation probability of the precursor state alcohol is four times larger on the center-Si-adatom/Si-rest-atom site than that on the corner-Si-adatom/Si-rest-atom site in either unfaulted-half or faulted-half unit cells as shown in Figs. 5.7b and 5.8c, d in **Part I**. That is, transport probability of the $H^{+\delta}$ to an electron-rich Si-rest atom adjacent to the Si adatoms in a half unit cell depends on the number of Si-rest atoms (either one or two). Accordingly, the

dissociation probability of a precursor ROH molecule on a Si-adatom/Si-rest-atom pair depends on the number of adjacent Si-rest atoms, either one or two. Finally, three unoccupied Si adatoms remain in every half unit cell, either the F-half or the U-half unit cell [2, 3]. An interesting fact is that the dissociation probability of precursor state of ROH molecules is fourfold higher on the ⟨Center-Si adatom/Si-rest atom⟩ site compared to that on the ⟨Corner-Si adatom/Si-rest atom⟩ site, for either CH_3OH or C_2H_5OH as observed in Fig. 5.8c. This result strongly indicates that the dissociation probability depends on the local conformation of the site and more directly depends on the number of rest Si-atoms adjacent to a Si adatom in this case. Constant sticking probability for the adsorption of methanol (CH_3OH) and ethanol (C_2H_5OH) up to the saturation coverage, as shown in Fig. 5.8b, indicates that precursor state molecules definitely seek out unoccupied [Si-adatom/Si-rest-atom] sites by rapid migration [2–5]. The bulky molecule of iso-propanol $(CH_3)_2CHOH$ also dissociates via a precursor state at a ⟨Si-adatom/Si-rest-atom⟩ pair site, but the apparent dissociation probability is lowered when the coverage exceeds 0.4; that is, the bulky group of $(CH_3)_2CHO$–Si disturbs the probability of seeking out an unoccupied Si-adatom/Si-rest-atom pair site.

The desorption process of molecules is more complex than adsorption, which may be illustrated by the spatial distribution of molecules desorbed from the surface as shown in Chap. 8 in **Part II**. When a Pd(110) surface exposed to NO at room temperature is heated in UHV, N_2 and NO desorb simultaneously at a temperature of ca. 490 K. If $^{14}NO(a)$ is adsorbed on a $^{15}N(a)$-adsorbed Pd(110) surface at room temperature, $^{15}N^{14}N$ is predominantly desorbed at 490 K. A more interesting phenomenon is the spatial distribution of N_2 desorbing at 490 K. The main desorption flux exhibits a very steep off-normal distribution along the ⟨001⟩ axis, which can be expressed by a $\cos^{46}(\theta \pm 38)$ distribution, with minor normal desorption given by $\cos^{4.2}\theta$ as shown in Fig. 8.2. It should be pointed out that the desorption temperature of N_2 in the temperature-programmed desorption is lower than that of NO(a) molecules on a Pd(110) surface. This result may suggest that adsorbed N(a) atoms move rapidly on the Pd(110) surface at a temperature lower than that of adsorbed NO(a), and a kind of molecular-beam-like reaction takes place in the two-dimensional space between an adsorbed NO(a) and a diffusing N(a) atom. This process is not a catalytic process; that is, no direct decomposition of NO into N_2 and O_2 takes place, as discussed in Chap. 8.

In practical catalysis, the catalyst surface becomes active by forming active sites or an active surface as illustrated in Fig. 1.1 [6]. One prominent example is the formation of an active surface on Pt–Rh alloy and on Pt/Rh or Rh/Pt bimetal surfaces in the presence of NO or O_2. Pt and Rh are not particularly active catalysts toward the reaction of $NO + H_2 \rightarrow 1/2\ N_2 + H_2O$ at temperatures below 400 K, but the Pt–Rh alloy or Pt/Rh bimetal surface changes to an extremely active catalyst at ca. 400 K toward the reaction of $NO + H_2 \rightarrow 1/2\ N_2 + H_2O$, as will be mentioned in Chap. 9 in this **Part II**. In this case, the surface becomes active by forming active ordered alloy layers during catalysis; that is, a two-dimensional ordered alloy layer is formed over the Pt–Rh alloy and Pt/Rh or Rh/Pt bimetal surfaces in O_2 or NO at ca. 400 K, which is referred to as chemical reconstruction. The newly formed

Pt–Rh ordered alloy surface is surprisingly active for the catalytic reduction of NO with H_2 [6] and may be a key material in the "three-way catalyst" developed for cleaning automobile exhaust gas.

One clear example showing the formation of active sites is observed on a lamellar MoS_2 crystal surface exposed to H_2. So far, the isomerization and the hydrogenation of olefins on metals have been explained by the Horiuti–Polanyi Mechanism, in which the two reactions are explained via common alkyl intermediates formed on metals by the reaction of olefins with adsorbed H(a). However, it was proved on MoS_2 that the function required of active sites is different for the two reactions, isomerization and hydrogenation of olefins. The two catalytic reactions were catalyzed only in the presence of H_2, but the two reactions were catalyzed independently on the different types of active sites formed on a single-crystal MoS_2 surface: One site is active for the isomerization reaction of olefins via alkyl intermediates but has no ability to promote the hydrogenation of olefins and the other site is active for the hydrogenation of olefins via alkyl intermediates but is less active for the olefin isomerization reaction, as described in detail in Sect. 10.2 in **Part II** [7, 8]. The alkyl intermediates for the two reactions were clearly distinguished on the MoS_2 by reaction with D_2. In this reason, the Horiuti–Polanyi Mechanism is an apparent phenomenon, rather than the mechanism for the catalysis.

Another interesting example is a reaction catalyzed by alternating dynamic cooperation of the two sites formed on the surface, which is olefin metathesis reaction, $2\ R_1CH = CHR_2 \rightarrow R_1CH = CHR_1 + R_2CH = CHR_2$, where the olefin reacts alternately with $Mo = CHR_1$ and $Mo = CHR_2$ on the $MoO_{3\text{-}X}$ surfaces. In the case of propene, $CH_2 = CH–CH_3$ reacts alternately with $Mo = CH_2$ and $Mo = CRCH_3$ sites. However, the existence of a hidden reaction, the so-called degenerated metathesis reaction, $CH_2 = CH–CH_3 + {}^*CH_2 = {}^*CH–{}^*CH_3 \rightarrow {}^*CH_2 = CH–CH_3 + CH_2 = {}^*CH–{}^*CH_3$, is ignored, because it is difficult to recognize without using isotope-labeled molecules. As discussed in Sect. 10.3, the turnover frequency of this hidden degenerate metathesis of propene is about 900 times faster on the $Mo = CH–CH_3$ site compared to that on the $Mo = CH_2$ site [9].

Catalytic oxidation of CO with O_2 on the Pt catalyst is a clasical reaction used to explain the mechanism of catalysis and the kinetics of catalytic reaction in textbooks, but this reaction reveals to us the complexity of catalysis in the presence of promoting materials and H_2O, as discussed in Sect. 10.4. This reaction has been explained in textbooks as a model reaction for catalysis, and the kinetics has been explained by the Langmuir–Hinshelwood Mechanism. This explanation was well supported by the experiment of Golchet and White on Pt foil [10]. As shown in Fig. 7.3, adsorption of CO(a) and O(a) on the Pt foil depends on the P_{CO}/P_{O2} ratio (at constant P_{O2}) at 453 and 485 K, and the adsorption of CO(a) and O(a) on a Pt foil is given by dynamic balance of the adsorption rate of CO(a) and its oxidation reaction with O(a). The amount of CO(a) and O(a) on a Pt surface becomes very low at the P_{co}/P_{O2} ratio of log $(P_{co}/P_{O2}) \approx -5.0$ to -5.3, where the oxidation rate of adsorbed CO(a) with O(a) exceeds the adsorption rate of CO and O_2. If the ratio of P_{co}/P_{O2} exceeds this balanced ratio, adsorption of CO(a) is steeply increased to an

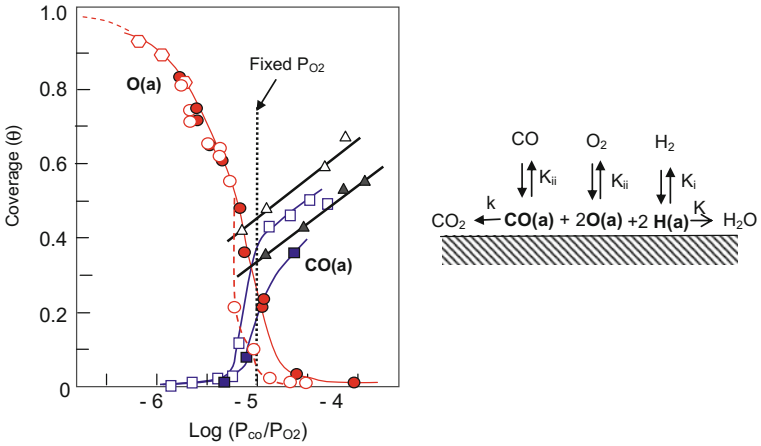

Fig. 7.3 Adsorbed CO(a) and O(a) on a Pt foil during oxidation reaction at 453 and 485 K attained by changing the pressure ratio of P_{CO}/P_{O2}, where the P_{CO} was changed by keeping P_{O2} at a constant pressure given at a *broken line*; O(a) (○, ●) and CO(a) (□, ■) at 453 and 485 K (solid). Adsorption isotherm of CO(a) (▽) at 453 and (▼) 485 K (solid) [10]

adsorption equilibrium curve, and if the ratio of P_{co}/P_{O2} is lower than this critical ratio, the Pt surface is covered with adsorbed O(a). To establish a dynamic balance between the adsorption of CO(a) and O(a) and their reaction, the rapid surface diffusion of adsorbed species is indispensable to establish the Langmuir–Hinshelwood Mechanism in catalysis.

It should be pointed out that the apparent homogeneous reactivity of adsorbed CO(a) on Pt foil does not mean equal reactivity of all adsorbed CO(a) on the Pt surface; rather, the rapid migration of adsorbed CO(a) smears the heterogeneity of the surface and inhomogeneous reactivity of adsorbed species on the surface, which is a fundamental requirement to establish the L–H Mechanism. In fact, if we compare the intrinsic reactivity of linearly bonded CO and bridge-bonded CO on the Pt surface with O_2, the bridge-bonded CO is more reactive than the linearly bonded CO with respect to O_2 as discussed in Sect. 10.4 in **Part II**.

The reaction kinetics (rate equation) and the rate of catalytic reaction are explained by the reaction at the rate-determining slow step, but it should be remembered that all the other rapid processes are indispensable in catalysis, but the roles of the rapid processes are very often ignored in considering the catalysis. For example, if a catalytic reaction is attained by cooperation of two functional sites on the surface, rapid transport of intermediates between the two sites is indispensable. If the rapid step is disturbed, the catalytic reaction stops. A typical example is the internal rotation of intermediates, which is usually rapid, but if an internal rotation is prevented on the sites, a reaction requiring rotation stops, as shown in Fig. 10.5. It should be remembered that the entire series of rapid processes is indispensable in catalysis, but their importance tends to be forgotten in practical catalysis. An illustrative example in practical catalysis is described in the preferential oxidation

(PROX) reaction of CO in H_2 discussed in Sect. 10.4 of **Part II**. The oxidation of CO on a Pt/CNT catalyst (carbon nanotubes) is markedly enhanced by H_2O if the CNT has Ni–MgO or FeO_x at its terminal end; that is, the Pt and the Ni–MgO cooperate to promote the oxidation of CO of CO + 1/2 O_2 + n H_2O → CO_2 + n H_2O at 40 °C. This oxidation reaction of CO is essentially different from our known ordinary oxidation reaction of CO + 1/2 O_2 → CO_2 on Pt. This experiment proved that the role of Ni–MgO is not the activation of the Pt catalyst, but instead to provide a new CO oxidation reaction, where the role of H_2O, described by an equation CO + 1/2 O_2 + n H_2O → CO_2 + n H_2O, is as a kind of molecular catalyst.

A promoting effect of alkali metals or ions (Li^+, Na^+, and K^+) is often observed in various catalytic reactions. The catalytic oxidation of formaldehyde (HCHO + O_2 → H_2O + CO_2) on Pt/TiO_2 [11] and the water–gas shift reaction (CO + H_2O → H_2 + CO_2) on Au particles [12] are typical examples. So far, the role of alkali metals or ions observed in these two reactions has been explained by the activation of metals, such as formation of $PtO(OH)_x$ alkali metal ion species and Au–$O(OH)_x$–(Na or K) but no change of mechanism has been premised to explain the effect of alkali metals on various reactions. The real role of promoting materials in catalysis is far more complex, so it is very often described by a vague term, the synergy effect on metals, but we should make clear the role of promoting materials, as discussed in Sect. 10.5 of **Part II**.

References

1. Z-X. Xie and K-I. Tanaka, Surf. Sci. 479 (2001) 26.
2. K-I. Tanaka and Z-X. Xie, J. Chem. Phys., 122 **(2005)** 054706.
3. H-J. Liu, Z-X. Xie, H. Watanabe, J. Qu, and K-I. Tanaka, Phys. Rev. B 73 **(2006)** 165421.
4. Z-X. Xie, Y. Uematsu, X. Lu, and K-I. Tanaka, Phys. Rev., B 66 **(2002)** 125306.
5. K-I. Tanaka, Y. Nomoto, and Z-X. Xie, J. Chem. Phys., 120 **(2004)** 4486.
6. K-I. Tanaka and Hong He, Catal. Today, 201 **(2013)** 2.
7. K-I. Tanaka, Adv. in Catal., Vol. 33, 99–158 **(1985)**.
8. K-I. Tanaka and T. Okuhara, Catal. Rev. Sci. and Eng. 15 (2) **(1977)** 249.
9. K-I. Tanaka, Appl. Catalysis. A, General,188 **(1999)** 37.
10. A. Golchet and J.M. White, J. Catal. 53 **(1978)** 266.
11. C. Zhang, F. Liu, Y. Zhai, H. Ariga, N. Yi, Y. Liu, K. Asakura, M. Flytzani-Stephanopoulos and Hong He, Angew. Chem. Int. 31 **(2012)** 9628.
12. Y. Zhai, D. Pierre, R. Si, W. Deng, P. Ferrin, A.U Nilekar, G. Peng, J. A. Herron, D.C. Bell, H. Saltsburg, N. Mavrikakis and M.F. Stephanopoulos, Sci. 329 **(2010)** 1633.

Chapter 8
Spatial Distribution of Molecules Desorbing with Surface Reaction

Abstract When temperature of Pd(110) is raised in a flow of NO + H_2, N_2, N_2O and NO are simultaneously desorbed at ca. 490–495 K and the catalytic reaction of NO + H_2 → 1/2 N_2 + H_2O is followed at about 500 K. If ^{14}NO is adsorbed on a ^{15}N/Pd(110) surface, $^{14}N^{15}N$ and ^{15}NO are simultaneously desorbed at 490–495 K. Interestingly, the N_2 desorbed at ca. 490 K takes on a very sharp off-normal spatial distribution expressed by $\cos^{46}(\theta \pm 38°)$ towards to the ⟨001⟩ axis. The result strongly suggests that the N_2 is formed by a surface reaction with anisotropic collision of moved N(a) with adsorbed NO(a). In contrast, the N_2 formed by the catalytic reaction of NO + H_2 → 1/2 N_2 + H_2O takes on a $\cos\theta$ distribution, indicating thermal equilibrium is attained.

Keywords Reaction of NO with Cu-atoms on Cu(110) · Formation of (–Cu–O–) and Cu_3N on Cu(110) · Simultaneous desorption of N_2 and NO from Pd(110) and Pd(211) · Off-normal spatial distribution of N_2 · Anisotropic collision of N(a) with NO(a) on Pd(110) · Spatial distribution of N_2 · Catalytic reaction of NO with H_2 on Pd(110) · Short–life precursor · Simultaneous desorption of N_2 and NO from a hybrid [Ag_4n + (–Ag–O–)]ag(110) surface

Homo-atomic molecules such as H_2, O_2, and N_2 on metals provide one kind of adsorbed species or quasi-compound, but hetero-atomic molecules such as CO, NO, and H_2O may form two different quasi-compounds upon reaction with surface metal atoms. Adsorption of NO on the Cu(110) surface is a prominent example, where (−CuO−) and (Cu_3N) are formed by the reaction with Cu atoms which diffuse out onto terraces from steps in the surface at room temperature. The (−CuO−) strings grow via precursor species $(CuO)^{\neq}$ formed on the terrace, which self-assembled in a (2 × 1) array on the Cu(110) surface at room temperature as shown in Fig. 5.3a in **Part I**. In contrast, the simultaneously formed (Cu_3N) dots are immobile at room temperature, so that (Cu_3N) dots are distributed randomly over the Cu(110) surface, as shown in Fig. 5.3a [1]. By raising the temperature of the Cu(110) to 600 K in UHV, the Cu_3N dots are ordered in a p(2 × 3) array on the Cu(110) surface, so that the two quasi-compounds, (−CuO−) strings and Cu_3N dots, form two ordered phases,

K. Tanaka, *Dynamic Chemical Processes on Solid Surfaces*,
DOI 10.1007/978-981-10-2839-7_8

p(2 × 3) Cu(110)–N and p(2 × 1)Cu(110)–O. As these quasi-compounds are stable and do not decompose to N_2 and O_2, no decomposition of NO occurs on the Cu(110) surface. When the surface is exposed to more NO, additional bright dots indicated with the arrow "A" appear to form on a part of the p(2 × 3) Cu(110)–N surface as shown in Fig. 5.3b, which suggests the presence of a 2nd layer with a pseudo-five-fold coordination structure.

The (−CuO−) strings are stable on the Cu(110) surface, but the (−CuO−) strings prepared on the Ag(110) surface are less stable, and a reversible change of (−CuO−) $\rightleftharpoons (Cu_2)_3 + O_2$ takes place at 550 K, as shown in Fig. 5.1. However, Cu_3N formed on Cu(110) cannot be destabilized by additives. Therefore, no decomposition of NO into N_2 and O_2 occurs, although the decomposition of NO ($2\ NO \rightarrow N_2 + O_2$) is thermodynamically favorable.

Before considering the reaction taking place on the surface, we turn our attention once again to the adsorption and desorption of molecules, which is the transfer of molecules between the 3-dimensional gas phase and the 2-dimensional space with its anisotropic interactions. The desorption process of molecules is not a simple reverse process of adsorption, because desorption of molecules is necessarily preceded by two-dimensional complex dynamic motion and reaction of adsorbed atoms, and if an exothermic process is involved in desorption, a desorbed molecule may keep a part of the excess energy. Desorption of N_2 from a NO-adsorbed Pd (110) surface by raising the temperature is a representative example, where the N_2 molecule is formed by anisotropic collision of an adsorbed NO(a) with a mobile N (a) atom on the Pd(110), which is named "**reaction-mediated desorption**" (it was referred to as "desorption-mediated reaction" in the reference) [2, 3]. The N_2 formed by the catalytic reaction of NO with H_2 on the Pd(110) surface is essentially different from the N_2 formed by reaction-mediated desorption and by the recombination of adsorbed N(a) atoms, as will be shown below.

If a metal is heated in vacuum, adsorbed species on the metal are desorbed, which is known as the temperature programmed desorption (TPD) spectrum. The TPD of CO/W(100) [4], H/Ni surfaces [5–8], N/W(110) [9], and N/Ru(0001) [10] surfaces are typical examples showing different desorption temperatures depending on the metal, crystal plane, and molecule. The bonding form of adsorbed molecules on metal surfaces was inferred by Madey and Yates [11, 12] by using the Electron Stimulated Desorption Ion Angular Distribution (ESDIAD) technique, and adsorption bonding was also inferred by photo-induced adiabatic desorption (PID) [13–17]. The adiabatic desorption of molecules or atoms measured by ESD and PID is essentially different from the desorption of molecules by raising temperature and by surface chemical reactions.

If the adsorption and desorption of molecule are reversible via precursor state, the spatial distribution of desorbing molecules from surface obeys to $\cos\theta$, but the spatial distribution of molecules desorbing from the surface is not so simple. A typical example is the desorption of CO_2 molecules by the reaction of adsorbed CO(a) with adsorbed O(a). The spatial distribution of CO_2 molecules desorbed from a Pt-surface by the reaction of CO(a) with O(a) by raising the temperature was

studied by Matsushima [18, 19], and showed that the spatial distribution of CO_2 was given by a simple $\cos^n \theta$ function with "n" > 1. The occurrence of "n" larger than unity was explained as the desorption of a CO_2 molecule with excess kinetic energy along the repulsive potential normal to the Pt surface. However, the spatial distribution of molecules desorbed from the surface with some reactions is not as simple as can be described by such a one-dimensional repulsive potential perpendicular to the surface. In fact, as will be described below, the spatial distribution of N_2 molecules desorbing from the Pd(110) surface is different depending on the preceding chemical processes in desorption.

Ikai and Tanaka studied the spatial distribution of desorbed molecules from the Pd(110) [3, 20] and Pd(211) [21] surfaces in TPD (Temperature Programmed Desorption) in UHV and by TPR (Temperature Programmed Reaction) in NO + D_2 or NO + H_2. The spatial distribution of molecules desorbing from the surface was measured by rotating a quadrupole mass spectrometer through a collimation chamber with two slits, 3 mm and 6 mm in diameter, as described schematically below. The distance from the sample surface to the 1st 3 mm slit was 25 mm and the 2nd 6 mm slit was 72 mm away from the 1st slit, and the spatial distribution of desorbed molecules was measured by rotating the sample.

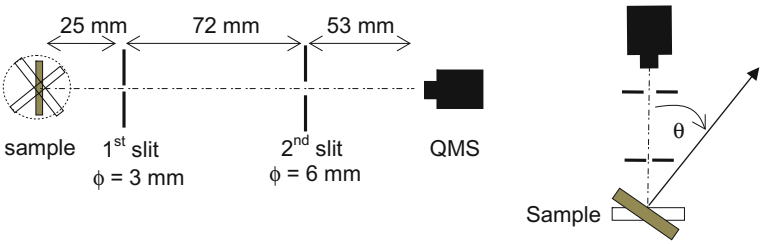

Collimated detection of molecules desorbing from the surface.

When the adsorption coverage of NO on a Pd(110) surface was low, simultaneous desorption of NO, N_2 and N_2O was observed by raising temperature in vacuum at 490–495 K. As the adsorption coverage of NO increased, an additional desorption of NO appeared at ca. 370 K [2]. Adsorption of NO at the short bridge site was suggested by RAIRS [22], and NEXAFS [23], and Sharpe et al. [24] suggested that all NO molecules adsorb without dissociation in molecular form at temperatures below 420 K. To clarify the simultaneous desorption of NO, N_2, and N_2O at 490–495 K, a ^{15}N/Pd(110) surface prepared by glow discharge in $^{15}N_2$ was exposed to ^{14}NO(a) (0.36 L) at room temperature. As shown in Fig. 8.1a ^{14}NO, $^{14}N^{15}N$ and $^{15}N^{14}NO$ were simultaneously desorbed on raising the temperature to 490–495 K, but the amounts of $^{14}N_2$ and $^{15}N_2$ were very small [3, 20]. These results suggest that the N(a) and/or NO(a) becomes motile on the surface, and the N_2 and N_2O desorbing at 490–495 K are provided by the reaction of ^{15}N(a) with ^{14}NO(a). When the adsorption of NO was increased, an additional desorption peak

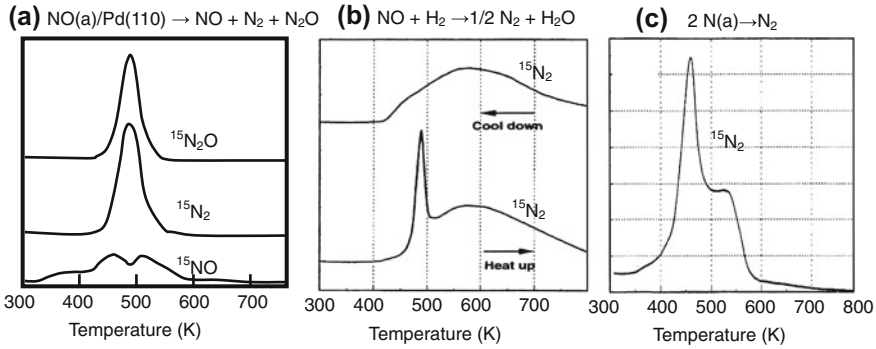

Fig. 8.1 **a** Temperature programmed desorption (TPD) spectrum from a ^{15}NO adsorbed Pd(110) surface, where the surface was exposed to ^{15}NO for 0.36 L at 300 K. **b** Temperature programmed reaction (TPR) spectra attained on a Pd(110) surface by raising temperature in a flow of ^{15}NO (5×10^{-8} Torr) + D_2 (5×10^{-6} Torr) and by lowering the temperature. **c** The TPD spectrum of a ^{15}N(a)-adsorbed Pd(110) surface [3, 20]

of NO was observed at ~370 K, but no simultaneous formation of N_2 or N_2O was observed at this temperature. From these results, ^{15}N(a) and/or ^{14}NO(a) becomes mobile when the temperature is raised, and set off the simultaneous desorption of $^{15}N^{14}N$ and $^{15}N^{14}NO$ with ^{14}NO at 490–495 K.

The results are described by three reactions, reaction-(1), reaction-(2) and reaction-(3) of Eq. (8.1i), where reaction-(2) $^{15}N(a) + {}^{14}NO(a) \rightarrow {}^{14}N^{15}N + O(a)$ is a "**reaction-mediated desorption**" forming N_2. If a ^{15}N/Pd(110) surface is heated in UHV, two $^{15}N_2$ desorption peaks appear, a large peak at around 460 K (lower than 490 K) and a small peak 540 K, as shown in Fig. 8.1c. The desorption temperature of N_2 at 460 K is undoubtedly lower than the simultaneous desorption of N_2, N_2O and NO at 490–495 K observed in Fig. 8.1a. This result suggests that the recombination of mobile N(a), reaction-(1) $2\,N(a) \rightarrow N_2$ in Eq. (8.1i), is disturbed in the presence of adsorbed NO(a) molecules.

If a Pd(110) surface was heated in a flow of 5×10^{-8} Torr $^{15}NO + 5 \times 10^{-6}$ Torr D_2, a sharp desorption peak of $^{15}N_2$ appeared at ~490 K, which was followed by a broad peak of $^{15}N_2$ (~430–800 K) with a maximum at 580–590 K as shown in Fig. 8.1b (the maximum depends on the adsorption of NO(a) and H(a) on the surface). If the temperature was lowered from ~800 K in a flow of $^{15}NO + D_2$, the broad $^{15}N_2$ band with a maximum at 580–590 K was reproduced, but no desorption peak of $^{15}N_2$ at ~490 K reappeared, as shown in Fig. 8.1b. These results strongly indicate that the amount of adsorbed ^{15}N(a) during the catalytic reaction $^{15}NO + D_2 \rightarrow 1/2\ {}^{15}N_2 + D_2O$ on the Pd(110) surface is very small. As a result, neither the reaction $^{15}N(a) + {}^{15}NO(a) \rightarrow {}^{15}N_2 + O(a)$ nor the reaction $^{15}N(a) + {}^{15}N(a) \rightarrow {}^{15}N_2$ occurs in temperature lowering experiments.

To infer the mechanism of simultaneous desorption of NO, N_2, and N_2O at ~490 K, the spatial distribution of desorbed NO, N_2O and N_2 was studied [3, 20, 21]. As shown in Fig. 8.2a, b, simultaneously desorbing N_2, N_2O and NO

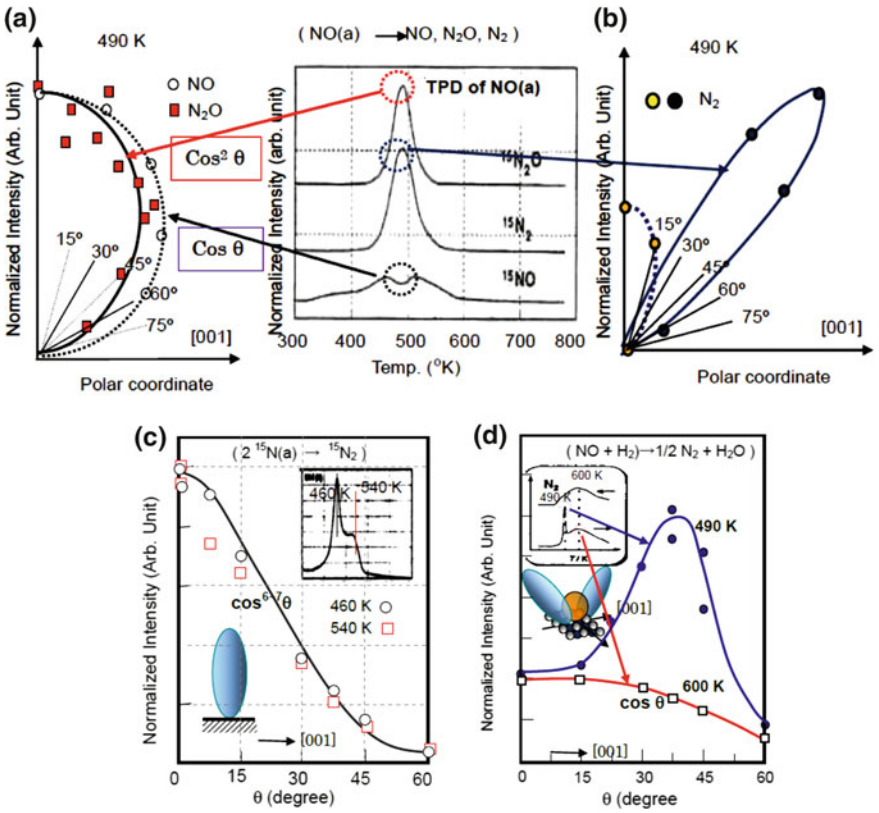

Fig. 8.2 Spatial distribution of NO, N_2O and N_2 simultaneously desorbed at 490 K from a NO adsorbed Pd(110) surface; **a** NO (cos θ) and N_2O ($\cos^2\theta$), and **b** Spatial distribution of N_2 ($0.9\cos^{4.2}(\theta) + 1.9\cos^{46}(\theta \pm 38°)$), and the TPD spectra of NO, N_2, and N_2O attained on a Pd(110) surface exposed to 0.36 L of ^{15}NO at 300 K. **c** Spatial distribution of N_2 desorbed by the recombination of N(a) at 460 K (*open circles*) and at 540 K (*solid squares*) from N(a) adsorbed Pd (110) surface. **d** Spatial distribution of N_2 formed by the reaction-mediated desorption at 490 K and by the catalytic reaction ($NO + H_2 \rightarrow 1/2\ N_2 + H_2O$) measured at 600 K [20]

showed entirely different spatial distributions, which may reflect the different formation mechanisms of N_2 and N_2O by the reaction with NO(a) at 490 K. The most remarkable result was the spatial distribution of N_2, which was very sharp off-normal anisotropic desorption toward the [001] direction. The anisotropic off-normal desorption along the [001] axis strongly suggests an anisotropic surface reaction between NO(a) and N(a), that is, "**the reaction-mediated desorption**" takes place by the reaction of NO(a) with anisotropic mobile N(a) along the [001] axis [3, 20].

The short-lived precursor $(N\cdots NO)^{\neq}$ given by the anisotropic surface collision of N(a) with NO(a) along the $\langle 001 \rangle$ axis, $^{15}NO(a) + {}^{14}N(a) \rightarrow (N\cdots NO)^{\neq} \rightarrow {}^{15}N^{14}N + O(a)$, gives the anisotropic off-normal emission of $^{15}N^{14}N$ as shown in Fig. 8.2b.

In other words, such an anisotropic collision of N(a) with NO(a) along the ⟨001⟩ direction is similar to an atom beam reaction of N(a) with an anisotropic momentum in a two-dimensional surface.

Pd(110)

Reaction-(1) $2\,{}^{15}N(a) \rightarrow {}^{15}N_2$

Reaction-(2) ${}^{15}N(a) + {}^{14}NO(a) \rightarrow (N\ NO)^{\neq} \rightarrow {}^{14}N^{15}N + O(a)$ **Eq. (8.1i)**

Reaction-(3) $(N\ NO)^{\neq} \rightarrow N_2O(a) \rightarrow N_2O$

Ag(110)

Reaction-(4) $Ag_4N \rightarrow N^{\neq}$ 520 K

Reaction-(5) $Ag_4N + N^{\neq} \rightarrow N_2$ 520 K **Eq. (8.1ii)**

(-Ag-O-) + $N^{\neq} \rightarrow$ NO 520 K

Reaction-(6) (-Ag-O-) $\rightarrow O_2$ 600 K

If precursor state $(N\cdots NO)^{\neq}$ is quenched in molecular form, it desorbs as N_2O at 490 K by reaction-(iii). It should be remembered that the N_2O molecule formed on the surface undergoes rapid rotation on the surface, so that it cannot maintain the molecular axis in a certain direction. Taking these facts into account, we can confidently conclude that the simultaneously desorbed N_2 is not the decomposition product of N_2O formed on the surface, because the N_2O molecule undergoes rapid rotation on the surface at 490 K. Therefore, an anisotropic off-normal emission of N_2 along the [001] direction such as shown in Fig. 8.2b is evidently not the decomposition of N_2O.

Similar simultaneous desorption of NO, N_2 and N_2O was also observed on a Pd (211) surface at 510 K on raising the temperature in NO + H_2, but the spatial distribution of desorbing molecules was more complex than that observed on the Pd (110) surface [21]. N atoms adsorbed on a Pd(211) surface by exposure to a N_2^+ ion glow discharge desorbed perpendicular to the crystal surface of Pd(211) at 470 K, which is a lower temperature than the simultaneous desorption of N_2 with NO at 510 K. The N_2 desorbing at 470 K is similar to the desorption of N_2 at 460 K from the Pd(110) surface with no adsorbed NO.

The simultaneous desorption of N_2 and NO from the Pd(211) at 510 K was also studied by using a ^{15}N(a) pre-adsorbed surface. A ^{15}N/Pd(211) surface prepared by glow discharge of $^{15}N^+$ and/or $^{15}N_2^+$ was exposed to ^{14}NO for 0.36 L at room temperature. $^{15}N^{14}N$ and ^{14}NO were simultaneously desorbed at 510 K with minor desorption of $^{15}N^{15}N$. The spatial distributions of these desorbed molecules were measured along the direction parallel to the [1-1-1] direction on the (211) crystal plane [21]. The main $^{15}N^{14}N$ followed $\cos^{12}(\theta + 26°)$, that is, off-normal to the Pd (211) crystal plane (normal to the [100] steps), whereas the minor product $^{15}N^{15}N$ desorbed normal to the Pd(211) crystal plane. An interesting fact was that the desorption of $^{14}N_2$ at 470 K from a ^{14}N/Pd(211) surface with no adsorption of NO(a) exhibited a distribution normal to the Pd(211) crystal plane. These phenomena suggest that the adsorbed NO(a) may retard the recombination of adsorbed N(a),

2 N(a) → N_2, on Pd(110) and Pd(211) surfaces, which reveals the importance of the dynamic motion of each adsorbed species on the surface in chemical reactions and in catalysis.

Reaction by the collision of mobile atoms with different adsorbed species was also observed on a [p(2 × 1)(-AgO-) + p(2 × 3)Ag_4N] Ag(110) surface by raising the temperature [25]. The Ag-surface is inactive towards the dissociation of N_2 molecules but a p(2 × 3) Ag(110)–N surface is attainable by exposing it to a glow discharge of N_2^+ and/or N^+ at room temperature. The STM image of a p(2 × 3) Ag(110)–N surface formed by annealing is similar to that of the p(2 × 3) Cu(110)–N surface, which suggests an array of Ag_4N in the [110] direction. As shown in Fig. 8.3b, the p (2 × 3) Ag(110)–N surface gave a desorption of N_2 by raising temperature, spectrum-(i), with a maximum at ∼520 K on raising temperature [26]. If this p(2 × 3) Ag (110)–N surface was exposed to O_2, the LEED pattern gave a combined pattern of [p (2 × 3)-N + p(2 × 1)-O]. As shown in Fig. 8.3a, the STM image of the [p(2 × 3)-N + p(2 × 1)-O] Ag(110) surface showed the growth of (–Ag–O–) strings perpendicular to the (2 × 3) Ag_4N domains, forming a hybrid of [Ag_4N + (–Ag–O–)] surface. When a hybrid of [Ag_4N + (–Ag–O–)] surface was heated in vacuum, a large desorption peak of NO with simultaneous desorption of N_2 was observed at 490–520 K, and was followed by the desorption of O_2 at 600 K as shown in the desorption spectra-(ii) in Fig. 8.3b [25, 26]. These results suggest that the $N^{\neq}$ formed on the surface at 500 ∼ 520 K by the reaction-(4) in Eq. (8.1)-ii undergoes reactive collision with Ag_4N to form N_2 by the reaction-(5) in Eq. (8–1)-ii, and simultaneous collision of $N^{\neq}$ with (–AgO–) forms NO at 500 ∼ 520 K as observed in Fig. 8.3b. If the N_2 and NO are formed by the collision of $N^{\neq}$ with Ag_4N and (–Ag–O–) on the Ag (110) surface according to reaction-(5) of Eq. (8.1ii), it is a reaction-mediated desorption, too.

From this view point, the spatial distribution of N_2 and NO simultaneously desorbing at 520 K from Ag(110) surface was studied. As shown in Fig. 8.4c and d, the N_2 and O_2 desorb perpendicular to the surface with a distribution expressed by $\cos^n \theta$. In contrast to the N_2 and O_2 desorbing with homo-atomic recombination of N(a) or O(a), the NO formed by the recombination of N(a) with O(a) has a different spatial distribution along the [001] and [1–10] directions. As shown in Fig. 8.4b, the spatial distribution of NO has two maxima along the [001] direction, one at 0° (normal to the surface) and the other at ∼17° off-normal to the surface. It should be emphasized that both the normal and off-normal desorption of NO have a sharp spatial distribution along the [001] direction, which can be described by $\cos^{40-50}(\theta - \alpha)$, where α = 0 or 17, but the desorption of NO along the [1–10] direction has only a perpendicular component as shown in Fig. 8.4a. On the other hand, the spatial distribution of N_2 desorbing at 520 K along [001] from a p(2 × 3)–N Ag(110) surface has a maximum intensity perpendicular to the surface, but the distribution is not a simple function described by $\cos^n \theta$ as shown in Fig. 8.4c, which may reflect the local anisotropic collision of Ag_4N with $N^{\neq}$

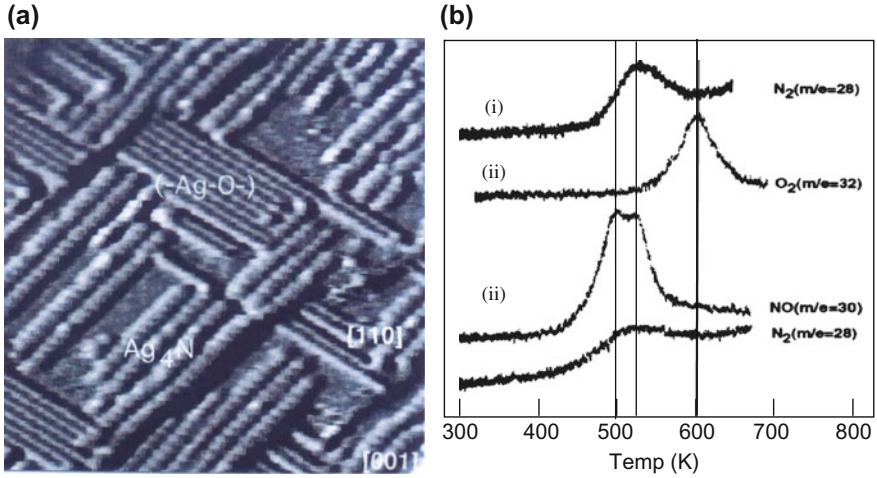

Fig. 8.3 **a** A hybrid surface of [Ag_4N + (–Ag–O–)], giving [p(2 × 3)-N + p(2 × 1)-O], attained by growing (–Ag–O–) strings on a (2 × 3)Ag(110)-N surface [25]. **b** TPD spectra attained by raising temperature at 3 K/s. (*i*) Desorption of N_2 from p(2 × 3)-N Ag(110), (*ii*) Desorption of N_2, O_2 and NO from a [p(2 × 3)-N + p(2 × 1)-O] Ag(110) surface, where N_2 and NO desorbs at 490–520 K and O_2 desorbs at 600 K [26]

exhibiting a reactive and/or complex repulsive potential for the desorption of N_2 with large excess kinetic energy. In contrast, the spatial distribution of O_2, which is formed by the reaction of O(a) with (–Ag–O–) on a p(2 × 1)-O Ag(110) surface, follows a $\cos^4 \theta$ distribution along the [001] direction as shown in Fig. 8.4d.

If two molecules collide in vacuum (3-D space), the product molecules are released depending on the collision axis of the two molecules. Kohguchi et al. [27] studied the collision of O atoms ($^1D_2$-state) with CD_4 with kinetic energy of 5.6 kcal/mole. They observed the OD emitted in two spatial directions: one was scattered in the forward and the other was scattered in the backward direction. They explained this result by the formation of short life intermediates $D_3C–D\cdots O$ and $D–O\cdots CD_3$ depending on form of the collision of O and CD_4. They speculated that a short-lived alcohol-like precursor gave by the backward-scattering of OD, whereas the head-on collision of the symmetric CD_4 molecule with an O atom gave the forward-scattered OD. In contrast to the collision of an atom with a molecule in vacuum, the collision of moving species with stationary adsorbed species on the surface is more strictly regulated on the surface. The collision reaction of labile $N^{\neq}$(a) with stationary adsorbed NO(a) on the Pd(110) surface, NO (a) + $N^{\neq}$(a) → $(N\cdots NO)^{\neq}$ → N_2 + O, gives anisotropic emission of N_2. The LEED pattern of the Pd(110) surface changes from (1 × 1) to p(1 × 3) at

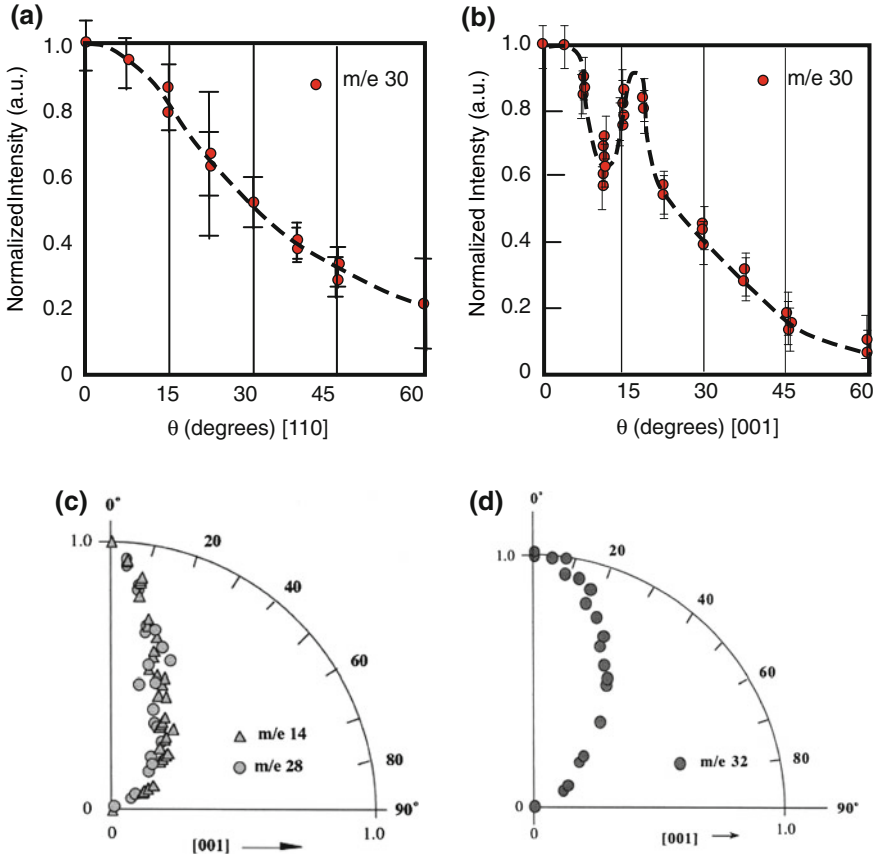

Fig. 8.4 Reaction-mediated desorption of NO on Ag(110) surface [25]. **a** Spatial distribution of NO along the [001] direction desorbing from [p(2 × 3)-N + p(2 × 1)-O] Ag(110) at 520 K. **b** Spatial distribution of NO along the [110] direction desorbing from [p(2 × 3)-N + p(2 × 1)-O] Ag(110) at 520 K. **c** Spatial distribution of N_2 along the [001] direction desorbing from p(2 × 3)-N Ag(110) at 520 K. **d** Spatial distribution of O_2 along the [001] direction desorbing from p(2 × 1) Ag(110) at 600 K

0.02 L, p(1 × 3) + p(3 × 1) at 0.2 L, and p(3 × 1) + p(2 × 1) at 30 L, but the desorption temperature and the coverage of NO have little effect on the spatial distribution of N_2, N_2O, and NO desorbed by the reaction of labile $N^{\neq}$(a) with adsorbed NO(a). This fact indicates that the long-range structure has little effect on the molecules produced by "the reaction-mediated desorption", which depends on the short range interaction of the adsorbed species.

If we consider once again the formation mechanisms of N_2 on the Pd(110) surface, N_2 is formed by the following three reactions at different temperatures, (i) N(a) + N(a) $\rightarrow$ N_2, (ii) N(a) + NO(a) $\rightarrow$ 1/2 N_2 + O(a), and (iii) catalytic reaction of NO + H_2 $\rightarrow$ 1/2 N_2 + H_2O. The spatial distribution of these N_2 molecules reflects the formation mechanism for N_2. N_2 molecules desorbed from Pd (110) at 490 K by reaction-(ii) exhibit a narrow spatial distribution at $\sim$38° off-normal toward the ⟨001⟩ axis as shown in Fig. 8.2b, which is expressed by 0.9 $\cos^{4.2}(\theta)$ + 1.9 $\cos^{46}(\theta \pm 38°)$. The distribution of N_2 molecules desorbed at 490 K overlaps with a small fraction of a perpendicular special distribution expressed by $\cos^{4.2}\theta$. This perpendicular desorption suggests the formation of N_2 by the recombination process of N(a) atoms, 2 N(a) $\rightarrow$ N_2, but it is suppressed in the presence of adsorbed NO(a) on the Pd(110) surface, which is similar to the spatial distribution $\cos^{6-7}(\theta)$ of N_2 desorbed at 460 K shown in Fig. 8.2c. The simultaneously desorbed N_2O at 490 K has a spatial distribution of $\cos^2\theta$ as shown in Fig. 8.1a. Another noteworthy result was that the N_2 formed by the catalytic reaction of NO + H_2 $\rightarrow$ 1/2 N_2 + H_2O in the temperature range of $\sim$430–800 K shown in Fig. 8.1b exhibits a cos θ distribution for the N_2 formed at 600 K in Fig. 8.2d. That is, the N_2 molecules produced by catalytic reaction are in thermal equilibrium. The NH_3 and the H_2O formed by non-catalytic reactions at 490 K in a flow of NO + H_2 (NO 1×10^{-8} and H_2 1×10^{-6} Torr) should also be mentioned since the NH_3 and H_2O exhibit spatial distributions expressed by $\cos^2\theta$ and cos θ, respectively. Taking these results into account, we could say that the desorption process of molecules with chemical reactions is not so simple as is described by a one-dimensional repulsive potential perpendicular to the surface as supposed by Matsusima [18, 19].

In the photo-decomposition of adsorbed HBr on the LiF(001) surface, emitted H atoms lose their kinetic energy before they leave the surface, that is, the kinetic energy is different from that of the H atoms produced by photolysis of HBr in the gas phase. The H_2 molecules formed by the collision of H atoms with HBr on the LiF(001) surface, H + HBr $\rightarrow$ H_2 + Br, exhibit a non-Boltzmann kinetic energy distribution. However, a small fraction of the direct photofragment of the adsorbed HBr gives a 55 $\pm$ 5° off-normal $\cos^n\theta$ distribution with a large n-value, which reflects the orientation of the adsorbed molecules [13]. In the case of photo-dissociation of N_2O adsorbed on the Pt(111) surface, ballistic release of O atoms occurs toward the tilted axis of the molecular bond of N_2O at 35°, which suggests rapid recoil of O atoms off-normal, with no collision [28, 29]. If $N_2^{\neq}$ leaves from the surface without thermal equilibration, the desorbing N_2 molecules produced by 2 N(a) $\rightarrow$ $N_2^{\neq}$ $\rightarrow$ N_2 preserve a certain amount of kinetic energy, so that they take a spatial distribution given by $\cos^{6-7}\theta$, as shown in Fig. 8.2c. We consider once again the mechanism of the anisotropic off-normal desorption of N_2 molecules toward the ⟨001⟩ axis on the Pd(110) surface at 490 K and the N_2 molecules formed by the decomposition of N_2O on the surface. Adsorbed N_2O molecules should undergo rapid rotation on the surface, so that the N_2 formed via the decomposition of N_2O on the surface cannot exhibit an anisotropic distribution. Accordingly, we could deduce the formation of very short-lived $(N\cdots NO)^{\neq}$ by the

anisotropic collision of NO(a) with N(a) along the $\langle 001 \rangle$ axis on the Pd(110) surface, which decomposes to N_2, NO(a) + N(a) $\rightarrow$ $(N\cdots NO)^{\neq} \rightarrow N_2^{\neq}$ + O(a), which is evidently different from the decomposition of N_2O.

References

1. N. Takehiro, F. Besenbacher, F. Laegsgaard, K-I. Tanaka, and I Stensgaard, Surf. Sci. 397 **(1998)** 145.
2. M. Ikai, Hong He, C. E. Borroni-Bird, H. Hirano, K-I. Tanaka, Surf. Sci. 315 **(1994)** L973.
3. M. Ikai and K-I. Tanaka, Surf. Sci. 357/358 **(1996)** 781.
4. D.R. Horton and R.I. Masel, Surf. Sci., 125 **(1983)** 699.
5. J.N. Russell,Jr., I. Chorkendorff, A.-M. Lanzillotto, M.D. Alvey, and J.T. Yates, Jr., J. Chem. Phys., 85 **(1986)** 6186.
6. H.J. Robota, W. Vielhaber, M.C. Lin, J. Segner, and G. Ertl, Surf. Sci.,155 **(1985)** 101.
7. K.-H. Allers, H. Pfnür, P. Feulner, and D. Menzel, Surf. Sci., 286 **(1993)** 297.
8. K.D. Rendulic and A. Winkler, Surf. Sci., 299/300 **(1994)** 261.
9. R.C. Cosser, S.R. Bare, S. M. Francis, and D.A. King, Vacuum, 31 **(1981)** 503.
10. H. Dietrich, K. Jacobi, and G. Ertl, J. Chem. Phys., 105 **(1996)** 8944.
11. T.E. Madey and J.T. Yates,Jr., Surf. Sci., 63 **(1977)** 203.
12. R.D. Ramsier and J.T. Yates,Jr., Surf. Sci. Rept. 12 **(1991)** 243.
13. E.B.D. Bourdon, C.-C. Cho, P. Das, J.C. Polanyi, C.D. Stanners and G.-Q. Xu, J. Chem. Phys., 95 **(1991)** 1361.
14. F.M. Zimmermann and W. Ho, Surf. Sci. Rept., 22 **(1995)** 127.
15. E. Hasselbrink, S. Jakubith, S. Nettesheim, M. Wolf, A. Cassuto and G. Ertl, J. Chem. Phys., 92 **(1990)** 3154.
16. X-L. Zhou, X-Y. Zhu, and J.M. White, Surf. Sci. Rept. 13 **(1991)** 73.
17. L.J. Richter and R.R. Cavanagh, Prog. Surf. Sci., 39 **(1992)** 155.
18. T. Matsushima, J. Chem. Phys. 91 **(1989)** 5722.
19. T. Matsushima, J. Chem. Phys. 93 **(1990)** 1464.
20. M. Ikai and K-I. Tanaka, J. Phys. Chem., B, 103 **(1999)** 8277.
21. M. Ikai and K-I. Tanaka, J. Chem. Phys., 110 **(1999)** 7031.
22. R. Raval,M.A. Harrison, S.Haq, and D.A. King, Surf. Sci. 294 **(1993)** 10.
23. J. Shingh, W.K. Walter, A. Atrei, and D.A. King, hem. Phys. Lett.185 **(1991)** 426.
24. R.G. Sharpe, and M. Bowker, Surf. Sci.,360 **(1996)** 21.
25. K. Moriwaki, T. Matsumoto, M. Ikai, and K-I. Tanaka, Chem. Phys. Letters 292 **(1998)** 500.
26. Y. Matsumoto, Y. Okawa, K. Suzuki, K. Mukai, and K-I. Tanaka, J. Am. Chem. Soc.,118 **(1996)** 9676.
27. H. Kohguchi, Y. Ogi, and T. Suzuki, Phys. Chem. Chem. Phys.10 **(2008)** 7222.
28. D.P. Masson, E.J. Lanzendorf, A.C. Kummel, Phys. Rev. Lett., 74 (**1995**) 1799.
29. D.P. Masson, E.J. Lanzendorf, A.C. Kummel, J. Chem. Phys., 102 **(1995)** 9096.

Chapter 9
Formation of Active Ordered Layer on Pt–Rh Catalyst

Abstract Pt and Rh are stable metals taking very high melting temperatures (Pt: 1,997 K, Rh: 2,249 K) and they form a random alloy. The Pt and Rh are not so active catalyst for the reaction of NO + H_2 → 1/2 N_2 + H_2O, and the surface of Pt–Rh alloy itself is also not so active for this reaction. However, a $Pt_{0.25}Rh_{0.75}$(100) alloy surface changes to an extremely active surface in O_2 at ca. 400 K, where the alloy surface is transformed from random to an ordered alloy layer with a (3 × 1) structure, and the same active (3 × 1) ordered layer is established on the Pt/Rh(100) and Rh/Pt(100) bimetallic surfaces. Once a (3 × 1) ordered layer is established, which is stable up to ca. 800 K in vacuum. STM image shows that the ordered $Pt_{0.25}Rh_{0.75}$(100) alloy surface takes a composite array of Pt and (Rh–O) rows in a (3 × 1) array, and the ordered alloy layer can keep up to ca. 800 K. The ordered Pt–Rh alloy layer is a new material being active for the reduction of NO with H_2, and the active hybrid ordered alloy layer is an active component of the three-way Pt–Rh catalyst developed for removal of NO_x, CO, and hydrocarbons in automobile exhaust gas.

Keywords Reduction of NO with H_2 · Catalytic activity of Pt(100) · Pt(110) · Rh (110) · Rh(100) and $Pt_{0.25}Rh_{0.75}$(100) · Active $Pt_{0.25}Rh_{0.75}$(100) alloy surface · Activation of Pt/Rh(100) and Rh/Pt(100) bimetal surfaces · Ordered array of Pt and Rh atoms on the active p(3 × 1)$Pt_{0.25}Rh_{0.75}$(100) surface · Electrochemical preparation of Pt and Rh bimetal surfaces

It is known that Pt and Rh are the fundamental component metals of "three-way catalyst" developed for removing NO_x, CO, and hydrocarbons in automobile exhaust gas. Pt and Rh are stable metals with high melting temperature (Pt; 1,997 K, Rh; 2,249 K), and they form a random alloy of an fcc crystalline structure. The catalytic activity of Pt and Rh single-crystal surfaces for the reaction of NO + H_2 → 1/2 N_2 + H_2O depends on the crystal planes as shown in Fig. 9.7a, b, but even the active Pt or Rh crystal planes are far lower than the Pt–Rh alloy surface activated during the catalytic reaction as mentioned below. Pt–Rh alloy or Pt/Rh or Rh/Pt bimetals are undoubtedly an important component of the "three-way catalyst"

K. Tanaka, *Dynamic Chemical Processes on Solid Surfaces*,
DOI 10.1007/978-981-10-2839-7_9

developed to remove NO_x, CO, and hydrocarbons in automobile exhaust gas. However, freshly prepared Pt/Rh bimetals and Pt–Rh alloy surface are not so active for the reaction of NO with H_2, but these surfaces change to extremely active surface for this reaction during catalysis. To elucidate the origin of high catalytic activity of Pt–Rh alloy and/or bimetal catalysts, a model reaction of $NO + H_2 \rightarrow 1/2\ N_2 + H_2O$ was studied on single-crystal $Pt_{0.25}Rh_{0.75}(100)$ alloy, Pt/Rh(100), Rh/Pt(110), Pt/Rh(100), and Pt/Rh(110) bimetal surfaces.

As will throughly described in this chapter, an ordered Pt–Rh alloy layer formed in O_2 is responsible for the catalytic activity of $Pt_{0.25}Rh_{0.75}(100)$ alloy and Rh/Pt or Pt/Rh bimetallic single-crystal surfaces [1–8]. That is, a random alloy $Pt_{0.25}Rh_{0.75}(100)$ surface transforms to an ordered alloy layer in O_2 or in a flow of $NO + H_2$ at ~400 K by a chemical reconstruction, and the ordered alloy layer established on the Pt–Rh alloy is extremely active for the reaction $NO + H_2 \rightarrow 1/2\ N_2 + H_2O$.

Nieuwenhuys et al. [9] studied the change of surface composition of $Pt_{0.25}Rh_{0.75}(100)$ alloy in vacuum by raising the temperature step-by-step from 830 to 1,300 K. As shown in Fig. 9.1a, the Pt fraction starts to change at ~900 K and attains a maximum at ~1,000 K and declines toward the bulk composition of Pt/Rh = 1/3 at 1,300 K. When the temperature is lowered from 1,300 K, a reversible change in the Pt fraction takes place from 1,300 K to ca. 1,000 K. This result indicates that the Pt–Rh alloy surface can take the equilibrium composition at the corresponding temperature at higher than 1,000 K, but the change of surface composition in vacuum becomes very slow at lower than 1,000 K, which is in good agreement with an empirical rule known as the Tammann temperature (surface atoms become able to move at half the melting point).

Tsong et al. [10] studied the depth profile of Pt and Rh atoms on a Pt–Rh alloy tip by using FIM (field ion microscopy). The layer-by-layer analysis of $Pt_{0.552}Rh_{0.448}(111)$ and $Pt_{0.552}Rh_{0.448}$ (001) planes on the alloy tip annealed at 973 K showed a Pt-enriched topmost layer and Pt-depleted 2nd layer (Rh-enriched) as shown in Fig. 9.1b, and they concluded the oscillation of the composition in several layers. However, the layer-by-layer composition below the 3rd layer is almost the equal to the bulk composition (55%), that is, the top two layers of the Pt–Rh alloy have a characteristic temperature-dependent equilibrium composition in vacuum above 1,000 K. In fact, the compositional change of the $Pt_{0.25}Rh_{0.75}(100)$ alloy surface is very slow at temperatures below 1,000 K in vacuum, as shown in Fig. 9.1a. That is, the composition of the 3rd layer and layers deeper than that is almost equal to the bulk composition of the Pt–Rh alloy (no oscillation of the composition was confirmed).

However, if a Pt-enriched clean $Pt_{0.25}Rh_{0.75}(100)$ surface is heated in O_2, the $p(3 \times 1)$ LEED pattern appears with a change in the Pt/Rh and O/Rh ratios at rather low temperature (~400 K), and this new composition is held up to ~750 K in vacuum as shown in Fig. 9.2 [3, 5]. It is noteworthy that the $p(3 \times 1)$ $Pt_{0.25}Rh_{0.75}(100)$–O surface changes to the (1×1) $Pt_{0.25}Rh_{0.75}(100)$ surface on exposure to H_2 at room temperature, and the (3×1) surface is readily recovered upon exposure to O_2 at room temperature. That is, a reversible change in the LEED

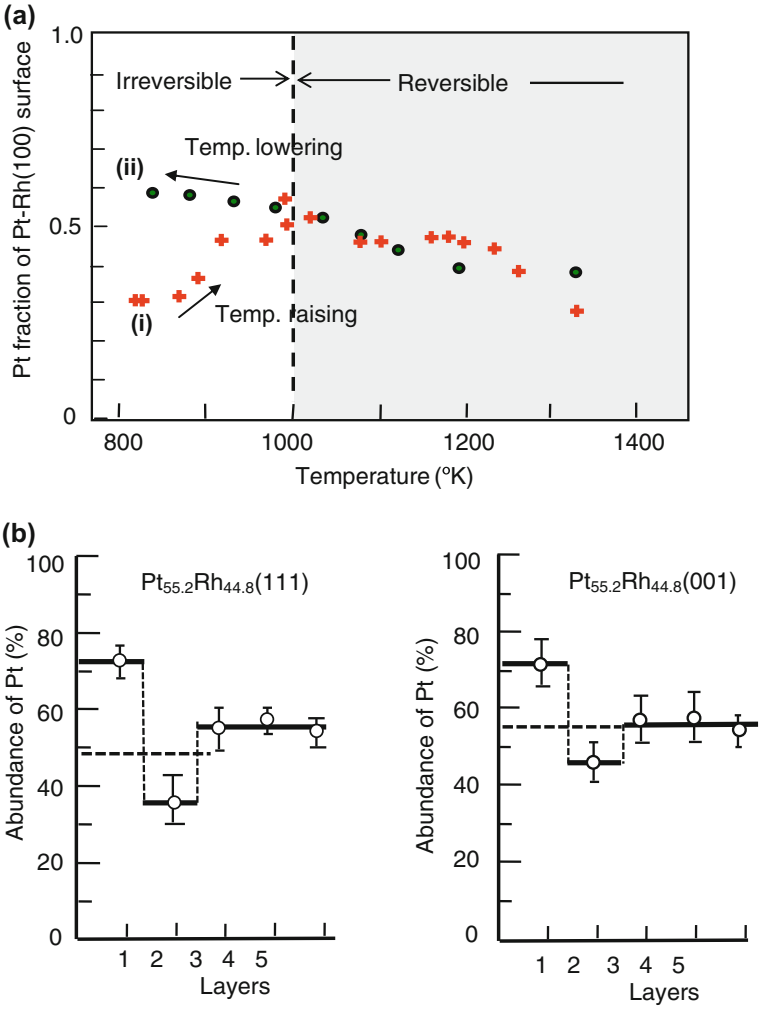

Fig. 9.1 **a** The $Pt_{0.25}Rh_{0.75}(100)$ surface reaches an equilibrium composition at temperatures higher than 1000 K in vacuum, but it is difficult to attain at an equilibrium composition at temperatures lower than 1000 K [9]. **b** Layer-by-layer analysis of a $Pt_{44.8}Rh_{55.2}$ alloy tip annealed at 700 °C for 5 min by field sublimation method [10]. Pt-enriched topmost layer and a Pt-depleted 2nd layer are formed on either (111) or (001) plane

pattern between the $p(3 \times 1)$ $Pt_{0.25}Rh_{0.75}(100)$–O in O_2 and the $p(1 \times 1)$ $Pt_{0.25}Rh_{0.75}(100)$ in H_2 (Pt and Rh have almost equal cross section in the LEED pattern) takes place at room temperature by a redox reaction of the surface. It is noteworthy that once a $p(3 \times 1)$ surface is formed on the $Pt_{0.25}Rh_{0.75}(100)$ surface at 400 K in O_2, the ordered two-dimensional array of Pt and Rh atoms is stable up to ca. 800 K in vacuum, and the $p(3 \times 1)$ surface is recovered at room temperature on exposure to O_2 as shown in Fig. 9.2. That is, a two-dimensional ordered array of

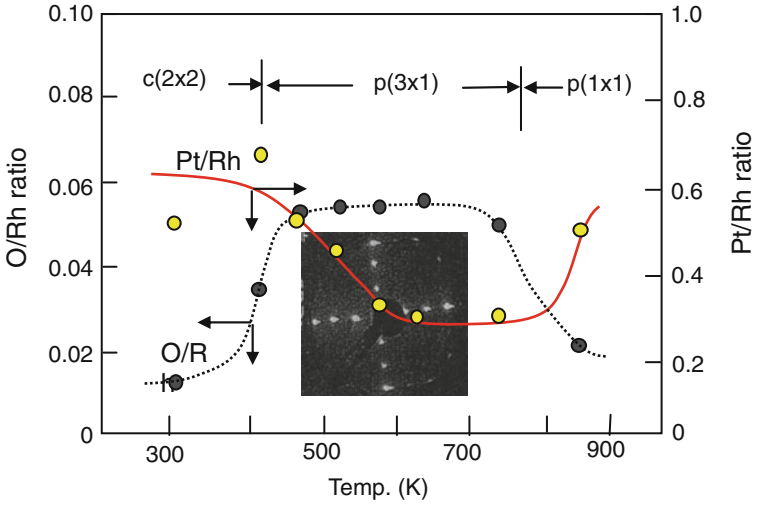

Fig. 9.2 The composition and structure of $Pt_{0.25}Rh_{0.75}(100)$ changing with temperature on heating for 5 min in O_2 (10^{-7} Torr). A characteristic p(3 × 1) LEED pattern appears at ~400 K with a remarked change in the O/Rh and Pt/Rh ratios [3, 5]

Pt and Rh is established on the $Pt_{0.25}Rh_{0.75}(100)$ surface at ~400 K in O_2, and this two-dimensional ordered alloy layer established on the $Pt_{0.25}Rh_{0.75}(100)$ alloy surface is stable up to 800 K in vacuum, because the p(3 × 1) LEED pattern is recovered upon exposure to O_2 at room temperature as described below.

The two-dimensional ordered array layer of Pt and Rh is formed by the reaction of Rh atoms with oxygen on the Pt–Rh random alloy surface, which is referred as "**chemical restructuring**" or "**chemical reconstruction**" [11]. As mentioned above, an ordered array of Pt and Rh atoms established on the $Pt_{0.25}Rh_{0.75}(100)$ alloy surface is stable in vacuum at 800 K, because the p(1 × 1) surface attained at 800 K gives the p(3 × 1) structure in O_2 at room temperature that is, the reversible change of p(3 × 1) $\rightleftharpoons$ p(1 × 1) is attained by exposing the surface to O_2 and H_2. I would say that this is an example of "*a form of matter with its own chemistry*" in Hoffmann's words. The array of Pt and Rh atoms on the p(3 × 1) $Pt_{0.25}Rh_{0.75}(100)$ surface was elucidated by STM as shown in Fig. 9.9 and described in more detail below [8, 12].

Figure 9.3 [7, 13] shows the UHV chamber designed for the preparation of the bimetallic surfaces of Pt/Rh(100), Pt/Rh(110), Rh/Pt(100), and Rh/Pt(110) by electrochemical deposition of Pt or Rh atoms in an electrochemical cell attached to the UHV chamber [3–5, 7, 11]. Ready deposition of high-melting-point metals such as Pt or Rh at room temperature is one advantage of electrochemical deposition. By firmly pushing a cone-shaped holder head onto the O-ring at the gate valve, the cubic reactor cell was effectively separated from the main UHV chamber (10^{-10} Torr). By this procedure, the pressure in the cubic reactor cell was able to be kept at any desired pressure from 10^{-8} Torr to one atmospheres. Bimetallic Pt/Rh

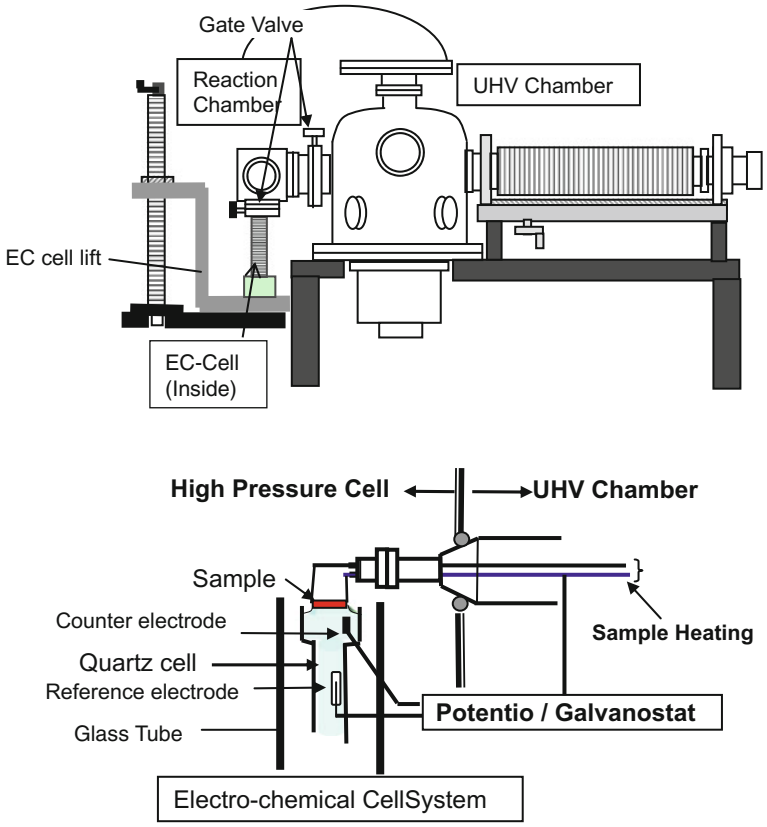

Fig. 9.3 UHV chamber equipped with a high-pressure cubic cell for chemical reaction and electrochemical reaction. The cubic cell is separated from the UHV chamber by pushing the cone-shaped holder head into the O-ring of the gate valve. Electrochemical process on a single-crystal metal surface is performed by making meniscus contact with the solution in the cubic cell [7, 13]

(100), Rh/Pt(100), Pt/Rh(110), and Rh/Pt(110) surfaces were prepared by electrochemical deposition in the cubic reactor filled with argon gas (Ar). After the deposition of the desired amount of metal, the crystal wafer was pulled back into the main UHV chamber and subjected to characterization by LEED, AES, and XPS. After the characterization of bimetallic wafer, it was again transferred back into the cubic reactor cell and subjected to catalytic reactions [5].

Figure 9.4 shows the cyclic voltammograms of various crystal planes of Pt and Rh attained in a 0.05 M H_2SO_4 solution: (a) (5 × 20)Pt(100) and (b) p(1 × 2)Pt (110), and (c) Rh(100) and (d) Rh(110) crystal planes annealed at 1,100 K in the UHV chamber (10^{-10} Torr) [4, 11, 14], that is, the sample prepared in UHV chamber was transported into the cubic cell filled with Ar, and the cyclic voltammogram of the single-crystal surfaces was attained by making meniscus contact with an electrolyte solution in the cubic cell filled with argon gas.

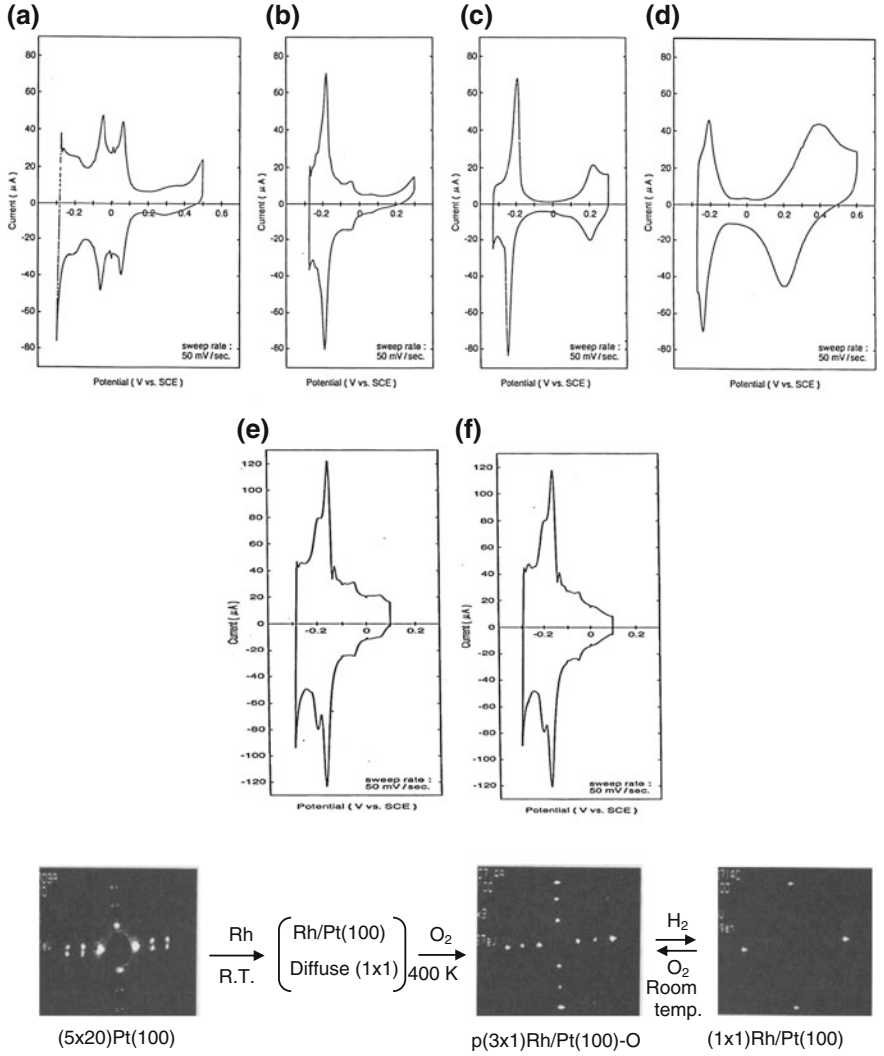

Fig. 9.4 Cyclic voltammograms for the clean surfaces in a 0.05 M H_2SO_4 solution; **a** (5 × 20)Pt (100), **b** (1 × 2)Pt(110), **c** (1 × 1)Rh(100), **d** (1 × 1)Rh(110), **e** p(3 × 1)Rh/Pt(100)–O, and **f** p (1 × 1) Rh/Pt(100) prepared by exposure to H_2 (θ_{Rh} = 0.8). Diffuse (1 × 1) LEED pattern of an as-deposited Rh/Pt(100) surface (1.5 ML of Rh) changed to a sharp p(3 × 1) pattern in 1×10^{-7} Torr of O_2 at 340–400 K. The reversible change between the p(3 × 1) and p(1 × 1) surfaces was attained at room temperature by exposure to 1×10^{-7} Torr of H_2 and 1×10^{-7} Torr of O_2, respectively [3, 4, 11, 14]

It is known that the cyclic voltammogram of the reaction $H^+ + e \rightleftharpoons H(a)$ depends on the metal and crystal planes. The (5 × 20)Pt(100) surface with no detectable contaminant by the XPS analysis gave the two peaks at −0.05 and +0.06 V (vs. SCE) as shown in Fig. 9.4a, which are slightly different from the voltammogram reported in the literature [15, 16]. Scortichini et al. [17] assigned the peak at +0.06 V to strongly bonded H(a) atoms to the defects on the Pt(100). After the immersion of the (5 × 20) Pt(100) surface at −0.28 V, the Pt(100) surface was converted into the p(1 × 1) LEED pattern with high-background intensity, which suggested imperfect flatness of the surface, but no oxygen peak was detected by the XPS analysis on the (5 × 20)Pt(100) surface. The total current of the two peaks of 195 μC/cm^2 of Pt(100) (after removing the double-layer charge) was very close to the 208 μC/cm^2 calculated for full adsorption of an H atom on every Pt atom, which is close to the value of 210 $\pm$ 10 given by Scortichini et al. [17]. Therefore, the two peaks may be due to the two different states of H(a) on the (5 × 20) Pt(100) surface. In contrast, the cyclic voltammogram of the p(1 × 2)Pt(110) surface attained by heating in UHV at 1,200 K had one peak at −0.18 V as shown in Fig. 9.4b. In this experiment, the p(1 × 2)Pt(110) was transferred into the cubic chamber filled with Ar and immersed at −0.28 V of potential. The Pt(110) surface immersed at −0.28 V (SCE) gave p(1 × 1) LEED pattern with high-background intensity. The desorption peak of H(a) attained on the Pt(110) surface was about 200 μC/cm^2 by correcting the double-layer charge. This value is similar to that of the literature [18], but is clearly more than the 146 μC/cm^2 calculated for one hydrogen atom on each Pt atom on the (1 × 1) flat surface. The difference may be due to the adsorption of bisulfate ions on the (1 × 1)Pt(110) surface.

The coulombic charge of the voltammogram of the Rh(110) surface shown in Fig. 9.4d was about 161 μC/cm^2 after subtracting the double-layer charge, which was very close to the value of 157 μC/cm^2 calculated for one H atom on each Rh atom on the (1 × 1) flat surface. The oxidation and reduction peaks of H(a) ($H(a) \rightleftharpoons H^+ + e$) on the Rh(100) surface appeared at −0.19 and −0.26 V (SCE) in the cyclic voltammogram are shown in Fig. 9.5a (same as Fig. 9.4c), and the oxygen wave is observed at +0.1 to +0.3 V. The coulombic charge for the hydrogen desorption peak (shadowed) on the Rh(100) surface in 0.05 M H_2SO_4 was about 237 μC/cm^2, which was very close to 222 μC/cm^2, as calculated by assuming one H atom on each Rh atom on a (1 × 1) surface.

Followed by the characterization of the single crystal surfaces, a series of bimetallic surfaces were prepared. A single-crystal metal surface was brought into meniscus contact with a solution containing metal ions, and some amounts of metal ions were deposited on it by repeating the cyclic voltammogram. The desired amounts of Rh atoms were deposited on the surface by repeating the potential sweep for 1–15 cycles (see Fig. 9.5b), and 0.8 ML of Rh was deposited on the Pt(100) surface in a H_2SO_4 solution (5×10^{-2} M) containing 5×10^{-5} M $RhCl_3$. A bimetallic Rh/Pt(100) surface ($\theta_{Rh} = 0.8$) prepared by the electrochemical deposition was washed with distilled water in the cubic cell filled with Ar gas and transferred to the UHV chamber for surface characterization. The as-deposited Rh/Pt(100) surface gave a diffuse (1 × 1) LEED pattern which changed to a diffuse

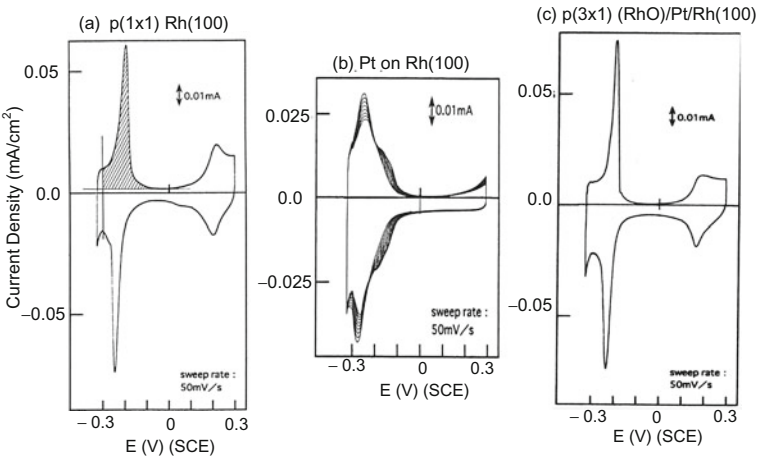

Fig. 9.5 **a** Cyclic voltammogram of a Rh(100) surface obtained in contact with a 0.05 M H_2SO_4 solution. **b** Cyclic voltammogram of a Rh(100) surface in contact with a 0.05 M H_2SO_4 + 5 x 10^{-5} M $PtCl_4$ solution for 5th ~ 12th cycles. **c** Cyclic voltammogram of a hybrid surface of p(3 × 1) (-RhO-)(Pt)/ Rh(100) surface attained by annealing in O_2 (1x10^{-7} Torr) at 600 K for 20 min

p(3 × 1) pattern in 10^{-7} Torr of O_2 at 340 K. On raising the temperature up to 400 K in O_2, the pattern changed to a very sharp p(3 × 1) LEED pattern as shown in Fig. 9.4 [3–5, 14]. Once the p(3 × 1)Rh/Pt(100)–O surface was attained, as mentioned previously, the reversible change between the (1 × 1) Rh/Pt(100) in H_2 and the (3 × 1) Rh/Pt(100)–O in O_2 took place at room temperature. The cyclic voltammogram of the p(3 × 1) Rh/Pt(100)–O surface is shown in Fig. 9.4e and that of the p(1 × 1)Rh/Pt(100) surface attained in H_2 is shown in Fig. 9.4f. It should be pointed out that the voltammograms in (e) and (f) are the same, that is, the array of Pt and Rh atoms takes no change by the redox reaction of the surface.

The variation of the cyclic voltammogram of the (1 × 1) Rh(100) surface with Pt deposition was monitored in a solution of 5 × 10^{-5} M $PtCl_4$ in 0.05 M H_2SO_4; about 1.1 ML of Pt deposition was attained on the Rh(100) surface (θ_{Pt} = 1.1) after 15 cycles as shown in Fig. 9.5b [4]. The as-deposited Pt/Rh(100) (θ_{Pt} = 1.1) surface with a high-background (1 × 1) LEED pattern changed to a diffuse (3 × 1) LEED pattern at ~500 K on heating in 1 × 10^{-7} Torr of O_2 and became a sharp (3 × 1) LEED pattern at temperatures higher than 500 K (500–600 K). It is noteworthy that the formation temperature of the (3 × 1) ordered surface in O_2 is 100–200 K higher on the Pt/Rh(100) surface compared to that on the Rh/Pt(100) and $Pt_{0.25}Rh_{0.75}$(100) alloy surfaces. However, once the (3 × 1)Pt/Rh(100)–O surface is formed, the surface undergoes reversible change between the (1 × 1)Pt/Rh(100) in H_2 and the p (3 × 1) surface in O_2 at room temperature as that on the (3 × 1)Rh/Pt(100)–O and

(3 × 1)$Pt_{0.25}Rh_{0.75}$(100) surfaces. The cyclic voltammogram of the (3 × 1) Pt/Rh (100)–O surface shown in Fig. 9.5c was also equal to that of p(3 × 1)Rh/Pt(100)–O, and p(3 × 1)$Pt_{0.25}Rh_{0.75}$(100)–O surfaces. It is worthy of note that the voltammograms of these p(3 × 1) surfaces are very similar to the voltammogram of the Rh (100) surface shown in Fig. 9.5a. As mentioned above, this two-dimensional ordered Pt–Rh alloy layer formed by heating in O_2 is stable in vacuum up to ~800 K. This two-dimensional ordered alloy layer formed on the (100) crystal planes exhibits a reversible change in LEED pattern between the (1 × 1) and the p(3 × 1) structures at room temperature upon exposure to H_2 or O_2.

It should be pointed out that the thermal stability of as-prepared clean Pt/Rh(100) and Rh/Pt(100) surfaces in vacuum is quite different from the stability of the (3 × 1)Pt/Rh(100) and p(3 × 1)Rh/Pt(100) ordered surfaces. That is, as-prepared Pt/Rh(100) bimetal surface (θ_{Pt} = 1.1 ML) formed by deposition of Pt was stable in vacuum even at 1,000 K for 20 min and 1,050 K for 10 min as shown by the Pt_{4f} peak in Fig. 9.6a, but the as-prepared Rh/Pt(100) bimetal surface formed by deposition of Rh was not as stable at 1,000 K, and the $Rh3d_{5/2}$ peak completely disappeared within 15 min at 1,000 K, as shown in Fig. 9.6b [3, 8]. Once the p(3 × 1) ordered alloy is established on the Pt/Rh(100)–O, Rh/Pt(100)–O, and $Pt_{0.25}Rh_{0.75}$(100)–O surfaces by heating in 10^{-7} Torr of O_2, the (3 × 1) ordered array of Pt and Rh atoms is stable even at 800 K in vacuum, and the catalytic reaction of NO + H_2 → 1/2 N_2 + H_2O proceeds at temperatures higher than ca. 400 K as shown in Fig. 9.8a.

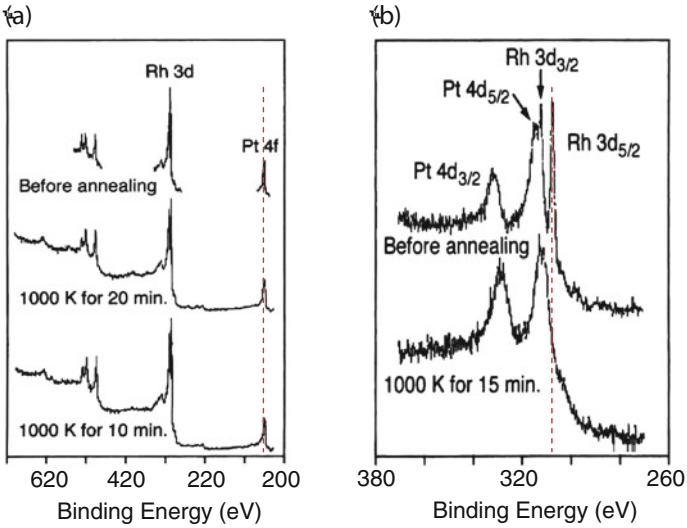

Fig. 9.6 Thermal stability of Pt atoms enriched on Rh(100) surface and that of Rh atoms enriched on Pt(100) surface. The XPS spectrum of **a** Pt/Rh(100) and **b** Rh/Pt(100) changes with time on heating at 1,000 and 1,050 K in UHV [3, 8]

Figure 9.7 shows the temperature-programmed reaction (TPR) attained on (a) Pt(100) and Pt(110); (b) Rh(100), Rh(110), and p(3 × 1)Pt/Rh(100); (c) Pt(110) and p(2 × 2)Rh/Pt(110); and (d) Rh(110) and p(2 × 4)Pt/Rh(110) surfaces by raising the temperature in a flow of 5.8×10^{-9} Torr NO + 1.6×10^{-8} Torr H_2. It is clear that the catalytic activity of Pt and Rh single-crystal surfaces for the reaction $NO + H_2 \rightarrow 1/2\ N_2 + H_2O$ depends markedly on the crystal plane, that is, Pt(100) ≫ Pt(110) and Rh(110) > Rh(100) as shown in Fig. 9.7a, b. However, the catalytic activity of the bimetal surfaces was dramatically improved by heating in 10^{-7} Torr of O_2 or in a flow of 5.8×10^{-9} Torr NO + 1.6×10^{-8} Torr H_2; the activity was markedly improved at ca. 400 K as shown in Fig. 9.7b Pt/Rh(100), (c) Rh/Pt(110), and (d) Pt/Rh(110), and their activity for the reaction of

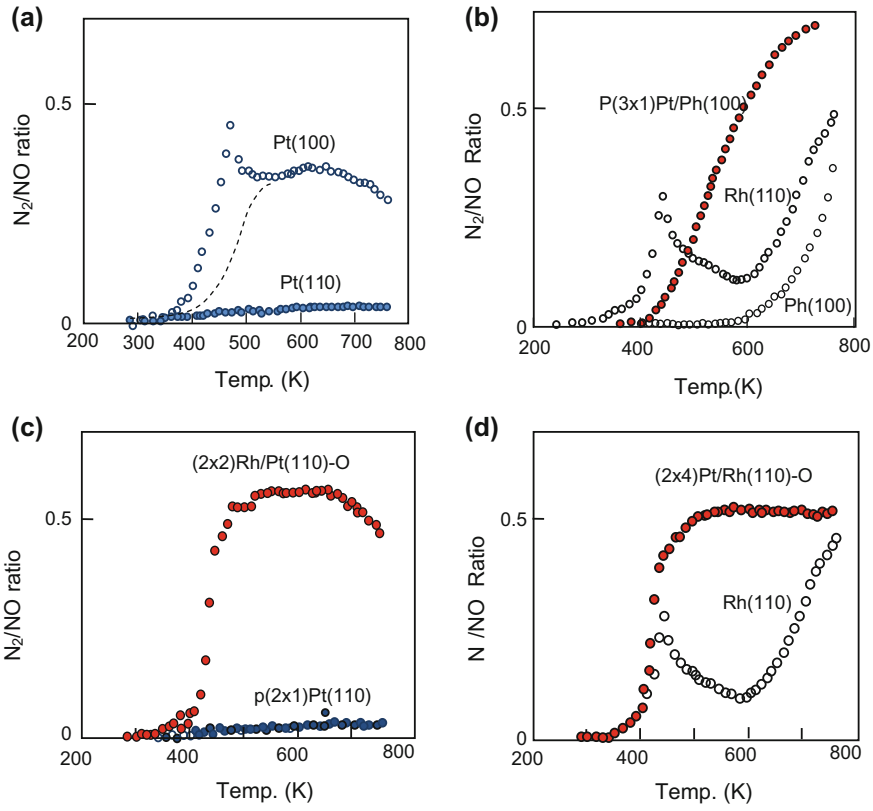

Fig. 9.7 Temperature-programmed reaction (TPR) attained in a flow of 5.8×10^{-9} Torr NO + 1.6×10^{-8} Torr H_2 on single-crystal surfaces. **a** (5 × 20)Pt(100) and p(1 × 2)Pt(110) surfaces. No desorption peak of N_2 appeared at 450–480 K in the temperature lowering process (*dotted line*). **b** Rh(100), Rh(110), and p(3 × 1)Pt/Rh(100) surfaces. **c** p(2 × 1)Pt(110) and p(2 × 2)Rh/Pt(110) surfaces. **d** p(1 × 1)Rh(110) and p(2 × 4)Pt/Rh(110) surfaces [4, 6, 11, 14, 19, 20]

$NO + H_2 \rightarrow 1/2\ N_2 + H_2O$ was almost equal as shown in Fig. 9.7b–d [4, 6, 11, 14, 19, 20].

These results strongly suggest the formation of a common active material on the Pt/Rh(100), Rh/Pt(110), and Pt/Rh(110) surfaces in the presence of O_2 or NO. It was also confirmed that a $Pt_{0.25}Rh_{0.75}(100)$ alloy surface, Rh/Pt(100), and Pt/Rh (100) bimetallic surfaces, which gave almost equal high catalytic activity on forming the p(3 × 1) surfaces in O_2 at ca. 400 K as shown in Fig. 9.8a [3, 4, 14]. From these results, we can confidently conclude that the formation of a two-dimensional ordered alloy layer is essential for the highly active Pt–Rh alloy and Pt/Rh or Rh/Pt bimetallic catalysts. This phenomenon bears a striking resemblance to the activity of Fe surfaces for the ammonia synthesis reaction, which depends strongly on the crystal plane, whereas the Fe surface covered with Al_2O_3 changes to a crystal-plane-independent highly active surface after heating in H_2O, as shown in Fig. 6.4. These results substantiate the formation of an active new material, *a form of matter with its own chemistry,* on the Pt/Rh bimetallic and Pt–Rh

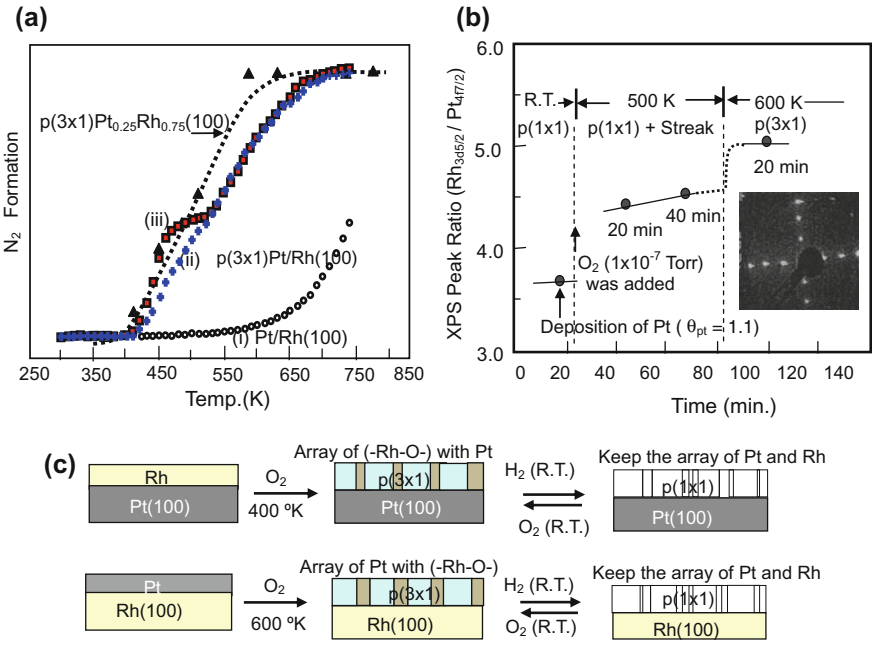

Fig. 9.8 **a** A flow reaction of NO (1×10^{-6} Torr) + H_2 (2×10^{-6} Torr) → 1/2 N_2 + H_2O on the Pt–Rh alloy and Pt/Rh bimetallic surfaces. (*i*) p(1 × 1)Pt/Rh(100) annealed at 1000 K for 5 min in UHV. (*ii*) p(3 × 1)Pt/Rh(100) attained in 1×10^{-7} Torr O_2 at 780 K for 10 min. (*iii*) A repeat run (*ii*). The activity of p(3 × 1)$Pt_{0.25}Rh_{0.75}$(100) is indicated with a *dotted line*. **b** The Rh/Pt ratio increases in 1×10^{-7} Torr of O_2 at 500 and 600 K, and the p(3 × 1)Pt/Rh(100) surface (θ_{pt} = 1.1 ML) is attained. **c** A schematic model for the formation of the p(3 × 1) layer on Pt/Rh(100) and Rh/Pt(100) in O_2, and the reversible p(3 × 1) ⇌ p(1 × 1) change by H_2 and O_2 at room temperature [3]

alloy surfaces by chemical reconstruction, which is the origin of the superior catalytic activity of Pt/Rh bimetallic and Pt–Rh alloy surfaces for the reaction $NO + H_2 \rightarrow 1/2\ N_2 + H_2O$.

Activation of a Pt/Rh(100) bimetal surface (1.1 ML of Pt) in O_2 requires a temperature of ca. 580 K, as shown in Fig. 9.8b, which is a significantly higher temperature than that of the formation of an active p(3 × 1) Rh/Pt(100)–O surface at ca. 400 K. That is, the higher temperature required for the formation of the p(3 × 1)Pt/Rh(100) surface is due to the low mobility of the topmost-layer Pt atoms, which inhibit the formation of the p(3 × 1) array of Rh atoms. However, once the p(3 × 1)Pt/Rh(100)–O surface was formed at 580–600 K in O_2, the catalytic activity for the reaction of $NO + H_2 \rightarrow 1/2\ N_2 + H_2O$ was the same on p(3 × 1)Pt/Rh(100)–O, p(3 × 1)Rh/Pt(100) and p(3 × 1)$Pt_{0.25}Rh_{0.75}$(100) surfaces as shown in Fig. 9.8a with line-(ii) and a broken line. Figure 9.8c shows an illustration of the formation of ordered alloy layers on the p(3 × 1)Pt/Rh(100), p(3 × 1)Rh/Pt(100), and p(3 × 1)$Pt_{0.25}Rh_{0.75}$(100) surfaces during the $NO + H_2 \rightarrow 1/2\ N_2 + H_2O$ reaction.

Taking these results into account, our target is the real ordered array of Pt and Rh atoms on the p(3 × 1)$Pt_{0.25}Rh_{0.75}$(100)–O surface. It is difficult to distinguish the Rh and Pt atoms on the $Pt_{0.25}Rh_{0.75}$(100) alloy surface by STM, but the array of Pt and Rh atoms on the alloy surface was successfully distinguished on the p(3 × 1)$Pt_{0.25}Rh_{0.75}$(100)–O surface by STM [12], as shown in Fig. 9.8.

The most important result observed on the p(3 × 1)$Pt_{0.25}Rh_{0.75}$(100)–O surface was the three different STM images (i)–(iii) on the same p(3 × 1)$Pt_{0.25}Rh_{0.75}$(100)–O surface, depending on the bias potential, as shown in Fig. 9.9a. The Pt and (–Rh–O–) were accidentally distinguished by an abrupt change of the W tip during scanning, which gave the STM images shown in the image-(iv). The upper half of the image-(iv) is equal to the image-(iii), and the lower half is equal to the image-(ii), respectively. The image-(iv) leads us to a conclusion that a single structure of the p(3 × 1)$Pt_{0.25}Rh_{0.75}$(100)–O surface gives the three different STM images, image-(i), image-(ii), and image-(iii). In other words, the three different STM images were observed by the change of the W-tip. The array of Pt and that of Rh atoms on the p(3x1)$Pt_{0.25}Rh_{0.75}$(100)-O surface was accidentally clarified by an image–(iv) obtained during scanning, in which the image–(ii) and the image–(iii) were appeared on the same STM image-(iv), that is, the W-tip was changed during scanning.

As shown in Fig. 9.4, the as-deposited Rh/Pt(100) surface (1.5 ML of Rh) with diffuse (1 × 1) LEED pattern changes to a sharp p(3 × 1) pattern at 340–400 K in 1×10^{-7} Torr of O_2, which undergoes reversible change of p(3 × 1) ⇌ p(1 × 1) at room temperature by exposure to 1×10^{-7} Torr of H_2 or 1×10^{-7} Torr of O_2. This is similar to the rapid change of a (3 × 1)$Pt_{0.25}Rh_{0.75}$(100)–O surface to a p(1 × 1) surface at room temperature upon H_2 exposure. The ordered alloy layer of Pt–Rh atoms established on the $Pt_{0.25}Rh_{0.75}$(100) surface is stable in vacuum at

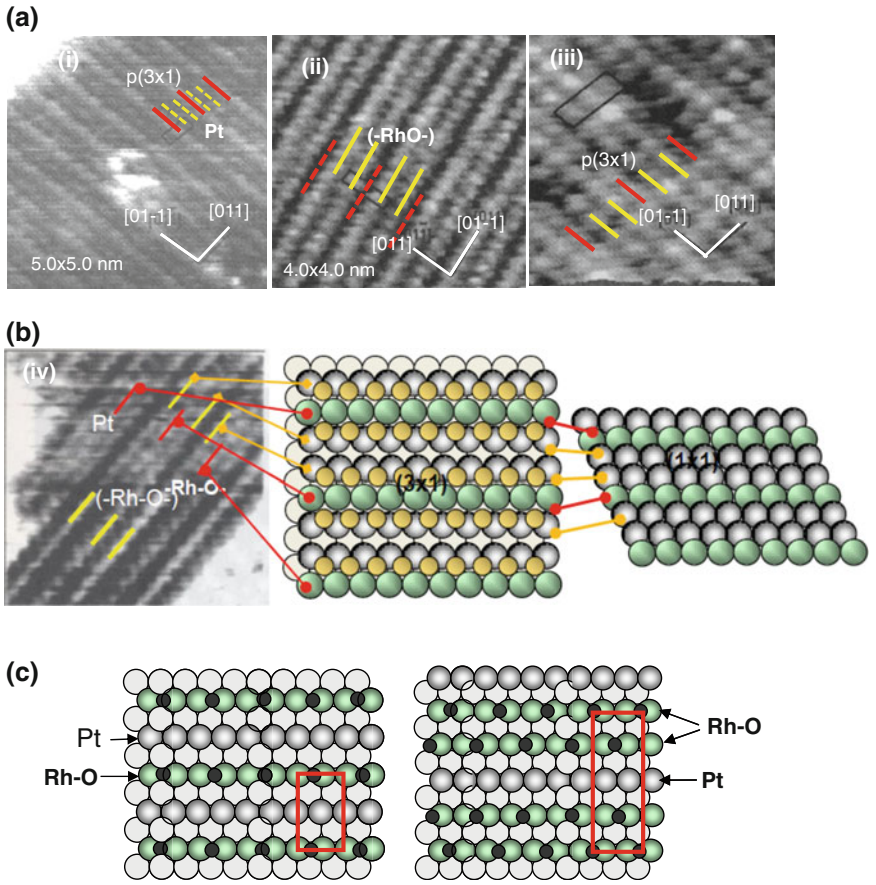

Fig. 9.9 **a** STM images of a p(3 × 1)$Pt_{0.25}Rh_{0.75}$(100)–O surface changed by bias potentials. (*i*) Pt rows in the topmost layer (*white arrow*) and in the 2nd-layer (*red arrow*). (*ii*) The image of (–Rh–O–) rows. (*iii*) The image of Pt rows and (–Rh–O–) rows. (*iv*) The STM image skipped from one to another due to a change in the *top* of the tip. **b** A model of p(3 × 1) $Pt_{0.25}Rh_{0.75}$(100)–O. The *lines* correspond to those shown in the STM image (*i*). **c** Models of (2 × 2)Rh/Pt(110)–O and (2 × 4)Pt/Rh(110)–O surfaces [12, 21]

800–850 K, because the p(3 × 1) surface is recovered again at room temperature by exposure to O_2. That is, the p(3 × 1) $Pt_{0.25}Rh_{0.75}$(100)–O surface is a two-dimensional ordered alloy of Pt–Rh atoms established by a "**chemical reconstruction**" with O_2. The reversible change of p(3 × 1) $\rightleftharpoons$ p(1 × 1) taking place on the ordered Pt–Rh alloy layer at room temperature is responsible for the oxidation of H_2 with O_2 by a redox reaction on the Pt–Rh alloy surface as shown in

Fig. 9.9b, and the ordered array of Pt and Rh atoms giving p(3 × 1) in O_2 is stable up to the temperature of 800–850 K in vacuum.

As mentioned above, the catalytic activity of Pt(100), Pt(110), Rh(100) and Rh (110) surfaces for the reaction of NO with H_2 depends on the metal and their crystal plane. In contrast, not only the reconstructed p(3 × 1)$Pt_{0.25}Rh_{0.75}$(100)–O and p(3 × 1) Pt/Rh(100)−O surfaces but also the reconstructed (2 × 2)Rh/Pt(110)–O and (2 × 4)Pt/Rh(110)–O surfaces have almost equal catalytic activity, as shown in Figs. 9.8a and 9.7c, d. Taking this fact into account, the array of Pt and Rh atoms on planes other than the (100)-plane is quite interesting. The bimetallic surface of Rh/Pt(110) and Pt/Rh(110) prepared by electrochemical deposition changes to (2 × 2)Rh/Pt(110)–O and (2 × 4)Pt/Rh(110)–O on raising the temperature in O_2, by which the surface becomes extremely active for the reaction of NO with H_2 as shown in Fig. 9.7c, d, which is very similar to the formation of active p(3 × 1) Pt/Rh(100) and p(3 × 1) Rh/Pt(100) surfaces in O_2 at 400 K. Taking these results into account, formation of a common active structure such as shown in Fig. 9.9c was deduced on the Rh/Pt(110) and Pt/Rh(110) surfaces, which is very similar to the array of Pt and Rh on the p(3 × 1)$Pt_{0.25}Rh_{0.75}$(100) surface. In summary, we conclude the formation of a two-dimensional active ordered alloy layer on the Pt–Rh alloy and Pt/Rh or Rh/Pt bimetallic surfaces, which is responsible for the structure-insensitive catalytic activity of Pt–Rh catalysts.

An additional change in the p(3 × 1)$Pt_{0.25}Rh_{0.75}$(100)–O surface is attained on exposure to high-pressure O_2, where the proportion of Rh atoms is increased to more than 2/3 of the total surface atoms. This is recognized by the decreasing Pt/Rh ratio with increasing O/Rh ratio and the changing LEED pattern from the p(3 × 1) to c(2 × 20), as shown in Fig. 9.10a. This is a two-dimensional phase change of ordered alloy by the Pt/Rh ratio with oxygen. The p(3 × 1) ordered alloy changes to the c(2 × 20) structure on the $Pt_{0.25}Rh_{0.75}$(100)–O surface, where the Pt rows are compressed by the growth of (–Rh–O–) strings, as observed in the STM image in Fig. 9.9a. The compressed c(2 × 20) $Pt_{0.25}Rh_{0.75}$(100)–O surface is apparently similar to the c(2 × 20)Pt(100) structure attained on a clean Pt(100) surface. That is, the density of atoms on the c(2 × 20)$Pt_{0.25}Rh_{0.75}$(100)–O surface is higher than that on the p(3 × 1)$Pt_{0.25}Rh_{0.75}$(100)–O surface [21]. In fact, if c(2 × 20) $Pt_{0.25}Rh_{0.75}$(100)–O is heated in UHV, a large O_2 desorption peak appears at ∼830 K and the structure changes from the c(2 × 20) array to the p(3 × 1), and is followed by a change to the p(1 × 1) array at 930 K with a small peak of O_2 desorption, as shown in Fig. 9.10b. Taking these results into account, the two-dimensional ordered alloy-layer surfaces, either p(3 × 1) or c(2 × 20), are responsible for the superior activity of the Pt–Rh alloy and/or Pt/Rh bimetallic surfaces for the reaction of $NO + H_2 \rightarrow 1/2\ N_2 + H_2O$.

The CeO_2/Pt(111) surface becomes active for the oxidation of CO observed by Lambert et al. [22] is another interesting example. Catalytic activity for CO oxidation on Pt(111) is suppressed, as expected, by increasing the coverage of CeO_2 on the Pt(111) surface, and the surface covered with one monolayer of CeO_2 becomes passive for CO adsorption and CO oxidation. However, if the Pt(111) surface is

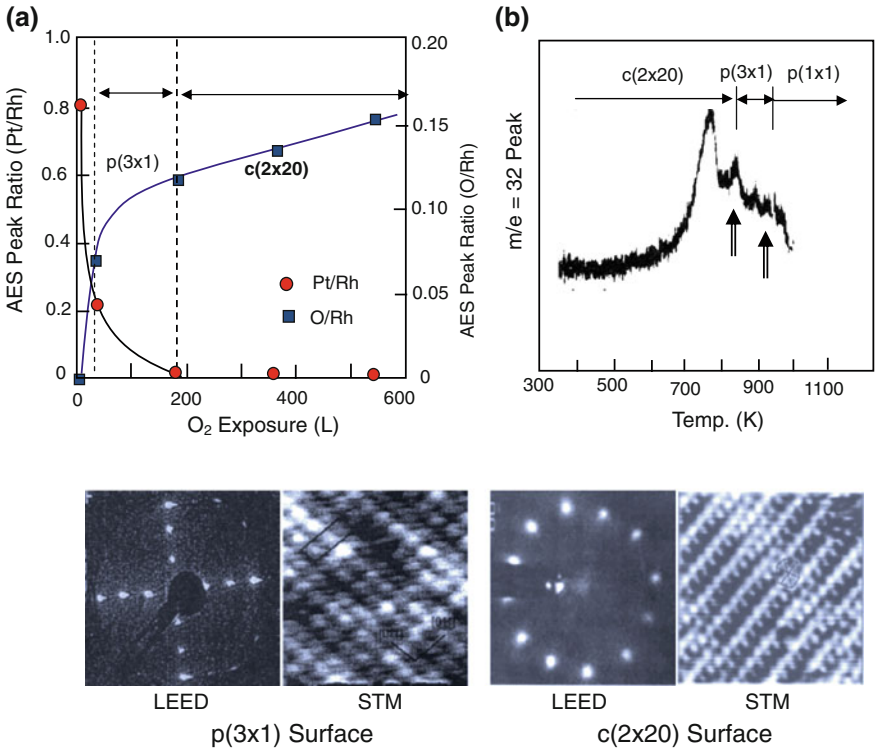

Fig. 9.10 Change of p(3 × 1)$Pt_{0.25}Rh_{0.75}$(100)–O surface to a hexagonal c(2 × 20) surface on exposure to high-pressure O_2 at 700 K. The TPD spectrum of a c(2 × 20) surface gives two O_2 desorption peaks at 830 and 930 K, and the c(2 × 20)$Pt_{0.25}Rh_{0.75}$(100)–O surface is changed to the p(3 × 1) surface after desorption of the 1st O_2 peak. The p(3 × 1) surface changes to the p (1 × 1) surface after the desorption of the 2nd O_2 peak at 930 K [12, 21]

covered with more than two monolayers of CeO_2, the surface suddenly becomes active for CO oxidation as shown in Fig. 10.31a. Interestingly, no CO adsorption was observed on this active CeO_2/Pt(111) surface during CO oxidation, that is, the oxidation of adsorbed CO is more rapid than the adsorption of CO on the surface. In other words, the adsorption of CO is the rate-determining process of the oxidation of CO on the CeO_2/Pt(111) surface. This fact proves that the lattice oxygen of the CeO_2 layers reacts very rapidly with CO and the reacted lattice oxygen is rapidly recovered by gas-phase O_2, which is essentially different from the catalytic oxidation of CO(a) on the Pt surface explained by the traditional model. It is noteworthy that a CeO_2 layer less than two layers thick passivates the Pt surface, but the CeO_2 layer becomes suddenly active when the CeO_2 becomes more than two layers thick on the Pt surface.

In Chap. 6 of **Part I**, it was shown that the methanation reaction on the Ni surface becomes active for by forming Ni_4C, and the Fe surface covered with Al_2O_3

Table 9.1 The SMSI effect on adsorption of H_2 and CO on precious metals [23]

Metals (2%)	Ru		Rh		Pd		Os		Ir		Pt	
Reduce (°C)	200	500	200	500	175	500	200	500	200	500	200	500
H/M	0.23	0.06	0.71	0.01	0.93	0.05	0.21	0.11	1.60	0.00	0.88	0.00
CO/M	0.64	0.11	1.15	0.02	0.53	0.02	–	–	1.19	0.00	0.65	0.03
BET (m^2/g)	45	46	48	43	42	46			48	45		

becomes active for the ammonia synthesis reaction by forming Fe_xN. The active CeO_2 layers on the Pt(111) surface are similarly considered to represent the formation of an active surface compound. On the other hand, if the surface is covered with a passive material, the surface loses catalytic activity. A typical phenomenon is known as the SMSI (strong metal support interaction) effect, which is passivation of precious metals supported on TiO_2 for the adsorption of CO and H_2 observed by Tauster et al. [23]. As shown in Table 9.1, a moderate amount of CO and H_2 are adsorbed on precious metals supported on TiO_2 when the metals are reduced at 200 °C. However, if the metals are reduced at 500 °C, adsorption of CO and H_2 becomes nearly zero.

Passivation of metals supported on TiO_2 is caused by spreading of a TiO_x layer over the metal surface upon evacuation at high temperature. Adsorption of CO and H_2 on the metals is disturbed by the TiO_x layer spread but is recovered by treating with O_2. The SMSI effect observed on the precious metals supported on TiO_2 is well explained by the wetting of the metal surface with a reduced form of TiO_{2-x}.

Wetting of a metal surface with an oxide layer was demonstrated on a Pd(111) surface with VO_2. The VO_2 layer on the Pd(111) surface was reduced to a s-V_2O_3 layer by exposure to H_2 for 2.3 L at 250 °C as shown by the STM image-(b) in Fig. 9.11, and the γ-VO_2 layer was recovered by exposing the s-V_2O_3 layer to O_2 at 250 °C [24]. When a Pd(111) surface covered with s-V_2O_3 was exposed to O_2 for 90 L at 250 °C, the surface was reconstructed into bare Pd(111) areas and areas with zig–zag–V_6O_{14} and (4 × 4)-V_5O_{14} patches, as shown by STM image-(c). The (4 × 4)-V_5O_{14} areas grew in large sheets on heating at 250 °C in H_2 for 2.8 L as shown by the STM image-(d), which is similar to the image-(b) for a surface covered with s-V_2O_3. That is, the bare area on a VO_2-deposited Pd(111) surface changes reversibly by wetting the surface with as-V_2O_3 layer in H_2 and removing the s-V_2O_3 layer by forming VO_2, V_4O_{15}, and V_4O_{16} in O_2.

The SMSI effect for the adsorption of CO and H_2 is explained well by the passivation of the metal surface. However, the presence of a small amount of H_2O gives a dramatic change in the oxidation reaction of CO, $CO(a) + O(a) \rightarrow CO_2$, in the presence of some oxides. The preferential oxidation (PROX) reaction of CO in H_2 is a typical case. In this case, the reaction is expressed by the equation $CO(a) + 1/2\ O_2 + H_2O \rightarrow CO_2 + H_2O$, where the H_2O molecule promotes the oxidation of CO as a kind of molecular catalyst, which is essentially different from the traditional reaction mechanisms as will be discussed in Sect. 10.4 of **Part II**.

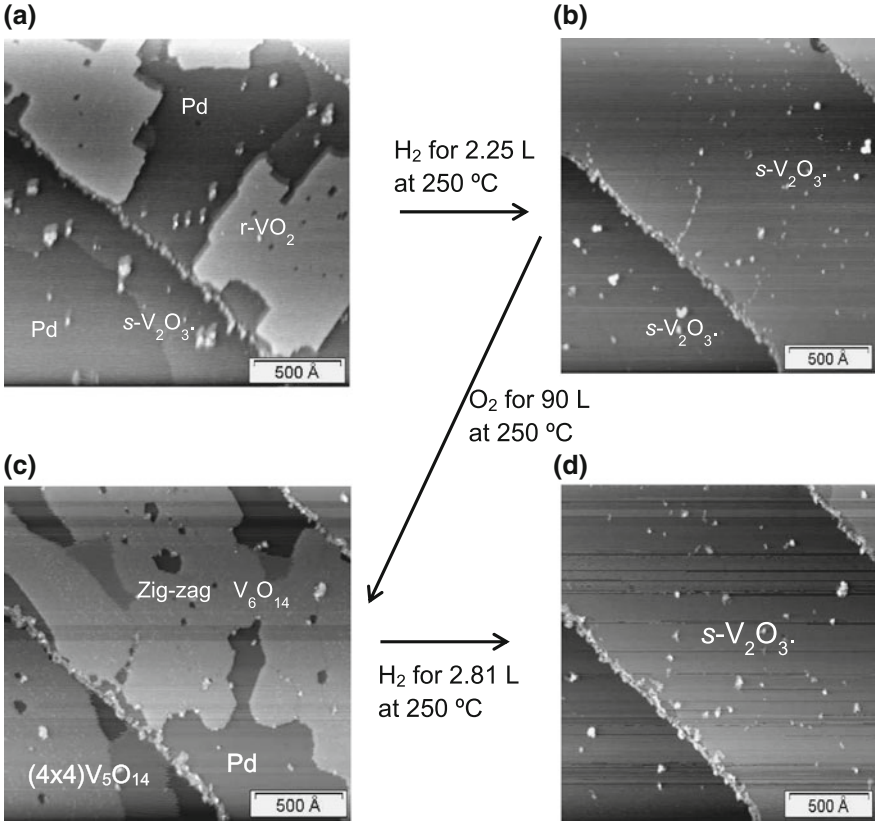

Fig. 9.11 Reversible change of the wettability of VO_x overlayer on a Pd(111) surface on heating in H_2 and O_2 [24]

References

1. K-I. Tanaka, Surf. Sci. 357/358 **(1996)** 721.
2. K-I. Tanaka, ACS Symposium Series 656 Solid-Liquid Electrochemical Interfaces, Chapter 18 **(1997)** 245 –273. Edt. By G. Jerkiewicz, M. P. Soliaga, K. Uosaki, and A. Wieckowski.
3. H. Tamura and K-I. Tanaka, Langmuir, 10 **(1994)** 4530.
4. H. Tamura, A. Sasahara, and K-I. Tanaka, J. Electroanal. Chem.,381 **(1995)** 95.
5. M. Taniguchi, E.K. Kuzembaev and K-I. Tanaka, Surf. Sci., 290 **(1993)** L711.
6. A. Sasahara, H. Tamura, and K-I. Tanaka, Catal. Lett., 28 **(1994)** 161.
7. K-I. Tanaka and A. Sasahara, Interfacial Electrochemistry, Chapt. 28, p 493–512. Ed. By A. Wieckowski, (ISBN: 0-8247-6000-x) Marcel Dekker, Inc., N.Y. and Basel **(1999)**.
8. K-I. Tanaka, Appl. Catal. A. General, 188 **(1999)** 37.
9. J. Siera, F.C.M.J.M. van Delft, A.D. van Langeveld, and B.E. Nieuwenhuys, Surf. Sci., 264 **(1992)** 435.
10. T.T. Tsong, D.M. Ren and M. Ahmad Phys. Rev. B38, **(1988)** 7428.
11. K-I. Tanaka, ACS Symposium Series 656 Solid-Liquid Electrochemical Interfaces, Chapter 18 **(1997)** 245–273. Edt. By G. Jerkiewicz, M. P. Soliaga, K. Uosaki, and A. Wieckowski.

12. Y. Matsumoto, Y. Okawa, T. Fujita and K-I. Tanaka, Surf, Sci. 355 **(1996)** 109.
13. T. Yamada, T. Misno, K-I. Tanaka, and Y. Murata, J. Vac. Sci. Technol. A 7(4) **(1989)** 2808.
14. A. Sasahara, H. Tamura, and K-I. Tanaka, J. Phys. Chem.,100 **(1996)** 15229.
15. H. Kita, S. Ye, A. Aramata, and N. Furuya, J. Electroanal. Chem.,295 **(1990)** 317.
16. K. Yamamoto, D. Kolb, R. Kotz, and G. Lehmpfuhl, J. Electroanal. Chem. 96 **(1979)** 233.
17. C.L. Scortichini, and C.N. Beilley, J. Electro. Chem., 139 **(1982)** 233.
18. Korotkikh D. Amand and J. Clavilier, J. Electroanal. Chem. 233 (1987) 251.
19. A. Sasahara, H. Tamura, and K-I. Tanaka, J. Phys. Chem., B 101 **(1997)** 1186.
20. K-I Tanaka and A. Sasahara, J. Molec. Catal, A Chemicals, 155 **(2009)** 13.
21. Y. Matsumoto, Y. Aibara, K. Mukai, K. Moriwaki, Y. Okawa, B.E. Nieuwenhuys and K-I. Tanaka, Surf. Sci. 377/379 **(1997)** 32.
22. C. Hardacre, R.M. Ormerod, R.M. Lambert, J. Phys. Chem.,98 **(1994)** 10901.
23. S.J. Tauster, S.C. Fung, and R.L. Garten, J. Am. Chem. Soc., 100 **(1978)** 170.
24. S. Surnev, J. Schoiswohl, G. Kresse, M.G. Ramsey, and F.P. Netzer, Phys. Lev. Lett., 89 **(2002)** 24610.

Chapter 10
Dynamic Chemical Processes in Catalysis

Abstract In conventional thinking, catalytic activity of metals is tacitly considered as an intrinsic property of metals such that Pt is active, but Au is inactive. On the other hand, we know experimentally and theoretically that the adsorption bond of molecules on metals takes perturbation of additives. Based on them, the role of promoting materials is so often explained by the term "synergetic effect" or "activation of metals," but this is awkward explanation as proved in "selective oxidation of CO in H_2 improved by H_2O" mentioned in Sect. 10.4. I could say that true mechanism of catalysis is difficult to deduce without clarifying the dynamics of chemical processes including the roles of active sites or active materials on the surface. One important strategy to make clear the mechanism of catalysis is how to remove unnecessary migration of intermediates on the surface during catalysis. One prominent example is the "hydrogenation of olefins" and simultaneously catalyzed isomerization of olefins. As proved in Sects. 10.1 and 10.2, the two reactions are evidently distinguished by preventing unnecessary migration of H atoms over the catalyst. Another example is the "selective oxidation of CO in H_2 improved by H_2O" on a Pt/CNT catalyst discussed in Sect. 10.4, on which the migration of OH^- ion from promoting materials to Pt and Au particles is indispensable process. "Metathesis reaction of olefins" is another type of dynamic processes as mentioned in Sect. 10.3. That is, the metathesis reaction of α-olefins (CH_2=CHR) is catalyzed by alternative reaction of olefin with two active intermediates, Mo=CH_2 and Mo=CHR. However, the hidden metathesis reaction named "degenerate metathesis" proceeds on each Mo=CH_2 and Mo=CHR sites. Interestingly, this degenerate metathesis of propene, CH_2=CH−CH_3 + CD_2=CD−CD_3 → CD_2=CH−CH_3 + CH_2=CD−CD_3, on the Mo=CH–CH_3 sites takes place 100–900 times more frequently compared to that on the Mo=CH_2 sites. These practical reactions prove that the catalysis cannot be rationalized without clarifying the dynamic chemical processes on the surface.

Keywords Isomerization reaction of olefins · Hydrogenation reaction of olefins · Olefin metathesis reaction · Preferential oxidation of CO in H_2 · Roles of promoting materials · Selectivity and activity · Role of H_2O as molecular catalyst · Intermediates · Rate-determining step

K. Tanaka, *Dynamic Chemical Processes on Solid Surfaces*,
DOI 10.1007/978-981-10-2839-7_10

10.1 Isomerization Reaction of Olefins

The hydrogenation and the isomerization reaction of olefins are simultaneously enhanced on metals by adding H_2, which has been explained by the existence of common alkyl intermediates as expressed by Eq. (10.1), as suggested by the Horiuti–Polanyi mechanism [1]. However, simultaneous enhancement of the two reactions by H_2 does not necessarily mean common alkyl intermediates in the two reactions, because step (ii) in Eq. (10.1) is indispensable for hydrogenation, but it is not required for olefin isomerization. Moreover, the reversibility of step (i) is required for the isomerization of olefins, but the reversibility is not required for olefin hydrogenation. This means that the function required for active sites may not be the same for hydrogenation and isomerization of olefins. In fact, as shown below, these two reactions are independently catalyzed on different active sites.

$$\begin{array}{l} CH_2{=}CH{-}CH_2{-}CH_3 + H(a) \xrightarrow{+\,(i)} \\ \qquad\qquad\qquad\qquad [CH_3{-}CH{-}CH_2{-}CH_3] \xrightarrow[(ii)]{+\,H(a)} CH_3{-}CH_2{-}CH_2{-}CH_3 \\ CH_3{-}CH{=}CH{-}CH_3 + H(a) \xleftarrow{-\,(i)} \end{array} \qquad \text{Eq. (10.1)}$$

If all chemical processes of a catalytic reaction are accomplished on an isolated active site, one can recognize the active site with a different function. However, if an intermediate undergoes rapid migration between the two sites, the difference of the two sites is erased. In other word, the roles of two sites could be distinguished if the migration of intermediates are regulated.

Based on this idea, the hydrogenation and the isomerization of olefins were studied on the MoS_2 catalyst [2, 3]. A MoS_2 surface heated in a vacuum has no activity for isomerization of but-1-ene at room temperature. If H_2 is added, however, the isomerization of but-1-ene to but-2-ene and the hydrogenation of but-1-ene to butane are simultaneously catalyzed, which looks to support the Horiuti–Polanyi mechanism. However, if D_2 was added instead of H_2, a notable result contradicting the Horiuti–Polanyi mechanism was attained, that is, the isomerization of but-1-ene produced merely but-2-ene-$[^2H]_0$ having no D atoms (deuterium atoms are described as $[^2H]$ in molecular formulas in this book), but the hydrogenation of but-1-ene yielded butane-1,2-$[^2H]_2$ as the main hydrogenated product [2, 3]. This result is evidently in conflict with the Horiuti–Polanyi mechanism given by Eq. (10.1). Interestingly, the hydrogenation of but-1-ene with a mixed gas of H_2 and D_2 on the MoS_2 catalyst provided butane-$[^2H]_0$ and butane-$[^2H]_2$, that is, no hydrogen isotope scrambling proceeds during hydrogenation reaction, although simultaneous isomerization yielded only but-2-ene-$[^2H]_0$. In the absence of but-1-ene, however, $H_2 + D_2 \rightleftharpoons HD$ isotopic equilibration was very rapidly established on the MoS_2, that is, the isotopic equilibration reaction of H_2 and D_2 was effectively disturbed by but-1-ene. If we compare these results on MoS_2 with the hydrogenation of but-1,3-diene with D_2 on a Cu catalyst, the hydrogenation of but-1,3-diene with D_2 on Cu catalysts yielded but-1-ene-$[^2H]_0$ [4], that

is, no D atoms were apparently involved in the hydrogenation product. In contrast, the hydrogenation of but-1,3-diene with D_2 on MoS_2 catalysts yielded predominantly but-1-ene-$[^2H]_2$ [5]. If the hydrogenation of but-1,3-diene proceeds via the sec-butenyl intermediate, the intermediate should be $CH_2D–*CH–CH=CH_2$ (*C is bonded to active site) on the MoS_2 catalyst, whereas the intermediate on the Cu catalyst should be $CH_3–*CH–CH=CH_2$ containing no D atoms. The difference is well explained by the dynamic behavior of intermediates on the two catalysts. Strong adsorption of but-1,3-diene retards the adsorption of D_2 on Cu surface, but the exchange reaction of small amount of adsorbed D(a) with large amount of adsorbed butadiene takes place rapidly via sec-butenyl intermediate. As a result, the hydrogenation of butadiene on the Cu catalyst predominantly proceeds with H(a) atoms. As a result, the hydrogenation of but-1,3-diene with D_2 on the Cu catalyst is actually the reaction of H(a) with but-1,3-diene via the $CH_3–*CH–CH=CH_2$ intermediate. On the other hand, the hydrogenation of but-1,3-diene on the MoS_2 catalyst proceeds on the active sites with D atoms by forming the $CH_2D–*CH–CH=CH_2$ intermediate as described below. It should be remembered that sec-butenyl is the reaction intermediate of the hydrogenation reaction of but-1,3-diene on either MoS_2 and Cu, but the dynamic behavior of adsorbed hydrogen is entirely different between Cu and MoS_2 surfaces, which is responsible for the difference between Cu and MoS_2 catalysts in the hydrogenation of but-1,3-diene with D_2. In other words, the different dynamic behavior of intermediates on the surface is responsible for the apparent difference of Cu and MoS_2 in catalysis.

From this point of view, we have to consider carefully the meaning of the result attained by using $^1H–(^{15}N, \alpha\gamma)^{12}C$ nuclear reaction analysis to discriminate between H atoms on or in the near-surface layers of Pd by Wilde et al. [6]. They explained the effect of impurity carbon on the isomerization and hydrogenation of but-1-ene on a $Pd–Al_2O_3/NiAl(110)$ catalyst by premising the Horiuti–Polanyi mechanism. It should be remembered that the different phenomena observed in catalysis do not necessarily mean the different functions of the Pd catalyst, but are caused by the different kinetic behaviors of H atoms in Pd. Similar confusion is very often observed regarding the role of promoting materials, which is caused by apparent kinetics or by providing new functions. Catalysis of Ni foil contaminated with S atoms instead of C atoms is an interesting example making clear the difference of the two mechanisms in catalysis.

The hydrogenation and isomerization of olefins are simultaneously catalyzed on Ni surface in the presence of H_2. If deuterium-labeled olefins are used, one can recognize the hydrogen scrambling of olefins enhanced in the presence of H_2 and simultaneously catalyzed equilibration of $H_2 + D_2 \rightleftharpoons 2\ HD$. If a Ni surface is contaminated with H_2S (S/Ni), the surface loses catalytic activity for the hydrogenation of olefins as well as for the $H_2–D_2$ equilibration reaction. However, the isomerization of but-1-ene to but-2-ene and hydrogen exchange among the olefins are catalyzed on the S/Ni surface in the presence of H_2, although no isotope equilibration of $H_2 + D_2 \rightleftharpoons 2\ HD$ occurs, as shown in Fig. 10.1b. That is, the S/Ni

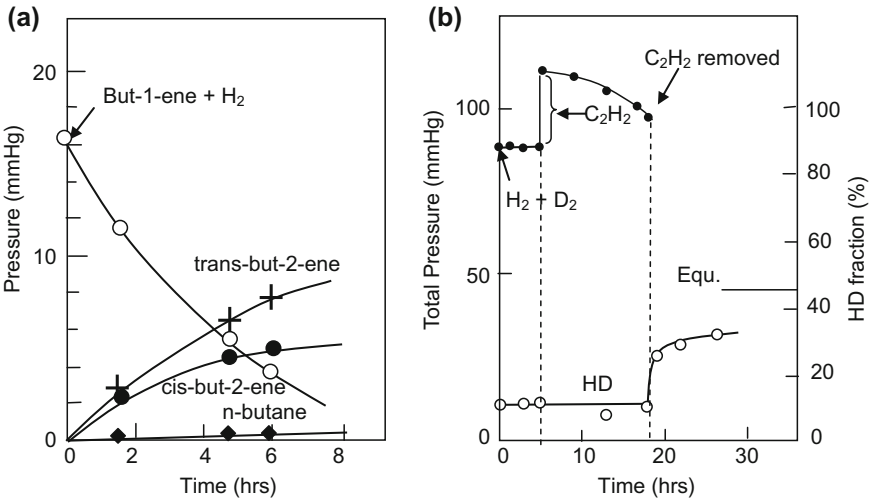

Fig. 10.1 **a** Isomerization of but-1-ene (16.3 mmHg) proceeds in the presence of H_2 (32.9 mmHg) but the hydrogenation of but-1-ene is very slow on a sulfided Ni surface at 394 K. **b** No H_2–D_2 (H_2/D_2 = 2/3) equilibration proceeds on a H_2S-treated Ni foil at 393 K. When the surface becomes active for the hydrogenation of acetylene with an induction time of 5.1 h, the surface also becomes active for H_2–D_2 equilibration as proved by removing acetylene at 18.0 h from the gas phase by trapping at liquid N_2 temperature, but the surface quickly loses its activity [7, 8]

surface is inactive for the $H_2 + D_2 \rightleftharpoons 2$ HD equilibration for 5 h, but this S/Ni catalyst catalyzes the hydrogen exchange reaction between but-1-ene-$[^2H]_0$ and but-1-ene-$[^2H]_8$ and the isomerization reaction of but-1-ene to but-2-ene in the presence of H_2 [7, 8].

From these results, we can deduce an important conclusion, that is, the S/Ni surface promotes the isomerization of but-1-ene to but-2-ene via sec-butyl intermediates and the hydrogen exchange of but-1-ene and but-2-ene via n-butyl and/or sec-butyl intermediates in the presence of H_2, but the S/Ni surface has no activity to promote the hydrogenation of but-1-ene and but-2-ene to butane, although the isomerization proceeds via butyl intermediates. Another important feature is that the isomerization of but-1-ene is catalyzed by adding D2 as shown in Fig. 10.1a, but but-2-ene formed by the isomerization of but-1-ene catalyzed in D_2 involves few D atoms. However, it was confirmed that the rapid hydrogen exchange of but-1-ene and but-2-ene via n-butyl and/or sec-butyl intermediates takes place in the presence of H2. The results suggest the existence of the two sites with different functions on the S/Ni surface, one is active for the isomerization and hydrogen exchange reaction of olefins via alkyl intermediates, but, these sites are inactive for the hydrogenation of olefins as well as for the $H_2 + D_2 \rightleftharpoons 2$ HD equilibration reaction and the hydrogen exchange of olefins with D_2, which are responsible for the two distinctive catalytic abilities of the S/Ni surface.

As mentioned above, the S/Ni surface is inactive for the hydrogenation of olefins. However, if an inactive S/Ni surface is exposed to CH≡CH (acetylene), the S/Ni surface gradually becomes active toward the hydrogenation of acetylene with H_2 or D_2 as shown in Fig. 10.1b, but no equilibration reaction of $H_2 + D_2 \rightarrow 2\,HD$ proceeds in the presence of acetylene. If the C_2H_2 was removed from reactant gas of ($C_2H_2 + H_2 + D_2$) by trapping C_2H_2 at liq. N_2 temperature, the $H_2 + D_2 \rightarrow 2\,HD$ was catalyzed for a time on the S/Ni surface as shown in Fig. 10.1b. From these experiments, we can conclude that the S/Ni surface that becomes active for the hydrogenation of acetylene is also active for the $H_2 + D_2 \rightleftharpoons 2\,HD$ equilibration, but the H_2–D_2 equilibration reaction is disturbed by the strong adsorption of acetylene on active sites. Therefore, if acetylene is removed from the gas phase, the H_2–D_2 equilibration reaction is catalyzed for a while, but the surface slowly reverts to the inactive surface in the absence of acetylene [7, 8]. This implies that an inactive S/Ni surface for the hydrogenation reaction and for the H_2–D_2 equilibration reaction becomes active by a reconstructive activation induced by the strong adsorption of acetylene. The reconstructed surface is unstable without the adsorbed acetylene, so that the surface reverts to the original inactive surface for the hydrogenation if acetylene is removed from the gas phase. From these results, we can derive the two important facts: (i) The S/Ni surface is inactive for the H_2–D_2 equilibration reaction and for the hydrogenation of acetylene and olefins but is active for the isomerization and hydrogen scrambling of olefins in the presence of H_2. (ii) The inactive S/Ni surface for the hydrogenation of acetylene and for the equilibration of $H_2 + D_2 \rightleftharpoons 2\,HD$ becomes active by a reversible reconstruction induced by the strong adsorption of acetylene. Accordingly, if acetylene is removed from the gas phase, the surface is active for the H_2–D_2 equilibration for a while at 393 K, but the surface gradually loses the activity for the hydrogenation reaction and is returned to the S/Ni surface being active only for the isomerization of olefins.

The results observed on the S/Ni surface suggest the local reconstruction of the Ni sites by the strong adsorption bond of acetylene with Ni atoms, and the reconstructed sites are active for the H_2–D_2 equilibration and for the hydrogenation of acetylene, that is, the S/Ni surface is labile during catalysis.

The idea of catalytic function controlled by the local conformation of sites was strictly proved on the MoS_2 single-crystal surface by Tanaka [2], that is, the function of active sites is well explained by the degree of coordinative vacancy of outcropped Mo sites on the flank of MoS_2. The evacuated MoS_2 surface has no catalytic activity for the isomerization of but-1-ene in the absence of H_2, but in the presence of H_2, the isomerization and hydrogenation of but-1-ene are catalyzed at room temperature (100 °C on single crystal, because of low surface area) as shown in Fig. 10.2, which is essentially different from the activation of the S/Ni surface shown in Fig. 10.1a. The isomerization of but-1-ene is catalyzed on the S/Ni surface with no induction time by the addition of H_2, but no hydrogenation reaction of but-1-ene occurred. However, this S/Ni surface becomes active for the hydrogenation of acetylene by the strong adsorption of acetylene, and the surface active for the hydrogenation reaction is also active for the H_2–D_2 equilibration, which is similar to the MoS_2 surface.

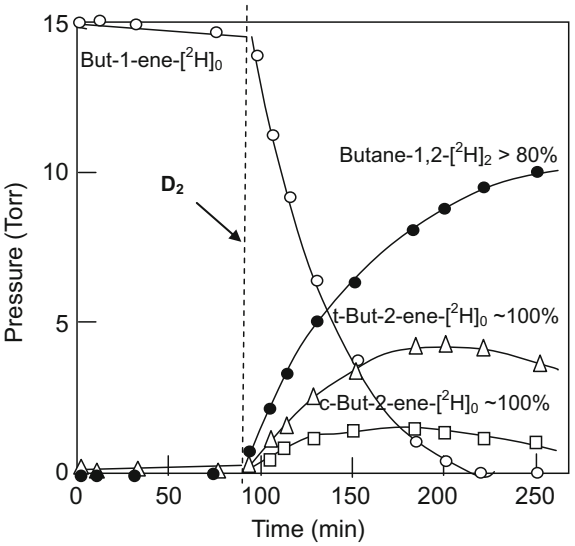

Fig. 10.2 The hydrogenation and isomerization of but-1-ene on MoS_2 enhanced by D_2 at room temperature. The isomerization reaction yields but-2-ene-$[^2H]_0$ (including no deuterium atoms), but the hydrogenation produces butane-1,2-$[^2H]_2$ in more than 80% yield [2, 9]

It is evident that the isomerization and hydrogenation of but-1-ene are catalyzed with no induction time on MoS_2 in the presence of H_2 or D_2. This simultaneous hydrogenation and isomerization reaction of olefins seemingly support the Horiuti–Polanyi mechanism via common butyl intermediates, but this traditional mechanism is evidently denied by using D_2. That is, the hydrogenation of but-1-ene with D_2 yielded butane-1,2-$[^2H]_2$ in more than 80%, which means the hydrogenation reaction proceeds via butyl-$[^2H]_1$ by more than 90% ($0.9 \times 0.9 = 0.81$) [2, 9]. However, the simultaneously taking place isomerization of but-1-ene formed but-2-ene involving no D atoms, which means the sec-butyl intermediate for the isomerization of but-1-ene contains no D atoms. The results are in clear contradiction to the Horiuti–Polanyi mechanism, that is, the hydrogenation and the isomerization of but-1-ene are catalyzed evidently via different alkyl intermediates on the MoS_2.

On the other hand, if a mixed gas of (2-methyl-but-1-ene + cis-but-2-ene) was admitted on an evacuated MoS_2 powder (fine crystals) with no H_2, no isomerization of cis-but-2-ene to trans-but-2-ene occurred, but the isomerization of 2-methyl-but-1-ene to 2-methyl-but-2-ene proceeded at room temperature, as shown in Fig. 10.4a. If H_2 was added to the mixture of (cis-but-2-ene + 2-methyl-but-1-ene) in the course of reaction, the isomerization of cis-but-2-ene to trans-but-2-ene was selectively enhanced, but the isomerization of 2-methyl-but-1-ene to 2-methyl-but-2-ene took no effect of H_2, as shown in Fig. 10.4a [2, 10]. From these results, we can deduce at least the three different catalytic reactions on the MoS_2 surface: one that is active for the double-bond shift isomerization of 2-methyl-but-1-ene without H_2, a second that is active for the double-bond shift isomerization of but-1-ene to but-2-ene and cis-to-trans isomerization of but-2-ene in the presence of H_2, and a third that is active for the hydrogenation of olefins with H_2.

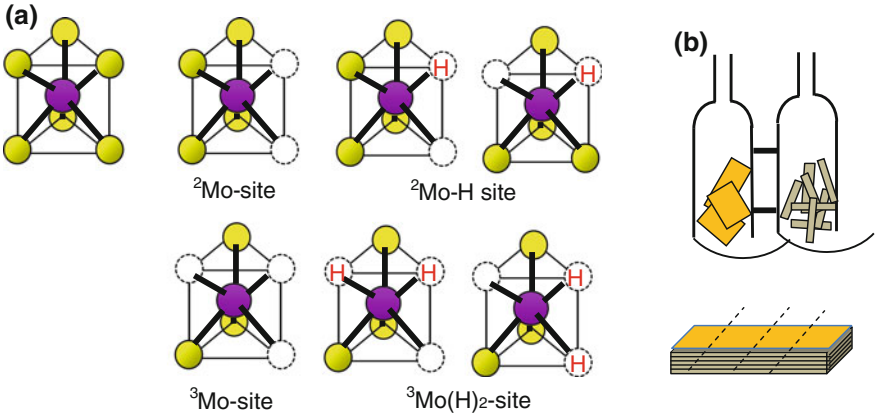

Fig. 10.3 **a** The prismatic structure of one Mo bonded with six sulfur atoms in MoS_2. Various forms of unsaturated Mo sites crop out on the flank of MoS_2 single-crystal wafers. **b** A twin reactor used to compare the catalytic activity of cut and uncut MoS_2 [9]

These functional sites that independently promote the corresponding reactions were clarified on single-crystal MoS_2, as described below in detail.

Crystalline MoS_2 has a lamellar stacking structure as described schematically in Fig. 10.3a, where the Mo^{4+}-ion is surrounded with six $S^{=}$-ions in hexagonal prismatic coordination (2-H structure). The basal plane of the MoS_2 crystal consists of a close-packed sulfur layer, and the outcropped Mo ions on the flank of the lamellar crystals have several types of coordinative vacancies. The coordinative vacancies on the Mo sites outcropped on the flank of lamellar crystals are schematically described by the prismatic models in Fig. 10.3a. The different coordinative vacancies are considered to be the origin of the two distinctive catalytic reactions of the MoS_2 surface. To clarify the location of active sites on the MoS_2 surface, the following three reactions were carried out by preparing two forms of MoS_2 single-crystal catalyst: One was thinly peeled MoS_2 wafers and the other was minced MoS_2 wafers. Equal weights of the two forms of MoS_2 crystal were put in a twin reactor such as shown in Fig. 10.3b.

TThe isomerization of cis-2-butene was performed on the MoS_2 single-crystal catalysts by using the twin reactor at 100 °C in the presence of H_2. As shown in Fig. 10.4b, the isomerization of cis-but-2-ene to trans-but-2-ene was catalyzed on the cut single-crystal MoS_2 (A) loaded in one of the twin reactors, but no appreciable isomerization of cis-but-2-ene was observed on the uncut MoS_2 (B) [9]. In contrast, the isomerization of 2-methyl-but-1-ene to 2-methyl-but-2-ene was catalyzed without H_2 at an equal rate on the cut and uncut MoS_2 wafers as shown in Fig. 10.4c, which proved that the isomerization of 2-methyl-but-1-ene takes place on the basal plane [2, 11]. Taking these results into account, it was concluded that H^+ ions (Brönsted acid) existing on the basal S plane of the MoS_2 wafer are responsible for the isomerization of 2-methyl-but-1-ene according to Eq. (10.2). The activity of the

H^+ ion (acidity) that exists on the basal plane is sufficient to form the tertiary cation, but it is not high enough to form the sec-butyl-cation, so that no isomerization of cis-but-2-ene occurs on the basal plane.

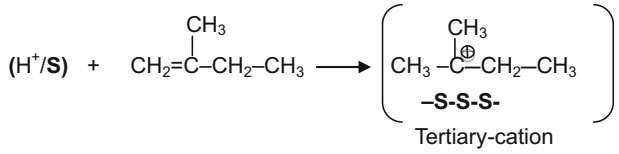

Eq. (10.2)

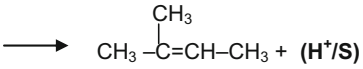

In contrast, the rotational isomerization of cis-but-2-ene to trans-but-2-ene and the double-bond shift isomerization of but-1-ene to but-2-ene, Eqs. (10.3i) and (10.3ii), were catalyzed in the presence of H_2 (or D_2) on the cut MoS_2 single crystals at 100 °C, as shown in Fig. 10.4b, d. It is noteworthy that the cis-to-trans isomerization of but-2-ene had about 1 h of induction time after the addition of H_2 as observed in Fig. 10.4b, and a similar induction time was also observed in the isomerization of but-1-ene to but-2-ene as shown in Fig. 10.4d. If the isomerization reaction takes place via sec-butyl intermediates as described by Eqs. (10.3i) and (10.3ii), the restricted rotations of intermediates correspond to the induction time as described by Eqs. (10.3i) and (10.3ii). The restricted rotation of the –CHD–CH_3 group in sec-butyl-$^2[H]_1$ in Eq. (10.3i), i.e., Fig. 10.4b, and the restricted rotation of the sec-butyl-$[^2H]_1$ intermediate on the Mo site in Eq. (10.3ii), i.e., Fig. 10.4d, are responsible for the induction time. These results evidently show the importance of dynamic motion of intermediates on active sites in catalysis.

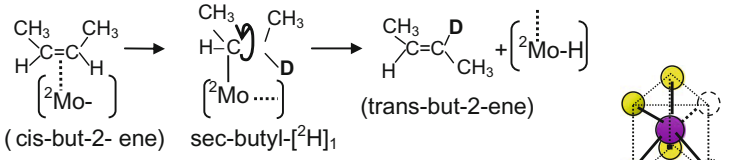

Eq. (10.3i)

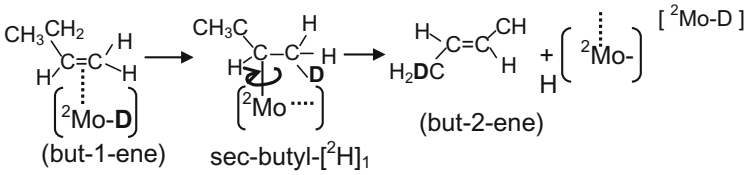

Eq. (10.3ii)

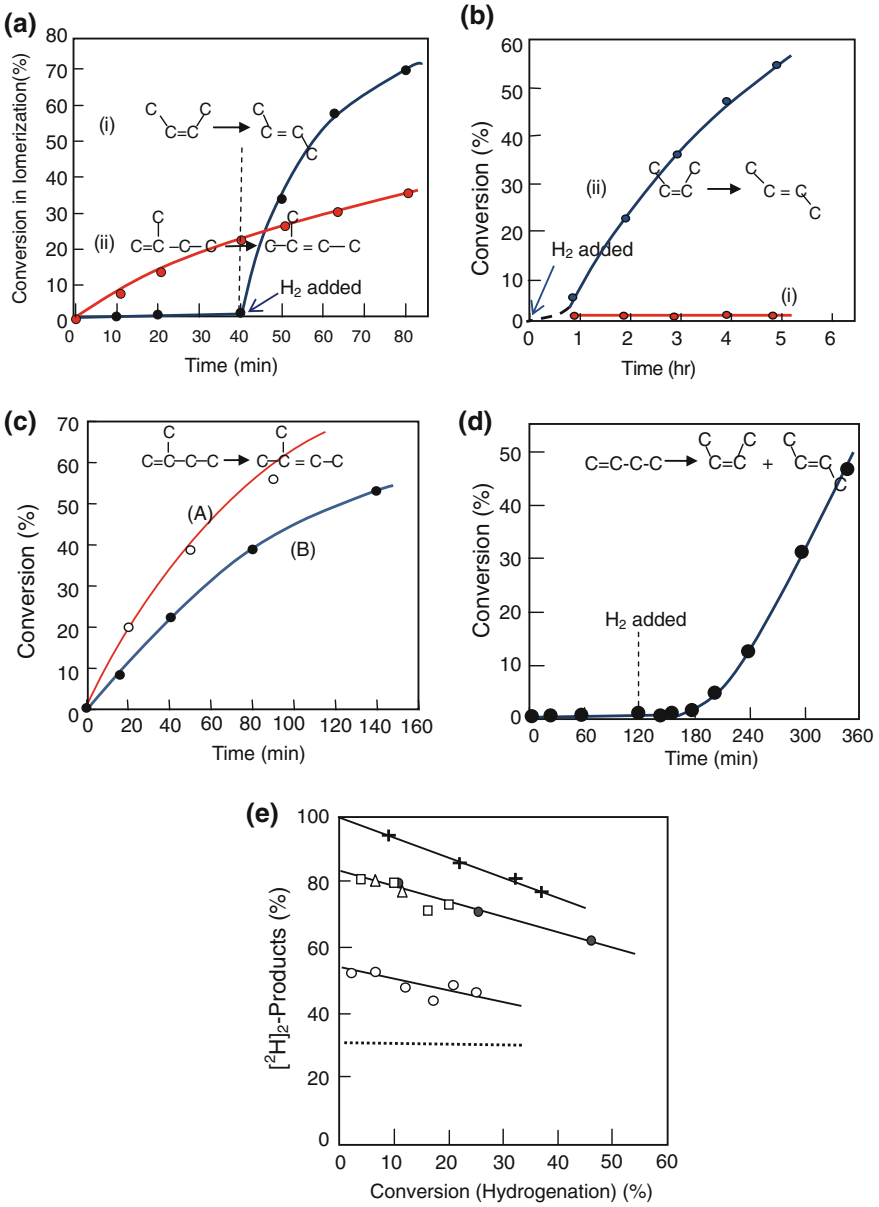
(a)
Conversion in Isomerization(%)
Time (min)
(i)
(ii)
H2 added
(b)
Conversion (%)
Time (hr)
(ii)
(i)
H2 added
(c)
Conversion (%)
Time (min)
(A)
(B)
(d)
Conversion (%)
Time (min)
H2 added
(e)
[2H]2-Products (%)
Conversion (Hydrogenation) (%)

◂**Fig. 10.4** **a** Isomerization of 2-methyl-but-1-ene to 2-methyl-but-2-ene (**O**) and cis-but-2-ene to trans-but-2-ene (●) on MoS_2 powder catalyst at room temperature. H_2 selectively enhances cis-to-trans isomerization of but-2-ene. **b** (i) Uncut MoS_2 single crystal is inactive at 100 °C, but (ii) cut MoS_2 single crystal becomes active for the isomerization of cis-2-butene with ca. 1-h induction time. **c** Cut MoS_2 (A) and uncut MoS_2 (B) crystals showed similar activity for the isomerization of 2-methyl-but-1-ene at 100 °C. **d** MoS_2 single crystal becomes active for the isomerization of but-1-ene (25 Torr) by adding H_2 (25 Torr) with a significant induction time (ca. 60 min) at 100 °C. **e** Molecular identity of D_2 was retained in the hydrogenation of olefins and but-1,3-diene on MoS_2 powder: but-1,3-diene (+), but-1-ene (Δ), cis-but-2-ene (□), and propene (●) at room temperature and ethylene (**O**) at 0 °C. Dotted line indicates the calculated value of ethane-$[^2H]_2$ when D atoms adopt an equilibrium distribution in ethylene [9, 11]

Dynamics of Intermediates in the Isomerization Reaction of Olefins on ^{2}Mo site: Rotational motion of sec-butyl intermediates on ^{2}Mo−D sites: (i) cis-to-trans isomerization of but-2-ene and (ii) but-1-ene to but-2-ene.

As described in Fig. 10.3a, outcropped Mo sites on the flank of MoS_2 crystals have different coordinative vacancies expressed as ^{2}Mo and ^{3}Mo sites, which have two and three coordinative vacancies. When MoS_2 is exposed to H_2, the ^{2}Mo and ^{3}Mo sites are quickly changed to ^{2}Mo–H and ^{3}Mo$(H)_2$ sites with no appreciable induction time, which is confirmed by the rapid equilibration of $H_2 + D_2 \rightleftharpoons 2$ HD with no appreciable induction time. As a result, alkyl intermediates are formed on these ^{2}Mo–H and ^{3}Mo$(H)_2$ sites with no induction time, and the hydrogen exchange reaction between C_2H_4 and C_2D_4 via ethyl intermediate ($-C_2H_4D$ or $-C_2D_4H$) takes place with no induction time. In contrast, a clear induction time (ca. 70 min.) was observed only in the isomerization of cis-but-2-ene to trans-but-2-ene in the reaction of ($C_2H_4 + C_2D_4$ + cis-but-2-ene + D_2), as shown in Fig. 10.5. The hydrogen exchange between C_2H_4 and C_2D_4 proceeds via ethyl intermediates (Mo–CH_2–CH_2D or Mo–CD_2–CD_2H), and the cis-to-trans isomerization of but-2-ene occurs via the sec-butyl intermediate (CH_3–*CH–C_2H_5, *C bonded to Mo); these two reactions proceed via alkyl intermediates on common active sites, but a significant induction time is observed only in the cis-to-trans isomerization of but-2-ene. That is, the hydrogen exchange between C_2H_4 and C_2D_4 requires rotation of $-CH_2D$ and $-CD_2H$ groups on the sites, and the cis-to-trans isomerization of but-2-ene requires rotation of the rather large $-C_2H_5$ group. In other words, the difference observed in the two reactions is due to the size of the rotating alkyl groups, either $-CH_3$ or $-C_2H_5$, as described by Eq. (10.3i).

As shown in Figs. 10.4b and 10.5, the cis-2-butene-to-trans-but-2-ene isomerization has an induction time of 60–70 min after the addition of H_2, and the but-1-ene-to-but-2-ene isomerization also has an induction time of ∼60 min (1 h) after the addition of H_2 at 100 °C, as shown in Fig. 10.2d. The difference between the two isomerization reactions is merely the effect of the size of the alkyl groups on rotation, as described by Eqs. (10.3i) and (10.3ii). When the cis-but-2-ene-to-trans-but-2-ene isomerization starts with a certain induction time, the hydrogen exchange reaction between C_2D_4 and cis-but-2-ene is concomitantly catalyzed. This result proves that the two reactions take place on the same active sites, but the rotational motion of the bulky butyl group is prevented during the induction time.

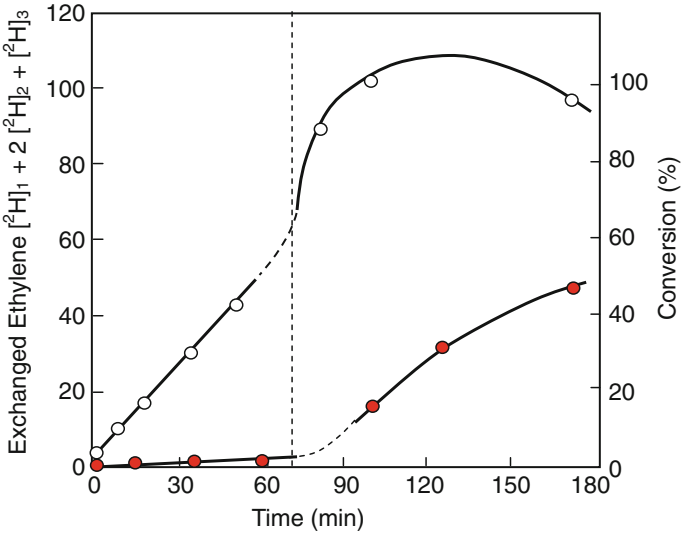

Fig. 10.5 Hydrogen exchange reaction observed in a mixture of (C_2H_4 + C_2D_4 + cis-but-2-ene-$^2H_0$ + D_2) on MoS_2 single-crystal catalyst at 100 °C. Hydrogen mixing between C_2H_4 and C_2D_4 occurs with no induction time, but the isomerization of cis-but-2-ene to trans-but-2-ene with hydrogen exchange has an induction time of about 1 h. When cis-to-trans isomerization of cis-but-2-ene is catalyzed, the hydrogen exchange between ethylene and but-2-ene is also enhanced. The total yield of the exchange reaction of ethylene (C_2H_3D + 2 $C_2H_2D_2$ + C_2HD_3) (**O**) is enhanced when the isomerization of cis-but-2-ene to trans-but-2-ene starts after an induction time (●) [9]

The rotational barrier for alkyl groups on the active sites may be lowered by a change of local conformation with coordination of alkyl intermediates. As a result, the cis-to-trans isomerization of but-2-ene and the hydrogen exchange reaction between but-2-ene and C_2D_4 exhibit the same induction time, as shown in Fig. 10.5. From these results, we can confidently conclude that the internal and external rotational motion of alkyl intermediates on active sites is an indispensable dynamic process in catalysis. The potential barrier for the rotational motion of bulky groups is lowered by the reconstruction of ^{2}Mo–H sites (alkyl–^{2}Mo sites), which provides more space for the rotation of bulky groups during the induction time, but the practical reconstruction process of the sites during the induction time is not clear at the present time.

Let us consider again the mechanism of the isomerization reaction of olefins on MoS_2. As described by Eq. (10.3i), cis-to-trans isomerization of but-2-ene requires the intramolecular rotation of the (–CH**D**CH_3) group on the (^{2}Mo–) sites, that is, neither the exchange of D atoms nor the cis-to-trans isomerization of cis-but-2-ene occurs if the rotation of the –CH**D**CH_3 group is prohibited on the (^{2}Mo–) site. The isomerization of but-1-ene to but-2-ene on the ^{2}Mo–D sites requires the rotation of the C_2H_5–*CH–C**D**H_2 intermediate on the (^{2}Mo–) site. In other words, the rotation

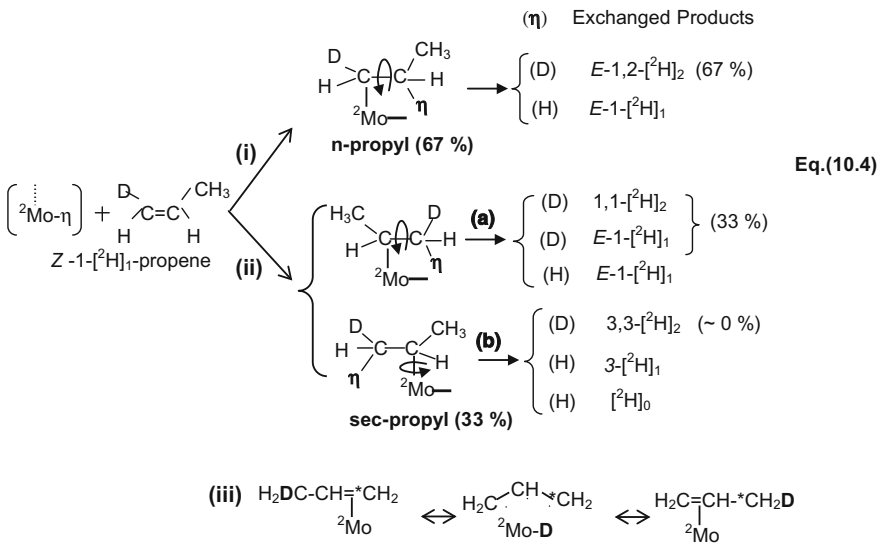

Scheme 10.1 Exchange mechanism of hydrogen in propene via n-propyl and sec-propyl on ^{2}Mo-η site (η = H or D) [2, 12, 13]

of the C_2H_5–*CH–C**D**H_2 intermediate on the (^{2}Mo–) site is indispensable for the double-bond shift of but-1-ene to but-2-ene, as shown in Eq. (10.3ii), where the D atom transferred from the (^{2}Mo–D) site to form C_2H_5–*CH–C**D**H_2 does not return to the (^{2}Mo–) site, so that the –C**D**H_2 group remains in the product molecule according to the reaction CH_2D–CH=CH–CH_3 + (^{2}Mo–H) as described in Eq. (10.3ii). Although direct detection of the rotational motion of molecules or intermediates during catalysis is improbable, one can recognize indispensable internal and/or external rotation of intermediates in catalysis by tracing the D atom ([^{2}H]) in the molecules as described by Eqs. (10.3i) and (10.3ii) (Scheme 10.1).

For this purpose, Z-1-[^{2}H]$_1$–propene was prepared by the hydrogenation of (CH_3–C≡CD) by shaking methyl acetylene (CH_3–C≡CH) in an alkaline D_2O solution. We can deduce the rotational dynamics of the "n-propyl intermediate," step (i), and "sec-propyl intermediate," step (ii), on the ^{2}Mo–η site (η is H or D) by the hydrogen exchange reaction between *Z*-1-[^{2}H]$_1$-propene and propene-[^{2}H]$_6$, as described in Eq. (10.4). Rotation of the $–C_2H_5$ group in step (i) of Eq. (10.4) and rotation of the $–CH_3$ group in step (ii)(a) in Eq. (10.4) are required processes for hydrogen exchange in olefins on the ^{2}Mo–H sites. It should be noted that the sec-propyl (CH_3–*CH–CH_3) itself has a symmetric structure, whereas the sec-propyl group bonded to the ^{2}Mo site is an asymmetric intermediate because of the unsymmetrical structure of the ^{2}Mo site. Therefore, sec-propyl bonded to the ^{2}Mo site should rotate in order to exchange the hydrogen of the two $–CH_3$ groups in the CH_3–*CH–CH_3 intermediate on the ^{2}Mo site, as shown by step (ii)(b) in Eq. (10.4). If the rotation of the sec-propyl intermediate around the σ-bond to the ^{2}Mo site is more rapid than the desorption rate of propene, the two $–CH_3$ groups in $(CH_3)_2$CH–^{2}Mo exhibit dynamic symmetry in the

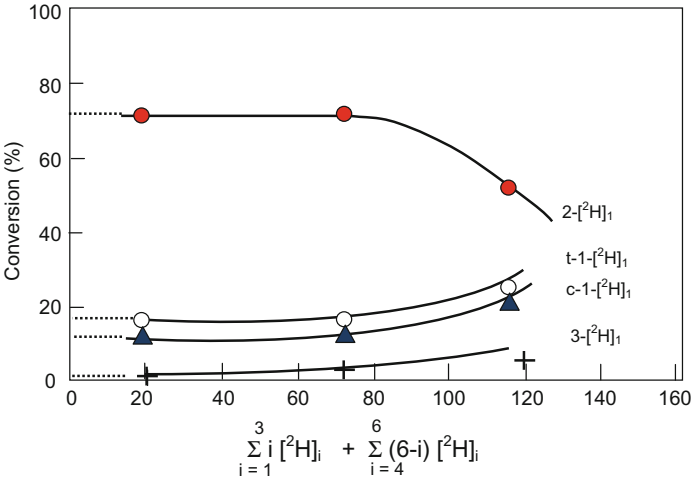

Fig. 10.6 Conformational isomers of D atom in propene-$[^2H]_1$ formed by hydrogen exchange in a (1 : 1) mixture of propene-$[^2H]_0$ and propene-$[^2H]_6$ in the presence of H_2 on MoS_2 at room temperature [13]

hydrogen exchange reaction of propene by step (ii)(b) in Eq. (10.4), and the statistical ratio of the hydrogen-exchanged propene is 1-$[^2H]_1$: 3-$[^2H]_1$ = (2/3 × 1/2) : (3/3 × 1/2) = 2 : 3.

Figure 10.6 shows the result of the hydrogen exchange reaction between propene-$[^2H]_6$ and propene-$[^2H]_0$. The ratio of (cis-1-$[^2H_1]$ + trans-1-$[^2H_1]$)/3-$[^2H]_1$ formed via an isopropyl intermediate is evidently different from the ratio 1-$[^2H]_1$/3-$[^2H]_1$ = 2/3 given by the rapid rotation of the isopropyl $(CH_3)_2CH–^2Mo$ intermediate, that is, propene-3-$[^2H]_1$: propene-1-$[^2H]_1$ = ∼1 : 33 as described in Eq. (10.4). That is, the two CH_3 groups in $(CH_3)_2CH–^2Mo$ are dynamically unsymmetrical on the ^2Mo site, which indicates that the rotational motion of $(CH_3)_2CH–$ is prohibited on the ^2Mo site.

The ratio of (propene-2-$[^2H_1]$)/(propene-1-$[^2H_1]$ + propene-3-$[^2H_1]$) = 67/33 ≈ 2/1 reflects the ratio of $C_2H_5–CH_2–^2Mo$ to $(CH_3)_2CH–^2Mo$ intermediates in the hydrogen exchange reaction (C_3H_6 + C_3D_6 + H_2) on the MoS_2 catalyst [12]. If the rotation of sec-propyl bonded to the ^2Mo site were free, the ratio of the 3-$[^2H]_1$ to the 1-$[^2H]_1$ would be 1 : 1, but the 3-$[^2H]_1$ to the 1-$[^2H]_1$ was nearly ∼1 : 33. This result indicates that the rotation of sec-propyl around the σ-bond to the ^2Mo site in step (ii)(b) in Eq. (10.4) is strongly hindered although the rotation of the $–CH_3$ group in step (ii)(a) in Eq. (10.4) is rapid. As a result, the intermolecular hydrogen exchange of propene forming 2-$[^2H_1]$ and 1-$[^2H_1]$ takes place rapidly, while intramolecular hydrogen exchange forming propene-3-$[^2H]_1$, step (iii) in Eq. (10.4), is rather slow on the ^2Mo sites [9, 12].

On the other hand, no hydrogen exchange occurs during hydrogenation of olefins on the $^3Mo(H)_2$ sites, which is clearly confirmed by the hydrogenation of but-1,3-diene with molecular HD via a σ-bonded butenyl intermediate. In this reaction, 3-$[^2H]_1$-but-1-ene and 4-$[^2H]_1$-but-1-ene were formed in the ratio 3-$[^2H]_1$/4-$[^2H]_1$ = 1.40 by the oriented addition of HD, which is very close to the hydrogen isotope effect observed in the hydrogenation of but-1,3-diene with $H_2 + D_2$. It is also evident that no intramolecular hydrogen transfer via σ-butenyl to π-allyl occurs on the ^3Mo site, as described by the step (iii) in Eq. (10.4) [10].

From the same perspective, the hydrogen exchange between propene-$[^2H]_6$ (CD_2=CD–CD_3) and but-1-ene-$[^2H]_0$ (CH_2=CH–C_2H_5) and also the hydrogen exchange between but-1-ene-$[^2H]_8$ and but-1-ene-$[^2H]_0$ were studied on a single-crystal MoS_2 catalyst at 100 °C. As shown in Table 10.1, the conformational isomers of propene-$[^1H]_1$ of CHD=CD–CD_3 and CD_2=CH–CD_3 adopt the ratio 1-$[^1H]_1$/2-$[^1H]_1$ = 27.4/63.7, and the ratio 1-$[^1H]_1$/2-$[^1H]_1$ of but-1-ene-$[^1H]_1$ (CHD=CD–C_2D_5/CD_2=CH–C_2D_5) exhibits the ratio 1-$[^2H]_1$/2-$[^2H]_1$ = 33.6/66.4 [11, 12]. The isomers of but-1-ene-$[^2H]_1$ formed by the hydrogen exchange reaction are in the ratio of 1-$[^2H]_1$/2-$[^2H]_1$ = 28.7/71.3 as shown in Table 10.2 [5], which is very close to the ratio of 1-$[^2H]_1$/2-$[^2H]_1$ = 33.6/66.4 obtained for but-1-ene-$[^2H]_1$ in Table 10.1 and 33/67 for propene-$[^2H]_1$ in Fig. 10.6. The ratio of n-alkyl-^2Mo to sec-alkyl-^2Mo evaluated by the hydrogen exchange reaction was almost equal for propene and but-1-ene. From these results, we can conclude that the adsorption of α-olefins (CH_2=CH–R) on the ^2Mo–H sites exhibits a common ratio of n-alkyl to sec-alkyl on the ^2Mo–H sites.

These results were the first experimental evidence proving the dynamic motion of intermediates on active sites is restricted by the conformation of active sites [2]. The rotational motion of intermediates on active sites is shown to be an indispensable process in catalysis. More strictly, the rotational dynamics of intermediates can be recognized when the desorption rate of product molecules is faster than the restricted rotational motion of intermediates as illustrated in Scheme 10.2, where the alkyl intermediates are on sites with anisotropic conformation.

Table 10.1 Conformational isomers of propene-$[^1H]_1$ and but-1-ene-$[^2H]_1$ formed by hydrogen exchange between propene-$[^2H]_6$ and but-1-ene-$[^2H]_0$ on single-crystal MoS_2 at 100 °C [11]

Propene-$[^2H]_5$ (%)	Propene-$[^1H]_1$			but-1-ene-$[^2H]_1$			
	1-$[^1H]_1$	2-$[^1H]_1$	3-$[^1H]_1$	1-$[^2H]_1$	2-$[^2H]_1$	3-$[^2H]_1$	4-$[^2H]_1$
26.7	27.4	63.7	8.9	33.6	66.4	0	0
43.8	36.5	57.0	6.5	47.9	52.1	0	0

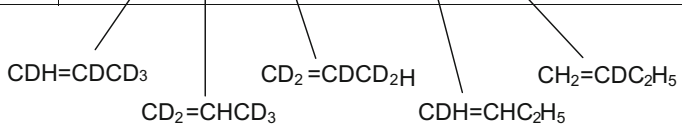

Table 10.2 Conformational isomers of but-1-ene-$[^2H]_1$ formed by hydrogen exchange between but-1-ene-$[^2H]_0$ and but-1-ene-$[^2H]_8$ on MoS_2 catalysts [12]

Catalysts	Time (min.)	Temp. (°C)	*Z*-1-$[^2H]_1$	*E*-1-$[^2H]_1$	2-$[^2H]_1$	3-$[^2H]_1$	4-$[^2H]_1$
Single Crystal	20	100	14.2	14.5	71.3	0	0
Powder	3	R.T.	15.9	16.0	68.1	0	0

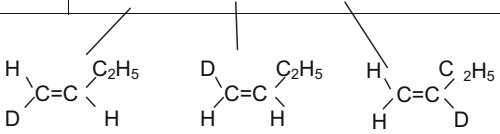

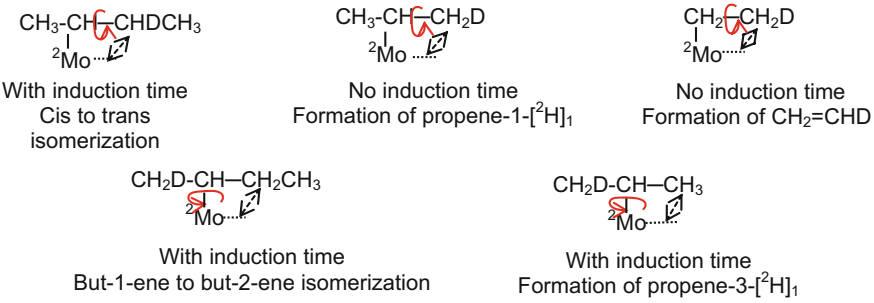

Scheme 10.2 Internal rotation of bulky group is hindered during induction time for the hydrogen exchange and isomerization of olefins. The hindered rotation may be released by the local reconstruction of sites during the induction time

Off-normal desorption of N_2 shown in Fig. 8.2 is an example of desorption of N_2 via $(N{\bullet\bullet}NO)^{\neq}$ with shorter life than the rotation.

As shown in this chapter, hydrogen exchange of olefins occurs by a cyclic working of the sites between ^{2}Mo-alkyl and ^{2}Mo–H sites with the adsorption and desorption of olefins. It should be noted that ^{2}Mo-alkyl cannot undergo further hydrogenation to alkane, because the H_2 molecule cannot dissociate on the ^{2}Mo-alkyl site. It should be emphasized that the ^{2}Mo–H site is also inactive for the H_2–D_2 equilibration reaction, because the ^{2}Mo–H site also has no ability to dissociate D_2 molecules. These phenomena are in marked contrast to the ^{3}Mo sites having one more coordination vacancy, as described in the next Sect. 10.2. The ^{3}Mo site changes to a $Mo(D)_2$ site on exposure to D_2, and alkyl-^{3}Mo–D is formed by the reaction with olefins, which then undergo further hydrogenation to form the corresponding alkane-$[^2H_2]$. It is noteworthy that the first step of the hydrogenation of adsorbed olefins on the $^3Mo(H)_2$ site is the formation of alkyl-^{3}Mo–H, which is rather irreversible, as described in more detail in the following chapter. The

rate-determining step of the formation of alkyl-^{3}Mo–H is responsible for the apparent irreversibility in olefin hydrogenation on the $^{3}Mo(H)_2$ sites. Therefore, it can be said that the Horiuti–Polanyi mechanism fails at least for the MoS_2 catalyst, even though olefin isomerization and hydrogenation are simultaneously catalyzed via alkyl intermediates on the MoS_2 catalyst. It should be realized that the two catalytic reactions have at least one different elementary process, which may require for their different functions in catalysis. In the case of isomerization and hydrogenation of olefins, the sites with two coordinative vacancies, ^{2}Mo–H sites, fulfill the required function for the isomerization of olefins, but the ^{2}Mo–H sites do not fulfill the required function for the hydrogenation of olefins and the H_2–D_2 equilibration reaction. If H atoms undergo rapid exchange between the ^{2}Mo sites and ^{3}Mo sites on the MoS_2 catalyst, however, the difference of these two sites is smeared, although the two sites independently contribute to the catalytic reactions, as discussed in more detail in Sect. 10.2.

10.2 Hydrogenation Reaction of Olefins

As it was mentioned in Sect. 10.1, MoS_2 surface evacuated at 450 °C has no catalytic activity for isomerization of but-1-ene in the absence of H_2, but the isomerization and the hydrogenation of but-1-ene are simultaneously catalyzed by adding H_2 as shown in Fig. 10.2. Simultaneous catalysis of the hydrogenation and isomerization of olefins does not mean the reaction via common alkyl intermediates. When an evacuated MoS_2 is exposed to H_2, ^{2}Mo–H and $^{3}Mo(H)_2$ sites are simultaneously formed on the edge of the MoS_2, but these two sites have different ability in catalysis. If unnecessary migration of H atoms is prohibited, one can distinguish the two sites in catalysis. According to this idea, the function of ^{2}Mo–H sites being different from that of $^{3}Mo(H)_2$ sites in catalysis was proved by using hydrogen isotope in Sect. 10.1.

This reasoning was conclusively proved by an experiment of the isotopic scrambling of hydrogen in (C_2H_4 + C_2D_4 + H_2 + D_2) performed on a MoS_2 catalyst treated with H_2S at 300 °C. By this treatment with H_2S, the population of ^{3}Mo sites for hydrogenation and H_2–D_2 equilibration reactions was decreased, and the rate of the two reactions, $C_2H_4 + C_2D_4 \rightarrow C_2H_3D + C_2D_3H$ and $H_2 + D_2 \rightarrow 2\ HD$, became comparable. One can clearly demonstrate the existence of the two types of active sites on the MoS_2 surface by the two isotope equilibration reactions simultaneously proceeding in a mixture of (C_2H_4 + C_2D_4 + H_2 + D_2), where the ratio was adjusted to C_2H_4/C_2D_4 = 3/2 (10 Torr) and H_2/D_2 = 2/3 (20 Torr). The D/H isotope ratio in hydrogen gas was adjusted to $^{D}\Phi_H$ = 3/5, and that in ethylene was $^{D}\Phi_E$ = 2/5 as shown in Fig. 10.7, so that the three different hydrogen isotope equilibration reactions, (i) C_2H_4/C_2D_4 ($^{D}\Phi_H$ = 2/5), (ii) H_2/D_2 ($^{D}\Phi_H$ = 3/5), and (iii) D_2/C_2H_4 or H_2/C_2D_4 in Eq. (10.5), were simultaneously monitored under the same conditions [14].

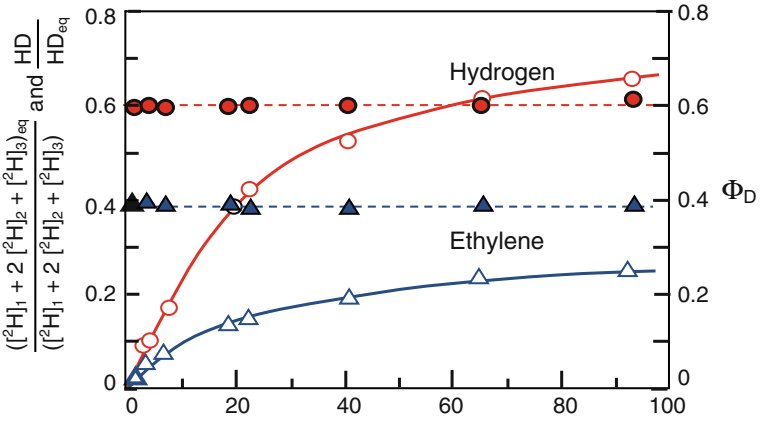

Fig. 10.7 Hydrogen scrambling in a mixture of (C_2H_4 + C_2D_4 + H_2 + D_2) taking place on an evacuated MoS_2 powder catalyst at room temperature, where the MoO_2 was pretreated with H_2S at 300 °C. The deuterium fraction in gas phase was adjusted to be Φ_D = 2/5 in ethylene (C_2H_4/C_2D_4 = 3/2) (▲) and Φ_D = 3/5 in hydrogen (H_2/D_2 = 2/3) (●). Isotope mixing proceeds in ethylene (△) and in hydrogen (○), but no hydrogen mixing occurs between hydrogen and ethylene (no change of Φ_D), which proves independent catalysis of $C_2H_4 + C_2D_4 \rightarrow C_2H_3D + C_2HD_3$ and $H_2 + D_2 \rightarrow 2\,HD$ on MoS_2 [14]

As shown in Fig. 10.7, the hydrogen exchange between C_2H_4 and C_2D_4, reaction (i), and the H_2–D_2 equilibration, reaction (ii), in Eq. (10.5) proceeded simultaneously on the MoS_2 catalyst, but the deuterium fraction ($^D\Phi_H$) in hydrogen and in ethylene, adjusted to $^D\Phi_E$ = 2/5 in ethylene and $^D\Phi_H$ = 3/5 in hydrogen, keeps the initial values of $^D\Phi_H$ without coming close to each other.

$$\begin{array}{lll} (\mathbf{i}) & C_2H_4 + C_2D_4 \rightarrow C_2H_3D + C_2D_3H & (^D\Phi_H = 2/5) \\ (\mathbf{ii}) & H_2 + D_2 \rightarrow 2HD & (^D\Phi_H = 3/5) \\ (\mathbf{iii}) & C_2H_4 + D_2 \rightarrow C_2H_3D + HD & \end{array} \qquad (10.5)$$

This result proves that the hydrogen exchange reaction between D_2 and ethylene (C_2H_4), reaction (iii), is very slow on this catalyst. That is, the hydrogen exchange between C_2H_4 and C_2D_4 and the isotope equilibration of H_2–D_2 are independently catalyzed on the catalyst, which strongly supports the existence of active sites with different functions as proposed by the ^{2}Mo–H and ^{3}Mo(H)$_2$ sites. The three catalytic reactions are selectively catalyzed on either ^{2}Mo–H or ^{3}Mo(H_2) sites as described schematically in Fig. 10.8.

When MoS_2 is exposed to D_2, the ^{2}Mo site changes to a ^{2}Mo–D site and the ^{3}Mo site changes to a ^{3}Mo(D)$_2$ site with no appreciable induction time. When an olefin molecule is isomerized on the ^{2}Mo–D site, the ^{2}Mo–D site is changed to ^{2}Mo–H by the first molecule isomerized on this site, and the subsequent isomerization of olefins is preferentially catalyzed on the ^{2}Mo–H sites instead of ^{2}Mo–D sites, because the hydrogen exchange of the ^{2}Mo–H site with D_2 is very slow. It should

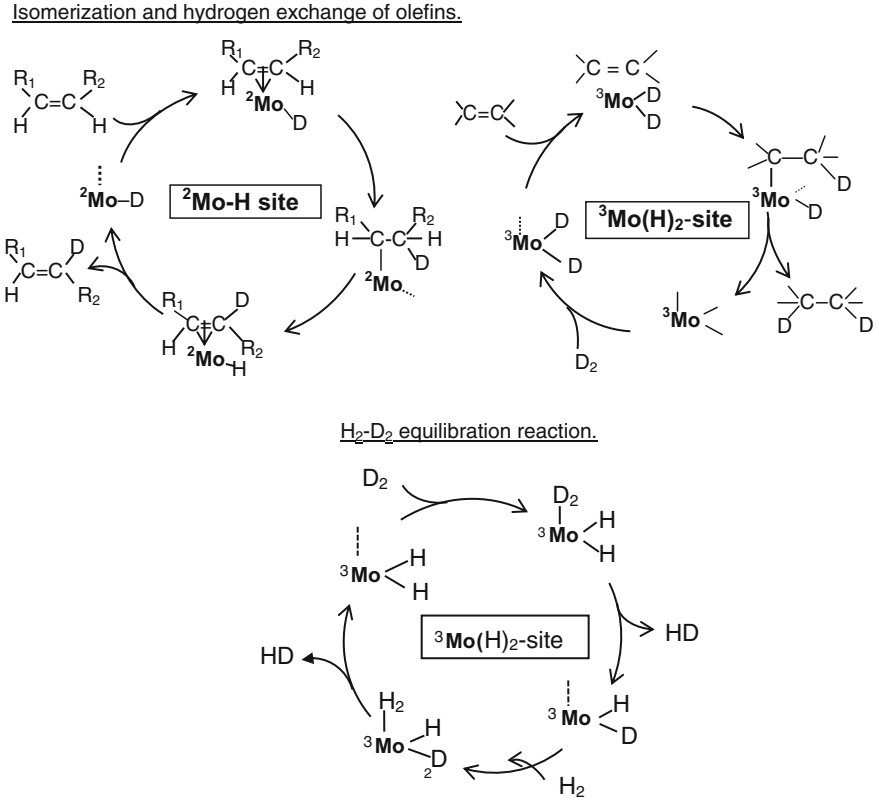

Fig. 10.8 The isomerization of olefins on the ^{2}Mo–H site is independent from the hydrogenation of olefins and the H_2–D_2 equilibration on the ^{3}Mo(H)$_2$ site [2]

be noted that if the H atoms undergo rapid exchange between the two different sites of ^{2}Mo–H and ^{3}Mo(H)$_2$, the reaction on the ^{2}Mo–H sites is difficult to distinguish from that on the ^{3}Mo(H)$_2$ in catalysis by using hydrogen isotopes. Fortunately, hydrogen scrambling among the ^{2}Mo–H and ^{3}Mo(D)$_2$ sites by surface diffusion or via reaction is very slow, so that the roles of ^{2}Mo–H and ^{3}Mo(D)$_2$ sites in catalysis are clearly differentiated by reaction using hydrogen isotopes. From these experiments, we learn the importance to remove the unnecessary migration of intermediates, and it may be attained by performing the reaction in the lower dimensional space (MoS_2 provides one-dimensional space). This idea will contribute again to solve the complex reaction mechanism in the oxidation of CO enhanced by H_2O by carbon nanotubes, pseudo one-dimensional material, in Sect. 10.4.

As mentioned in preceding Sect. 10.1, not only the chemical reactions but the dynamic motion of the intermediates, including the rotation and transport of intermediate, should be considered to understand the molecular mechanism of catalysis on the surface. The cis-to-trans isomerization and double-bond shift

isomerization of olefins catalyzed on the ^{2}Mo–H sites necessarily accompany the hydrogen exchange of olefins according to the reactions (i) and (ii) in Eq. (10.4). When an α-olefin such as but-1-ene (CH_2=CH–CH_2CH_3) or propene (CH_2=CH–CH_3) is adsorbed on a ^{2}Mo–H site, either "n-Alkyl-^{2}Mo" or "sec-Alkyl-^{2}Mo" is formed according to Eq. (10.4). As shown in Fig. 10.6 and Tables 10.1 and 10.2, the ratio of n-alkyl-^{2}Mo to sec-alkyl-^{2}Mo was experimentally determined to be ca. 7/3, that is, n-alkyl is preferred to sec-alkyl. This ratio reflects the relative population of n-alkyl to sec-alkyl in the hydrogen exchange reactions. The local conformation of ^{2}Mo–H sites (see MoS_2 models in Fig. 10.3) may determine the preferential form of an alkyl intermediate on the site, which is more evident in the hydrogenation of olefins on the ^{3}Mo site, as will be discussed below.

The intermediates of catalytic hydrogenation of α-olefins, either n-alkyl or sec-alkyl, had not been experimentally identified although preferential contribution of sec-alkyl was suggested by the calculation. Tanaka et al. proposed a new experimental method to identify the intermediates of the hydrogenation of α-olefins (CH_2=CH–R) and but-1,3-diene (CH_2=CH–CH=CH_2) by the orientation obtained in the addition of an HD molecule [11, 15, 16]. The orientation in the addition of HD is compared to the isotope effect in the hydrogenation of H_2 and D_2 in the hydrogenation of α-olefins (CH_2=CH–R), and we can deduce the intermediate on the $^{3}Mo(H)_2$ sites which is either the n-alkyl (*CH_2–CH_2–R) or sec-alkyl (CH_3–*CH–R) intermediate (*C is bonded to Mo). Scheme 10.3(i) and (ii) in Eq. (10.6) describes the hydrogenation of but-1,3-diene (CH_2=CH–CH=CH_2) via n-butenyl and sec-butenyl intermediates on the $^{3}MoH_2$ sites.

This new method was first applied to the hydrogenation of but-1,3-diene with HD, H_2, and D_2 on the MoS_2 catalyst [16], in which the molecular identity of HD, H_2, and D_2 was strictly retained, as shown in Fig. 10.9. As described in Eq. (10.6), the hydrogenation of but-1,3-diene (CH_2=CH–CH=CH_2) with HD yields either

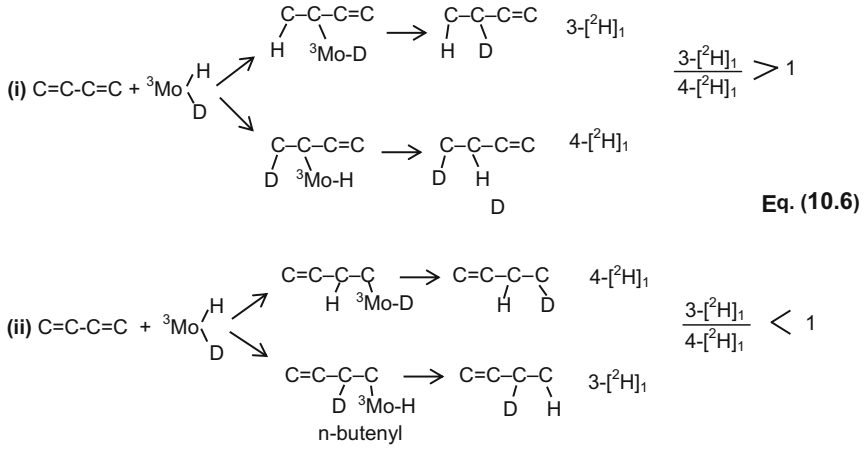

Scheme 10.3 Hydrogenation of but-1,3-diene with HD via n-butenyl and sec-butenyl intermediates on the ^{3}Mo site

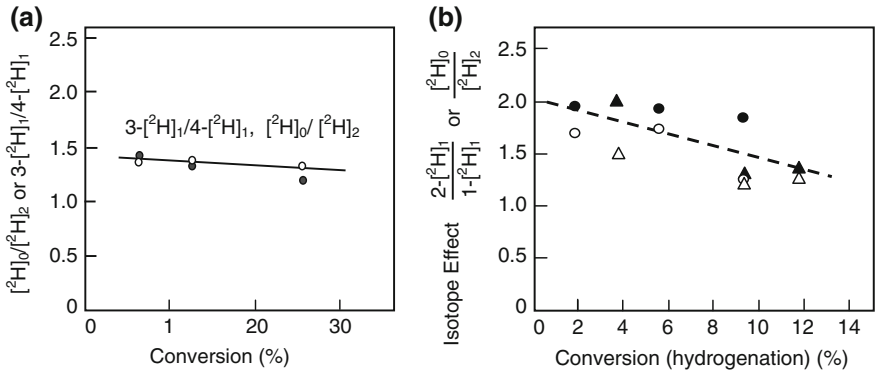

Fig. 10.9 **a** Isotope effect observed in the hydrogenation of but-1,3-diene with $H_2 + D_2$ on a MoS_2 catalyst (but-1-ene-$[^2H]_0$/but-1-ene $[^2H]_2$) (●), the orientation in the hydrogenation with HD molecule to but-1,3-diene, and the ratio (3-$[^2H]_1$/4-$[^2H]_1$) in but-1-ene-$[^2H]_1$ (◯) [16]. **b** Isotope effect observed in the hydrogenation of α-olefins (propene and but-1-ene) with $H_2 + D_2$, that is, propane-$[^2H]_0$/propane-$[^2H]_2$ (◯), butane-$[^2H]_0$/butane-$[^2H]_2$ (△), and the orientation in the addition of HD to α-olefins propane-2-$[^2H]_1$/propane-1-$[^2H]_1$ (▲) and butane-2-$[^2H]_1$/butane-1-$[^2H]_1$ (●) [17]

but-1-ene-3-$[^2H]_1$ or but-1-ene-4-$[^2H]_1$ depending on the intermediate (n-butenyl or sec-butenyl (σ-allyl)), where the orientation in the addition of HD to but-1,3-diene is decided by the first atom added to the but-1,3-diene on the ^{3}MoHD sites, which is either H or D. The ratio depends on the hydrogen isotope effect in the addition of H and D to α-olefins and but-1,3-diene (CH_2=CH–R and CH_2=CH–CH=CH_2) on the ^{3}MoHD sites. Therefore, the orientation in the addition of the HD molecule should be equal to the hydrogen isotope effect attained in the hydrogenation of α-olefins and but-1,3-diene with H_2 and D_2. As shown in Fig. 10.9a, but-1-ene-3-$[^2H]_1$ prevailed over the formation of but-1-ene-4-$[^2H]_1$ (3-$[^2H]_1$/4-$[^2H]_1$ > 1), and the ratio of 3-$[^2H]_1$/4-$[^2H]_1$ was equal to the isotope effect observed in the hydrogenation with H_2 and D_2, which strongly suggested that the hydrogenation of but-1,3-diene proceeds preferentially via the sec-butenyl intermediate as described by Eq. (10.7), and the hydrogenation of but-1,3-diene does not occur via σ-allyl (isobutenyl) to π-allyl conversion.

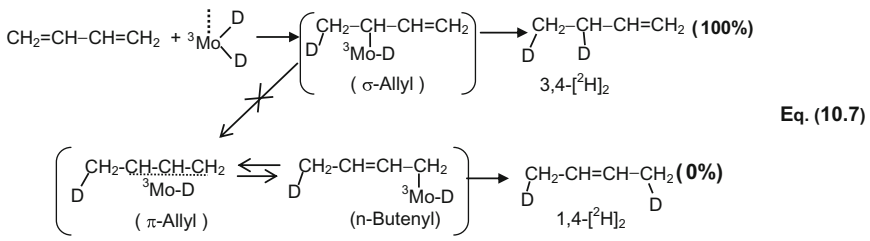

Eq. (10.7)

As shown in Fig. 10.4e, in the hydrogenation of α-olefins (CH_2=CH_2, CH_2=CH–CH_2, CH_2=CH–CH_2–CH_3) with D_2, the molecular identity of D_2 is retained by about 85%, except for ethylene. Taking these results into account, the intermediates were evaluated for the hydrogenation of α-olefins (CH_2=CH–CH_3, CH_2=CH–CH_2–CH_3), either n-alkyl, Eq. (10.8i), or sec-alkyl, Eq. (10.8ii), by hydrogenation with HD.

As described in Eqs. (10.8i) and (10.8ii), the first step on the ^{3}MoHD sites is the addition of either H or D to the olefin in the hydrogenation of α-olefins with HD, and the ratio of (2-[^{2}H]$_1$)/(1-[^{2}H]$_1$) is given by the isotope effect in the addition of H or D on the ^{3}MoHD sites. If the hydrogenation proceeds via the n-alkyl intermediate, the ratio (2-[^{2}H]$_1$)/(1-[^{2}H]$_1$) is less than 1, but if the hydrogenation proceeds via the sec-alkyl intermediate, the ratio (2-[^{2}H]$_1$)/(1-[^{2}H]$_1$) is larger than 1. As shown in Fig. 10.9b, the ratio of (alkane-2-[^{2}H]$_1$)/(alkane-1-[^{2}H]$_1$) is clearly >1 and is in good agreement with the isotope effect observed in the hydrogenation with H_2 and D_2, that is, the alkane-[^{2}H]$_0$ /alkane-[^{2}H]$_2$ ratio for the hydrogenation of propene and but-1-ene (CH_2=CH–CH_3 and CH_2=CH–CH_2–CH_3) with H_2 and D_2. Taking these results into account, we can conclude that the hydrogenation of α-olefins proceeds via sec-alkyl intermediates on the ^{3}Mo[H]$_2$ site [12, 13]. It should be remembered that the hydrogen exchange of α-olefins on the ^{2}Mo–H sites proceeds via both n-alkyl and sec-alkyl intermediates in a ratio of (n-alkyl/sec-alkyl) ≈ 7/3, the ratio of (i)–(ii) in Eq. (10.4) of Scheme 10.1, but the hydrogenation of α-olefins on the ^{3}Mo[H]$_2$ sites takes place solely via sec-alkyl intermediates. The ^{3}Mo[H]$_2$ site has more open space compared to the ^{2}Mo–H site, and this may favor the sec-alkyl intermediates on the ^{3}Mo[H]$_2$ sites. This phenomenon is quite similar to the ligand size effect observed in the reaction of nickel hydride, giving n-propyl over sec-propyl Ni-complexes in the dimerization reaction, by Wilke et al. [18].

The idea and method developed on the MoS_2 catalyst were applied to the hydrogenation of olefins and butadiene on oxides. It is known that evacuated oxides such as ZnO [19, 20], Cr_2O_3 [21], Co_3O_4 [22], ZrO_2 [23], ThO_2 [24], MgO [25], and CdO [26] are active for the isomerization and hydrogenation of olefins as well as for H_2–D_2 equilibration. The oxygen vacancies formed on the Cr_2O_3 and Co_3O_4 surfaces by evacuation or reduction were suggested to be the active sites, which might be similar to the ^{2}Mo- and ^{3}Mo-sites on the MoS_2 catalyst. However, the manner of dissociation of H_2 on such oxides as ZnO, MgO, and CdO is quite different from that on the Cr_2O_3 and Co_3O_4 and MoS_2. A typical case is the dissociation of H_2 on ZnO, on which H_2 undergoes dissociation not in a hemolytic manner but in a heterotic way into $H^{+\delta}$ and $H^{-\delta}$ as proved by Eischens et al. on ZnO by using infrared (IR) spectroscopy in 1962 [27]. They showed that dissociation of H_2 forms Zn–H (1712 cm^{-1}) and O–H (3490 cm^{-1}) on ZnO, and the intensity increased with H_2 pressure and saturated at 30–40 Torr. This was a groundbreaking work using IR spectroscopy, which led to the IR spectroscopy being used widely to study the adsorption and catalysis on solid surfaces.

The oriented dissociation of HD molecules on ZnO shown by Kokes et al. [28, 29] was one important result obtained by IR spectroscopy. They found unusual temperature-dependent orientation in the adsorption of HD molecules on ZnO. That is, the adsorption of HD molecule at room temperature prefers to take orientation-[**I**], whereas the adsorption at 233 K (–40 °C) prefers to take orientation-[**II**] described in Eq. (10.10). The temperature-dependent reversal orientation in the adsorption of HD on ZnO was explained by two different mechanisms, where one orientation is the kinetic orientation due to the adsorption rate and the other is determined by the adsorption equilibrium. The orientation of HD in the dissociation on ZnO at –40 °C is a kinetically favored orientation, whereas the orientation at room temperature reflects the adsorption equilibrium.

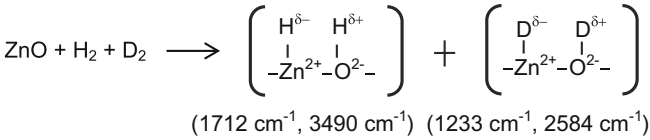

Eq. (10.9)

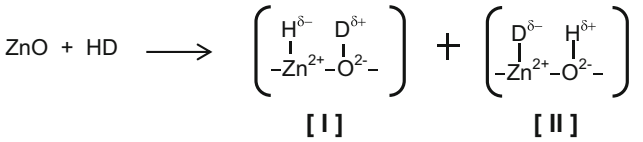

Eq. (10.10)

	[I]	[II]
Room temp.	75%	25%
–40 °C (233 K)	20–25%	80–75%

On the other hand, the hydrogenation of olefins with D_2 on ZnO selectively forms alkane-$[^2H]_2$, and the hydrogenation of but-1,3-diene with D_2 forms but-1-ene-$[^2H]_2$ with a small amount of but-2-ene-$[^2H]_2$. That is, the molecularity of the D_2 is preserved in the hydrogenation reaction. Taking this fact into account, Tanaka et al. [19] performed the hydrogenation of but-1,3-diene with an equilibrium mixture of (H_2 + D_2 + HD) (H_2 : HD : D_2 = 25.0 : 52.3 : 22.7) at room temperature and at –40 °C. The ratio of hydrogenated products (but-1-ene-$[^2H]_0$: but-1-ene-$[^2H]_1$: but-1-ene-$[^2H]_2$]) was almost equal to the ratio of H_2 : HD : D_2 as shown in Table 10.3. The ratio of (but-1-ene-$[^2H]_0$/but-1-ene-3,4-$[^2H]_2$) normalized by the ratio of H_2/D_2 took the value of unity, as shown in Fig. 10.10, that is, no hydrogen isotope effect was observed in the hydrogenation rate of but-1,3-diene with H_2, D_2, and D_2 molecules on ZnO, which is in marked contrast to the hydrogenation of but-1,3-diene on MoS_2. A small amount of but-2-ene simultaneously formed also had a similar deuterium distribution to that observed in but-1-ene.

However, the hydrogenation of but-1,3-diene with HD on ZnO clearly gave a temperature-independent orientation, that is, but-1-ene-3-$[^2H]_1$/but-1-ene-4-

Table 10.3 Hydrogenation of but-1,3-diene with H_2, D_2, and HD on ZnO at room temperature and −40 °C [19]

Temp. (°C)	Conv. (%)	Hydrogen gas H_2 HD D_2	Buat-1-ene $[^2H]_0$ $[^2H]_1$ $[^2H]_2$	cis-But-2-ene $[^2H]_0$ $[^2H]_1$ $[^2H]_2$
RT	5.7	25.0 52.3 22.7	23.2 55.4 21.4	30.8 50.6 18.5
RT	13.6	1.7 97.4 0.9	6.6 **91.0**(a) 2.3	13.1 83.3 3.6
-40°	5.6	1.7 97.7 0.6	3.5 **95.4**(b) 1.0	– – –

Temp.	CH_2=CH–CHD–CH_3	CH_2=CH–CH_2–CH_2D
R.T	75.4	24.6
- 40°C	75.2	24.8

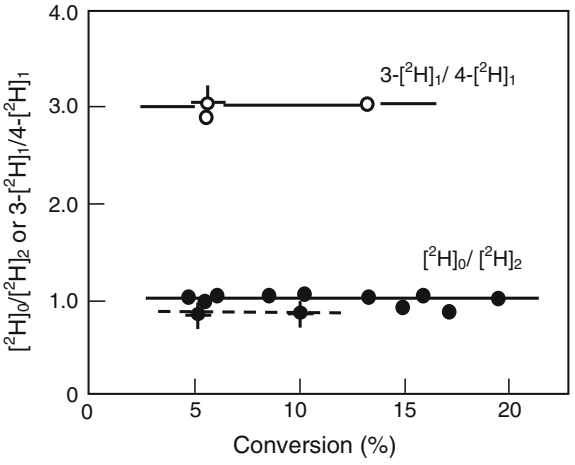

Fig. 10.10 Isotope effect in the hydrogenation of but-1,3-diene with H_2 + D_2 on ZnO catalyst ($[^2H]_0/[^2H]_2$) at room temperature (●) and −40 °C (⊕) and the orientation in addition of HD, forming but-1-ene-3-$[^2H]_1$ and but-1-ene-4-$[^2H]_1$ at 3 : 1 ratio at room temperature (⊖) and −40 °C (○) [19]

$[^2H]_1$ = 75/25 at room temperature and at –40 °C as shown in Table 10.3 and Fig. 10.10. This fact definitely indicates that the orientation observed in the hydrogenation of but-1,3-diene with HD is not due to the isotope effect in the reaction of H or D with but-1,3-diene, but is given by the orientation of the HD molecule adopted in its dissociation on ZnO, which should be the same at room temperature and –40 °C. Taking these results into account, the n-butenyl intermediate is formed by holding the orientation of the HD molecule on ZnO with adsorbed but-1,3-diene as described by Eq. (10.11i) [19], but not via sec-butenyl CH_2–*CH–CH=CH_2 : *C bonds to Zn or π-ally intermediates as shown in Eq. (10.11ii).

This mechanism is consistent with the kinetics in the hydrogenation of propene and but-1,3-diene on ZnO reported by Naito et al. [20]. They showed that the

hydrogenation of propene had a square root dependence on hydrogen pressure ($P_H^{1/2}$), whereas the hydrogenation of but-1,3-diene had a first-order dependence on hydrogen pressure and concluded that H_2 molecules reacted directly with adsorbed but-1,3-diene. However, as shown in Fig. 10.10, the hydrogenation of but-1,3-diene with H_2 and D_2 showed no isotope effect (but-1-ene-$[^2H]_0$/but-1-ene-$[^2H]_2$) = 1.0, but the hydrogenation with HD exhibited a marked orientation, with (but-1-ene-3-$[^2H]_1$/but-1-ene-4-$[^2H]_1$) = 3, which is similar to the orientation observed in the dissociation of HD on ZnO. Taking these results into account, the first-order dependence of the kinetics on H_2 pressure does not come from the direct reaction of H_2 molecules with adsorbed but-1,3-diene, but from the reactive dissociation of H_2 molecules on the ZnO surface followed by reaction with adsorbed but-1,3-diene.

(i) n-Butenyl (σ-Allyl) :

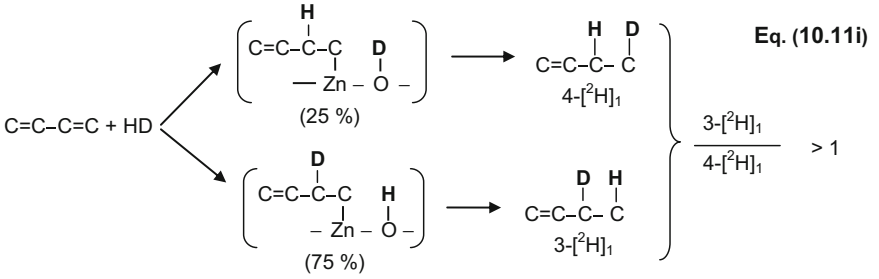

(ii) sec-Butenyl or π–Allyl :

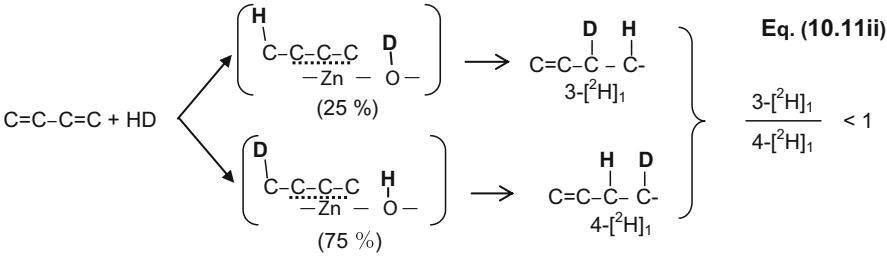

As has been discussed for MoS_2 and ZnO, the roles of the surface in catalysis are quite complex even in simple reactions such as H_2–D_2 equilibration, hydrogen exchange of olefins, isomerization of olefins, and hydrogenation of α-olefins, but-1,3-diene, and acetylene. Based on these findings, it is clearly necessary to

understand the dynamics of intermediates on active sites to achieve a proper understanding of catalysis. This problem will become more clear in the following sections (Sects. 10.3 and 10.4).

10.3 Metathesis Reaction of Olefins

In the preceding Sects. 10.1 and 10.2, the molecular mechanisms of catalysis were discussed from the viewpoint of the distinctive roles of active sites in the isomerization reaction of olefins and the hydrogenation reaction of olefins, acetylene, and but-1,3-diene on MoS_2 and ZnO. Flexible change of the conformation of active sites by the coordination of alkyl intermediates was suggested by the release of restricted intramolecular rotation of intermediates. In this Sect. 10.3, the "olefin metathesis reaction" catalyzed by alternative reaction of two alkylidene intermediates with olefin is discussed.

Olefin metathesis is a unique stoichiometric exchange reaction of alkylidene groups of olefins such as described by 2 CH_2=$CHCH_3$ → H_2C=CH_2 + CH_3CH=$CHCH_3$. Partly reduced or evacuated MoO_x, WO_x, and RuO_x are known to be active catalysts for the olefin metathesis reaction. This reaction was first found by Banks and Bailey on MoO_x [30], and was named as the tri-olefin process. As shown by Eq. (10.12), this reaction is an exchange reaction of alkylidene groups of olefin molecules, 2 R^1CH=CHR^2 → R^1CH=CHR^1 + R^2CH=CHR^2.

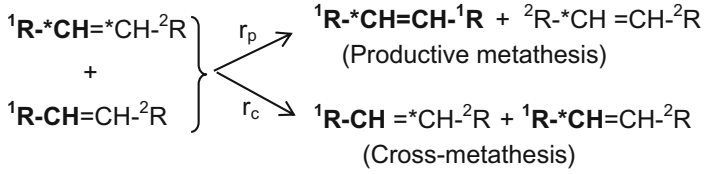

Eq. (10.12)

A key feature of this reaction is the operation of a set of two active sites, Mo=**CHR^1** (Mo=*CH_2) and Mo=**CHR^2**, (Mo=CH−*CH_3) as described in Scheme 10.5, where R^1CH=CHR^2 reacts alternately with a set of the two sites. In the case of ethylene, the reaction of CH_2=CH_2 + CD_2=CD_2 → 2 CH_2=CD_2 takes place with the formation of a set of Mo=**CH_2** and Mo=**CD_2**. As described by Eq. (10.12), the olefin metathesis reaction necessarily comprises the two reactions the so-called productive metathesis **(r_p)** and cross-metathesis **(r_c)**. However, the cross-metathesis **(r_c)** is usually ignored because the product olefins are the same as the reactant olefins. The cross-metathesis can be recognized only by using isotope-labeled olefins as designated with the asterisked carbon (*C) in Eq. (10.12). To understand the molecular mechanism of olefin metathesis, we have to study not only the productive metathesis but also the cross-metathesis as described in this chapter.

(i) n-Alkyl Intermediate:

Eq. (10.8i)

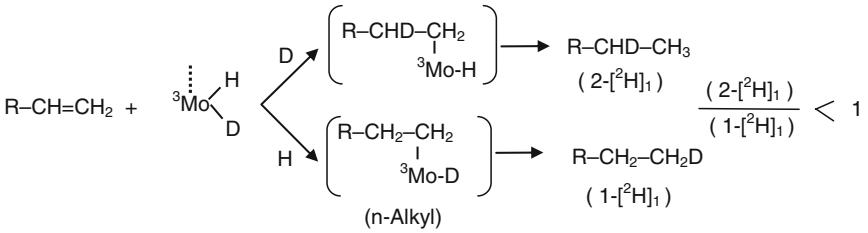

(ii) sec-Alkyl Intermediate:

Eq. (10.8ii)

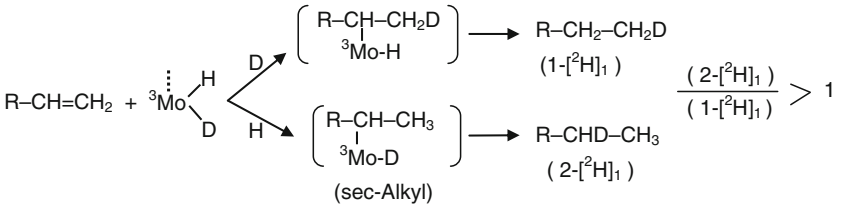

Scheme 10.4 Hydrogenation of α-olefins with HD. (i) n-butyl and (ii) sec-butenyl intermediates on the ^{3}Mo site

The molecular mechanism for olefin metathesis was settled by advances in the metal-alkylidene chemistry of W, Ti, Mo, and Ru metals. Chauvin [31] suggested the metallacyclobutane mechanism for olefin metathesis using metal-alkylidenes. As described in detail below, the overall metathesis reaction is composed of two catalytic reaction cycles, cycle-I and cycle-II, as shown in Scheme 10.5, where cycle-I corresponds to productive metathesis and cycle-II corresponds to cross-metathesis. The productive metathesis is given by the alternating reaction of the two alkylidene complexes with reactant olefin molecules as described by cycle-I. In contrast, the cross-metathesis occurs by reproducing the same alkylidene complexes in cycle-II.

Kress et al. [33] monitored the reactivity of the alkylidene complex $(L_2)(Br_2)$W=CHR (L is Bu^tCH_2O–) with cis–Me–CH=CH–Et by using in situ NMR spectroscopy, as shown in Fig. 10.11a. They showed that the $(L_2)(Br_2)$W=CHR complex was inactive for reaction with cis–Me–CH=CH–Et, but changed to being active if the $(L_2)(Br_2)$W=CHR complex formed a bond at X in Fig. 10.11b with $AlBr_3$ as shown by (2) and (4). That is, $AlBr_3$ exerts a strong effect on the reactivity of metal-alkylidene complexes with olefins, the W=CHR complex changes to W=CHMe and W=CHEt by reacting with cis–Me–CH=CH–Et, and the ratio of (W=CHEt)/(W=CHMe) = 4 was observed. That is, W=CHMe is more reactive than W=CHEt, where the total amount of W=CHMe + W=CHEt should be constant during the reaction, and the NMR spectra in Fig. 10.11a indicate the relative

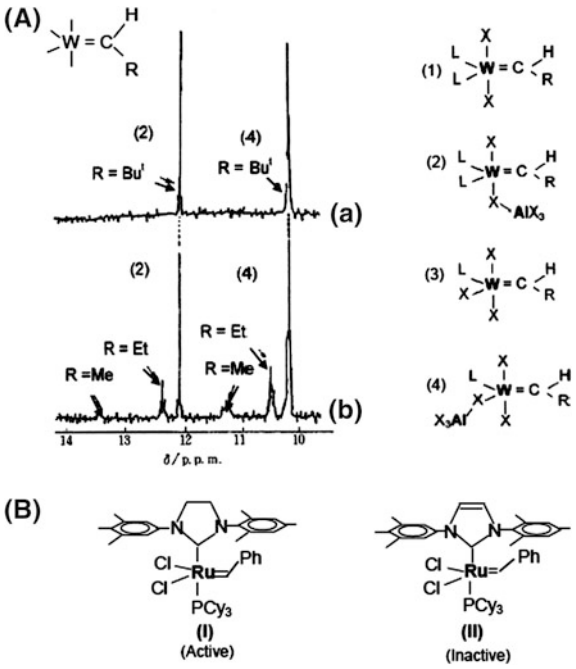

Fig. 10.11 **a** NMR spectra showing the reaction of $(L_2)(X_2)W{=}CHR$ complex with cis-$CH_3CH{=}CHEt$ at 268 K (mixture of (2) + (4) = 1 : 1). The $(L_2)(X_2)W{=}CHR$ becomes active by bonding with AlX_3, and W=CHMe and W=CHEt are formed in the ratio of 1 : 4. L=Bu^tCH_2O and X=Br [33]. **b** Ru=CHPh complex **(I)** is extremely active for the olefin metathesis reaction [34], but Ru=CHPh complex **(II)** with similar ligands has no catalytic activity [35]

reactivity of W=CHMe and W=CHEt with cis-Me–CH=CH–Me. From this viewpoint, it is quite revealing that a complex Ru=CHPh, complex-(I), known as the Grubbs catalyst [34] shown in Fig. 10.11b is extremely active, whereas the very similar complex-(II) synthesized by Nolan [35] has no catalytic activity for the olefin metathesis reaction. This fact indicates that reaction rate of olefins with metallacyclobutanes depends markedly on the labile structure of the metal-alkylidene with olefins. As is known from the reaction equation, olefin metathesis has a very small enthalpy change. That is, the population of W=CHMe and W=CHEt during reaction depends on the kinetic balance of the formation of metallacyclobutane intermediates and their decomposition reaction forming olefins.

In contrast to the highly variable activity of metal-alkylidene complexes depending on the ligands, the facile activity of oxides is a prominent advantage of heterogeneous catalysts, which can be attained by evacuation or partial reduction of some oxides at a suitable temperature. For example, MoO_x, WO_x, and RuO_x become active for olefin metathesis upon evacuation or by slight reduction with H_2 at moderate temperatures. As described below, controlled reduction of MoO_x/β-TiO_2 at 200 °C generates a catalyst that is active for olefin metathesis but inactive

toward the hydrogen scrambling of olefins [36]. Discovery of this catalyst has enabled us to study the mechanism of the degenerate olefin metathesis reaction by using deuterium-labeled olefins.

If Mo=CHR sites are formed on a MoO_x surface by exposure to some olefins, the surface becomes active for the olefin metathesis reaction, which is similar to the activation of the MoS_2 surface with the formation of ^{2}MoH and $^3MoH_2$ sites by exposure to H_2. The requirements for the formation of active Mo=CHR sites on the MoO_x surface by reaction with olefins are not clear, but if active Mo=CHR sites are synthesized on a passive MoO_x surface, the surface will be active only for the olefin metathesis reaction. This expectation was successfully confirmed on a MoO_3 film sublimated on a Pyrex glass reactor tube (~900 ML) prepared by heating a Mo filament in 0.2 Torr of O_2 [37]. By heating a Mo filament in O_2, MoO_3 was sublimated on the glass wall. The MoO_3-film prepared on the glass tube was cooled to liquid N_2 temperature and exposed to H atoms for 5 min (the H atoms were prepared by thermal dissociation of H_2 (0.3 Torr) on a hot Mo filament). The MoO_3 and/or MoO_{3-x} film prepared by this procedure was inactive for the metathesis reaction of propene at room temperature, as shown in Fig. 10.12a. However, if

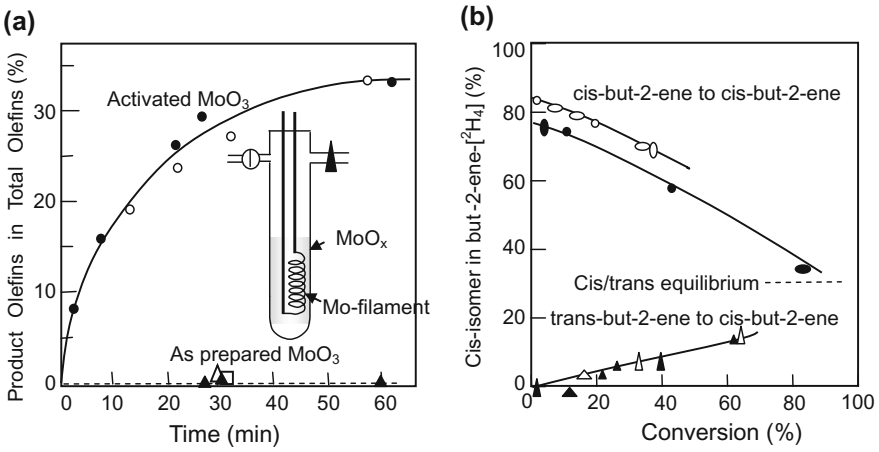

Fig. 10.12 **a** Metathesis reaction of propene (3 Torr) on a MoO_3 film sublimated on the wall of glass tube by flashing a Mo filament in O_2 at room temperature. As-prepared fresh MoO_3 film (▲) and MoO_{3-x} film treated with H_2 at liq. N_2 temperature (□) and 450 °C (△) showing no reaction. The MoO_{3-x} film was changed to a highly active catalyst for the metathesis reaction by the following treatment; ethylene (●) or propene (○) was condensed on the MoO_{3-x} film at liq. N_2 temperature and was followed by treating with H atoms at liq. N_2 temperature [37]. **b** Fraction of cis-but-2-ene-$[^2H]_4$ in the metathesis of (cis-but-2-ene-$[^2H]_0$ + cis-but-2-ene-$[^2H]_8$) and trans-but-2-ene-$[^2H]_4$ in the metathesis of (trans-but-2-ene-$[^2H]_0$ + trans-but-2-ene-$[^2H]_8$) (1 : 1 mixture) on MoO_3/β-TiO_2 (open symbols) and MoO_3/β-TiO_2 (solid symbols) activated with Sn $(CH_3)_3$. Retention of cis-to-cis conformation is ~80% (▲, △) and that of trans-to-trans conformation is ~100% (○, ●) (graph shows no trans-to-cis) in the initial conversion [38]

0.01 Torr of alkene (ethylene, propene, but-1-ene, or isobutene) was condensed on this inactive MoO_3 or MoO_{3-x} film at liq. N_2 temperature and then exposed to H atoms made by thermal dissociation of H_2 on the Mo filament for 3 min and then followed by evacuation at room temperature, the inactive MoO_3 and MoO_{3-x} films ((MoO_3: TF = 6×10^{-4} and MoO_{3-x}: TF = 3×10^{-3}) became highly active olefin metathesis catalysts as shown in Fig. 10.12a, and the turnover frequency was evaluated as TF = 0.5–0.6 (surprisingly high) at room temperature. By this activation procedure with H atoms, the activity for the olefin metathesis reaction was enhanced thousand-fold, but no appreciable hydrogen scrambling and/or isomerization of olefins (alkenes) occurred on this surface.

From this experiment, we deduced that Mo=CHR sites are selectively formed on the MoO_3 and MoO_{3-x} surfaces by the reaction with alkyls at liq. N_2 temperature. This activation process is described below, where the D atom is provided by the dissociation of D_2 on a hot Mo filament.

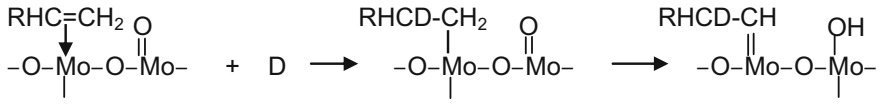

From this activation of condensed olefin with H atoms, a new activation method of the MoO_3 surface was conceived. One is to provide CH_3 radicals on the MoO_3 surface by the dissociation of $Sn(CH_3)_3$, and another is the reaction of adsorbed CH_2I_2 with Al or Mg atoms vaporized on the MoO_3 surface [39]. A completely oxidized inactive MoO_3/TiO_2 surface was changed to an extremely active catalyst, for the metathesis reaction by the adsorption of $Sn(CH_3)_3$ or by the reaction of adsorbed CH_2I_2 with evaporated Al or Mg.

The newly developed catalysts have superior activity for olefin metathesis, but are inactive for isomerization and hydrogen scrambling of olefins. Accordingly, we can evaluate the ratio of productive metathesis **(r_p)** to the cross-metathesis **(r_c)** of propene by using deuterium labeled propene as described by Eqs. (10.13i) and (10.3ii).

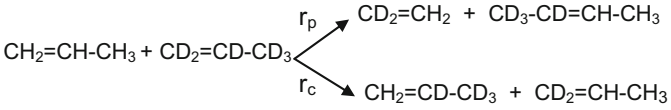

Eq. (10.13i)

Productive Metathesis of Propene; $R_p = (r_p\text{-}1) + 2\,(r_p\text{-}2) + (r_p\text{-}3)$:

(1) $CH_2{=}CH\text{-}CH_3 + CH_2{=}CH\text{-}CH_3 \rightarrow CH_2{=}CH_2 + \text{But-2-ene-}^2H_0$ **r_p-(1)**

(2) $CH_2{=}CH\text{-}CH_3 + CD_2{=}CD\text{-}CD_3 \rightarrow CD_2{=}CH_2 + \text{But-2-ene-}^2H_4$ 2 x **r_p-(2)**

(3) $CD_2{=}CD\text{-}CD_3 + CD_2{=}CD\text{-}CD \rightarrow CD_2{=}CD_2 + \text{But-2-ene-}^2H_8$ **r_p-(3)**

Cross-Metathesis of Propene; $R_c = r_c(1) + 2\,r_c(2) + r_c(3)$:

(1) $CH_2{=}CH\text{-}CH_3 + {*}CH_2{=}{*}CH\text{-}{*}CH_3 \rightarrow CH_2{=}{*}CH\text{-}{*}CH_3 + {*}CH_2{=}CH\text{-}CH_3$ **r_c-(1)**

(2) $CH_2{=}CH\text{-}CH_3 + CD_2{=}CD\text{-}CD_3 \rightarrow CH_2{=}CH\text{-}CH_3 + CD_2{=}CD\text{-}CD_3$ 2x **r_c-(2)**

(3) $CD_2{=}CD\text{-}CD_3 + {*}CD_2{=}{*}CD\text{-}{*}CD_3 \rightarrow CD_2{=}{*}CD\text{-}{*}CD_3 + {*}CD_2{=}CD\text{-}CD_3$ **r_c-(3)**

Eq. (10.13ii)

As described by Eq. (10.13i), the productive metathesis reaction taking place in a 1 : 1 mixture of C_3H_6 and C_3D_6 involves the four metathesis reactions, **r_p-(1)**, 2 × **r_p-(2)**, and **r_p-(3)**. If the hydrogen isotope effect is ignored, the four reactions proceed at an equal rate. Therefore, the overall rate of the productive metathesis reaction **(R_p)** is four times any one reaction rate in Eq. (10.13i), $\mathbf{R_p} = 4 \times \mathbf{r_p}\text{-(1)}$. At the same time, the four cross-metathesis reactions are composed of the two cross-metathesis reactions of **(r_c-1)** and **(r_c-3)** and the two self-crossing metatheses of **(r_c-2)** as described in Eq. (10.13ii). If the hydrogen isotope effect is ignored, these four cross-metathesis reactions proceed at an equal rate **(r_c)**, so that the overall rate of the cross-metathesis reaction ($\mathbf{R_c}$) is given by four times any one cross-metathesis reaction in **19(ii)**, $\mathbf{R_c} = 4 \times (\mathbf{r_c}\text{-2})$.

The results for the metathesis reaction of $C_3H_6 + C_3D_6$ on the MoO_3/TiO_2 and MoO_{3-x}/TiO_2 catalysts activated with $Sn(CH_3)_3$ are summarized in Table 10.4. The MoO_3/TiO_2 had no catalytic activity, but a partly reduced MoO_{3-x}/TiO_2 ($x < 0.7$) evacuated at 450 °C gave almost equal activity to that reported in references. If $Sn(CH_3)_3$ was adsorbed on the MoO_3/TiO_2 or MoO_{3-x}/TiO_2 catalyst, however, the activity for the metathesis reaction was enhanced 10^3–10^4 times [38]. As shown by reaction **cycle-I (r_p)** in Scheme 10.5, the productive metathesis of propene is catalyzed by alternating reaction of propene with $Mo{=}CH_2$ and $Mo{=}CHCH_3$ via metallacyclobutane intermediates. In contrast, the cross-metathesis of propene is attained by repeating the reaction of propene with $Mo{=}CH_2$ or $Mo{=}CHCH_3$ as described by reaction **cycle-I (r_c-1)** and reaction **cycle-II (r_c-2)** in Scheme 10.5. The relative reaction rate of the cross-metathesis to that of the productive metathesis was $\mathbf{R_c/R_p}$ = 10–27, as shown in Table 10.4, that is, the cross-metathesis of propene is 10–27 times faster than the productive metathesis forming ethylene and but-2-ene.

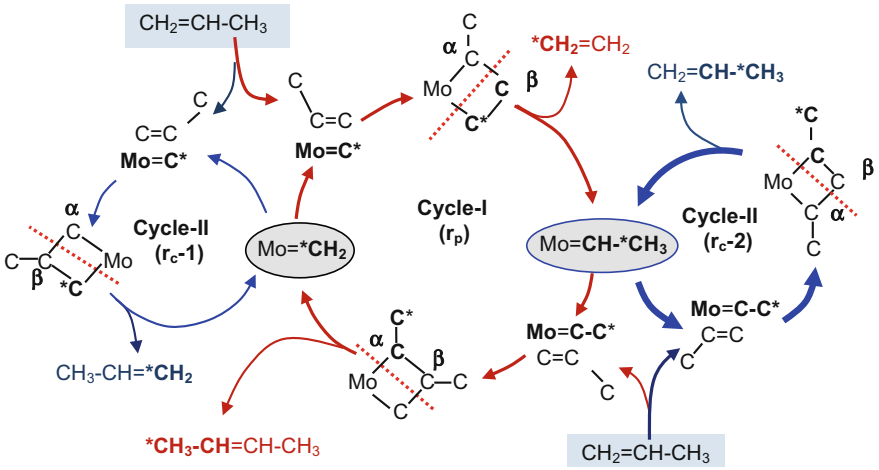

Scheme 10.5 Overall reaction scheme of the productive metathesis and cross-metathesis of propene via $Mo{=}CH_2$ and $Mo{=}CHCH_3$. The productive metathesis is catalyzed by the alternating reaction of propene with $Mo{=}CH_2$ and $Mo{=}CHCH_3(r_p)$, whereas cross-metathesis occurs by repeated reaction of $Mo{=}CHCH_3$ ($r_{c\text{-}1}$) and/or $Mo{=}CH_2$ ($r_{c\text{-}2}$) with propene. The relative turnover frequency of the three catalytic cycles depends on the lifetime and steady-state concentration of $Mo{=}CH_2$ and $Mo{=}CHCH_3$, and the frequency of the cycles is in the ratio of $\mathbf{r_{c1} : r_p : r_{c2}}$ = 1 : 10–30 : 100–900 [32]

Table 10.4 Turnover frequency (TF) of the productive metathesis of propene (formation of ethylene) and the cis/trans ratio observed in the but-2-ene

Catalyst	TF[a]	but-2-ene (trans/cis)[b]	R_c/R_p
$MoO_3/\beta\text{-}TiO_2$	0	–	–
$MoO_3/\beta\text{-}TiO_2 + Sn(CH_3)_3$	9.3×10^{-5}	<2.0	10
$MoOx/\beta\text{-}TiO_2$	2.0×10^{-7}	>5.0	6.7
$MoOx/\beta\text{-}TiO_2 + Sn(CH_3)_3$	5.2×10^{-4}	>5.0	27

The ratio of cross-metathesis to productive metathesis (r_c/r_p) in the metathesis reaction of propene-$^2H_0$ + propene-$^2H_6$ (1 : 1) on a activated MoO_x with $Sn(CH_3)_3$
[a]Turnover frequency of the formation of ethylene/Mo atom sec^{-1}
[b]Equilibrium value = 3.3 [38]

It is also known that the formation of *trans*-but-2-ene in the productive metathesis of propene is preferred over *cis*-but-2-ene (*trans/cis* > 5). The origin of trans-selective metathesis, *trans/cis* > 5, is due to either "**structural preponderance**" of metallacyclobutane intermediates or "**kinetic preponderance**" (reaction rate) in the formation of metallacyclobutane intermediates. The metathesis reaction of symmetric olefins such as but-2-ene (cis and trans C–C=C–C) is suitable to shed light on the mechanism of stereo-selective metathesis reactions, because the

reaction proceeds via a single-carbene complex of Mo=$CHCH_3$. The conformational heredity of the cis-to-cis or the trans-to-trans retention was studied by using deuterium-labeled but-2-enes: (cis-but-2-ene-$[^2H]_8$ + cis-but-2-ene-$[^1H]_8$) and (trans-but-2-ene-$[^2H]_8$ + trans-but-2-ene-$[^1H]_8$). As shown in Fig. 10.12b, either the cis or trans conformation of but-2-ene molecules was evidently retained in the product but-2-ene-$[^2H]_4$ molecules, but the cis-to-cis heredity was 80% in the metathesis of cis-but-2-ene, whereas the trans-to-trans heredity in the metathesis of trans-but-2-ene was almost 100% (the formation of cis-but-2-ene ≈ 0 in the figure) as shown in Fig. 10.12b. From this result, we can conclude that the preferential reaction path is decided by the stereo-conformational preponderance of the metallacyclobutane intermediates. Shrock et al. [40] showed a puckered ring structure for a W-cyclobutane, but Grubbs et al. [41] showed a flat structure for the Ti-cyclobutane ring by X-ray crystallographic analysis.

The sequence of feasible metallacyclobutane structures deduced from the trans or cis structure heredity is illustrated in Scheme 10.6. The relative preponderance of the stereo-structure of metallacyclobutanes is responsible for the trans or cis conformation heredity in the metathesis reaction, and the ratio of trans-to-trans, cis-to-cis, cis-to-trans, and trans-to-cis was evaluated at 40 : 37 : 0.8 : 0.2. That is, the conformational heredity of the trans-to-trans is 200 times the trans-to-cis structure heredity (40/0.2) in the olefin metathesis reaction. From this experiment, we can deduce the preponderance of metallacyclobutane stereo-structures depending on the $–CH_3$ groups at the α- and β-positions. That is, the $–CH_3$ groups at the α- and β-positions of metallacyclobutane intermediates give rise to the conformational preponderance, and the stereo-selectivity in olefin metathesis reactions is given by the sequence of "**conformational preference**" of the metallacyclobutane intermediates.

The *Z*-1-$[^2H]_1$-propene was prepared by the hydrogenation of 1-$[^2H]_1$-methyl acetylene ($CD{\equiv}CHCH_3$) obtained by shaking methyl acetylene in an alkaline D_2O solution with a Pd/C catalyst. The heredity of the conformation of the $[^2H]$ to $–CH_3$ in *Z*-1-$[^2H]_1$-propene was studied using a 1 : 1 mixture of (*Z*-1-$[^2H]_1$-

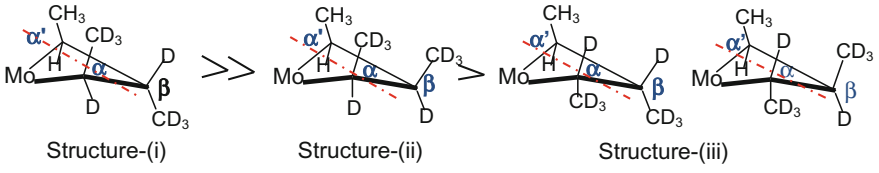

Scheme 10.6 The relative contribution of metallacyclobutane intermediates in metathesis of trans-but-2-ene and cis-but-2-ene. The cis-to-cis conformation heredity (cis-but-2-ene-$^2H_0$ + cis-but-2-ene-$^2H_8$) was 80%, and the trans-to-trans conformation heredity was nearly 100% (trans-but-2-ene-$^2H_0$ + trans-but-2-ene-$^2H_8$) containing a very small fraction of cis-but-2-ene-$[^2H]_4$. The relative contribution was as follows: structure (i) : structure (ii) : structure (iii) = 40–37 : 0.8 : 0.2

propene + $[^2H]_6$-propene) on the MoO_3/TiO_2–$Sn(CH_3)_3$ catalyst and a partly reduced MoO_x/TiO_2–$Sn(CH_3)_3$ catalyst [42]. The "stereo-specific metathesis" in the cross-metathesis of unsymmetrical molecules such as propene is described in Eq. (10.14), and the productive metathesis reaction of propene is described in Eqs. (10.15a) and (10.15b) in Scheme 10.7.

The "cross-metathesis" between Z-1-$[^2H]_1$-propene-$[^2H]_5$ and propene-$[^2H]_6$ is given by Eq. (10.14), which forms E-1-$[^1H]_1$-propene-$[^2H]_5$ or Z-1-$[^1H]_1$-propene-$[^2H]_5$ and 1-$[^2H]_2$-propene-$[^1H]_4$. On the other hand, the "productive metathesis" that occurs simultaneously forms cis-1,2-$[^2H]_2$-ethylene or trans-1,2-$[^2H]_2$-ethylene and cis-but-2-ene or trans-but-2-ene as shown by Eqs. (10.15a) and (10.15b).

The results of the cross-metathesis reaction between *Z*-1-$[^2H]_1$-propene and $[^2H]_6$-propene, given by Eqs. (10.14a) and (10.14), are shown in Fig. 10.13a, and those of the productive metathesis forming 1,2-$[^2H]_2$-ethylene and but-2-ene, given by Eqs. (10.15a) and (10.15b), are shown in Fig. 10.13b. It is known that the *Z*-1-$[^2H]_1$ conformation of the $-CH_3$ group in *Z*-1-$[^2H]_1$-propene is retained by forming *E*-1-$[^1H]_1$-propene-$[^2H]_5$ with $\sim$80% yield as described in Eq. (10.14a). If one considers that the purity of the *Z*-1-$[^2H]_1$-propene used was $\sim$90%, the value of $\sim$80% *E*-1-$[^1H]_1$-propene-$[^2H]_5$ indicates surprisingly high retention of the stereo-conformation of metallacyclobutane intermediates in the cross-metathesis reaction. In contrast, the ethylene molecules produced by the productive metathesis reaction, Eq. (10.15a), showed no conformational selectivity in the 1,2-$[^2H]_2$-ethylene produced (cis/trans = 1/1) although another product but-2-ene showed the preferential formation of trans-but-2-ene (trans/cis = 5–2) as described by Eq. (10.15b). It is still not clear whether the "**structural preponderance**" or "**kinetic feasibility**" (formation rate) is responsible for the conformational descent in the olefin metathesis reaction via metallacyclobutane intermediates. It is clear, however, that there is no conformational heredity in the formation of cis-1,2-$[^2H]_2$-ethylene or trans-1,2-$[^2H]_2$-ethylene in Eq. (10.15a); no selectivity appears for the puckered structure of the metallacyclobutane with one substituted CH_3-group as described in Eq. (10.15a). On the other hand, if two $-CH_3$ groups are substituted at the α- and β-positions of the metallacyclobutane ring, the preferential metallacyclobutane conformation depends on the two $-CH_3$ groups as described in Eq. (10.15b), and this is the origin of the preferential formation of trans-but-2-ene (trans-but-2-ene)/(cis-but-2-ene) = 5.0–2.0. If three $-CH_3$ groups are substituted at the α-, α'-, and β-positions of the metallacyclobutane ring, the three $-CH_3$ groups give a more clear effect on the stereo-conformation of methyl groups in metallacyclobutanes as described in Scheme 10.6, which is reflected by the ratio of (i)/(ii)/(iii) = 200–185/4/1 (40–37 : 0.8 : 0.2). Taking these results into account, we can conclude that the preferential stereo-structure of the metallacyclobutane intermediates in the metathesis reaction is given by "**kinetic feasibility**." The conformational descent in the metathesis reaction is attained by the "**formation rate**" of the metallacyclobutane intermediates instead of the "**conformational preponderance**." In other words, the formation of metallacyclobutanes is the rate-determining step for the olefin metathesis reaction, and the whole reaction scheme for the

(a) The Cross-Metathesis Reaction of *Z*-1-[^{2}H]$_1$-Propene:

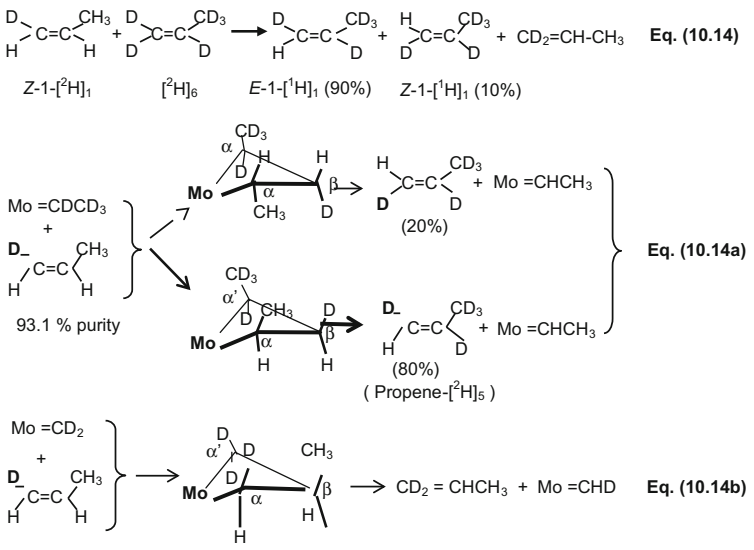

(b) Productive metathesis of Z-1-[^{2}H]$_1$-Propene.

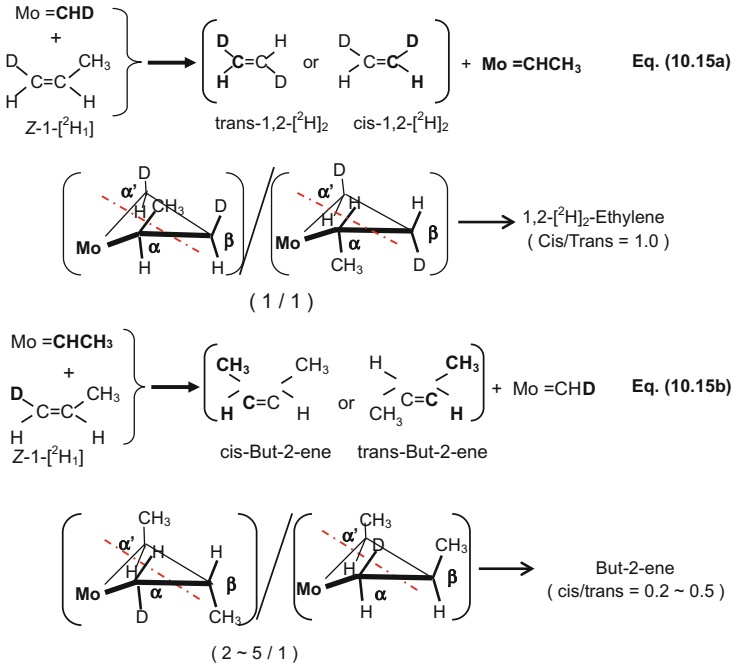

Scheme 10.7 Stereo-conformation of metallacyclobutane intermediates in the metathesis reaction of a 1:1 mixture of (Z-1-[^{2}H]$_1$-propene + [^{2}H]$_6$-propene) [42]. Equations (10.14a) and (10.14b) represent the cross-metathesis, and Eqs. (10.15a) and (10.15b) represent the productive metathesis. Isotopic purity of the propene used was Z-1-[^{2}H]$_1$-propene: 93.1%; [^{2}H]$_6$-propene: 97.2%; and the produced trans-but-2-ene-[^{2}H]$_8$: 94.8%

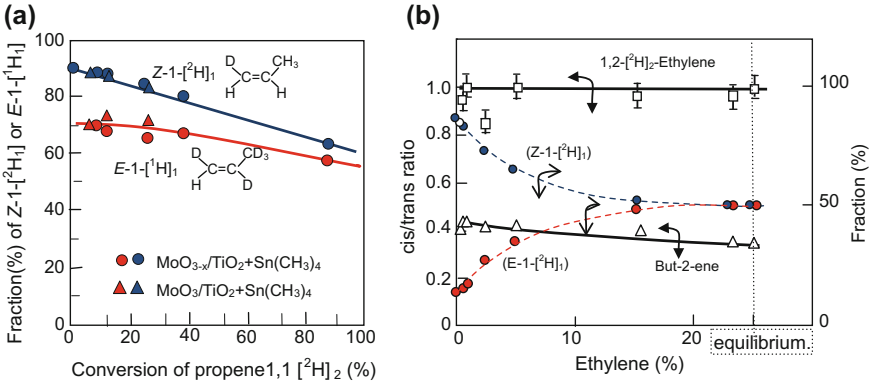

Fig. 10.13 **a** cross-metathesis of (Z-1-[^{2}H]$_1$-propene + propene-[^{2}H]$_6$) forming (CHD=C_2D_5 + CD_2=C_2H_5) on activated MoO_3/TiO_2–$Sn(CH_3)_3$ and MoO_x/TiO_2–$Sn(CH_3)_3$ catalysts. Fraction of E-1-[^{1}H]$_1$-propene in HDC=C_2D_5 (●, ▲) and Z-propene-1-[^{2}H]$_1$ (○, △) changing with the conversion (%) to the equilibrium composition. **b** Productive metathesis of Z-1-[^{2}H]$_1$-propene to 1,2-[^{2}H]$_1$-ethylene + but-2-ene on MoO_3/TiO_2–$Sn(CH_3)_4$. The ratio of (cis/trans) = 1 for 1,2-[^{2}H]$_2$-ethylene (□), but (cis/trans) = 0.45 for but-2-ene (◉). As the ethylene is increased (abscissa) by productive metathesis, the Z-1-[^{2}H]$_1$-propene (△) decreases with the increase of the E-1-[^{2}H]$_1$-propene (●) by cross-metathesis [42]

propene metathesis is described in Scheme 10.5, where cycle-I (r_p) gives productive metathesis, and **the two cycles of II** (r_c-1 and r_c-2) are responsible for cross-metathesis. The relative contribution of the three reaction cycles is in the ratio of (r_c-1 : r_p : r_c-2) = (1 : 10–30 : 100–900) [32]. Productive metathesis of propene is given by the alternating reaction of Mo=CH_2 and Mo=CH–CH_3 with propene, but the detectable intermediate during catalysis may be merely Mo=CH–CH_3, because the lifetime of Mo=CH_2 on the surface during the reaction should be very short.

10.4 Selective Oxidation of CO Improved by H_2O

As it was mentioned in preceding Chap 6 in Part I, surface metal atoms contribute directly in catalysis by forming labile intermediate compounds as in the methanation reaction of CO with H_2 on Ni catalysts and the ammonia synthesis reaction of N_2 with H_2 on Fe catalysts. That is, CO + 3 H_2 → CH_4 + H_2O on Ni catalysts proceeds via the hydrogenation of Ni_4C as shown in Fig. 6.1, and N_2 + 3 H_2 ⇌ 2 NH_3 on Fe catalyst may proceed via the hydrogenation of Fe_xN as shown in Fig. 6.4. In this mechanism, activity depends on the number of recycling metal atoms on the surface by forming labile intermediate compounds. This is analogous to the selective oxidation of propene to acrolein (CH_2=$CHCH_3$ + O_2 → CH_2=CHCHO + H_2O) on multi-component bismuth–molybdate catalyst, in which the activity depends on the number of replenished labile ionic lattice oxygen ions [43–47]. In another case of

catalysis is given by forming functional sites or new materials on the surface at the initial stage of the reaction provides active catalysts. The isomerization and the hydrogenation of olefins on MoS_2 in Sects. 10.1 and 10.2 and the metathesis reaction of olefins on MoO_{3-x} in Sect. 10.3 are prominent examples of this type of catalysis, where the functional sites are new materials which can work as catalyst only on the specific materials. The ^{2}Mo–H and ^{3}Mo(H)$_2$ sites formed on the edge of MoS_2 and the Mo=CHR sites formed on the MoO_{3-x} are prominent examples. In Sects. 10.1 and 10.2, it is shown that the reaction mechanism and the function of active sites in catalysis become clear by removing unnecessary migration of intermediates in catalysis. This would be a valuable concept to design highly efficient catalysts, and a practical example is discussed on the preferential oxidation of CO in H_2 in Sects. 10.4 and 10.5.

One advantage of heterogeneous catalysis is cooperation of two or more reactions taking place on the same surface. The reduction of NO gas with NH_3 on the Fe_2O_3–TiO_2 catalyst developed by Kato et al. [48, 49] is a good example. In this case, the oxidation of NO to NO_2 with O_2 occurs on Fe_2O_3–TiO_2, and subsequently, the reduction of NO_2 with NH_3 takes place on the same surface as shown in Fig. 10.14. That is, the oxidation reaction and the reduction reaction take place simultaneously by the different function of the surface for each reaction. However, if one wishes to make clear the individual function of each component working as a catalyst, the surface is an awkward material, because relevant phenomena depend on particle size, surface conformation, surface structure, and reaction atmosphere.

Consider the role of surface in catalytic oxidation of CO with O_2 on metals. This reaction has been studied as a model of catalysis and the activity of metals has been

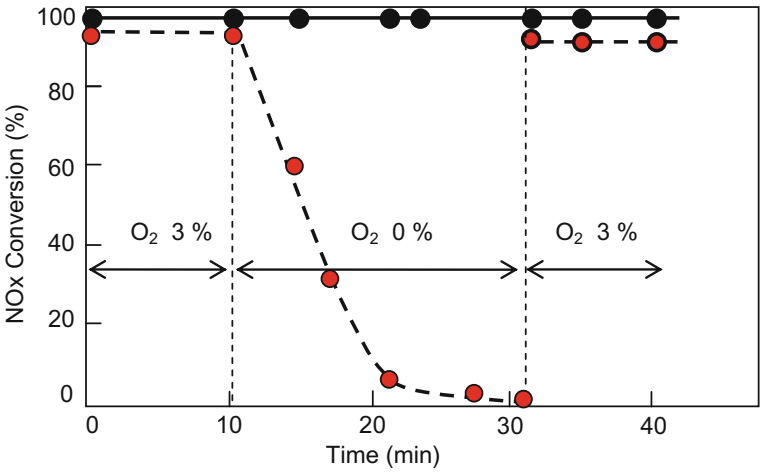

Fig. 10.14 De-NOx reaction of [NO (300 ppm) + NO_2 (300 ppm)] with NH_3 (660 ppm) (●) and the reaction of NO (300 ppm) with NH_3 (330 ppm) (●) enhanced by O_2 on Fe_2O_3–TiO_2 catalyst at 623 K in a flow rate of gas hourly space velocity = 30,000 h^{-1} [48]

vaguely considered as an intrinsic property of metals. For examples, the reactivity of adsorbed CO has been discussed in relating to the bonding form of CO(a) on metals, and the kinetics of the reaction of adsorbed CO(a) with O(a) has been rationalized based on the Langmuir–Hinshelwood mechanism. On the other hand, the oxidation of CO with O_2 on a Pt foil depends on the log (P_{CO}/P_{O2}) ratio as shown by Golchet and White [50] at 453 and 485 K, as shown in Fig. 7.3. That is, the amount of adsorbed CO(a) and O(a) during the catalytic reaction is decided by a dynamic balance of the adsorption rate of CO(a) and O(a) and followed subsequent reaction on the surface. According to this mechanism, the amount of CO(a) and O(a) on the Pt surface becomes almost zero at the value of log (P_{CO}/P_{O2}) = −5.3 to −5.0.

This experiment showed that the oxidation rate of CO(a) with O(a) on the Pt surface is more rapid than the adsorption rate of CO and O_2 under this experimental condition, so that the Pt surface became almost clean at a suitable ratio of CO(a) and O(a), log (P_{CO}/P_{O2}) = −5.3 to −5.0, where the inhomogeneous properties of adsorbed CO(a) on Pt are smeared by rapid migration of adsorbed CO(a). That is, the apparent uniformity of the surface does not mean the true uniform of the surface.

On the other hand, it is well known that the local electron density gives remarked effect on the adsorption of CO as proved experimentally by King et al. [51] on a thin single-crystal Ni-film (∼200 nm thick) by doping with K atoms. Effect of the local electron density on the adsorption of CO was directly detected by the infrared light emitted from behind of the Ni-film by using a pulse of 10^{12} CO molecules in 50 ns on thin Ni(100) and K^+/Ni(100) films. The result may suggest the presence of precursor state in adsorption, too, because the surface was not uniform. As shown in Fig. 10.15, the heat of the adsorption of CO on a clean Ni(100) surface increased from 124 to 190 kJ/mole on a Ni-film with 0.08 ML of K^+ and increased to 310 kJ/mole on a Ni-film with 0.3 ML of K^+. The broken lines in Fig. 10.15 represent a simulation deduced by assuming the equilibrium adsorption of CO on a heterogeneous Ni surface, with clean S_0 sites and K^+ coverage of 0.08 on S_1 sites or 0.3 on S_2 sites. The observed effect of the local charge on the adsorption of CO(a) can be explained by the adsorption model of CO(a) given by Blyholder [52]. It is also known that the adsorption of CO and its reactivity at the steps and/or kinks is different from that on the terraces.

The reactivity of adsorbed CO(a) on metals has been widely discussed by many investigators in relation to the bonding form of CO, and inactivity of Au surface is explained by its inability for the adsorption of CO, although very weak adsorption of CO was shown on Au particles deposited on MgO thin film at 30 K by the local negative charge [53]. As it will be discussed in this Sect. 10.4, catalytic oxidation of CO is markedly enhanced by H_2 (practically H_2O) on the Pt as well as on the Au catalyst in the presence of specific promoting materials. The role of promoting materials on catalytic oxidation of is not simple as it can be rationalized by such a naïve mechanism based on the bonding form or adsorption strength of CO on metals.

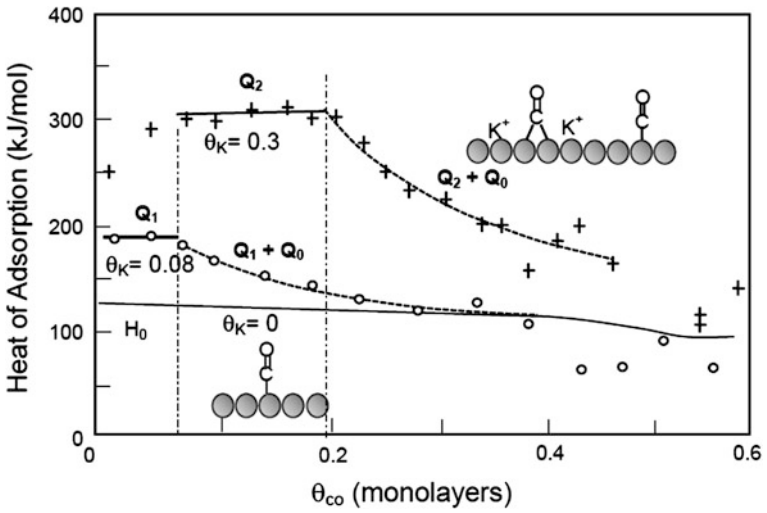

Fig. 10.15 Heats of adsorption of CO on Ni(100) film depending on the K coverage. $\theta_K = 0.08$ (○), $\theta_K = 0.3$ (+) [51]. The line for $\theta_K = 0$ shows estimated value on a clean surface

So far, catalytic oxidation of CO in H_2 on metals has been widely studied as a competitive catalysis of the two independent reactions on the same catalyst surface. The kinetics was explained by the competitive oxidation of the adsorbed CO(a) and H(a) with O(a), reaction (i) and reaction (ii) in Eq. (10.16), based on the Langmuir −Hinshelwood mechanism.

$$\begin{aligned} &\textbf{Reaction} - (\textbf{i}) : CO + 1/2\,O_2 \rightarrow [\mathbf{X_i}] \rightarrow CO_2; \quad (r_{co}) \\ &\textbf{Reaction} - (\textbf{ii}) : H_2 + 1/2\,O_2 \rightarrow [\mathbf{Y_i}] \rightarrow H_2O; \quad (r_H) \end{aligned} \tag{10.16}$$

$$r_{CO}/r_H \approx k_{co}(q_{CO})/k_H(q_H) = [k_{co}/k_H(K_{co})/(K_H)^{1/2}] \times (P_{co}/P_H^{1/2})$$

where k_{co} and k_H are the rate constants for the reactions of CO(a) and H(a) with O (a) and K_H, K_O, and K_{co} are the adsorption equilibrium constants of H(a), O(a), and CO(a), respectively. It is known that the adsorption of CO(a) on Pt is far stronger than that of H(a), $K_{co} \gg K_H$, whereas the reaction rate of H(a) with O(a) is far more rapid than that of CO(a), $k_H \gg k_{co}$, on the Pt surface; that is, $k_{co}/k_H \ll 1$ and $(K_{co})/(K_H)^{1/2} \gg 1$.

On the other hand, selective oxidation of CO in excess H_2 is an important reaction to produce CO-free H_2 gas in the industry. The steam-reforming reaction of methane, $CH_4 + H_2O \rightarrow 3\ H_2 + CO$ ($\Delta H = +205$ kJ/mole), is one reaction to produce H_2 gas, and the CO in H_2 gas is lowered by the water gas shift reaction, $H_2O + CO \rightleftharpoons CO_2 + H_2$ ($\Delta H = -42$ kJ/mol). By this reaction, the CO in H_2 can be lowered to an equilibrium concentration, but the complete removal of CO in excess H_2 is attained by the preferential oxidation (PROX) reaction of CO in H_2.

Korotkikh and Farrauto [54, 55] found that the catalytic activity of a 5 wt% Pt/γ-Al_2O_3 catalyst for the oxidation of CO in H_2 was markedly improved by adding FeO_x, and they explained the role of FeO_x as a synergetic effect on the Pt/γ-Al_2O_3 catalyst. The IR spectrum of linearly adsorbed CO(a) observed at 2084 cm^{-1} on the Pt/γ-Al_2O_3 and FeO_x/Pt/γ-Al_2O_3 catalysts at 30 °C was almost the same as shown in the spectra in Fig. 10.16a. That is, the FeO_x gives little effect on the adsorption of CO(a) on the Pt of FeO_x/Pt/γ-Al_2O_3, that is, the FeO_x gives little effect on the adsorption constant of K_{co} on Pt in Eq. (10.16). Taking these results into account, Korotkikh and Farrauto might consider that the FeO_x gave remarked influence on the k_H and k_{co} by the direct contact of FeO_x with the Pt, and it was explained as the "synergy effect" on Pt.

As like this, when the activity is improved by some promoting materials, it is explained by the kinetic parameter such as k and/or K in the kinetic equation, and the effect is so often explained by the term of "synergetic effect on metals" or "the formation of active form of metals."

I could say, however, it is difficult to understand the real mechanism in catalysis without clarifying the dynamics of intermediates in catalysis. We remember once again the oxidation of CO with O_2 on a Pt foil shown in Fig. 7.3. It is known that the amount of adsorbed CO(a) and O(a) on a Pt foil during catalytic reaction depends on a dynamic balance of the adsorption of CO(a) and O(a) to their subsequent reaction. When the ratio of P_{CO}/P_{O2} takes a value of log (P_{CO}/P_{O2}) = −5.0 to −5.3, a steady amount of CO(a) and O(a) on the Pt becomes very low, that is, the reaction rate of adsorbed species is far more rapid than the adsorption rate of CO and O_2 at 453–485 K corresponding pressures. If the ratio exceeds this value (increased P_{CO}), the adsorption amount of CO(a) is close to an equilibrium adsorption at corresponding CO pressures. On the other hand, if the ratio of P_{CO}/P_{O2} becomes lower than this value, the surface is almost covered with adsorbed O(a). These results indicate that the amount of CO(a) and O(a) on Pt surface is given by a dynamic balance of the adsorption of CO and O_2 and their reaction on the surface, and the reaction rate of CO(a) with O(a) is more rapid than the adsorption of CO at 453–485 K. The reaction of adsorbed CO(a) with O(a) on Pt is seemingly uniform, but this does not mean the uniformity of adsorbed CO(a) on the Pt, that is, rapid migration of adsorbed CO(a) smears the difference of adsorbed species over the Pt surface. Similar phenomenon was observed on a CeO_2/Pt(111) surface as will be discussed in Fig. 10.31.

Oxidation reaction of CO on Pt catalyst is well described by a series-connected water tank model shown in Scheme 10.9, that is, the amount of intermediates during catalysis is described by the water level corresponding to the chemical potentials of intermediates (ξ_1) and (ξ_2), and the amount of water indicates the amount of intermediates. In the case of the oxidation reaction of CO on Pt, ξ_1 is adsorbed CO(a) on the Pt. In the case of the results shown in Fig. 7.3, CO(a) (ζ_1) is very low during catalysis at P_{CO}/P_{O2} giving log (P_{CO}/P_{O2}) = −5.0 to −5.3 (P_{O2} held at a constant pressure). On the other hand, if the step (i) is more rapid than the step (ii), detectable amount of intermediate (ξ_1), in this case CO(a), should exist on the catalyst. If there would be additional slow step, step (iii), we can expect

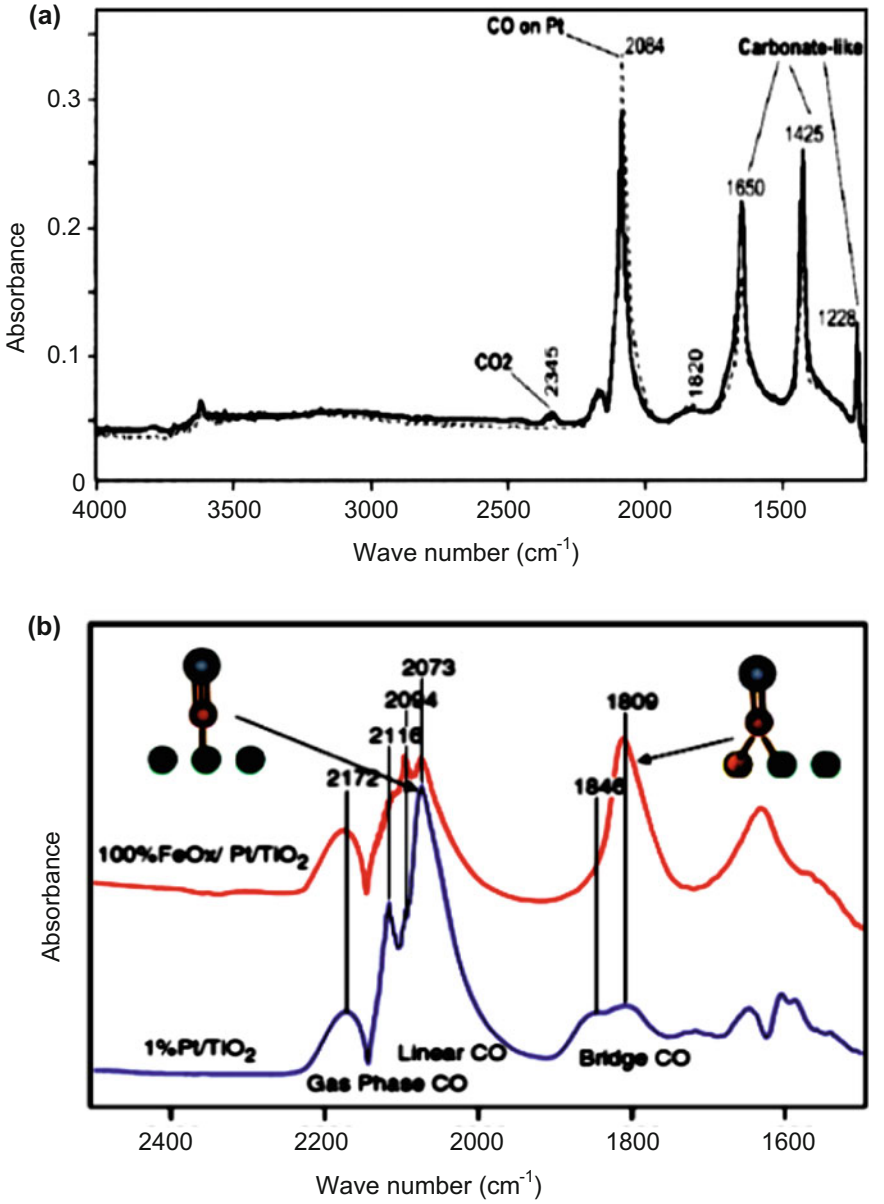

Fig. 10.16 **a** DRIFT spectra of adsorbed CO(a) on $FeO_x/Pt/\gamma\text{-}Al_2O_3$ (5 wt% Pt) (*solid line*) and $Pt/\gamma\text{-}Al_2O_3$ (*dotted line*) at 30 °C [54]. **b** DRIFT spectra of adsorbed CO(a) in a flow of CO + N_2 on Pt/TiO_2 (1 wt% Pt) and $FeO_x/Pt/TiO_2$ at 40 °C [56]

detectable amounts of both (ξ_1) and ($\xi_{2)}$ on the catalyst. According to this idea, the reaction rate of step (i), step (ii), and step (iii) in catalysis can be deduced from the dynamics of intermediates (ξ_1) and ($\xi_{2)}$ by in situ IR spectroscopy.

So far, the preferential oxidation of CO in H_2 on Pt catalyst is considered as a competitive oxidation of the two independent reactions as schematically shown in Scheme 10.8a. According to this mechanism, if the P_{co}/P_H ratio takes on a large value, that is, the pressure of CO is high, more selective oxidation of CO is attained, but if the P_{co}/P_H ratio becomes lower than a critical value, it is difficult to achieve the selective oxidation of CO. According to this reaction mechanism, the ratio of the adsorption constant of K_H/K_{co} or the ratio of rate constant k_H/k_{co} should be changed to attain the selective oxidation of a small amount of CO in excess H_2. So far the roles of promoting materials have been explained by a word of synergy effect on Pt or activation of Pt. However, as described in this Sect. 10.4, entirely different oxidation mechanism of CO is responsible for highly selective oxidation of CO in excess H_2 on Pt catalyst in the presence of promoting materials.

Tanaka et al. [58] found the oxidation of CO was markedly enhanced by H_2 and/or H_2O on a 1 wt% Pt/TiO_2 catalyst covered with a large amount of FeO_x (Fe/Pt/T iO_2 ≈ 100/1/100 in wt%), and the selective oxidation of CO in excess H_2 was attained at low temperature on the $FeO_x/Pt/TiO_2$ catalyst as shown in Fig. 10.18a, b [56, 59]. It should be pointed out that the 1 wt% Pt/TiO_2 and $FeO_x/Pt/TiO_2$ showed almost equal low catalytic activity for the oxidation of CO with O_2 in the absence of H_2 or H_2O at 60 °C. And the oxidation reaction of CO was enhanced by H_2 or H_2O only on the $FeO_x/Pt/TiO_2$ catalyst as shown in Fig. 10.18a, b. It should be reminded that no enhancement of the oxidation of CO by H_2 and H_2O

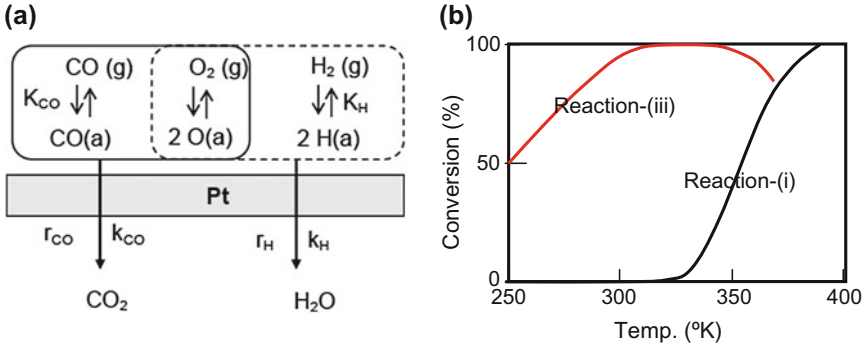

Scheme 10.8 **a** Schematic description of the competitive oxidation of CO(a) and H(a) with O(a) on Pt, which are independent reaction. **b** Temperature dependence of the oxidation of CO in reaction (i) and reaction (iii) on $FeO_x/Pt/TiO_2$. Catalytic oxidation of CO in H_2 on $FeO_x/Pt/TiO_2$ is given by (reaction (i) + reaction (iii)), but the contribution of the reaction (iii) is negligible on Pt/TiO_2

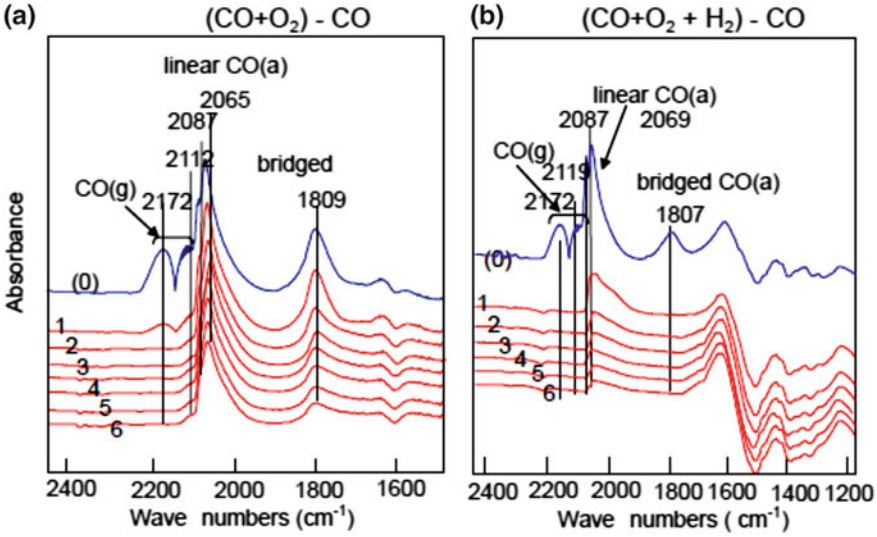

Fig. 10.17 Changes in in situ DRIFT peaks of CO(a) on a $FeO_x/Pt/TiO_2$ catalyst with time after CO was removed at 333 K. **a** Slow decrease of CO(a) on removing CO from ($CO + O_2 + N_2$). **b** Rapid decrease of CO(a) on removing CO from ($CO + H_2 + O_2 + N_2$). A series of spectra (1)–(6) were recorded with interval times of 5, 10, 15, 20, 30, and 45 min [59]

was observed on the Pt/TiO_2 catalyst as shown in Fig. 10.18c. It is evident that the role of FeO_x is not synergetic effect on Pt metals such as speculated by Korotkikh and Farrauto on the $FeO_x/Pt/\gamma\text{-}Al_2O_3$, but FeO_x is direct contribution to the oxidation reaction of CO as will be mentioned precisely below.

We confidently conclude that the low-temperature catalytic oxidation of CO taking place in the presence H_2O on the $FeO_x/Pt/TiO_2$ catalyst is essentially different from the oxidation of CO(a) with O(a) given by reaction (i) in Eq. (10.16). As it is evidenced below, H_2O molecule directly contributes to the selective catalytic oxidation of CO in H_2 on the $FeO_x/Pt/TiO_2$ catalyst, which is the reaction given by the reaction (iii) in Eq. (10.18). The difference of the two reactions, reaction (i) and reaction (iii), is illustrated in Scheme 10.8b. The reaction (i) is predominant oxidation reaction of CO at higher temperature, but the reaction (iii) taking place in the presence of H_2 or H_2O becomes predominant at lower temperature on the $FeO_x/Pt/TiO_2$ catalyst. So far, essential difference of these two reactions has not been recognized.

$$\textbf{Reaction}-(\textbf{iii}):\mathbf{n}(CO+1/2\,O_2)+\mathbf{H_2O}\rightarrow(\xi_2)\rightarrow n\,CO_2+\mathbf{H_2O} \qquad (10.18)$$

It should be pointed out that FeO_x itself has no catalytic activity for the oxidation of CO, but the FeO_x is indispensable materials for the catalytic oxidation of CO enhanced by H_2O on the Pt catalyst. As it will be shown below, H_2O molecule works as a kind of molecular catalyst in the presence of promoting materials, that is,

one H_2O molecule repeatedly promotes the oxidation of CO, and the "**n**" in the reaction (iii) of Eq. (10.18) means "**n**" times repeated contribution of one H_2O. In this respect, unusual selective oxidation of CO in H_2 reported by Fukuoka et al. [60] on the Pt nano-rods held in SiO_2 nanotube is quite interesting. As shown in Fig. 10.25, the Pt nano-rods supported inside the SiO_2 nanotubes showed extremely high selectivity for the PROX reaction of CO, but Pt nano-rods supported on the outer surface of the SiO_2 nanotubes showed almost the same as an ordinary Pt catalyst. They explained this phenomenon by the formation of "specific state of Pt in SiO_2 nanotubes."

This phenomenon is not the formation of such curious Pt, but we appreciate this result proving a definitive evidence for the new proposed reaction (iii) of Eq. (10.18): **n** (CO + 1/2 O_2) + H_2O → **n** CO_2 + H_2O. That is, high selectivity in SiO_2 nanotube is well rationalized by a large "n" values in reaction (iii). The mechanism of new catalytic oxidation of CO enhanced by H_2O, reaction (iii), is deduced by the dynamic in situ IR spectroscopy as mentioned below.

As mentioned in Sects. 10.1 and 10.2, unnecessary migration of intermediates should be removed to make clear the role of promoting materials in catalysis. According to this idea, the oxidation of CO enhanced by H_2 and/or H_2O was performed on Pt/CNT and Pt/CNT-p catalysts. The CNT (carbon nanotube) provides a quasi-one-dimensional surface, and Ni–MgO used to prepare the CNT is remained at its terminal end. Therefore, the Pt particles on the trunk surface of CNT are perfectly separated from the Ni–MgO localized at the terminal end. The Ni–MgO was removed by chemical purification on the CNT-p. As shown in Fig. 10.19, the oxidation of CO on the Pt/CNT was markedly enhanced by H_2, but no such enhancement was observed on the Pt/CNT-p. That is, the oxidation of CO given by reaction (iii) of Eq. (10.18) is catalyzed only on the Pt/CNT catalyst, which is similar to the oxidation of CO enhanced by H_2O only on the FeOx/Pt/TiO_2 catalyst. Taking these results into account, the mechanism of reaction (iii) on the FeOx/Pt/TiO_2 was precisely studied by the in situ DRIFT spectroscopy.

As it is known, the bridge-bonded CO on Pt is more reactive than the linearly bonded CO toward adsorbed oxygen. However, it does not mean the bridge-bonded CO is a significant intermediate in the catalytic oxidation of CO with O_2 on Pt. If adsorbed CO(a) undergoes rapid migration over the Pt surface during catalysis, the rate-determining reaction cannot distinguish the two forms of adsorbed CO in catalysis. From this point of view, in situ DRIFT spectra attained in a steady flow of (a) (CO + O_2) and (b) (CO + O_2 + H_2) on a FeO_x/Pt/TiO_2 catalyst shown in Fig. 10.17a, b are quite interesting. The blue spectrum in Fig. 10.17a was attained in a steady flow of (CO + O_2) and that in (b) was attained in a steady flow of (CO + O_2 + H_2). The spectra showing linearly bonded and bridge-bonded CO peaks were observed in either the presence or the absence of H_2. However, if CO was removed from the reactant gas, the in situ spectra were changed in dramatically different ways in the presence of H_2 or not as shown with the red spectra in Fig. 10.17a, b. That is, adsorbed CO(a) was decreased slowly in Fig. 10.17a, but bridge-bonded CO(a) and linearly bonded CO(a) were disappeared within a 10 min in Fig. 10.17b. This result indicates that adsorbed CO(a), either

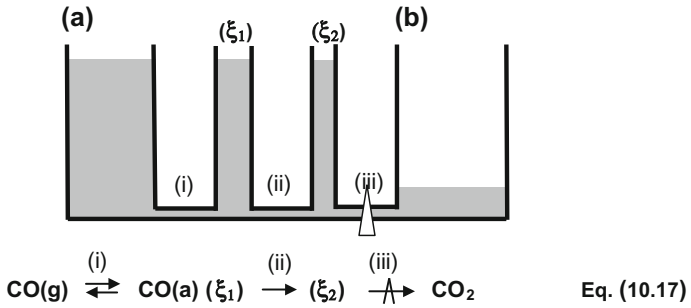

Scheme 10.9 A series-connected water tank model showing a steady-state of reaction. Water level shows chemical potential of the intermediates (ξ_1) and (ξ_2) of the reaction (*A*)–(*B*). Equation (10.17) is an oxidation reaction of CO via intermediates (ξ_1) and (ξ_2), and step (iii) is the rate-determining step [57]

linearly bonded CO(a) or bridge-bonded CO(a), on the Pt is very quickly changed to the intermediate (ξ_2) according to the reaction of Eq. (10.17) and Scheme 10.9.

As it was mentioned above, oxidation of CO by reaction (i) on ordinary Pt catalysts is not rapid below 60 °C as shown on the Pt/TiO_2 and $FeO_x/Pt/TiO_2$ catalysts in Fig. 10.18. However, in the presence of H_2O, reaction (iii) is catalyzed only on the $FeO_x/Pt/TiO_2$ catalyst. These results evidently prove that the role of FeO_x is not the activation of the Pt but is responsible to provide a new catalytic reaction (iii) on the $FeO_x/Pt/TiO_2$ catalyst.

So far, the role of promoting materials such as those observed on the oxidation reaction of CO on the $FeO_x/Pt/TiO_2$ catalyst has been explained by a term of "synergetic effect" on metals or of the formation of "active metals," but it is very little to consider in relation to the reaction mechanism. That is the same for other reactions such as the water gas shift reaction on Pt and Au catalysts improved by alkali metals [62] and active Au^{3+} ion on CeO_2 [63, 64] and low-temperature oxidation of HCHO on Pt improved by alkali metals [65]. The role of support materials of metal catalysts on activity was also explained by a similar way on the oxidation of CO on $Rh/Ce_{0.5}Zr_{0.5}O_2$, Pt−Rh/CeO_2, and Pt−Rh/CeO_2ZrO_2 catalysts [66] and Au nanoparticles supported on several oxides as shown in Fig. 10.29a. Haruta et al. [67, 68] found superior active Au catalyst for the oxidation of CO when the Au particles became smaller than ca. 3 nm on specific oxides. They supposed the formation of an active perimeter around the Au particles being smaller than 3 nm. In fact, a new active Au layer compound was reported by Chen and Goodman [69] as shown in Fig. 10.29b, but the active was unstable. On the other hand, Lambert et al. [70] found extremely reactive CeO_2 layer on Pt(111) surface when the CeO_2 layers take thicker than two monolayers as will be discussed in Sect. 10.5. These results may suggest the existence of new active materials or two-dimensional active materials having active lattice oxygen. The size of Au particles may not be the essential requisite of the activity as pointed out by Chen [69]. If the stability of active materials would depend on the particle size, however, flexible active materials may

depend on the size, which is an essential problem in catalysis. In this respect, activation mechanism of adsorbed O(a) or lattice oxygen ion by metal ions discussed on $Au^{+}-Au/\gamma\text{-}Al_2O_3$ [76, 105], $Au^{3+}-Au/\alpha\text{-}Fe_2O_3$ [72], $Fe^{3+}-Au/Fe_2O_3$ [72], and $Na^{+}-Pt/CNT$ [73] catalysts is interesting. Smit et al. [107] showed that the Au/Fe_2O_3 having few −OH groups had significantly low activity despite almost identical chemical composition and structure, and they concluded that the presence of OH groups was responsible for the low-temperature oxidation of CO, and bicarbonate was not the intermediate for the oxidation of CO. They proposed the oxidation of HCOO(a) intermediate with O(a) as described by an equation of 2 HCOO(a) + 2 O(a) → 2 CO_2 + H_2O and $Fe^{3+}O^{2-}$ + H_2O → $Fe^{3+}(OH)_2$.

As shown in Fig. 10.18 and 10.19, the Pt/TiO_2, Pt/CNT-p, and Pt/CNF-p catalysts with no promoting materials and the $FeO_x/Pt/TiO_2$, Pt/CNT, and Pt/CNF with promoting materials showed almost equal catalytic activity for the oxidation reaction of CO with O_2 in the absence of H_2 at 60 °C Whereas, the oxidation of CO was enhanced by H_2 (or H_2O) only on the $FeO_x/Pt/TiO_2$, the Pt/Graphite doped with Ni−MgO, Pt/CNT−Ni−MgO, and the Pt/CNF−FeO_x catalysts, as shown in Figs. 10.18a, b, and 10.19a, b and c. That is, the oxidation of CO given by reaction (i) and the oxidation of H_2 given by reaction (ii) of Eq. (10.16) on the Pt/TiO_2, Pt/CNT-p, and Pt/CNF-p catalysts take place independently as it is known on other Pt catalysts.

The oxidation mechanism of CO enhanced by H_2O in the presence of promoting materials was studied on the Pt/TiO_2 and $FeO_x/Pt/TiO_2$ catalysts by the in situ DRIFT (diffused reflectance infrared Fourier transform) spectroscopy. The in situ IR spectrum of CO(a) attained in a steady oxidation of CO on a $FeO_x/Pt/TiO_2$ catalyst is shown in Fig. 10.17a, b with blue IR spectra: (a) ($CO + O_2 + N_2$) and (b) ($CO + O_2 + H_2 + N_2$). At first glance, the spectrum of adsorbed CO(a) was observed in either the absence of H_2 (a) or the presence of H_2 (b). However, if CO was removed from reactant gas, the change of the in situ spectra with time was dramatically different either in the presence of H_2 (H_2O) or not, as shown in Fig. 10.17a, b with red spectra [56, 61]. This result indicates that the adsorbed CO(a) on Pt is changed to the (ξ_2) in Eq. (10.17) very rapidly in the presence of H_2, because desorption rate of CO should be very slow at this temperature (333 K). The reaction of (ξ_2) was attained by the time-resolved in situ DRIFT spectroscopy attained by removing CO or H_2 from a steady flow of reactant gas as illustrated by a series-connected water tank model in Scheme 10.9, that is, we can deduce the rate-determining step by this method. The desorption rate of adsorbed CO(a) on Pt is very slow at 333 K. Taking this fact into account, rapid erasure of CO(a) (ξ_1) is responsible for the rapid formation of the (ξ_2) in Eq. (10.17), and the intermediate (ξ_2) on the $FeO_x/Pt/TiO_2$ catalyst is decreased by the following reaction. From this point of view, the dynamics of intermediate (ξ_2) becomes the key to solving the role of FeO_x in the PROX reaction on $FeO_x/Pt/TiO_2$. Steady amount of CO(a) observed on the $FeO_x/Pt/TiO_2$ during catalysis is given by a dynamic balance of adsorption of CO molecules and subsequent reaction of adsorbed CO(a). The spectrum observed in Fig. 10.17a, b proves very rapid adsorption of CO on $FeO_x/Pt/TiO_2$, i.e., step (i) in

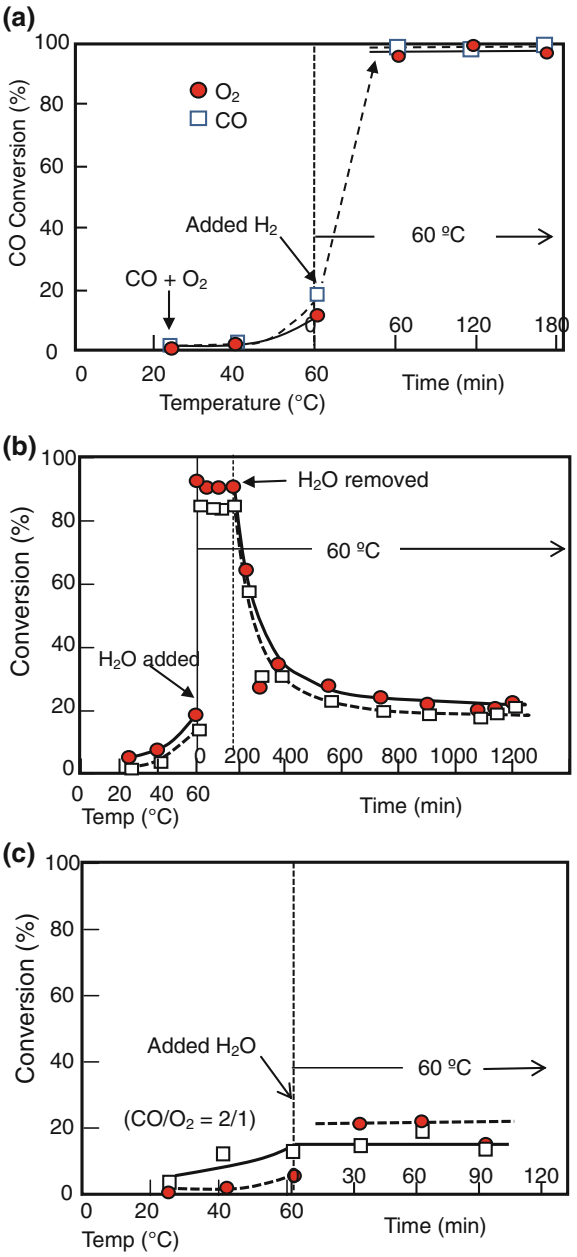

Fig. 10.18 CO conversion versus temperature up to 60 °C and the effect of H_2 and H_2O: **a** Oxidation of CO in a flow of [CO (3 mL/min) + O_2 (1.5 mL/mi) + N_2 (95.5 mL/min)] is enhanced by H_2 (15.0 mL/min) on a $FeO_x/Pt/TiO_2$ catalyst at 60 °C. **b** Oxidation of CO with O_2 enhanced by H_2O on a $FeO_x/Pt/TiO_2$ catalyst at 60 °C. **c** Oxidation of CO with O_2 is not enhanced by H_2O on the Pt/TiO_2 catalyst at 60 °C [56]

Eq. (10.17) takes place very rapidly on the $FeO_x/Pt/TiO_2$ catalyst in either the presence or the absence of H_2.

As observed in Fig. 10.18c, H_2O (or H_2) gives no effect on the oxidation of CO on the Pt/TiO_2 catalyst. In contrast, oxidation of CO on the $FeO_x/Pt/TiO_2$ catalyst is

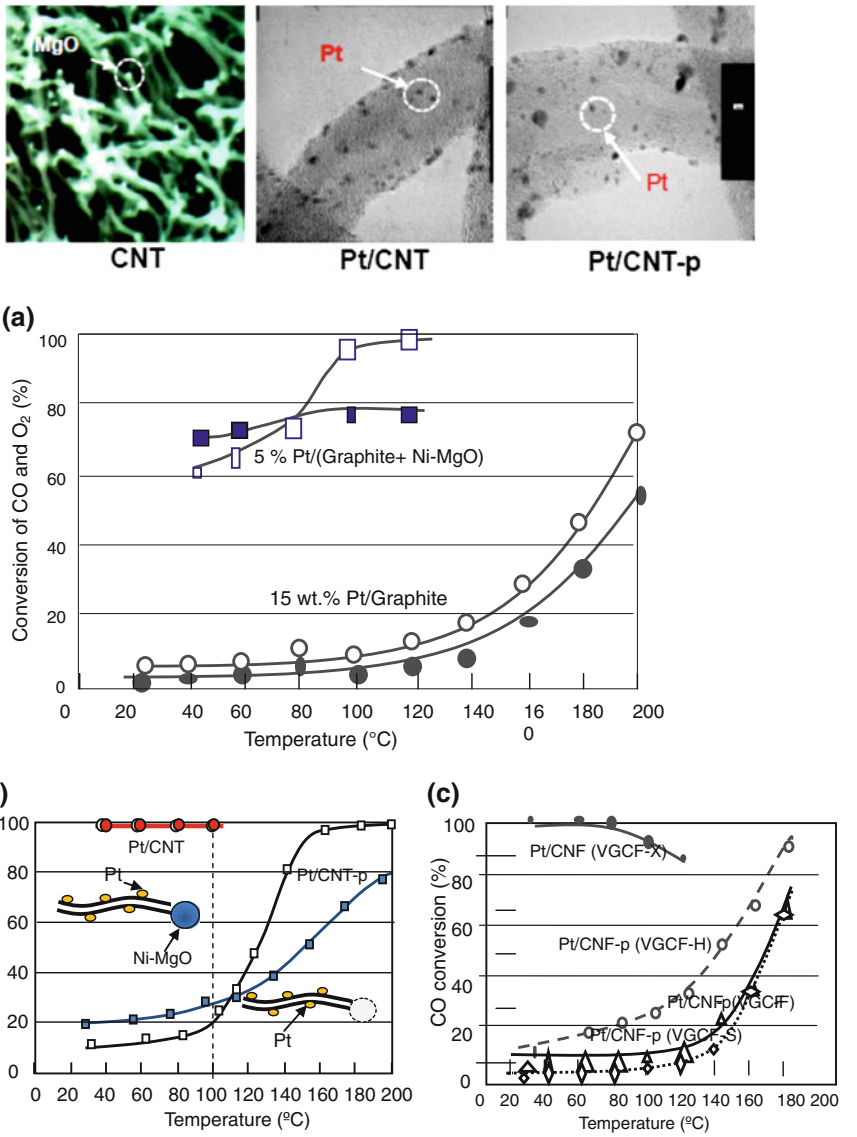

Fig. 10.19 TEM image of CNT, Pt/CNT, and Pt/CNT-p, where CNT-p is purified by chemically removing Ni–MgO at the terminal end. **a** Conversion of CO (*solid symbols*) and O_2 (*open symbols*) by flowing ($CO/O_2/H_2/N_2$ = 3.0/1.5/20/75.5 mL/min). 15 wt% Pt/graphite (0.8 g) (◯, ●) and 5 wt% Pt/graphite with 5 wt% of Ni–MgO (□, ■). **b** Conversion of CO (*solid*) and O_2 (*open*) by flowing 100 mL/min of ($CO/O_2/H_2$ = 1.5/1.5/42.0 mL/min) with a balance of N_2 over 15 wt% Pt/CNT and 15 wt% Pt/CNT-p (0.8 g.). **c** Conversion of CO by flowing 100 mL/min ($CO/O_2/H_2/N_2$ = 3.0/1.5/20.0/78.5 mL/min) over 5 wt% Pt/CNF (VGCF-X) and 5 wt% Pt/CNF-p (VGCF-F, VGCF-H, VGCF-S) [61]

markedly enhanced by H_2 or H_2O as shown in Fig. 10.18a, b. The in situ DRIFT spectra (red spectrum) attained by removing gas-phase CO in Fig. 10.17b show very rapid erasure of adsorbed CO(a) in the presence of H_2, but the spectra (red) in Fig. 10.17a show no such rapid erasure of CO(a) in the absence of H_2. This result suggests the rapid formation of intermediate (ξ_2) of step (ii) in the presence of H_2 (actually H_2O). As will be described below, the subsequent reaction step (iii) of (ξ_2) in Eq. (10.17) is the rate-determining step of the oxidation of CO enhanced by H_2 or H_2O. Therefore, the identification of intermediate (ξ_2) will be an important clue to determining the role of FeO_x in the oxidation of CO enhanced by H_2O. The blue IR spectrum in Fig. 10.17a, b was attained in a steady reaction of (a) ($CO + O_2$) and (b) ($CO + O_2 + H_2$) on the $FeO_x/Pt/TiO_2$ catalyst. A steady amount of adsorption of CO(a), i.e., (ζ_1), exists on the Pt during the reaction of ($CO + O_2 \rightarrow CO_2$) and ($CO + O_2 + H_2 \rightarrow CO_2$) (the ratio of bridge-bonded CO to linearly bonded CO is different), which indicates the rapid adsorption of CO taking place in a steady reaction as premised in the L-H mechanism on the Pt catalyst. In other words, step (ii) in Eq. (10.18) is very slow in the absence of H_2, but it becomes very rapid in the presence of H_2. As it is explained latter in detail, the reaction of adsorbed CO(a) enhanced by H_2O is not the reaction with adsorbed O(a), but the reaction with OH^- ion. Accordingly, the time-resolved red spectrum in Fig. 10.17b changed very rapidly in the presence of H_2, but the change of spectrum in (a) was very slow in the absence of H_2.

As it was mentioned in Sects. 10.1 and 10.2, if catalytic reaction is performed in a one-dimensional lowered space, we could remove the unnecessary migration of the intermediates. According to this idea, the oxidation of CO in H_2 was studied on the Pt supported on a pure graphite and purified CNT-p and CNF-p (removed Ni −MgO and FeO_x catalysts used in the preparation of CNT and CNF) [61]. The Pt was deposited on these surfaces by using a precursor compound, $Pt(NO_2)_2(NH_3)_2$. As shown by the TEM image shown in Fig. 10.19, Pt particles are perfectly separated from the Ni−MgO localized at a terminal end of the CNT.

The oxidation of CO was attained by flowing 100 mL/min of ($CO/O_2/H_2$ = 1.5/1.5/42.0 mL/min) with a balance of N_2 over a 15 wt% Pt/CNT catalyst (0.8 g) and 15 wt% Pt/CNT-p catalyst (15 wt% Pt/CNT corresponds to a 1 wt% for Pt/TiO_2 by the weight of carbon to TiO_2). As shown in Fig. 10.19b, nearly 100% CO conversion was attained at room temperature on the 15 wt% Pt/CNT catalyst, but the conversion of CO was very low, even at 100 °C, on the 15 wt% Pt/CNT-p catalyst with no Ni−MgO. As it was mentioned, the Pt particles are perfectly separated from the Ni−MgO on the Pt/CNT. This fact indicates the cooperation of Ni−MgO and Pt on the CNT. The cooperation of Pt and Ni−MgO was confirmed on pure graphite, where the Pt and Ni−MgO were held on the same basal plane of graphite. The Pt supported on the pure graphite had very low catalytic activity for the oxidation of CO, whereas the Pt supported on the graphite with Ni−MgO had very high activity for the selective oxidation of CO at low temperature, as shown in Fig. 10.19a.

This important result was more strictly confirmed by using the carbon nano-fiber (CNF) synthesized in the gas phase (Showa Denko Co.) by using ferrocene catalyst.

The catalyst was remained in a form of FeO_x at the terminal end of the CNF (VGCF-X; 150 nmϕ × 8 μmL). The FeOx on the VGCF-X was perfectly removed by heating at 2900 °C on the VGCF (150 nmϕ × 8 μmL), VGCF-H (150 nmϕ × 6 μmL), and VGCF-S (80 nmϕ × 10 μmL), that is, only the VGCF-X had FeO_x at the terminal end. As shown in Fig. 10.19c, the Pt/VGCF-X showed extremely high activity, and nearly 100% selective oxidation of CO (CO/O_2 = 2/1) was attained in a flow of CO (3.0 mL/min) + O_2 (1.5 mL/min) + H_2 (20.0 mL/min) + N_2 (78.5 mL/min) at 30 °C. In contrast, the Pt/CNF-p (Pt/VGCF, Pt/VGCF-H, and Pt/VGCF-S) had very low activity toward CO oxidation in H_2, and only ∼10% of CO was converted, even at 120 °C. These results are in quite good agreement with the results obtained on the Pt/CNT and Pt/CNT-p catalysts shown in Fig. 10.19b.

From these results, we can confidently conclude that catalytic oxidation of CO enhanced by H_2 or H_2O is attained by the cooperation of Pt with the Ni–MgO and FeO_x, and these promoting materials are not necessarily in contact with Pt particles. That is, the role of FeO_x and Ni–MgO is not a synergetic effect on the Pt, but is a direct participation to the oxidation reaction of CO. In other words, the oxidation of CO enhanced by H_2O or H_2 on Pt/CNT and Pt/CNF is essentially different from the catalytic reaction so far accepted for the CO + 1/2 O_2 → CO_2, the reaction (i) in Eq. (10.16). That is, a new reaction given by reaction (iii), **n** (CO + 1/2 O_2) + H_2O → **n** CO_2 + H_2O in Eq. (10.18), takes place as schematically described in Scheme 10.8b.

Before the spectroscopic identification of the key intermediate (ξ_2) in Eq. (10.18) on $FeO_x/Pt/TiO_2$ catalyst, the influence of H_2 or H_2O on the oxidation of CO on Pt/TiO_2 and $FeO_x/Pt/TiO_2$ catalysts is more precisely explained. When the temperature was raised step by step from room temperature to 60 °C in a flow of (CO (3 mL/min) + O_2 (1.5 mL/mi) + N_2 (95.5 mL/min)) with no H_2, the conversion of CO reached ∼20% on both 1 wt% Pt/TiO_2 and $FeO_x/Pt/TiO_2$ as shown in Fig. 10.18a, b and c. That is, Pt/TiO_2 and $FeO_x/Pt/TiO_2$ had almost equal catalytic activity for the oxidation of CO in the absence of H_2. If H_2 (15.0 mL/min) or H_2O was added to the reactant gas, however, the conversion of CO on the $FeO_x/Pt/TiO_2$ catalyst was abruptly increased from ∼20% to 90–100% at 60 °C as shown in Fig. 10.18a, b, whereas no such enhancement was observed on the 1 wt% Pt/TiO_2 (no FeO_x) catalyst as shown in Fig. 10.18c [56, 59]. If H_2 (20 mL/min) was replaced with an equal amount of D_2 in a flow (100 mL/min) of CO (3 mL/min) + O_2 (1.5 mL/min) + N_2 (95.5 mL/min) on a $FeO_x/Pt/TiO_2$ catalyst at 60 °C, a clear hydrogen isotope effect was observed in the conversion of CO as shown in Fig. 10.20a, and if H_2O was replaced with D_2O, a clear hydrogen isotope effect was also observed as shown in Fig. 10.20b at 60 °C [74].

It is evident that the oxidation of CO enhanced by H_2/D_2 and H_2O/D_2O exhibits almost equal hydrogen isotope effect of r_H/r_D = 1.4–1.5 for H_2/D_2 and H_2O/D_2O. The equal hydrogen isotope effect of H_2/D_2 and H_2O/D_2O indicates that the H_2O molecule is responsible for the oxidation of CO enhanced by H_2. That is, Eq. (10.18) is described as n(CO + 1/2 O_2) + H_2O → n CO_2 + H_2O. That is, one H_2O molecule reproduces "**n**" CO_2 molecules on the catalyst until it leaves the catalyst, and in this mechanism, the physical meaning of the "**n**" is as a kind of

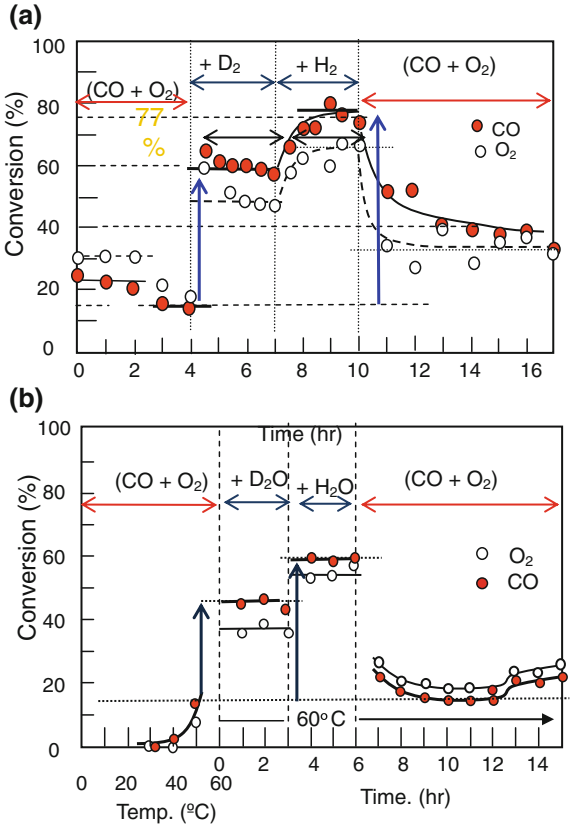

Fig. 10.20 Hydrogen isotope effect on the oxidation of CO (●) and O_2 (○) enhanced by H_2/D_2 and H_2O/D_2O. **a** Oxidation of CO in a flow (100 mL/min) of CO (3 mL/min) + O_2 (1.5 mL/min) + N_2 (95.5 mL/min) on FeO_x/Pt/TiO_2 at 60 °C and the effect of D_2 or H_2 (20 mL/min). **(b)** Effect of H_2O and D_2O on the conversion of CO and O_2 at 60 °C [74]

turnover number of H_2O molecules acting as a molecular catalyst on the FeO_x/Pt/TiO_2 catalyst. The larger the "**n**" value, the higher the selectivity for the oxidation of CO in H_2. It is evident that the selectivity for the oxidation of CO in H_2 depending on the "**n**" value of H_2O is essentially different from the selectivity given by the competitive oxidation of **reaction (i)** and **reaction (ii)** of Eq. (10.16).

The hydrogen isotope effect on the oxidation of CO suggests that the intermediates (ξ_2) involve hydrogen atom(s), and either the concentration of intermediate (ξ_2) or the rate constant at the rate determining step (iii) in Eq. (10.17) is responsible for the isotope effect. It is confidently concluded that the role of H_2O is not the activation of the Pt catalyst or the lattice oxygen, but instead makes a direct contribution to the oxidation of CO by forming intermediates (ξ_2) on the FeO_x/Pt/TiO_2 surface as will be shown below.

The oxidation of CO enhanced by H_2 and D_2 on the Pt/CNT catalyst exhibits also a hydrogen isotope effect, which is very close to the value of r_H/r_D = 1.4–1.5 on the FeO_x/Pt/TiO_2 catalyst [74] as shown in Fig. 10.21. It is more interesting that the oxidation of CO enhanced by hydrogen takes almost equal hydrogen isotope effects on FeO_x/Au/TiO_2 [75], Au/γ-Al_2O_3 [76], and Au/CeO_2 [77], and Costello

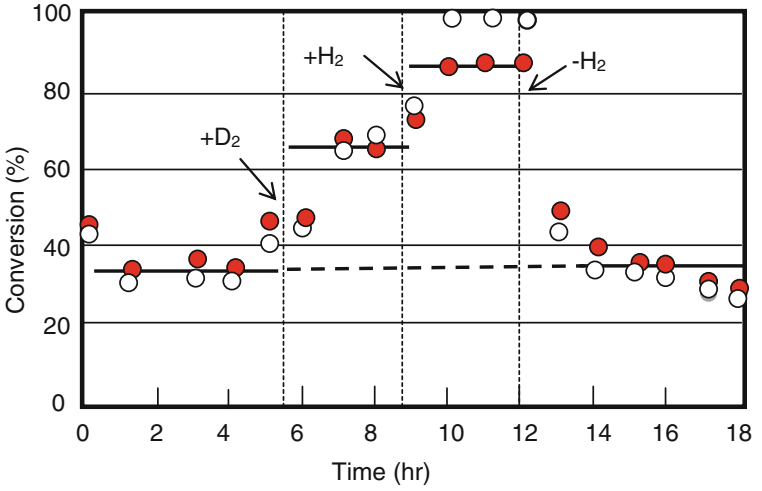

Fig. 10.21 Hydrogen isotope effect in the oxidation of CO enhanced by adding H_2 and D_2 on a 10 wt% Pt/CNT catalyst at 45 °C. Conversion of CO (●) and O_2 (○) in a flow of CO (3.0 mL/min) + O_2 (1.5 mL/min) + N_2 (95.5 mL/min) on adding H_2 or D_2 while maintaining the total flow rate of 100 mL/min [61]

et al. [76] proposed a hydroxyl–carbonyl species for the oxidation of CO on Au particles with Au^+-OH^-. Equal hydrogen isotope effect on these catalysts strongly suggested a common reaction mechanism for the oxidation of CO(a) enhanced by H_2 or H_2O, which may be a new oxidation reaction of CO via $HCOO^-$ ions on Pt proposed on the $FeO_x/Pt/TiO_2$ catalyst by Tanaka et al. [61, 74]. That is, the OH^- ion supplied from the promoting materials reacts with CO(a) on Pt to form $HCOO^-$, which very quickly changes to HCOO(a) by leasing an electron (e), and the released electron reacts with H^+ and O(a) to form highly reactive OH(a) on the Pt surface. As it will be described by the dynamics of in situ IR spectroscopy, the reaction of the OH(a) with HCOO(a) is the rate-determining reaction of the oxidation of CO enhanced by H_2O on the Pt. This new oxidation reaction of CO taking place on the Pt catalyst in the presence of promoting materials is very similar to the reaction taking place in hydrogen fuel cells. That is, the rapid transport of the OH^- ion from Ni−MgO or FeO_x to Pt is a key process of the oxidation of CO enhanced by promoting materials. The overall catalytic oxidation mechanism of CO enhanced by H_2O on the $FeO_x/Pt/TiO_2$ catalyst was deduced by the dynamics of in situ DRIFT spectroscopy, as mentioned in detail below.

An important fundamental concept in catalysis is that the catalytic processes are distinguished into the two stages: The 1st stage is the adsorption of reactant molecules on the surface, and the 2nd stage is the reaction of adsorbed species on the surface. When the adsorption of molecules is rapid, catalysis is controlled by the 2nd stage of reactions, and the overall reaction is controlled by the rate-determining slow step. The oxidation of CO on Pt foil shown in Fig. 7.3 is a prominent example

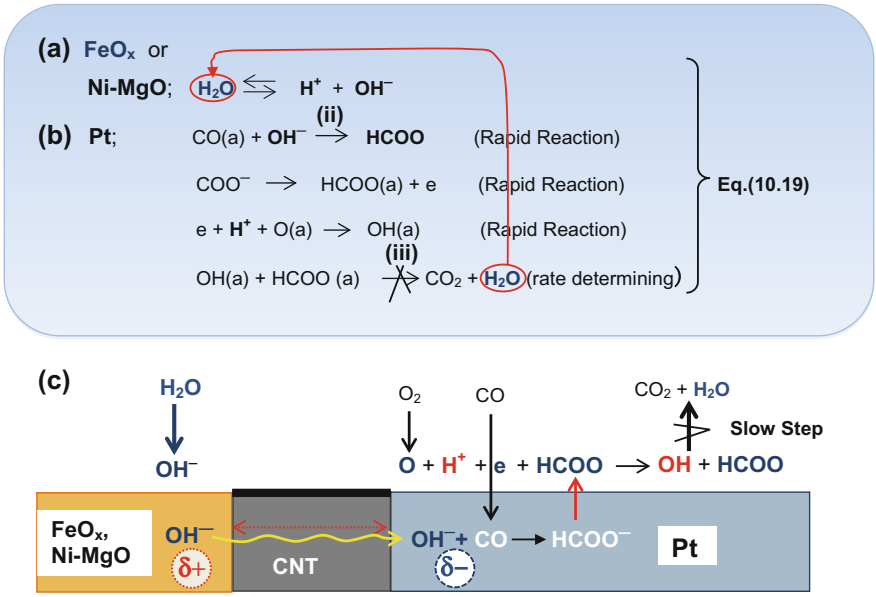

Scheme 10.10 **a** and **b**: Transported OH^- ion from FeO_x to Pt rapidly forms $HCOO^-$ anion by reaction with CO(a), where the transport of OH^- from FeO_x onto Pt occurs efficiently in the local electrostatic potential gradient made by equalization of the proton activity of H_2O on Pt and FeO_x [78] **c**: Overall reaction scheme promoted by H_2O on Pt and promoting materials

controlled by the 1st stage case, that is, the adsorption rate decided the overall rate when the pressure of CO and O_2 takes at log (P_{CO}/P_{O2}) = −5.0 to −5.3. The oxidation of CO enhanced by H_2O on Pt/CNT is quite different from this case. The OH^- ion transported from Ni−MgO to the Pt particles over a pseudo-one dimensional surface and reacts with adsorbed CO(a) on the Pt. The reaction of adsorbed CO(a) with O(a) is prohibited when the coverage CO(a) is high, but the reaction of CO(a) with OH− ion takes no retardation by adsorbed CO(a), and the overall reaction depends on the rate-determining slow reaction of HCOO(a) + OH (a) → CO_2 + H_2O on the Pt. As argued below, the driving force of the efficient transportation of OH^- ion is a local potential gradient made by the proton activity equalization of adsorbed H_2O between Ni−MgO or FeO_x and Pt particles, as described by Eq. (10.19b) and Scheme 10.10c.

The dynamic process of the formation of $HCOO^-$ and OH(a) and their reaction on the FeOx/Pt/TiO_2 catalyst were deduced by in situ DRIFT-IR spectroscopy. We observed a dynamic balance of step (i) and the following reaction of step (ii) in Fig. 10.17, where the adsorption rate of CO(a) (ξ_1) in Eq. (10.17) is sufficiently fast compared to the subsequent reaction forming (ξ_2) in either the presence or the absence of H_2, so that the blue spectrum showing adsorbed CO(a) was observed in the absence of H_2 in Fig. 10.17a and in the presence of H_2 in Fig. 10.17b, although the ratio of linearly bonded CO(a) to bridge-bonded CO (1809 cm^{-1}) was different

between (a) and (b) in Fig. 10.17. If CO is removed from the gas phase, however, adsorbed CO(a) cannot keep the dynamic balance as shown by the red IR spectra changing with time. Red spectra in Fig. 10.17a, b show the IR spectrum changing with time when the CO is removed from a steady flow of (a) ($CO + O_2$) and (b) ($CO + O_2 + H_2$) at 40 °C. The decrease of CO(a) was very slow in the absence of H_2, but was very rapid in the presence of H_2. It should be pointed out that the rapid decrease of adsorbed CO (ξ_1) does not mean the reaction of CO(a) with O(a), but is the rapid formation of intermediate (ξ_2) in step (ii) in Eq. (10.17). As it is mentioned below, the rate-determining slow reaction, step (iii), is followed by this rapid step [61, 78]. From this in-depth mechanism of the catalysis, it is clear that the difference in reactivity between the bridge-bonded CO(a) and linearly adsorbed CO on Pt has no practical meaning in the catalytic oxidation of CO enhanced by H_2 (actually H_2O) on the $FeO_x/Pt/TiO_2$ catalyst. Identification of the key intermediate (ζ_2) is essential to make clear the oxidation mechanism of CO enhanced by H_2 (or H_2O) on the $FeO_x/Pt/TiO_2$ catalyst.

In situ DRIFT spectra of catalyst involve not only the spectrum of intermediates but also the spectrum of all other adsorbed species existing on the catalyst. If the CO is removed from a steady flow of ($CO + O_2 + H_2 + N_2$) or ($CO + O_2 + N_2$), intermediate species relating to the catalytic reaction will be decreased from the surface by reactions. If an in situ DRIFT spectrum attained in a steady-state reaction of ($CO + H_2 + O_2 + N_2$) is subtracted from the in situ DRIFT spectrum attained by removing CO, the reactive intermediates will give negatively growing peaks as decreasing from the surface. Large negative peaks depict a large amount of intermediate species in a steady-state reaction on the catalyst. By this procedure, the real intermediates can be identified from the *time-resolved* in situ spectra. The in situ spectra obtained by removing CO from a steady flow of ($CO + O_2 + H_2 + N_2$) at 333 K are shown in Fig. 10.22, where the spectrum was recorded at time intervals of 30 s, 1, 5, 10, 20, 30, and 40 min [59, 79, 80].

The growth of the IR peaks with time indicates the decrease of corresponding intermediates from the surface with time by the reaction, which are CO(a) and intermediates (ξ_2). The CO removed from reactant gas reflects very rapid growth of the negative peaks at 2,172 and 2,119 cm^{-1}. At the same time, rapid decrease of linearly bonded CO(a) (2065, 2067 cm^{-1}) and bridge-bonded CO(a) (1836 cm^{-1}) by the reaction of step (ii), CO(a) $\rightarrow$ (ξ_2), in Eq. (10.18) was observed as the negative peaks grow, which is in good agreement with the red spectra indicating rapid reaction of adsorbed CO(a) in Fig. 10.17b. At the same time, rapid growth of large negative peaks was observed at 1522,1354, and 1296 cm^{-1} with time, which indicates the decrease of key intermediates (ξ_2) from the surface by the reaction.

From these time-resolved spectra, we can conclude that the adsorption of CO molecules on Pt and subsequent reaction of adsorbed CO(a) to intermediate (ξ_2), step (ii) in Eq. (10.17), is very rapidly on the $FeO_x/Pt/TiO_2$ surface, which means the decrease of intermediate (ξ_2) is the rate-determining reaction. The large negative peaks at 1,522 and 1,354 cm^{-1} with a shoulder at 1,296 cm^{-1} are very close to the spectrum observed in the oxidation of formaldehyde (HCHO) [80], the oxidation of CH_3OH on ZnO [81] and ZrO_2 [82], the adsorption of HCOOH [80–87], and a

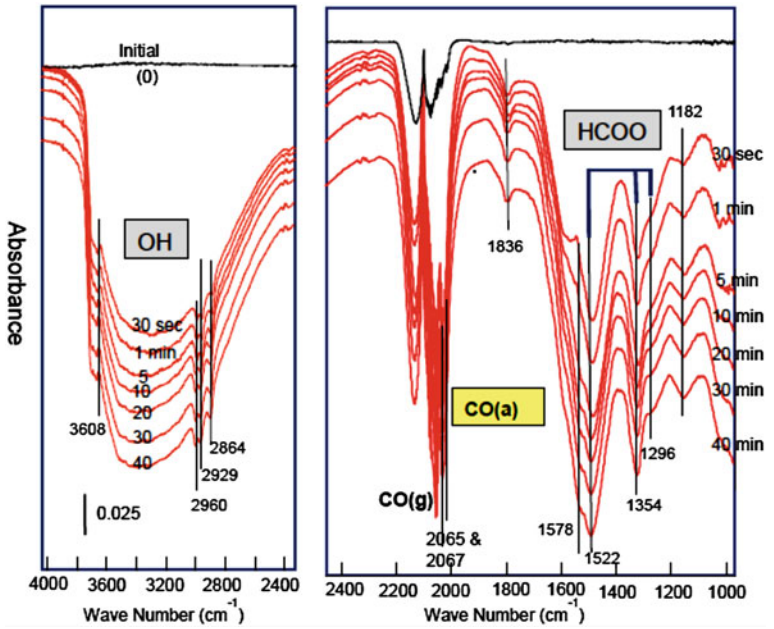

Fig. 10.22 The change in situ DRIFT spectrum of a $FeO_x/Pt/TiO_2$ catalyst after the CO was removed from a flow of ($CO + H_2 + O_2 + N_2$) at 333 K. The spectra (1)–(7) were obtained at time intervals of 30 s, 1, 5, 10, 20, 30, and 40 min after the removal of CO [59]

model calculation for HCOO(a) at 1,533, 1,377, and 1,334 cm^{-1} [59]. Taking these results into account, a key intermediate of (ξ_2) is assignable as HCOO(a) (formate) in the oxidation of CO enhanced by H_2O on the $FeO_x/Pt/TiO_2$ catalyst.

Another noteworthy result observed in the spectrum was the rapid growth of a large negative broadband at 3,000–3,800 cm^{-1} on the $FeO_x/Pt/TiO_2$ observed by removing CO from the gas phase, as shown in Fig. 10.22. Very rapid growth of this broadband may indicate the direct contribution of corresponding species to the reaction. It should be pointed out that the characteristic peaks expected for the adsorbed H_2O, the deformation vibration (scissors mode) peak at $\sim$1,650 cm^{-1}, and the symmetric stretching vibration were not observed in the surface. The amount of H_2O adsorbed on the surface should be sufficiently large during the oxidation of CO enhanced by H_2O or H_2. Taking this fact into account, the lack of the characteristic scissors mode of H_2O strongly proves that the catalyst surface is saturated with adsorbed H_2O during reaction of ($CO + H_2 + O_2$). That is, gas-phase CO gave no influence on the amount of H_2O on the catalyst surface.

Taking this fact into account, rapid growth of a large negative broadband at 3,000–3,800 cm^{-1} suggests the contribution of another key intermediate (ξ_2) to the reaction, which is a large amount of reactive OH(a) existing during the reaction on the Pt surface. If this is the case, the formation of reactive OH(a) on Pt is another important dynamic process providing a key intermediate of (ξ_2) of this catalytic

reaction, which is not the OH^- ion but is highly reactive OH(a). That is, the OH^- ion transported from the FeO_x to the Pt undergoes reaction with adsorbed CO(a), $CO(a) + OH^- \rightarrow HCOO^-$, which is a similar reaction known as an industrial reaction to produce HCOOH by the reaction of CO with $Ca(OH)_2$. The $HCOO^-$ formed on the Pt undergoes rapid release of an electron with rapid reaction of $e + O + H^+ \rightarrow OH(a)$. The subsequent reaction of HCOO(a) with OH(a) on the Pt surface, $OH(a) + HCOO(a) \rightarrow CO_2 + H_2O$, is the rate-determining reaction as described by step (iii) in Eq. (10.19). In this mechanism, the driving force for the effective transport of OH^- ions from FeO_x onto the Pt is the local electrostatic potential gradient established between FeO_x and Pt by the proton activity equalization of adsorbed H_2O molecules. These rapid processes are followed by the rate-determining slow reaction of HCOO(a) with OH(a), so that a steady-state concentration HCOO(a) and OH(a) on the Pt surface becomes large, and the two intermediates are decreased with an equal rate after removing gas-phase CO as shown in Fig. 10.23b. These results clearly show that the role of FeO_x in FeO_x/Pt/γ-Al_2O_3 is not a synergistic effect on Pt, but a new catalytic oxidation reaction of CO is established on the Pt in the presence FeO_x.

The oxidation mechanism of CO via HCOO(a) with OH(a) on the Pt is described in Eq. (10.19a). In this mechanism, worthy of remark is the role of H_2O molecule, which repeatedly contributes to the catalytic oxidation of CO. Taking account of the

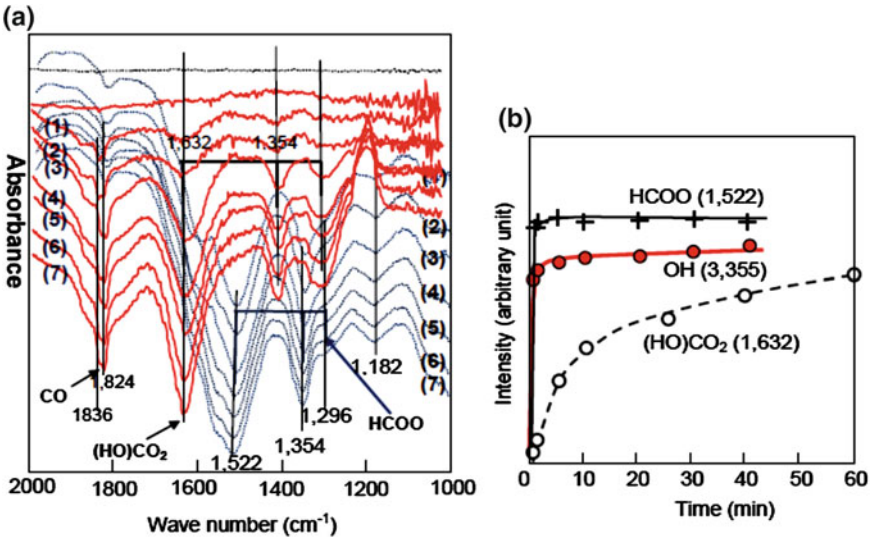

Fig. 10.23 **a** Change of in situ spectra with time when CO was removed from the gas phase in the presence of H_2 (*blue*) and in the absence of H_2 (*red*). The interval time from (1) to (7) was 30 s, 1, 5, 10, 20, 30, and 40 min. **b** The rapid growth of negative peaks for HCOO(a) (1,522 cm^{-1}) and the broad OH peak (3,355 cm^{-1}) (*solid lines*) indicate rapid removal of these species from the surface in the presence of H_2 within 1 min by the reaction, but the removal of bicarbonate peak (1,632 cm^{-1}) (*broken line*) observed in the absence of H_2 was quite slow [59]

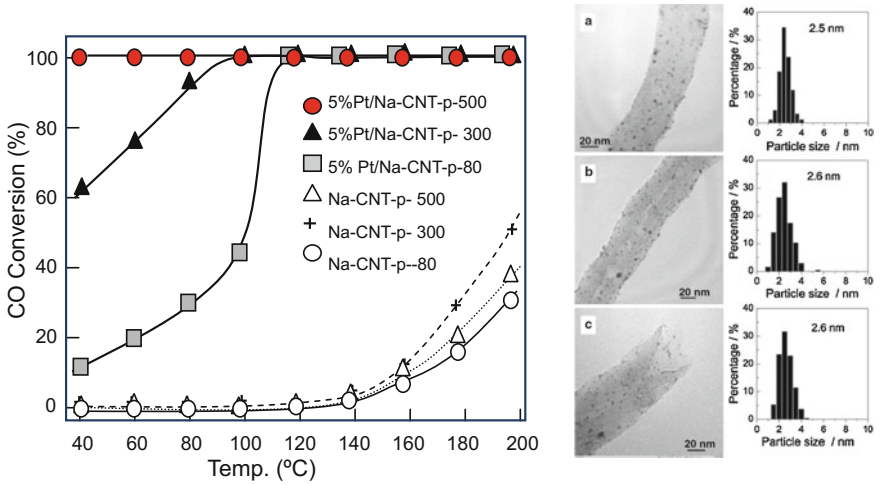

Fig. 10.24 Preferential oxidation of CO in H_2 on 5% Pt/CNT-p with intercalated Na^+. CO conversion was attained in a flow of (1% CO +1% O_2 + 50% H_2 + N_2) at F/W = 30,000 mL/ghr. Na^+ ions have little effect on the distribution and size of Pt particles [73]

oxidation of H_2 is the origin of H_2O, repeated contribution of H_2O improves the selectivity of the oxidation of CO in H_2, and ideal case is given by an equation of $\mathbf{n}$ (CO + 1/2 O_2) + $H_2O \rightarrow \mathbf{n}CO_2 + H_2O$ of Eq. (10.17).

Another interesting selective oxidation of CO in H_2 was reported by Yuan et al. on the Pt supported on Na^+−CNT-p-80 (doped Na^+ on CNT-p purified at 80 °C). The Na^+−CNT-p-300 and Na^+−CNT-p-500 were prepared by heating the Na^+−CNT-p 80 at 300 and 500 °C in Ar. Figure 10.24 shows the conversion of CO in a flow of (CO : O_2 : H_2 = 1 : 1 : 50) attained on the 5 wt% Pt/Na^+−CNT-p-80, 5 wt% Pt/CNT-p-300, and Pt/Na^+−CNT-p-500. The conversion of CO at 40 °C was markedly improved by increasing the calcination temperature for the Na^+−CNT, that is, 10% on Pt/Na^+−CNT-p-80, 60% on Pt/Na^+−CNT-p-300, and 100% on Pt/Na^+−CNT-p-500. They explained these results as a synergistic effect of Na^+ ion on the Pt catalyst that weakens CO adsorption bonds on Pt by invoking an ordinary competitive reaction mechanism, but I could say it is not a synergistic effect of Na^+ ion on the Pt catalyst, but the oxidation reaction of CO via HCOO(a) and OH(a) proposed on the FeO_x/Pt/TiO_2 catalyst. Na^+ ion may form Na_2CO_3 or $NaHCO_3$ on the Pt/Na^+−CNT-p-80, and Na_2CO_3 doped on carbon undergoes decomposition, because the K_2CO_3 doped on carbon undergoes decomposition at lower-than-normal decomposition temperature by heating in vacuum, and the K^+ ion may be dissolved into the carbon (K/C) at 650 °C [71]. In fact, the K/C prepared by heating at 650 °C had no catalytic activity for the isomerization of but-1-ene, but if O_2 was added, the surface changed to an active catalyst for the selective isomerization of but-1-ene to cis-but-2-ene (cis/trans = ∼3.7–4.0) via anionic allyl-intermediate at room temperature. Taking this result into account, the

role of Na^+ ion in the oxidation of CO on Pt/Na^+-CNT-p-500 is not a synergistic effect on Pt, but the formation of OH^- ion and its transports to the Pt take place on the Pt/CNT with Ni−MgO.

If one H_2O molecule promotes n-times the oxidation of CO as described by n (CO + 1/2 O_2) + H_2O → n CO_2 + H_2O, one H_2O molecule forms "**n**" CO_2 molecules. The H_2O molecule is provided by oxidation of H_2 in the PROX (preferential oxidation) reaction of CO in H_2. Therefore, "n" is a kind of turnover number of an H_2O molecule in the catalytic oxidation of CO, and the n/(n + 1) is a selectivity factor. As mentioned schematically in Scheme 10.9, observed oxidation of CO with O_2 is given by (reaction (i) + reaction (iii)), and reaction (iii) becomes predominant at low temperature, but reaction (i) becomes predominant at high temperature. If the contribution of reaction (i) is low, the selectivity is given by n/(n + 1), which is higher than 50% and attains nearly 100% by preventing H_2O molecules escaping from the catalyst.

From this point of view, the highly selective oxidation of CO in excess H_2 observed by Fukuoka et al. [60] on Pt nano-rods supported inside silica nanotubes is quite interesting. As shown in Fig. 10.25, the reaction was performed by raising the temperature starting from room temperature in a flow of (CO + O_2 + H_2 + N_2) of (1 : 1 : 93 : 5) % at 1,200 mL/hr (GHSV), and the oxidation of CO with nearly 100% selectivity was attained on the Pt nano-rods (3 nm × several hundred nm) held inside SiO_2 nanotubes at 80 °C. If the Pt particles were supported on the outer surface of the SiO_2 nanotubes, their activity and selectivity for the oxidation of CO in H_2 were almost equal to those of ordinary Pt/SiO_2 and Pt/Al_2O_3 catalysts as shown in Fig. 10.25. They explained these results as the formation of some "specific Pt" inside of SiO_2 nanotubes by premising the traditional competitive oxidation mechanism of CO and H_2.

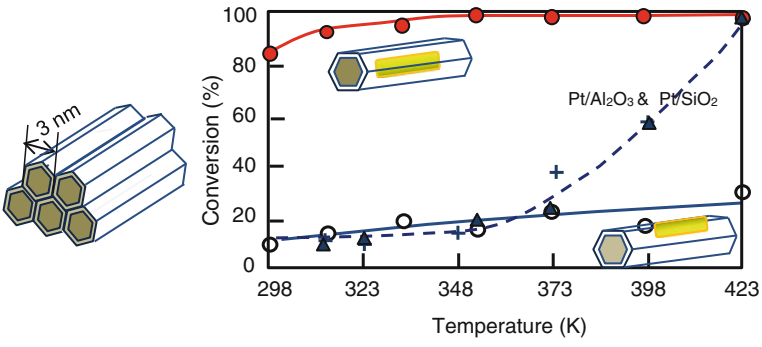

Fig. 10.25 Model of silica nanotubes and conversion of CO in the PROX reaction in excess H_2. Conversion of CO on Pt rods supported within SiO_2 nanotubes (●) and on the external surface of SiO_2 nanotubes (○) in a flow of (CO : O_2 : H_2 : N_2 = 1 : 1 : 93 : 5) % at GHSV = 1,200 over 100 mg catalyst (5 wt% Pt). Reference activities of Pt/SiO_2 (▲) and Pt/Al_2O_3 (+) are indicated with broken line [60]

However, their results significantly proved the new oxidation mechanism for the selective oxidation of CO in H_2 proposed in Scheme 10.10, that is, nearly 100% selective oxidation CO in H_2 is attainable "if H_2O molecules are confined in a limited space." If oxidation of CO is enhanced by H_2O on the Pt nano-rod held inside of SiO_2 nanotube by the mechanism proposed in Eq. (10.19), one H_2O molecule may repeatedly contribute to the oxidation of CO promoted on the Pt nano-rods in SiO_2 nanotube, because the effusion rate of H_2O molecules from the capillary is very slow compared to CO_2. If this is the case, catalytic oxidation of CO by the Pt nano-rod held in the SiO_2 nanotubes is an ideal case of the oxidation of CO promoted by H_2O via reaction of HCOO(a) with OH(a), where the "**n**" in equation $\mathbf{n}(CO(a) + 1/2\ O_2) + H_2O \rightarrow \mathbf{n}\ CO_2 + H_2O$ will take very large value.

According to this new concept for the selectivity proposed by $\mathbf{n}(CO + 1/2\ O_2) + H_2O \rightarrow \mathbf{n}\ CO_2 + \mathbf{H_2O}$, H_2O molecule is acting as a molecular catalyst on the surface, so that highly selective oxidation is preferential at lower than 80 °C. However, it would be possible to confine H_2O molecules in a space at higher temperature, and it would be possible to design highly selective and highly active catalyst working at high temperature. The highly selective PROX reaction of CO by Pt nano-rods in SiO_2 nanotubes observed in Fig. 10.25 at higher than 100 °C is an example. The presence of H_2O molecules confined in SiO_2 nanotubes was confirmed experimentally even at 398 K by the proton conductivity of TiO_2−P_2O_5 and 12-tungstophosphoric acid held within SiO_2 nanotubes. Yamada et al. [88] obtained 2×10^{-2} S cm^{-1} at 433 K (160 °C) for TiO_2−P_2O_5 in a mesoporous nano-composite, and Lu et al. [89] attained 3.4×10^{-2} S cm^{-1} at 473 K (200 °C) by using 12-tungstophosphoric acid in SiO_2 nanotubes, and a direct methanol fuel cell generating 235 mW cm^{-2} was accomplished at 423 K.

Another curious phenomenon observed by Yi et al. [77, 90] in the oxidation of CO in H_2 ($CO/O_2 = 1.0$, $CO/H_2 = 1/50$) on Au/CeO_2 catalysts is also well rationalized by this mechanism. They found that the selectivity for the oxidation of CO depends markedly on the crystalline shape as shown in Fig. 10.31, but the total consumption of oxygen is not affected by the crystalline shape of CeO_2. This is a case showing the selectivity depending on the residence time of H_2O by the support materials, that is, the residence time of the H_2O depends on the ratio of $(Au^+ + Au^{3+})/(Au^0 + Au^+ + Au^{3+})$ which takes different values depending on the crystalline shape on CeO_2, so that the crystalline shape on CeO_2 gives influence only on the selectivity for the oxidation of CO but not on the activity.

The mechanism of new catalytic oxidation of CO enhanced by H_2O encourages us to design high-performance catalysts by keeping H_2O molecules on the surface for longer time as it will be discussed in Sect. 10.5.

As it was mentioned above, the $FeO_x/Pt/TiO_2$ surface is saturated with H_2O molecules during the oxidation of CO in H_2. If we consider once again the mechanism of the catalytic oxidation reaction of CO enhanced by H_2O on the $FeO_x/Pt/TiO_2$ and Pt/CNT, efficient transport of OH^- anions should take place from the promoting materials to Pt in catalysis. Efficient transport of OH^- anions may take place according to an electrostatic potential gradient established between the Pt and promoting materials according to the proton activity of hydrated H_2O molecules. It

is similar to the oxide immersed in water, where the proton activity is different between the H_2O molecules hydrated on oxide and H_2O molecule of aqueous solution, so that proton activity equalization takes place between the hydrated oxides and aqueous solution by ionization of hydrated H_2O molecule (see Appendix). When this process takes place on the surface, electrostatic potential gradient is established by a different proton activity of adsorbed H_2O molecules on the Pt and promoting material. To keep the potential gradient during oxidation reaction of CO, OH^- anion should be efficiently transported from the FeO_x to Pt surface, where the driving force is a series-connected rapid reactions on the Pt: ($OH^- + CO(a) \rightarrow HCOO^- \rightarrow HCOO(a) + e$) and ($e + H + 1/2\ O_2 \rightarrow OH(a)$), and the overall oxidation reaction of CO is regulated by the reaction of HCOO(a) with highly reactive OH(a) on the Pt catalyst as described by Eq. (10.19b) [78]. As the Pt is perfectly separated from the Ni–MgO and FeO_x on Pt/CNT and Pt/CNF catalysts, the dynamic transportation of OH^- ion on the surface is indispensable in catalytic oxidation of CO enhanced by H_2O. As it was mentioned above, origin of the electrostatic gradient between the Pt and promoting material is the different proton activity of H_2O molecules adsorbed on different materials on a same surface, that is, proton activity equalization takes place over the hydrated surface. In other words, the acidic or basic nature of adsorbed H_2O molecules is different in Ni−MgO or FeO_x and Pt; more basic materials (H_2O has lower activity of H^+) take more positive charge (δ+) ($H^+/OH^- > 1$), less basic materials take more negative charge (δ−) ($H^+/OH^- < 1$) on the surface, and the hydrated surface should keep neutrality.

No such local electrostatic potential gradient appears without hydrated H_2O molecules on the FeO_x/Pt/TiO_2 and Pt/CNT−Ni−MgO surfaces, so that no catalytic oxidation reaction of CO via HCOO and OH takes place on the Pt surface as shown by an in situ DRIFT spectrum shown in Fig. 10.23a, b. In this in situ DRIFT spectrum, a slow decrease of bicarbonate peaks ($(OH)CO_2$) was observed on the surface. The dynamics of intermediates observed in the oxidation of CO in the presence of H_2 is a good example showing the complexity of catalysis, which is difficult to deduce by characterization of the catalyst by using EXAFS, TEM, XRD, etc., or by calculations based on a speculative mechanism.

We consider once again the origin of the potential gradient made by different proton activity of the H_2O molecules adsorbed on the catalyst surface. If two materials existing on a surface are hydrated, hydrated H_2O molecules on the two materials have different proton activity, so that the ionization equilibrium of H_2O molecules between the two materials makes local electrostatic gradient between the two materials. It is similar to the different zero point of charge (ZPC) of different oxides in aqueous solution (pH). So far, little attention has been paid to ionic processes on metal catalysts, but an ionic process should be considered if H_2O molecule is improved in the reaction. One experiment suggesting ionic process in catalysis was given by Boudart et al. [91]. They showed that the reduction of WO_3 mixed with Pt/Al_2O_3 powder occurs with H_2 only in the presence of H_2O or alcohols, that is, the reduction of pale yellow WO_3 to blue H_xWO_3 by H_2 occurred only in the presence of H_2O or alcohol molecules. This phenomenon was explained by the

transport of H^+ ions from the Pt surface onto the WO_3 with adsorbed water or alcohol molecules according to the reaction $WO_3(H_2O)_x + H_3O^+ + e \rightarrow H_xWO_3 + H_2O$, where the electron (e) is assumed to transport throughout the bulk. This process is similar to the reaction taking place in a hydrogen fuel cell, where the H_3O^+ and electron are formed on the Pt anode by the reaction ($1/2\ H_2 + H_2O \rightarrow H_3O^+ + e$). The H_3O^+ transported to the cathode through an ion-conductive membrane and the electron (e) transported through the external circuit react with O_2 at the anode, $2e + 1/2\ O_2 + 2\ H_3O^+ \rightarrow 3\ H_2O$.

It should be reminded that electrostatic potential effect was also observed in the selective reaction of Cu atoms with the $Ag{-}CO_3$ dots and $(-Ag-O-)$ strings coexisting on the Ag(110) surface shown in Fig. 5.2a [92, 93] and Scheme 5.1. If Cu atoms are vaporized by heating a Cu/W filament on a composite [$(2 \times 1)(-Ag-O-) + (Ag-CO_3)$ dots]/Ag (110) surface, Cu atoms selectively react with the (2×1) $(-Ag-O-)$ strings to form a new hybrid surface of [(1×2) $(-Cu-O-) + Ag-CO_3$ dots], on which the $(-Cu-O-)$ strings grow in the <1–10> direction perpendicular to the $(-Ag-O-)$ strings, with redistribution of the $Ag-CO_3$ dots as shown in Fig. 5.2b. On the other hand, if this composite [$(-Ag-O-) + (Ag-CO_3)$-dots]/Ag (110) surface is scanned by using a W-tip coated with Cu, the Cu atom selectively reacts with $Ag-CO_3$ dots instead of the $(-Ag-O-)$, as shown in Fig. 5.2c [93]. This may be the first experimental evidence proving the effect of local potential on the selectivity of chemical reactions.

Appendix:
When a metal oxide is immersed in water, the hydrated oxide surface takes a charge depending on the proton activity of the hydrated H_2O molecules to that of water, which is similar to the ionization of hydrated metal ions in aqueous solution. The ionization equilibrium of a metal ion in water depends on the proton activity of coordinated H_2O molecules as described by Eq. (10.20).

$$M(H_2O)_n^{\alpha+} + H_2O \rightleftharpoons M(H_2O)_{n-1}(OH)^{(\alpha-1)+} + H_3O^+ \qquad (10.20)$$

It is known that the proton activity of hydrated metal ions given by pK_a in aqueous solution depends markedly on the charge of the metal ions. It was accepted that the ionization equilibrium of hydrated metal ions with different charges (α) was difficult to compare on a common scale [94]. However, a valuable universal scale of the electronegativity (χ_α) for metals and metal ions by Eq. (10.21) was given by Tanaka et al. [95, 96], that is, the electronegativity (χ_α) takes a linear relationship between the proton activity of hydrated metal ions (pK_a value).

Here, we explain briefly the definition for the electronegativity of metal ions (χ_α) given by Eq. (10.21). As it is known, the concept of electronegativity was empirically derived by Pauling to explain the bond strength between heteroatoms, $A_2 + B_2 \rightarrow 2\ A-B$. A similar concept was more theoretically derived by Mulliken by an equation $\boldsymbol{\chi_0 = (I + A)/2}$, where "**I**" is the ionization energy of M^0 to M^{+1} ion and "**A**" is the electron affinity of M^0 to M^{-1} ion. As was pointed out by Iczkowski et al. [97], the electronegativity defined as $(I + A)/2$ by Mulliken is the

tangent to the ionization energy curve at charge of zero. If the ionization energy of metal atoms and ions is described by their ionic charge (α), a quadratic equation is attained as described by Eq. (10.21), and the tangent at charge zero is the Mulliken electronegativity.

$$\begin{aligned} I &= \sum I_\alpha = a\,\alpha + b\,\alpha^2 + \chi\alpha^3 + \cdots \sim a\,\alpha + b\,\alpha^2 \\ \chi_\alpha &= \partial \sum I_a / \partial\alpha \approx (1 + 2\,\alpha)\chi_o \end{aligned} \tag{10.21}$$

where χ_o is the electronegativity of neutral metal atoms, described by the Pauling electronegativity scale. If this idea is extended to metal ions, we can derive the electronegativity of metals and metal ions (χ_i). As shown in Fig. 10.26a, the proton activity of hydrated metal ions in aqueous solution has a linear relationship with the electronegativity of the metal ions (χ_α), which is given by Eq. (10.22i).

$$\mathrm{pKa} = 20(1 - \chi_\alpha/14) \tag{10.22i}$$

$$\mathrm{ZPC} = 16.8(1 - \chi_\alpha/22) \tag{10.22ii}$$

If a metal oxide is immersed in aqueous solution, its surface is hydrated with H_2O molecules, and the H_2O molecules undergo the ionization equilibrium expressed by $\mathrm{oxide(H_2O)_n} + H_2O \rightleftharpoons \mathrm{oxide(H_2O)_{n-1}(OH)^-} + H_3O^+$, where the surface charge depends on the proton activity of the hydrated surface with respect to that of liquid H_2O. When the proton activity (pH) of the surface becomes equal to that of the solution, surface charge becomes zero, which is the zero point of charge (ZPC); the ZPC of oxide surfaces indicates the proton activity of the hydrated oxide surface in aqueous solution. As shown in Fig. 10.26b, the ZPC of various oxides varies linearly with the electronegativity χ_I of the metal ions of oxides as expressed by Eq. (10.22ii).

The linear relationship in Fig. 10.26a, b asserts the formation of a potential gradient between the two different hydrated materials by proton activity equalization in adsorbed H_2O molecules. As the $FeO_x/Pt/TiO_2$ surface is saturated with H_2O during oxidation in a flow of ($CO + H_2 + O_2$), proton activity equalization of H_2O is established by adjusting the local concentration of $[OH^-]$ and $[H^+]$; $[OH^-]/[H^+] > 1$ on the FeO_x surface; and $[OH^-]/[H^+] < 1$ on Pt.

Hydrogenation of CO and CO_2 to CH_3OH is an important catalytic reaction. The activity of the Rh catalyst for the hydrogenation of (a) CO_2 and (b) CO is markedly influenced by the support oxides as shown in Fig. 10.27 [98]. Taking account of the valence of metal ions on the surface of oxides, the electronegativity of metal ions (χ_i) is an average parameter. We could speculate some sites on the oxides that contribute as promoting materials to the catalytic reaction of the formation of alcohols on Rh catalyst although it is not experimentally shown at the present time. If the role of support oxides is not the activation of Rh metals but the contribution to the catalytic reaction, we could deduce the role of support oxides by studying the dynamics of intermediates during reaction by in situ spectroscopy.

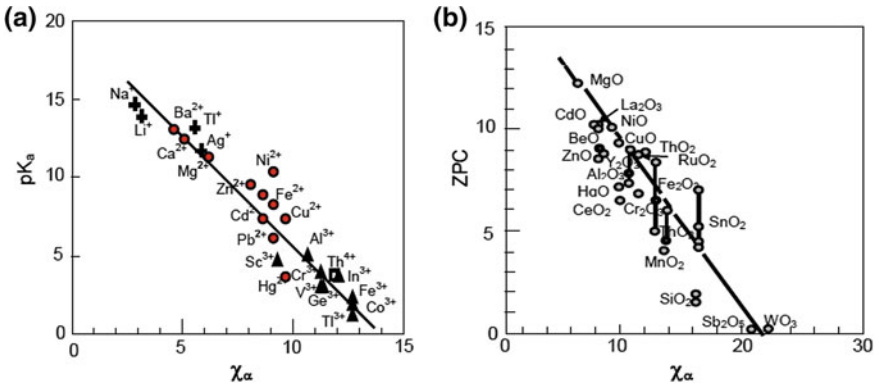

Fig. 10.26 a Ionization constant (pKa) of aqueous metal ions in water at 25 °C depending on the electronegativity of the +α valence ion (χ_α). **b** The pH of water providing zero point of charge (ZPC) of oxide surfaces plotted against the electronegativity of ions [96]

10.5 Roles of Promoting Materials in Catalysis

The role of promoting materials is one of the difficult problems in catalysis, as described in preceding Sect. 10.4. It might be more difficult to make clear the roles of support materials in catalysis. As shown in the Appendix of Sect. 10.4, the hydrogenation of CO and CO_2 to alcohol by Rh catalyst depends on support oxides as shown in Fig. 10.27, but the role of support oxides is no simple as is explained by Lewis acidity of metal ions [98], because the valence state of oxide surface should be quite heterogeneous. One interesting phenomenon is selective oxidation

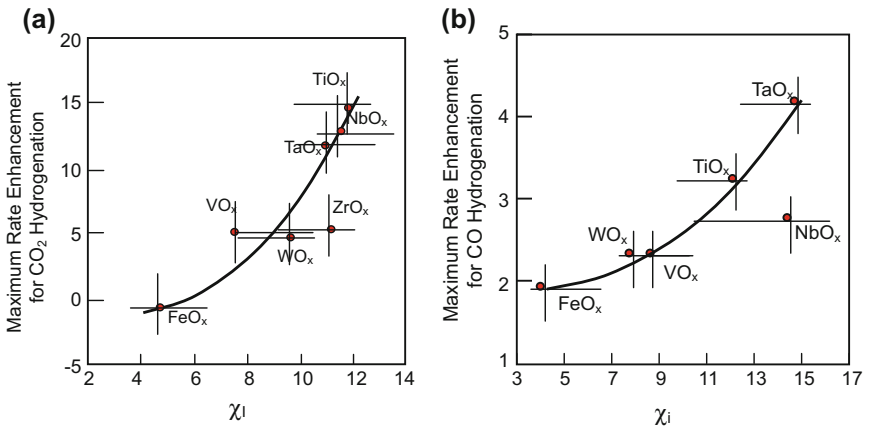

Fig. 10.27 Maximum enhancement in the rate of **a** CO_2 and **b** CO hydrogenation on Rh catalysts. Catalytic activity markedly depends on the electronegativity of metal ions of the support oxides [98]

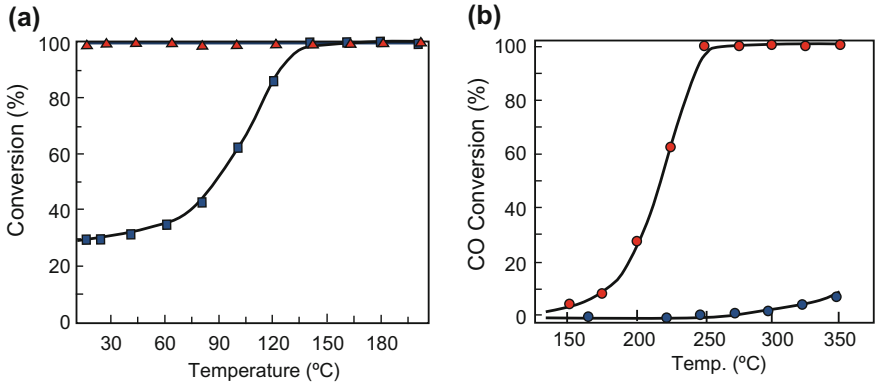

Fig. 10.28 Activation of Pt catalyst by alkali metals or ions. **a** Oxidation of HCHO with O_2 on 1% Pt/TiO_2 (■) and 2% Na-1% Pt/TiO_2 (▲). HCHO 600 ppm, O_2 20 vol.% with ~50% relative humidity. Total flow rate of 50 cm^3/min with balance gas of He [65]. **b** Water gas shift reaction on 1% Pt/SiO_2 (●) and 1% Pt/SiO_2 with 3% Na (●) catalysts [62]. Conversion of CO (2% CO + 10% H_2O) in a flow of He contact time of 0.09 g·s/cm^3

of CO in H_2 on Au catalyst supported on CeO_2 having different crystal shapes. The turnover number "**n**" of a H_2O molecule in the reaction (iii) of Eq. (10.18) is influenced by the Au^{3+} ions in CeO_2 as discussed below.

Zhang et al. [65] reported the oxidation of HCHO on a 1% Pt/TiO_2 catalyst, in which the activity was markedly improved by adding 1–2% of alkali metals; 100% conversion of HCHO (HCHO 600 ppm 20 vol.% O_2 in He with 50% relative humidity and flow rate of 50 cm^3/min) was achieved at room temperature, as shown in Fig. 10.28a. Characterization of the Na–Pt/TiO_2 catalyst by XANES and EXAFS suggested no Pt–Pt bonds existed, and it was concluded that atomic dispersion of Pt was attained by adding 1–2% Na. A similar promoting effect on the oxidation of HCHO was also confirmed for other alkali metals (Li and K on the Pt/TiO_2 catalyst) in the presence of H_2O. From these results, they concluded that alkali metals lead to dispersal of Pt in the form of $Pt{-}O(OH)_x$, which is the active site for the oxidation of HCHO on the Na–Pt/TiO_2 catalyst. The in situ DRIFT spectra during oxidation of HCHO on the Na–Pt/TiO_2 catalyst showed large HCOO(a) peaks. Based on these observations, they proposed an oxidation mechanism of $HCHO \rightarrow HCOO^- \rightarrow CO(a) + O(a) \rightarrow CO_2$, in which the decomposition of $HCOO^-$ to CO(a) was deduced as the rate-determining step on the $Na^+{-}Pt/TiO_2$ catalyst. However, oxidation of CO(a) is not very rapid, especially in the absence of Pt particles. Possibly, a reaction similar to that proposed on the $FeO_x/Pt/TiO_2$ catalyst, $HCOO(a) + OH(a) \rightarrow CO_2 + H_2O$, may take place. If this is the case, catalytic oxidation of HCHO with O_2 may occur by the formation of highly reactive OH(a) on the surface, which is similar to the oxidation of CO on Pt/CNT and Pt/CNF controlled by the transport rate of OH^- ions from Ni–MgO or FeOx onto Pt.

We consider once again the in situ IR spectra shown in Fig. 10.17a. When the gas-phase CO is removed, adsorbed CO(a) on the Pt is decreased rather slowly at 60 °C (333 K) by oxidation of CO(a) with O(a) in the absence of H_2. However, if H_2 is present (actually H_2O), CO(a) on the Pt (either bridge-bonded or linearly bonded) is very quickly changed to $HCOO^-$ by rapid reaction with OH^- ion on Pt, where OH^- ion is supplied from FeO_x onto Pt. Accordingly, the transport of OH^- ion from FeOx to Pt and the reaction of OH^- with CO(a) to form $HCOO^-$ should be more rapid than the rate-determining reaction, as shown in Fig. 10.17b. The rapid oxidation of HCHO on the Na^+−Pt/TiO_2 catalyst may not involve the oxidation of CO(a) with O(a), but instead, a new catalytic reaction of HCOO(a) with OH(a) may take place.

On the other hand, Stephanopoulos et al. [62] reported significant improvement of the water gas shift reaction on Pt/Al_2O_3 and Pt/SiO_2 by alkali metals and hypothesized the formation of active Pt$(OH)_x$ in the presence of alkali metals. However, it should be remembered that the water gas shift reaction proceeds at temperatures above 200 °C even on an active 3% Na–1% Pt/SiO_2 catalyst as shown in Fig. 10.28b, whereas the oxidation of HCHO on the Na^+−Pt/TiO_2 catalyst takes place at room temperature. As discussed in preceding Sect. 10.4, H_2O molecules function as a molecular catalyst to promote the reaction taking place between the two materials, FeO_x or Ni−MgO and Pt. The role of the H_2O molecule is essentially different from its contribution as a reactant molecule in the water gas shift reaction at temperatures higher than 200 °C, although the activity of Pt catalysts depends on the support oxides (SiO_2, Al_2O_3, and CeO_2), and alkali metals (K, Na) are promoters. It should be also pointed out that the activation energy of 70 $\pm$ 5 kJ/mole for the water gas shift reaction does not change on changing the support oxides (SiO_2, Al_2O_3, or CeO_2) or adding alkali metals (K, Na) [62]. These phenomena strongly indicate that the reaction mechanism is not changed by the alkali metals, which is essentially different from the new catalytic oxidation of CO involving H_2O. That is, the improved activity of the water gas shift reaction is caused by an increase in the active form of the Pt catalyst, perhaps Pt–alkali metal–$O_x(OH)_y$, but the mechanism of the water gas shift reaction itself is not changed.

The size effect of Au particles supported on specific oxides observed by Haruta et al. [67, 68] for the oxidation of CO is discussed once again in relation to the promoting materials. As shown in Fig. 10.29a, when the Au particles on specific oxides become smaller than 3 nm, the Au particles abruptly become a highly active catalyst for the oxidation of CO. This activity is not due to the role of Au^{3+} ions although Stephanopoulos et al. [63] hypothesized Au^{3+} ions as the active sites in relation to the water gas shift reaction on an Au/CeO_2 catalyst at 473 K. The physical meaning of the critical size of 3 nm is an unanswered problem, because the steep increase of activity as a function of particle size is difficult to explain in terms of the perimeter length of Au particles.

If the catalytic activity of a metal is changed by the support or promoting materials, it is generally explained by some effect on the metals such as the particle size, crystal form, or chemical form of the metal particles, but a change in the reaction mechanism due to the support or promoting materials has rarely been

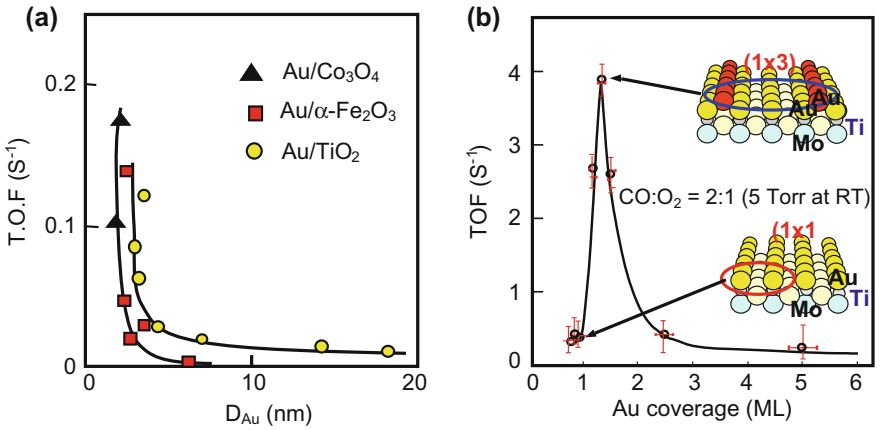

Fig. 10.29 **a** Activity of Au particles depending on the particle size supported on oxides, TiO_2, α-Fe_2O_3, and Co_3O_4, for the oxidation of CO [67]. **b** Highly active but unstable (1 × 3) Au–Bi layer for the oxidation of CO formed on TiO_x monolayer [69]

considered. As discussed in preceding Sect. 10.4, oxidation of CO on the Pt/TiO_2, Pt/CNT-p, and Pt/CNF-p catalyst takes no effect of H_2 and/or H_2O, but the oxidation of CO is markedly enhanced by H_2 or H_2O in the presence of the promoting materials such as Ni−MgO and FeO_x [61]. It was evident that the role of promoting materials is not the activation of Pt or providing an active form of Pt, but rather that a new catalytic oxidation reaction takes place in the presence of the promoting materials. From this perspective, the activity of Au catalysts reported on Au/TiO_2 [64], Au/Co_3O_4 and Au/α-Fe_2O_3 [68], Au/α-Fe_2O_3 [95], and pure Au powder (10 μm) overlaid with TiO_2 [102] is noteworthy. Hutchings et al. [72, 99] reported that the activity of Au/α-Fe_2O_3 catalysts depended on the calcination temperature: Calcination at 298 K yielded an active catalyst for CO oxidation, whereas the calcination of Au/α-Fe_2O_3 at 673 K gave very low activity. The effect of calcination temperature was explained by preferential oxidation of CO via a carboxylate intermediate on Au/α-Fe_2O_3 catalysts with Au^{3+} ions, which was evaluated by characterizing the core-level binding energy of Au($4d_{5/2}$) by XPS spectroscopy. On the other hand, Daniells et al. [101] also observed the oxidation of CO was enhanced by H_2O on Au/Fe_2O_3 catalysts at room temperature, but the activity dropped upon heating to 400 °C. Taking these results into account, they proposed the formation of the less stable bicarbonate, which reacts with OH^-, and that deactivation by heating at 400 °C was explained by the decrease of OH^-. This explanation proposed a catalytic reaction promoted by a new form of catalyst. Costello et al. [105] also observed the oxidation of CO on an Au/γ-Al_2O_3 catalyst at room temperature in the presence of H_2O or H_2 and proposed the oxidation of CO via bicarbonate, which undergoes decomposition by an ensemble operation of Au^+−OH^- with Au atoms, that is, the formation of an active Au catalyst was premised. Smit et al. [107] showed a significantly low activity for Au supported on

Fe_2O_3 with few −OH groups, even though the chemical composition and the structure were almost identical to a sample with high activity but more −OH groups. Therefore, they concluded that the presence of OH groups was responsible for low-temperature oxidation of CO, but that bicarbonates were not intermediates in this reaction. They proposed the reaction of the HCOO(a) intermediate with O(a) according to the equation 2 HCOO(a) + 2 O(a) → 2 CO_2 + H_2O with a process of $Fe^{3+}O^{2-}$ + H_2O → Fe^{3+} $(OH^-)_2$, which is very similar to the mechanism proposed on FeO_x/Pt/TiO_2. However, the origin of improved activity of MnO_x/Pt/Al_2O_3 [108], Ru−Pt/Al_2O_3 [93], CeO_2/Pt(111) [70], FeO/Pt(111) [103], Ru/Al_2O_3, and Pt-shell/Ru-core nanoparticles [110], and Pt nano-rods in SiO_2 nanotubes [59] is still not clear. We have to consider once again the origin of the activity and of its changes due to promoting materials, which are either the formation of an "**active catalyst**" or providing a "**new catalytic reaction**."

The activity of a catalyst is very often changed by promoting materials and by varying the pretreatment temperature of the catalyst, which is one origin of confusion concerning the activity. Consider once again the activity based on two distinctive processes: The 1st one is the rate of supply of molecules or ions to the active sites, and the 2nd is the subsequent reactions on the catalyst. One can readily understand the meaning of these two categories when considering the oxidation of CO on a Pt foil shown in Fig. 7.3. The observed phenomena on the Pt foil show that it is a typical case of the 1st category, in which the reaction rate is decided by the adsorption rate (collision number/sec) of CO molecules, because the surface reaction is more rapid than the supply of CO. The oxidation of CO enhanced by H_2O on Pt/CNT is another case of the 1st category, where the supply of OH^- ion from Ni−MgO to the Pt particles is the key step of this catalytic reaction, which is the 2-D diffusional supply of OH^- ion from Ni−MgO to Pt. In this case, however, an ionization equilibrium of H_2O is established between the Ni−MgO and Pt during catalysis, that is, the supply of OH^- ion from Ni−MgO or FeO_x to Pt is far more rapid than the rate-determining step of the reaction on Pt, HCOO + OH → CO_2 + H_2O. That is, as described in detail in preceding Sect. 10.4, the rate-determining reaction of HCOO + OH → CO_2 + H_2O on the Pt/CNT is obscured by the rapid preceding steps of the supply of OH^- ion and rapid adsorption of CO and O_2 on the Pt.

Stephanopoulos et al. [63] showed by Mössbauer spectroscopy that an active Au/Fe_2O_3 catalyst for low-temperature oxidation of CO in H_2 necessarily contained Au^{3+} ions and emphasized the lack of contribution of metallic Au particles to the water gas shift reaction on Au/CeO_2 at 473 K. It should be remembered that the water gas shift reaction, CO + H_2O → H_2 + CO_2, occurs at temperatures above 200 °C, but the oxidation of CO enhanced by H_2O proceeds at temperatures lower than 100 °C, that is, the two reactions are essentially different reactions. Au ions are indispensable, but metallic Au particles may not be required for the water gas shift reaction. In contrast, both Au ions and Au metal particles are required for the low-temperature oxidation of CO enhanced by H_2 or H_2O. This is a typical example confusing the essential difference between "**the activation of catalyst**" and "**providing a new reaction**." To demonstrate the difference between these roles, the

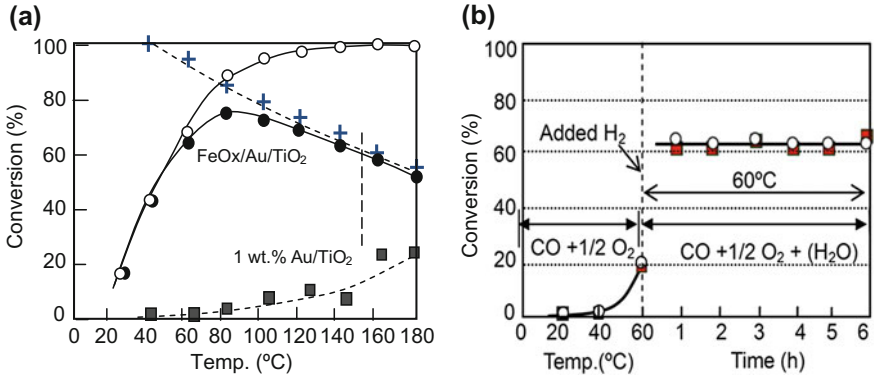

Fig. 10.30 **a** Oxidation of CO enhanced by H_2 on 1 wt% Au/TiO_2 and $FeOx/Au/Ti_2$ catalysts, where the amount of FeO_x is ~100 wt% with respect to TiO_2. Very low active 1 wt% Au/TiO_2 catalyst (■) changed to an active catalyst (●) for the selective oxidation of CO by adding a large amount of FeO_x on 1 wt% Au/TiO_2: conversion of CO(■), conversion of O_2 (○), and the selectivity for the oxidation of (+) in a flow of CO : O_2 : H_2 = 3.0 : 1.5 : 20 at 100 mL/min. **b** Conversion of CO (■) enhanced by H_2 at 60 °C on $FeO_x/Au/TiO_2$; the selectivity was nearly 100% as shown by conversion of O_2 (○). The flow rate was changed from 100 mL/min (CO : O_2 : N_2 = 3 : 1.5 : 95.5) to (CO : O_2: N_2 : H_2 = 3 : 1.5 : 75.5 : 20) by the addition of H_2 [75]

oxidation of CO was studied by using inactive large Au particles supported on TiO_2 (1 wt% Au/TiO_2). As shown in Fig. 10.19a, large Au particles supported on TiO_2 were inactive for the oxidation of CO in H_2 at temperatures below 100 °C. If this Au/TiO_2 catalyst was covered with a large amount of FeO_x, the $FeO_x/Au/TiO_2$ catalyst became active for the low-temperature oxidation of CO in H_2, as shown in Fig. 10.30a [75]. The role of FeO_x in the $FeO_x/Au/TiO_2$ catalyst may be the same as that in the $FeO_x/Pt/TiO_2$ catalyst shown in Fig. 10.18 and that of the FeO_x on the Pt/CNF catalyst shown in Fig. 10.19. That is, the role of FeO_x is not the activation of Au and Pt metals for the oxidation of CO with O_2, but to provide a new oxidation reaction of CO involving ionic intermediates in the presence of FeO_x.

In fact, the oxidation of CO enhanced on the $FeOx/Au/TiO_2$ catalyst by H_2 and D_2 exhibited a hydrogen isotope effect of r_H/r_D = 1.4, which is equal to the isotope effect of r_H/r_D = 1.4–1.5 observed on $FeO_x/Pt/TiO_2$ [74] and Pt/CNT [61, 102] catalysts shown in Figs. 10.19 and 10.21. It is noteworthy that an almost equal hydrogen isotope effect was reported on Au/CeO_2 [83] and $Au/\gamma\text{-}Al_2O_3$ [76]. A common isotope effect on these catalysts strongly supports the oxidation of CO by the same mechanism involving OH^- ions as observed on the $FeO_x/Au/TiO_2$ catalyst, that is, both Au^{3+} ion and metallic Au are indispensable for such a new oxidation reaction of CO as schematically described in Scheme 10.10. The role of Na^+ ion in the highly active Na^+−Pt/TiO_2 catalyst developed by Zhang et al. [65] for the low-temperature oxidation of HCHO is also not the activation of Pt, but providing a new catalytic reaction via ionic intermediates on the Pt catalyst.

As proved by using Pt/CNT and Pt/CNF with promoting materials and Pt/CNT-p and Pt/CNF-p with no promoting materials, the role of promoting materials need not be in contact with Pt on the support. One may understand the complexity of catalysis and how we confuse the role of promoting materials and the reaction mechanism.

Taking these results into account, superior catalytic activity of Au particles smaller than ~3 nm on specific oxides is perhaps a prerequisite for OH^- ions to react with CO, but it should be emphasized that the role of Au particles is essentially different from the role of Au^{3+} ions in the water gas shift reaction at 473 K proposed by Stephanopoulos et al. [63] on the Au/CeO_2 catalyst. From this viewpoint, the active Au surface shown in Fig. 10.29b reported by Chen and Goodman [69] is suggestive. They found an extremely active p(1 × 3) hybrid layer on an inactive p(1 × 1) Au layer on the surface of a TiO_x monolayer, which may create a new active material taking the form of a (1 × 3) hybrid Au layer, but this active layer is unstable as a catalyst for the oxidation of CO. Based on these results, they concluded that the size of Au particles is not an essential factor in the activity of Au catalysts, but the oxidation mechanism of adsorbed CO(a) on this unstable (1 × 3) hybrid Au layer is not clear.

As discussed in Part I of this book, the formation of unusual compounds on metals was confirmed by STM, which were named "**quasi-compounds**." On the other hand, the wetting growth of a TiO_x layer on precious metal surfaces is well known as the SMSI effect (strong metal support interaction). The oxide layer formed on metals does not necessarily lead to a passive surface; on some metal, the growth of oxide layers improves the activity for the catalytic activity for the oxidation of CO. Lambert et al. [70] observed unusual activity for the CeO_2 layers deposited on a Pt(111) surface for the adsorption and catalytic oxidation of CO. The adsorption and oxidation of CO on the Pt(111) were suppressed by depositing CeO_2 on the surface, and a passive surface was formed by the deposition of 1 ML of CeO_2 as shown in Fig. 10.31a, which is similar to the growth of a passive TiO_x layer on precious metals as observed in the SMSI effect. However, if the deposited CeO_2 layer was thicker than two monolayers, the $CeO_2/Pt(111)$ surface became suddenly active for CO oxidation, and the activity was almost equal to or greater than that of the Pt(111) surface. An interesting fact was that no adsorbed CO(a) was observed on this active $CeO_2/Pt(111)$ surface during the oxidation of CO. This phenomenon indicates that the oxidation rate of CO is faster than the adsorption rate of CO, which is similar to the result on the Pt foil observed in Fig. 7.3 for $\log (P_{co}/P_{O2}) = -5.0$ to -5.3, that is, the surface reaction of CO with oxygen is far more rapid than the adsorption of CO. In other words, reactive collision or adsorption of CO on this active $CeO_2/Pt(111)$ surface is the rate-determining step, and the reacted oxygen in CeO_2 layer is quickly recovered by O_2. The dynamic processes are similar to the rapid transport of OH^- ion from the FeO_x to Pt to react with adsorbed CO(a) to form $HCOO^-$. Transport process over the catalyst surface becomes clear by the reaction on the Pt/CNT, Pt/CNF, Pt/CNT-p, and CNF-p catalysts. Oxidation of CO(a) with O(a) on Pt is prohibited by strong adsorption of CO(a) at low temperature, but the reaction CO(a) with OH^- takes no retardation of

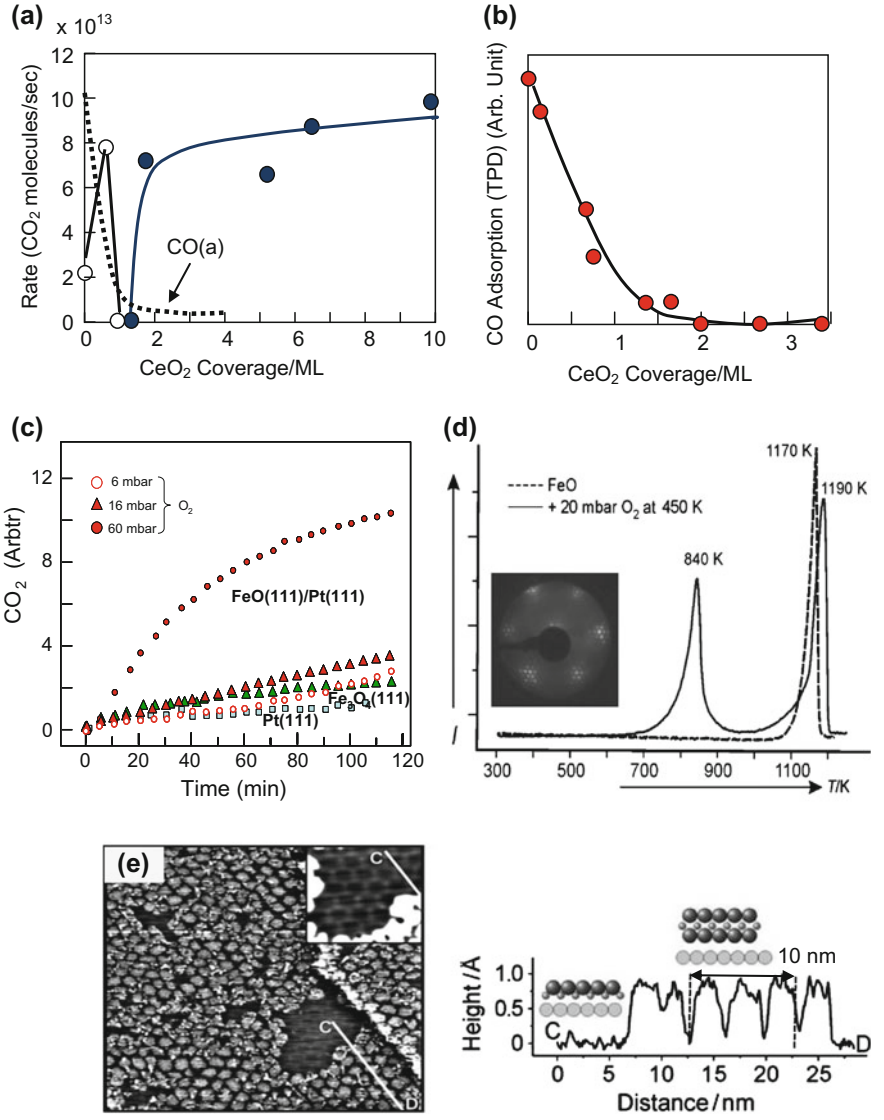

Fig. 10.31 **a** Adsorption and oxidation of CO on Pt(111) surface with deposited CeO_2. Activity of Pt was completely suppressed by one monolayer deposition of CeO_2, but the apparent activity was recovered by deposition of two or more monolayers of CeO_2 on the Pt surface. **b** Amount of CO adsorbed on Pt catalyst decreasing as increasing the deposition of CeO_2 on Pt(111) [70]. **c** Activity of FeO(111)/Pt(111) surface for the oxidation of CO at 450 K as a function of the total pressure of CO + O_2 (2 : 1). Activity of a nanometer-thick Fe_3O_4(111)/Pt(111) film in comparison with Pt(111) in CO + O_2 (40 : 20 mbar) at 450 K. **d** TPD spectra of a pristine FeO(111)/Pt(111) (*broken line*) and trilayer of (O–Fe–O–) on Pt(111) surface prepared in 20 mbar of O_2 at 450 K. **e** STM image of the FeO(111)/Pt(111) surface exposed to 5 mbar of O_2 at 300 K for 5 h and a proposed model of the surface layer [103, 104]

CO(a). The $HCOO^-$ formed on the Pt catalyst rapidly releases an electron and was followed by a reaction, $e + H^+ + O(a) \rightarrow OH(a)$, on the $FeO_x/Pt/TiO_2$ and Pt/CNF. Followed by these rapid steps, the rate-determining reaction HCOO (a) + OH $\rightarrow$ $CO_2 + H_2O$ takes place on the Pt.

A similar slow adsorption of O_2 followed by rapid surface reaction was also observed by Sun et al. [101, 105] for the oxidation of CO on FeO(111) multi-layers prepared on a Pt(111) surface in O_2. As shown in Fig. 10.31c, the FeO(111)/Pt(111) surface changes to an active surface for CO oxidation in 60 mbar of O_2, in which a specific trilayer structure is established, but this active surface has difficulty maintaining its high activity if the O_2 pressure becomes lower than a critical value. This phenomenon may indicate a dynamic balance of the formation of active FeO(111) multi-layers depending on the O_2 pressure, which is similar to the formation of labile CeO_2 layers on the Pt(111) surface, as observed in Fig. 10.31a. This phenomenon resembles a multi-component bismuth molybdates in the oxidation of propene to acrolein, CH_2=$CHCH_3 \rightarrow CH_2$=CHCHO, where the reactive lattice oxygen ion is quickly replenished with rapid diffusion attained by making multi-component oxides as described in Sect. 10.4.

Oxidation of CO with adsorbed O(a) on Pt is a simple reaction, but the reaction with labile lattice oxygen is far more complex, because it depends on the structure and a kind of quasi-compound of surface materials. Even if the oxidation reaction of CO to CO_2 on Pt, the reaction via $OH^- + CO \rightarrow HCOO^-$ is different catalytic oxidation of CO(a) with adsorbed O(a) on Pt, as was described in Sect. 10.4. This is the origin of the complexity of catalysis, and at the same time, it gives a hint of interesting oxidation reactions with labile OH^-.

As shown in Sect. 10.4, the catalytic oxidation of CO with O_2 improved by H_2 and/or H_2O on the $FeO_x/Pt/TiO_2$ [74], $FeO_x/Au/TiO_2$ [75], Pt/CNT [61], Au/CeO_2 [83], and $Au/\gamma\text{-}Al_2O_3$ [76] catalysts exhibits a common hydrogen isotope effect of r_H/r_D = 1.4–1.5 for H_2/D_2 and H_2O/D_2O. The same hydrogen isotope effect on these catalysts suggests a common reaction mechanism on these catalysts. However, the origin of the hydrogen isotope effect on the oxidation of CO enhanced by H_2/D_2 or H_2O/D_2O is not so clear, because the observed isotope effect is not the isotope effect on the rate constant, but on the rate of reaction. This means that the isotope effect on the concentration of key intermediates, OH(a)/OD(a) and HCOO (a)/(DCOO(a), $(\xi_2)_H/(\xi_2)_D$ in Eq (10.17), on the Pt surface should be considered.

If the oxidation of CO in H_2 takes place by the reaction involving H_2O, the selectivity is defined by the number of CO_2 molecules formed by a H_2O molecule during its residence time on the catalyst as expressed by $H_2O + \mathbf{n}$ (CO(a) + 1/2 O_2) $\rightarrow$ $H_2O + \mathbf{n}$ CO_2, where the H_2O molecule is formed by the oxidation of H_2.

From this viewpoint, selectivity of the oxidation of CO in H_2 (CO/O_2 = 1.0, CO/H_2 = 1/50) on the Au/CeO_2 catalysts changed by the crystalline shapes of CeO_2 observed by Yi et al. [77, 83] is quite interesting. As shown in Fig. 10.32, the conversion of CO depends on the crystalline shape of CeO_2 in the sequence polyhedra $\approx$ rods > cubes as shown in Fig. 10.32a, but the total consumption of O_2 by reaction with H_2 and CO is not affected by the crystalline shape of CeO_2, as shown in Fig. 10.32b. According to the definition proposed above, this means that

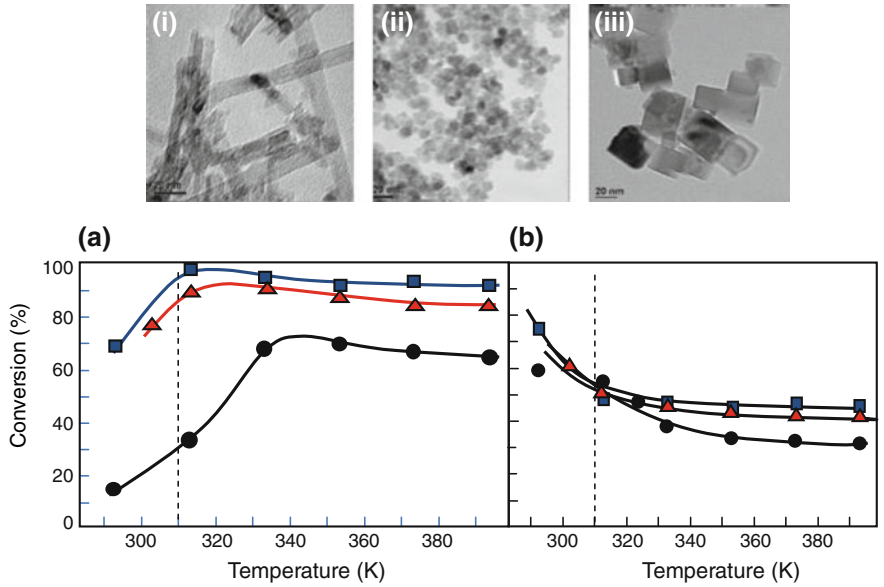

Fig. 10.32 TEM images of **(i)** Au/CeO_2 rods (0.92 wt%), **(ii)** Au/CeO_2 polyhedra (0.83 wt%), and **(iii)** Au/CeO_2 cubes (0.92 wt%). **a** Conversion of CO and **b** conversion of O_2 attained in the oxidation of CO in a flow of (CO(1%) + O_2 (1%) + H_2 (50%) + N_2) at 30,000 mL/g hr. on Au/CeO_2 rods (●), Au/CeO_2 polyhedra (■), and Au/CeO_2 cubes (▲) [77]

the residence time of H_2O depends on the crystalline shape of CeO_2. An interesting fact is that the fraction of $(Au^+ + Au^{3+})/(Au^0 + Au^+ + Au^{3+})$ depends on the crystal shape of CeO_2 according to the ratio (cube) : (polyhedron) : (rod) = 25.3 : 46.0 : 61.5 (%). It is also noteworthy that the oxidation of CO enhanced by H_2/D_2 exhibits a hydrogen isotope effect of $r_H/r_D = 1.44$ on the three Au/CeO_2 catalysts [83], which is almost equal to that observed for the oxidation of CO enhanced by H_2O on $FeO_x/Pt/TiO_2$, Pt/CNT, and $FeO_x/Au/TiO_2$ catalysts. The same isotope effect suggests the same oxidation mechanism of CO enhanced by H_2O on the Au/CeO_2 catalyst, that is, the oxidation of CO on Au metals is supported by OH^- ion transported from Au^{3+} to Au metal driven by the electrostatic gradient established by adsorbed H_2O. The value of "**n**" depends on the residence time of H_2O on the CeO_2, which depends on the fraction of $(Au^+ + Au^{3+})/Au$. In other words, a surface with a larger $(Au^+ + Au^{3+})/Au$ ratio offers a longer residence time for H_2O molecules on the surface, which results in the selectivity of the oxidation of CO in H_2 being influenced by the fraction of $(Au^+ + Au^{3+})$ ions on Au/CeO_2. The residence time of H_2O depending on the $(Au^+ + Au^{3+})$ ions at 150–170 K is responsible for the selective oxidation of CO in H_2 influenced by the crystal shape of CeO_2. We become aware that this phenomenon is caused by the residence time of a H_2O molecule in the 2-D space, which corresponds to the residence time of H_2O in the 3-D space of SiO_2 nanotubes holding Pt nano-rods inside the nanotubes, as in

Fig. 10.25. It should be realized that this phenomenon is essentially different from the role of nonmetallic Au^{3+} ion in the water gas shift reaction on Au/CeO_2 catalysts at temperatures above 473 K reported by Stephanopoulos et al. [63].

References

1. J. Horiuti and M. Polanyi, Trans. Farad. Soc., 30 **(1934)** 1164.
2. K-I. Tanaka, Adv. in Catalysis., Vol. 33, 99–158 **(1985)**.
3. K-I. Tanaka and T. Okuhara, Catal. Rev. Sci. and Eng. 15 (2) **(1977)** 249.
4. E. Nishimuyra, Y. Inoue, and I. Yasumori, Bull. Chem. Soc. Jpn., 48 **(1975)** 803.
5. T. Okuhara, K-I. Tanaka, and T. Miyahara, J.C.S. Chem. Comm. **(1976)** 42.
6. M. Wilde, K. Fukutani, W. Ludwig, B. Brandt, J-H. Fischer, S. Schauermann, and H-J. Freund, Angew. Chem. Int. Ed. 47 **(2008)** 9289.
7. A. Takeuchi, K-I. Tanaka, and K. Miyahara, J. Catal., 40 **(1975)** 94.
8. A. Takeuchi, K-I. Tanaka, and K. Miyahara, J. Catal., 40 **(1975)** 101.
9. K-I. Tanaka and T. Okuhara, J. Catal., 78 **(1982)** 155.
10. T. Okuhara and K-I. Tanaka, JCS., Faraday Trans. I. 75 **(1979)** 1403.
11. T. Okuhara and K-I. Tanaka, J. Phys. Chem.,82 **(1978)** 1953.
12. T. Okuhara and K-I. Tanaka, JCS, Faraday Trans. I, 75 **(1979)** 7.
13. T. Okuhara and K-I. Tanaka, J. Am. Chem. Soc. 98 **(1976)** 7884.
14. K-I. Tanaka, T. Okuhara, T. Sato, and K. Miyahara, J. Catal.,43 **(1976)** 360.
15. T. Okuhara, K-I. Tanaka and K. Tanabe, Chem. Comm. **(1977)** 180.
16. T. Okuhara and K-I. Tanaka, JCS, Chem. Comm. **(1976)** 199.
17. T. Okuhara, T. Kondo, K-I. Tanaka, and K. Miyahara, J. Phys. Chem., 81 **(1977)** 90.
18. B. Bogdanovic, B. Henc, H-G. Mussel, D. Walter and G. Wilke, Ind. Eng. Chem., 62 (12) **(1970)** 34.
19. K-I. Tanaka, T. Okuhara, K. Aomura, and K. Miyahara, JCS, Faraday Trans. I, 77 **(1981)** 1697.
20. S. Naito, Y. Sakurai, H. Shimizu, T. Onishi, and K. Tamaru, Trans. Faraday Soc., 67 **(1971)** 1529.
21. R.I. Burwell, Jr., A.B. Littlewood, M. Cardew, G. Pass and C.T.H. Stoddart, J. Am. Chem. Soc., 82 **(1960)** 6272.
22. K-I. Tanaka, H. Nihira, and A. Ozaki, J. Phys. Chem., 74 **(1970)** 4510.
23. Y. Yamaguchi and J. Hightower, J. Am. Chem. Soc., 99 **(1976)** 4201.
24. Y. Imizu, K. Tanabe and H. Hattori, J. Catalysis, 56 **(1979)** 303.
25. H. Hattori, Y. Tanaka and K. Tanabe, J. Am. Chem. Soc., 98 **(1976)** 4652.
26. K-I. Tanaka and T. Okuhara, J. Catalysis, 65 **(1980)** 1.
27. P. Eishens, W.A. Pliskin and M.S.D. Low, J. Catal., 1 **(1962)** 180.
28. R.J. Kokes, A.L. Dent, C.C. Chang and L.T. Dixon, J. Am. Chem. Soc., 94 **(1972)** 4429.
29. A.L. Dent and R.J. Kokes, J. Am. Chem. Soc.,92 **(1970)** 6709, ibid, 92 **(1970)** 6718.
30. R.L. Banks and G.C. Bailey, Ind. Eng. Chem., Prod. Res. Dev., 3 **(1964)** 170.
31. J.L. Herisson and Y. Chauvin, Makromol. Chem. 141 **(1971)** 161.
32. K-I. Tanaka, Appl. Catal. A. General, 188 **(1999)** 37.
33. J. Kress, W. Wesolek, and J.A. Osborn, J.C.S., Chem. Comm., **(1982)** 514.
34. M. Scholl, S. Ding, C.W. Lee, and R.H. Grubbs, Org. Lett. 1 **(1999)** 953.
35. J. Hung, E.D. Stevens, S.P. Nolan, J.L. Petersen, J. Am. Chem. Soc., 121 **(1999)** 2674.
36. K. Tanaka, K-I. Tanaka, and K. Miyahara, J.C.S. Chem. Comm. **(1980)** 666.
37. M. Kazuta and K-I. Tanaka, J.C.S. Chem. Comm. **(1987)** 616.
38. K. Tanaka and K-I. Tanaka, J.C.S. Chem. Comm. **(1984)** 748.
39. M. Kazuta and K-I. Tanaka, J. Catal., 123 **(1988)** 164.

40. C.J. Scaverian, J.C. Dewan, and R.R. Schrock, J. Am. Chem. Soc., 108 **(1986)** 2771.
41. J.B. Lee, G.J. Gajda, W.P. Schaefer, T.R. Haward, T. Ikariya, D.A. Straus, and R.H. Grubbs, J. Am. Chem. Soc., 103 **(1981)** 7358.
42. K. Tanaka, K-I. Tanaka, H. Takeo, and Chi Matsumura, J. Am. Chem. Soc., 109 **(1987)** 2422.
43. G. W. Keulks, J. Catalysis, 19 **(1970)** 232.
44. W. Ueda, Y. Moro-oka, T. Ikawa, J. Catalysis, 70 **(1981)** 409.
45. W. Ueda, Y. Moro-oka, T. Ikawa, J. Catalysis, 88 **(1984)** 214.
46. M. W. J. Wolf and Ph.A. Batist, J. Catalysis, 32 **(1974)** 25.
47. G. Vlaic, P. Vornasiero, S. Geremia, J. Kaspar, and M. Graziani, J. Catal., 168 **(1997)** 386.
48. A. Kato, S. Matsuda, F. Nakajima, M. Imanari, and Y. Watanabe, J. Phys. Chem., 85 **(1981)** 1710.
49. A. Kato, S. Matsuda, T. Kamo, F. Nakajima, H. Kuroda, and T. Narita, J. Phys. Chem., 85 **(1981)** 4099.
50. A. Golchet and J.M. White, J. Catal. 53 **(1978)** 266.
51. N. Al-Sarraf, J.T. Stuckless and D.A. King, Nature, 360 **(1992)** 243.
52. G. Blyholder, J. Phys. Chem., 68 **(1964)** 2772.
53. X. Lin et al, J. Am. Chem. Soc. 132 **(2010)** 7745.
54. X. Liu, O. Korotkikh, R. Farrauto, Appl. Catal., A. General, 226 **(2002)** 293.
55. O. Korotkikh and R. Farrauto, Catal. Today, 62 **(2000)** 249.
56. K-I. Tanaka, M. Shou, Hong He, and X. Shi, Catal. Letters, 110 **(2006)** 185.
57. K. Tamaru, Dynamic Heterogeneous Catalysis, Academic Press, London, New York, San Francisco **(1978)**.
58. M. Show, K-I. Tanaka, K. Yoshioka, Y. Moro-oka, and S. Nagano, Catal. Today, 90 **(1904)** 255.
59. K-I. Tanaka, M. Show, Hong He, X. Shi, and X. Zhang, J. Phys. Chem., C, 113 **(2009)** 12427.
60. A. Fukuoka and M. Ichikawa, Topics in Catal. 40 **(2006)** 103.
61. K-I. Tanaka, M. Shou, and Y.Yuan, J. Phys. Chem., C 114 **(2010)** 16917.
62. Y. Zhai, D. Pierre, R. Si, W. Deng, P. Ferrin, A.U Nilekar, G. Peng, J. A. Herron, D.C. Bell, H. Saltsburg, N. Mavrikakis and M.F. Stephanopoulos, Science 329 **(2010)** 1633.
63. Q. Fu, H. Saltsburg, and M. Flytzani- Stephanopoulos, Science, 301 **(2003)** 935.
64. M. Yang, S. Li, Y. Wang, J.A. Hrron, Y. Xu, L.F. Allard, S. Lee, J. Huang, M. Mavrikakis, and M.F. Stephanopoulos, Science **(2014)** 1260526.
65. C. Zhang, F. Liu, Y. Zhai, H. Ariga, N. Yi, Y. Liu, K. Asakura, M. Flytzani-Stephanopoulos and Hong He, Angew. Chem. Int. 51 **(2012)** 9628.
66. Y. Zhang, S. Anderson, and M. Muhammaed, Appl. Catal., B6 **(1995)** 325.
67. M. Haruta, Catal. Today, 36 **(1997)** 153.
68. M. Haruta,N.Yamada,T. Kobayashi, and S. Iijima, J. Catal. 115 **(1989)** 301.
69. M.S. Chen and D.W. Goodman, Science,306 **(2004)** 252.
70. C. Hardacre, R.M. Ormerod, R.M. Lambert, J. Phys. Chem.,98 **(1994)** 10901.
71. S.Yokoyama, K-I. Tanaka, and M. Seisho, JCS. Chem. Comm. **(1981)** 1061.
72. G.J. Hutchings, M.S. Hall, A.F. Carley, P. London, B.E. Solsona, C.J. Kiely, A. Herzing, M. Makkee, J.A. Moulijn, A. Overweg, J.C. Fierro-Gonzalez, J. Guzman, and B.C. Gates, J. Catal., 242 **(2006)** 71.
73. Chao Wang, Guangquan Yi, Haiqiang Lin, and Youzhu Yuan, Inter. J. of Hydrogen Energy, 37 (2012) 14124.
74. M. Shou and K-I. Tanaka, Catal. Letters, 111 **(2006)** 115.
75. M. Shou, H. Takekawa, D-Y. Ju, T. Hagiwara, Daling Lu, and K-I. Tanaka, Catal. Letters. 108 **(2006)** 119.
76. C.K. Costello, J.H. Yang, H.Y. Law, Y. Wang, J.N. Lin, L.D. Marks, M.C. Kung and H.H. Kung, Appl. Catal. A. General 243 **(2003)** 15.
77. G. Yi, Z. Xu, G. Guo, K-I. Tanaka and Y. Yuan, Chem. Phys. Lett. 479 **(2009)** 128.
78. K-I. Tanaka, Hong He, and Y. Yuan, RSC, Advances, 5 **(2015)** 949.

79. K-T. Tanaka, Hong He, M. Shou, X. Shi, Catal. Today, 175 **(2011)** 467.
80. X. Shi, K-I. Tanaka, Hong. He, M. Shou, W. Xu, and X. Zhang, Catal. Lett., 120 **(2008)** 210.
81. A. Ueno, T. Onishi, and K. Tamaru, Trans. Farad. Soc.,67 (197193585).
82. G.Y. Popova, Y.A. Chesalov, T.V. Andnishkevich, I.I. Zhkhalov, and E.S. Stoyanov, J. Mpl. Catal. A, 158 (2000) 345.
83. G. J. Millar, C.H. Rochester and K.C. Waugh, J. Catal. 155 (1995) 52.
84. C. Adamo and V. Barone, J. Chem. Phsy. 108 (1998) 664.
85. Z. Chang and G.Thornton, Surf. Sci., 459 (2000) 303.
86. C. Zhang, Hong He, and K-I. Tanaka, Appl. Catal. B, 65 (2006) 37.
87. J. Rasko, T. Kecskers, and J. Kiss, J. Catal. 224 (2004)261.
88. M. Yamada, D. Li, I. Honma, and H. Zhou, J. Am. Chem. Soc. 127 **(2005)** 13092.
89. J.L. Lu, H. Tang, S. Lu, H. Wu, and S. Ping Jiang, J. Mater. Chem., 21 **(2011)** 6668.
90. G. Yi, H. Yang, B. Li, H. Lin, K-I. Tanaka and Y. Yuan, Catal. Today, 157 **(2010)** 83.
91. R.B. Levy and M. Boudart, J. Catalysis, 32 **(1974)** 364.
92. Y. Okawa and K-I. Tanaka, Surf. Sci., 344 **(1995)** 1207.
93. Y. Okawa and K-I. Tanaka, Appl. Phys. Lett., 70 **(1997)** 3371.
94. F. Basolo and R.G. Pearson, Mechanism of Inorganic Solution, John Wiley & Sons, Inc. New York **(1958)**.
95. K-I. Tanaka, Bull. Chem Soc. Japan, 46 **(1973)** 3887.
96. K-I. Tanaka and A. Ozaki, J. Catal. 8 **(1967)** 1.
97. R.P. Iczkowski and J.L. Magrave, J. Am. Chem. Soc., 83 **(1962)** 3547.
98. A.Boffa, C. Lin, A.T. Bell, and G.A. Somorjai, J. of Catal. 149 (1994) 149.
99. N.A. Hodge, C.J. Kiely, R. Whyman, M.R.H. Siddiqui, G.J. Hutchings, Q.A. Pankhurst, F. E. Wagner, R.R. Rajaram, and S.E. Golunski, Catal. Today, 72 **(2002)** 133.
100. Y. Matsumoto, K. Sakamoto, Y. Okawa, S. Suto,and K-I. Tanaka, J. Chem. Phys., 107 **(1997)** 1.
101. S.T. Daniells, M. Kallee and J.A. Moulijn, J. Catal. 100 **(2005)** 39.
102. M.A. Bollinger and M.A. Vannice, Appl. Catal. B, 8 **(1996)** 417.
103. Y-N. Sun, Z-H. Qin, M. Lewndowski, E. Carrasco, M. Sterrer, S. Shaikhutdinov, and H. J. Freund, J. Catalysis, 266 **(2009)** 359.
104. Y-N. Sun, L. Giordano, J. Goniakowski, M. Lewandowski, Z-H. Qin, C. Noguera, S. Shaikhutdinov, G. Pacchioni, and H-J. Freund, Angew. Chem. 122 **(2010)** 4520.
105. C.K. Costello, M.C. Kung, H-S. Oh, Y. Wang, and H.H. Hung, Appl. Catal. A: General 232 **(2002)**159.
106. M.D. Kolb, G. Lehmpfuhl, and M.S. Zei, J. Electroanal. Chem., 179 **(1984)** 289.
107. G. Smit, N. Strukan, M.W.J. Craje, and K. Lazar, Appl. Catal. A: General 252 **(2006)**163.
108. J.L. Ayastuy, M.P. Gonzalez-Marcos, J.R. Gonzalez-Velasaaco, and M.A. Gutierrez-Ortiz, Appl. Catal., B 70 **(2007)** 532.
109. Se H. Oh, and R.M. Sinkevitch, J. Catal. 142 **(1993)** 254.
110. S. Alayoglu, A. U. Nilckar, M.Mavrikakis, B. Eichhorn, Nat. Mater. 7 **(2008) 333**.
111. K-I. Tanaka, M. Shou, H. Zhang, Y. Yuan, T. Hagiwara, A. Fukuoka, J. Nakamura and Daling Lu, Catal. Letters, 126 **(2008)** 89.

Chapter 11
Concluding Remarks

Abstract In this book, various unique new materials and their chemical reactions are taken up on solid surfaces as the reactions are restricted in two-dimensional space. Catalysis is attained by repeating the reaction of these new materials on the surface. By removing unnecessary migration of reaction intermediates during catalysis, one can deduce more accurate reaction mechanisms of catalysis. It would be very nice if this book would make wariness in spinning facile stories of catalysis by using an average data of catalyst attained and characterized by various instruments without care of dynamics of chemical reactions on the surface.

When we consider the surface as a newly formed material by breaking of three-dimensional solid materials, the chemical reaction of surface atoms provides additional new materials on the surface. According to this idea, we could say that no one knows the real chemical properties of solid materials. In fact, when two-dimensional materials such as graphene, carbon nano-tubes, graphite, and a lamellar compound MoS_2 are considered, we can know that the properties of the edge made by breaking are different from these of the two-dimensional materials. It is clearer, considering a polymer molecule, that the properties of the radial or ion made by breaking are substantially different from the properties of polymer molecule itself. From this point of view, the phenomena taking place on the surface are considered as the chemical properties of unusual materials existing on the solid materials.

According to this idea, the reaction of surface atoms with adsorbed atoms or molecules will provide additional new materials that can exist only on a specific surface. The growth of (–Ni–O–) and (–Ni–H–) strings and their 2-D array on a Ni (110) surface exposed to O_2 and H_2, as shown in Fig. 4.2, is a prominent example. The new compounds have their own structure and own stoichiometry likely molecules, but these compounds cannot be taken out from the surface. Therefore, they are named "**quasi-compounds**" in this book. Some quasi-compounds undergo reversible chemical reactions only on the specific surface; a typical example is the reaction of $(Cu_2)_4 + O_2 \rightleftharpoons (–Cu–O–)_n$ on the Ag(110) surface, as shown in Fig. 5.1. Furthermore, the reaction of a quasi-compound of (–Ag–O–) with CO_2 forms

K. Tanaka, *Dynamic Chemical Processes on Solid Surfaces*,
DOI 10.1007/978-981-10-2839-7_11

additional new quasi-compound of ($AgCO_3$), which provides a hybrid surface of [(–Ag–O–) + ($AgCO_3$)] on the Ag(110) surface. The reaction of these quasi-compounds formed on the Ag(110) surface represents unique reaction. If Cu atoms are vaporized on this hybrid surface, the Cu atoms react selectively with the (–Ag–O–) strings, and a new hybrid surface of [(–Cu–O–) + ($AgCO_3$)] is formed on the Ag(110) surface. Interestingly, if the hybrid surface of [(–Ag–O–) + ($AgCO_3$)] is scanned with a STM W-tip contaminated with Cu atoms and undergoes another selective reaction with ($AgCO_3$), a hybrid [(–Ag–O–) + (–Cu–O–)] pattern is formed on the Ag(110) surface. That is, we can regulate the selective reaction of Cu atoms by local electrostatic field as shown in Fig. 5.2, and it is named "atom painting." This phenomenon suggests controlled chemical reactions of quasi-compound on the surface by using the local electrostatic field.

When an atom or molecule is transported from gas phase to two-dimensional space of the surface, the atoms and molecules lose the freedom via precursor states on the surface. The morphology of growing metal particles under the electrochemical potential, as shown in Fig. 2.3, suggests the growth of metal particles via a 2-D precursor array of metal atoms, which is more likely to the reconstructed surface observed under the electrochemical potential. We can recognize more strictly the existence of precursor state molecules in the dissociation of alcohol molecules (ROH) on the (7 × 7)-Si(111) surface, where the dissociation probability of a precursor ROH molecule within a half-unit cell on the (7 × 7)-Si(111) surface is given by local conformation of Si adatoms, that is, the dissociation probability of a precursor-state ROH on a Si adatom becomes four times larger when the number of Si rest atoms adjacent to a Si adatom becomes two times.

A feature of materials formed on the surface is that some materials are passive but some others are active for chemical reactions. If materials undergo repeated reaction over a surface, one can recognize the surface as a catalyst for a specific reaction. However, the role of promoting materials improving catalytic reactions is one of the difficult problems, because promoting materials are not active as catalyst. A good example is the oxidation of CO with O_2 enhanced by H_2 or H_2O on Pt catalyst, which occurs only in the presence of some specific promoting materials as discussed in Sects. 10.4 and 10.5. In this case, a local electrostatic gradient established between the Pt and promoting materials by ionization equilibrium of H_2O molecules, $H_2O \rightleftharpoons H^+ + OH^-$, is quite important.

In **Part-II**, it is precisely described how the dynamic reaction mechanism in catalysis is derived. When a chemical reaction takes place on a surface, all processes are restricted in two-dimensional space, which is essentially different from the reaction in gas phase or in liquid phase. In other words, the dynamics of intermediates should be restricted in two-dimensional space with anisotropic interactions.

In this book, one important strategy to deduce the correct mechanism in catalysis is presented: how to remove unnecessary processes of the intermediates in catalysis. A typical example is the hydrogenation of olefins and the isomerization of olefins on the one-dimensional edge of MoS_2. By restricted surface migration of H atoms, it was proved that the active sites for the hydrogenation are different from those for

the isomerization of olefins on lamellar MoS_2 (in 1-D space), which are well rationalized by models such as ^{2}Mo-H and $^3Mo(H)_2$ sites. Furthermore, one can recognize a restricted internal rotation of bulky alkyl group in intermediates in a catalytic reaction as shown in Fig. 10.5 in Sect. 10.1.

Considering the reverse process, the desorption of molecules takes place via a precursor state. When a Pd(110) surface adsorbed with NO is heated in vacuum, N_2 and NO are simultaneously desorbed at 490 K. The N_2 takes a very narrow "off-normal spatial distribution" along the $\langle 001 \rangle$ axis expressed by a $\cos^{46}(\theta \pm 38°)$ distribution, which is a symbolic phenomenon reflecting the anisotropic collision of N(a) and NO(a) in two-dimensional space of Pd(110) surface, where the anisotropic collision of adsorbed NO(a) molecule with diffused N(a) gives a very sharp off-normal emission of N_2 from the Pd(110), as shown in Fig. 8.2. However, this reaction is not the catalytic reaction forming N_2 by the reaction of NO with H_2 on Pd(110) and the N_2 by the catalytic reaction that takes on cos θ distribution with thermal equilibration.

The metathesis reaction of propene, $2\ CH_2 = CH–CH_3 \rightarrow CH_2 = CH_2 + CH_3CH_2 = CH–CH_3$, is also a catalytic reaction by forming functional sites on the surface. When a MoO_3 is exposed to propene, $Mo = CH_2$ and/or $Mo = CHCH_3$ are synthesized on the surface, and the metathesis reaction proceeds by alternating reaction of propene with $Mo = CH_2$ and $Mo = CHCH_3$. In this metathesis reaction, the two reactions are simultaneously proceeded, one is productive metathesis and the other is the degenerate metathesis reaction expressed by $CH_2 = CH–CH_3 + CD_2 = CD–CD_3 \rightarrow CH_2 = CD–CD_3 + CD_2 = CH–CH_3$. We cannot recognize the degenerate metathesis, but it was shown 10–30 times more frequently compared to the productive metathesis reaction by using deuterium-labeled molecules. If we compare the degenerate metathesis reaction on $Mo = CH_2$ to $Mo = CH–CH_3$, the turnover frequency of the reaction is 100–900 times on the $Mo = CH–CH_3$, that is, the reaction dynamics is very sensitive to the intermediate species formed on the surface, as described in Sect. 10.3.

In some catalytic reactions, key intermediates are steadily formed by the reaction of surface metal atoms with molecules. Formation of CH_4 by the hydrogenation of CO with H_2 on Ni surface and formation of NH_3 by the hydrogenation of N_2 with H_2 on Fe catalysts are typical examples. The activity of Ni surfaces depends on the number of Ni atoms which can contribute to the formation of labile Ni_4C on the Ni surface. The Ni_4C is hydrogenated to CH_4 via CH_2. The activity of Fe surfaces depends also on the number of Fe atoms forming labile Fe_xN on the Fe surface. The Fe_xN is hydrogenated to NH_3 via NH and NH_2 on the Fe surface.

Finally, the role of promoting materials in catalysis is discussed in Sects. 10.4 and 10.5. Promoting materials are quite important in practical catalysis, but the promoting effect is mostly found empirically. Therefore, the role of promoting materials is vague, and it is very often explained by the terms "synergetic effect" or "activation of metals." In Sects. 10.4 and 10.5 in **Part-II**, the role of promoting materials is discussed and observed on the oxidation of CO enhanced by H_2 and/or H_2O. Catalytic oxidation of CO on Pt/Al_2O_3 and Pt/TiO_2 catalyst takes no effect of H_2 or H_2O, but the oxidation of CO with O_2 is markedly enhanced by H_2 and/or H_2O on the $FeO_x/Pt/Al_2O_3$ and $FeO_x/Pt/TiO_2$ catalyst. So far, the role of promoting

materials such as observed on the oxidation of CO has been explained as an activation of Pt or a synergetic effect on Pt by premising the reaction of adsorbed CO(a) with O(a) on Pt. The oxidation of CO on the Pt/CNT–p and Pt/CNF–p catalyst takes no effect of H_2 as shown in Fig. 10.19, but the oxidation of CO is markedly enhanced by H_2 on the Pt/CNT and Pt/CNF catalysts. The difference is that the CNT and CNF have Ni-MgO and FeO_x at their terminal end, but CNT–p and NF–p purified these promoting materials. It was evidently proved that the Pt particles are perfectly separated from the promoting materials of Ni–MgO and FeO_x on the Pt/CNT and Pt/CNF. It is evident that the role of promoting materials is not the synergy effect made by contacting/promoting materials with Pt.

Systematic spectroscopic studies with in situ DRIFT spectroscopy on the FeO_x/Pt/TiO_2 catalyst presented a new catalytic oxidation reaction of CO via HCOO(a) with OH(a) on the Pt. The role of promoting materials is to provide OH^- ions to Pt, and the OH^- ion react with CO(a) to form $HCOO^-$ on the Pt, which is followed by the rate-determining reaction of HCOO(a) with highly reactive OH(a), which is a new catalytic oxidation of CO. This new catalytic oxidation of CO represents an important role of H_2O molecules, that is, H_2O molecules act as a molecular catalyst working in two-dimensional space. The role of H_2O molecule is described by an equation of $\mathbf{n}(CO + 1/2\ O_2) + H_2O \rightarrow \mathbf{n}\ CO_2 + H_2O$, where "**n**" is a turnover number of H_2O molecule, that is, number of CO_2 molecules produced by one H_2O until it leaves from the catalyst surface. According to this mechanism, the selectivity for the oxidation of CO in H_2 is given by n/(n + 1). According to this mechanism, we can expect the selectivity of 50% ∼ ca.100% depending on the residence time of H_2O molecules. The selective oxidation of CO in H_2 on the Pt-nano-rods held inside the SIO_2- nano-tubes, as shown in Fig. 10.25, proves well this new concept for the selective oxidation of CO in H_2.

Finally, I wish to mention that our basic knowledge of supported catalysts has been completely changed in these last 25 years by astonishing instrumental developments, so that the characterization of metals supported on oxides becomes popular. However, we have to beware of excessive dependence on the instrumental characterization of catalysts, as this sometime hinders the sound understanding and sound development of catalysis by forgetting to prove the chemical reaction itself. There is still a large barrier hindering our understanding of the dynamics in chemical processes taking place in two-dimensional space of the surface. It would be not so difficult to characterize active catalyst by using various tools, but the mechanism of catalysis is difficult to clarify without the dynamics of intermediates in catalysis. We could anticipate the real mechanism only by well-planned experiments. For this reason, we should be wary of facile spinning stories depending on the instrumental characterization.